

Explore the nature of dark matter in the context of galaxy formation

Thesis by
Xuejian Shen

In Partial Fulfillment of the Requirements for the
Degree of
Doctor of Philosophy in Physics

The logo for the California Institute of Technology (Caltech), featuring the word "Caltech" in a bold, orange, sans-serif font.

CALIFORNIA INSTITUTE OF TECHNOLOGY
Pasadena, California

2023
Defended May 19, 2023

© 2023

Xuejian Shen

ORCID: 0000-0002-6196-823X

All rights reserved except where otherwise noted

ACKNOWLEDGEMENTS

I would like to express my profound gratitude to my advisor, Prof. Philip Hopkins, for his invaluable guidance, support, and mentorship throughout the course of my graduate research. His expertise, dedication, and patience have been indispensable in shaping my academic and personal development. I am truly grateful for the opportunity to work under his supervision.

I extend my appreciation to my thesis committee members, Prof. Kathryn Zurek, Prof. Sunil Golwala, and Prof. Christopher Martin, for their insightful feedback, constructive criticism, and valuable suggestions. Their expertise and commitment to advancing the field have served as an inspiration to me.

My sincere thanks go to my colleagues in the Physics and Astronomy department for their constant encouragement, camaraderie, and invaluable assistance in the laboratory and fieldwork. Our stimulating discussions and shared experiences have made this journey both enjoyable and enlightening.

I would like to express my gratitude to the Texas Advanced Computing Center for granting me access to their computing facilities and invaluable resources.

I am immensely grateful for the unwavering support and love of my family. To my parents, Pu Wang and Jixiang Shen, thank you for believing in me and providing a strong foundation upon which I could build my dreams. Your constant encouragement has been the driving force behind my pursuit of academic excellence.

Lastly, I would like to extend my deepest gratitude to my partner, Yihong Huang, for her love, understanding, and patience throughout this journey. Your unwavering support and shared laughter have been a source of strength and motivation during challenging moments.

This thesis is dedicated to all those who have contributed to my growth as a researcher and to the advancement of knowledge in the field of cosmology and galaxy formation.

ABSTRACT

The nature of dark matter (DM) is a fundamental question in modern cosmology. Despite its significant role in various physical processes throughout the Universe, the particle nature of DM remains elusive. With the non-detection of classical candidates (e.g. WIMPs), the theoretical space for DM is becoming increasingly open. This thesis revolves around studying the nature of DM in the context of structure formation and we will focus on a category of DM with self-interactions (SIDM), which can be constrained only through astrophysical probes if DM has no coupling with the standard model particles. Utilizing advanced cosmological hydrodynamical simulations, we examine the effects of DM elastic and dissipative self-interactions on galaxy structure and their interplay with baryonic physics processes. Our numerical studies encompass a range of systems, such as Local dwarf galaxies, massive galaxy clusters in the Local Universe, and rare massive quasar-host galaxies at high redshift ($z \gtrsim 6$). In Local dwarf galaxies, we analyze the unique signatures of dissipative self-interacting DM (dSIDM) with typical self-interaction cross-section $\sigma/m \sim 0.1\text{-}10 \text{ cm}^2 \text{ g}^{-1}$ and dissipation factor ~ 0.5 . We find a universal cuspy central density profile and systematic changes in halo morphology in dSIDM. By comparing our results with observations, we derive constraints for effective parameters of dSIDM and identify the parameter space where it remains viable and exhibits interesting observational implications. For a similar type of dSIDM with fairly low $\sigma/m \lesssim 0.05 \text{ cm}^2 \text{ g}^{-1}$, we also explore the possibility that the direct collapse of dSIDM halos at high redshift can seed supermassive black holes and serve as progenitors for massive bright quasars observed at high redshift. This scenario predicts a large population of quiescent supermassive black holes (SMBHs) at high redshift, which could be tested by future LISA observations. Lastly, in Local massive galaxy clusters, we compare the X-ray morphology of hot gas in observed clusters with simulations of elastic SIDM. Although SIDM models with large interaction cross-sections ($\sigma/m \gtrsim 0.5 \text{ cm}^2 \text{ g}^{-1}$) are favored, uncertainties from cooling and feedback physics in galaxy clusters must be taken into account. This thesis summarizes the findings and constraints on DM properties, with a particular emphasis on its potential self-interactions, as derived from a combination of research projects.

PUBLISHED CONTENT AND CONTRIBUTIONS

- [1] Xuejian Shen, Philip F. Hopkins, Lina Necib, Fangzhou Jiang, Michael Boylan-Kolchin, and Andrew Wetzel. Dissipative dark matter on FIRE - I. Structural and kinematic properties of dwarf galaxies. *MNRAS*, 506(3):4421–4445, September 2021. doi: 10.1093/mnras/stab2042.
- [2] Xuejian Shen, Thejs Brinckmann, David Rapetti, Mark Vogelsberger, Adam Mantz, Jesús Zavala, and Steven W. Allen. X-ray morphology of cluster-mass haloes in self-interacting dark matter. *MNRAS*, 516(1):1302–1319, October 2022. doi: 10.1093/mnras/stac2376.
- [3] Xuejian Shen, Philip F. Hopkins, Lina Necib, Fangzhou Jiang, Michael Boylan-Kolchin, and Andrew Wetzel. Dissipative Dark Matter on FIRE: II. Observational signatures and constraints from local dwarf galaxies. *arXiv e-prints*, art. arXiv:2206.05327, June 2022. doi: 10.48550/arXiv.2206.05327.
- [4] Huangyu Xiao, Xuejian Shen, Philip F. Hopkins, and Kathryn M. Zurek. SMBH seeds from dissipative dark matter. *J. Cosmol. Astropart. Phys.*, 2021(7):039, July 2021. doi: 10.1088/1475-7516/2021/07/039.

Xuejian Shen is the leading author of all these four projects. Xuejian Shen was involved in the conception of the project, designing and performing numerical simulations, data analysis, building (semi-)analytical models as well as writing manuscripts.

TABLE OF CONTENTS

Acknowledgements	iii
Abstract	iv
Published Content and Contributions	v
Table of Contents	v
List of Illustrations	viii
List of Tables	xxxvii
Chapter I: Introduction	1
1.1 Motivations for DM alternative to collisionless cold DM	1
1.2 DM with self-interactions	2
1.3 Beyond Local dwarf galaxies	5
Chapter II: Dissipative DM – Simulations	9
2.1 Abstract of the chapter	9
2.2 Simulations	12
2.3 Relevant time scales	14
2.4 Simulation Results	21
2.5 Halo shape	37
2.6 Discussion	40
2.7 Comparison with other simulation physics	47
2.8 Summary of the chapter	51
Chapter III: Dissipative DM – observational constraints	55
3.1 Abstract of the chapter	55
3.2 Simulations	56
3.3 Galaxy baryonic content	61
3.4 Galaxy circular velocity profiles	68
3.5 Satellite counts	79
3.6 Summary of the chapter	82
3.7 Resolution dependence of satellite properties	84
Chapter IV: Dissipative DM – SMBH seeding	87
4.1 Abstract of the chapter	87
4.2 Simulating black hole formation in isolated halos	87
4.3 Cosmological evolution and abundance of SMBHs	100
4.4 Consistency with low redshift SMBHs	114
4.5 Observational constraints of tdSIDM	118
4.6 Summary of the chapter	119
4.7 Convergence Testing	121
4.8 Considerations in Centrifugal Barrier and Fragmentation	122
4.9 Consideration of the universal collapse fraction	126
Chapter V: Signatures of elastic SIDM in cluster mass halos	129
5.1 Abstract of the chapter	129

5.2 Simulations	130
5.3 Observational samples	132
5.4 Methods	134
5.5 Results	138
5.6 Discussions	151
5.7 Summary of the chapter	156
Chapter VI: Conclusions	159
6.1 DSIDM – simulations and observational signatures	159
6.2 SIDM in massive high-density systems	161
6.3 Future works	163
Bibliography	164

LIST OF ILLUSTRATIONS

<i>Number</i>	<i>Page</i>
2.1	
Top: Relevant time scales of the physical processes involved in dSIDM halos versus one-dimensional velocity dispersion of the system.	
We have assumed that the local DM density is $\rho_{\text{dm}} = 2 \times 10^8 M_{\odot}/\text{kpc}^3$, a typical value at dwarf galaxy centers. We show the collision time scale (t_{coll}) and dissipation time scales (t_{diss}) of all the dSIDM models studied in this chapter as well as the dynamical time scale (t_{dyn}). All the time scales are normalized by the Hubble time scale at $z = 0$ ($t_{\text{h}} \equiv 1/h_0$). The dissipation time scales are calculated assuming $f_{\text{diss}} = 0.5$. The shaded regions show the typical one-dimensional velocity dispersions in the classical (e.g. Milky Way satellites) and bright dwarf galaxies (e.g. LSB galaxies). In dwarf galaxies, dissipation and collision time scales are much larger than the dynamical time scale, but can become considerably shorter than the Hubble time scale. The velocity-dependent model becomes less dissipative ($t_{\text{diss}}/t_{\text{h}}$ becomes larger) in more massive galaxies (with larger velocity dispersion) while models with constant cross-sections become more dissipative.	
Bottom: Dissipation time scales versus one-dimensional velocity dispersion of the system with f_{diss} varying from 0.1 to 0.9.	
The symbols are the same as the top panel. For each model, the upper boundary of the shaded region corresponds to the case $f_{\text{diss}} = 0.1$ and the lower boundary corresponds to the case $f_{\text{diss}} = 0.9$.	
	10

2.2 Visualizations of four DM halos in simulations with CDM versus dSIDM. The images are DM surface density maps, projected along the z -direction of simulation coordinates, at $z = 0$ with a logarithmic stretch. The dynamical ranges are adjusted based on the maximum/median intensities of the pixels (but remain the same for the same halo). The side lengths of the images are all chosen to be $0.8 \times R_{\text{vir}}$ of the CDM run. In the first row, we show the halos in the CDM. In the second row, we show the halos in the velocity-dependent dSIDM model. In the third row, we show halos in the dSIDM model with constant cross-section $1 \text{ cm}^2 \text{ g}^{-1}$. The halos are ordered from left to right by their virial masses. In each image, the outer dotted circle indicates the radius R_{500} (the density enclosed is 500 times the critical density at $z = 0$) which represents the overall size of the halo. The inner dashed circle indicates the radius $R_{\text{core}} \equiv 10 \times R_{0.1\%}$ (the mass enclosed in a sphere of radius $R_{0.1\%}$ is 0.1% the virial mass of the halo) which represents the core size of the halo. Comparing the core sizes, the halos in the dSIDM model are visibly more concentrated than their CDM counterparts. For the velocity-dependent dSIDM model, since the self-interaction cross-section decreases in more massive halos, the increased concentration of halo is less apparent in more massive halos. For the dSIDM with constant cross-section, halos of all masses are consistently more concentrated than their CDM counterparts. 18

- 2.3 **A gallery view of the structural and kinematic properties of dwarf galaxies in simulations.** From top to bottom, in each row, we show the three-dimensional total mass density ($\rho_{tot} = \rho_{dm} + \rho_{star} + \rho_{gas}$), circular velocity ($V_{circ} \equiv \sqrt{GM_{enc}^{tot}(r)/r}$), the three-dimensional velocity dispersion of DM ($\sigma_{3d} \equiv \sqrt{\sigma_r^2 + \sigma_\theta^2 + \sigma_\phi^2}$), velocity anisotropy of DM ($\beta \equiv 1 - (\sigma_\theta^2 + \sigma_\phi^2)/2\sigma_r^2$), and rotation velocity versus velocity dispersion of DM (V_{rot}/σ_{3d}) averaged in spherical shells as a function of galactocentric distance for three simulated galaxies. We compare three categories of DM models: CDM, eSIDM (elastic SIDM model with a constant cross-section $1 \text{ cm}^2 \text{ g}^{-1}$), and dSIDM (dissipative SIDM models with various cross-sections, as defined in Table 2.1). The gray shaded regions in the first row of plots indicate $0.2\% - 0.8\% R_{vir}^{cdm}$, which is the aperture we will later use to measure the slopes of the density profiles (see Section 2.4 and Figure 2.5-2.7). The gray dashed horizontal line in the fourth row is a reference line, indicating isotropic velocity dispersion ($\beta=0$). In general, dSIDM models produce cuspy central density profiles in the simulated dwarf galaxies, as opposed to the cored central density profile in CDM and eSIDM models. As a consequence, the circular velocities at the center of the galaxies increase. In dSIDM models with $(\sigma/m) \geq 1 \text{ cm}^2 \text{ g}^{-1}$, coherent rotation of DM becomes prominent, and random velocity dispersion is suppressed. 19
- 2.4 **Stellar mass versus halo mass relation of galaxies in simulations.** The stellar masses and halo masses of simulated dwarf galaxies are presented with open markers (as labeled). We compare them with the observational results derived through abundance matching from Moster et al. [1], Brook et al. [2], Garrison-Kimmel et al. [3]. The black dashed lines show $\sim 95\%$ inclusion contour assuming the scatter of the relation estimated in Garrison-Kimmel et al. [3]. Regardless of the DM model, the simulated galaxies are consistent with the observational relation. 22

- 2.5 *Left: Total mass density profiles of the classical dwarf galaxies in simulations.* The three classical dwarfs presented here are m10q, m10b and m10v. The total mass density profiles in different DM models are shown (as labeled). They can be compared to the NFW profiles derived by fitting the density profiles at large radii of the halos ($0.5 r_{1/2}^{\text{cdm}} < r < 20 r_{1/2}^{\text{cdm}}$), and the ratios of the density profiles to the NFW fits are shown in the lower sub-panel. The gray shaded region denotes the range of radii where we measure the slopes of the density profiles below. The purple dotted vertical line indicates the average convergence radius (~ 70 pc) of the classical dwarfs (see Table 2.1).
- Right: Local power-law slopes of density profiles of the classical dwarf galaxies.* The slopes are derived by fitting the nearby density profile with the power-law. In these classical dwarfs, the CDM model predicts cored central density profiles due to baryonic feedback. The eSIDM model produces cores of slightly bigger sizes and shallower slopes. The dSIDM model with $(\sigma/m) = 0.1 \text{ cm}^2 \text{ g}^{-1}$ still produces cored profiles but with higher central densities and steeper slopes than their CDM counterparts. The dSIDM models with effective cross-section $> 0.1 \text{ cm}^2 \text{ g}^{-1}$ all produce cuspy central density profiles with power-law slopes centering around -1.5 . These profiles are even steeper than the NFW profiles. 23

2.6 *Left: Total mass density profiles of the bright dwarf galaxies in simulations.* The three bright dwarfs presented here are m11a, m11b, and m11q. The notation is the same as Figure 2.5. The purple dotted vertical line here indicates the average convergence radius (~ 200 pc) of the bright dwarfs (see Table 2.1). *Right: Local power-law slopes of the density profiles of the bright dwarf galaxies.* In these bright dwarfs, the CDM model again predicts cored central density profiles with even larger cores (\sim kpc) than the classical dwarfs due to stronger baryonic feedback. The eSIDM model produces cores of similar sizes and slopes. The velocity-dependent dSIDM model has relatively low effective cross-sections ($\sim 0.01 \text{ cm}^2 \text{ g}^{-1}$) in these dwarfs. This model still produces cores but with slightly higher central densities than their CDM counterparts. The dSIDM models with relatively high effective cross-sections ($\gg 0.01 \text{ cm}^2 \text{ g}^{-1}$) still produce cuspy and power-law-like central density profiles. The power-law slopes center around -1.5 with a scatter from -2 to -1 . . . 26

2.7 Slopes of the central density profiles of dwarf galaxies in the simulation suite. The slopes are measured at $0.2 - 0.8\% R_{\text{vir}}^{\text{cdm}}$. The slopes measured in simulations with different DM models are shown in open markers (as labeled). Galaxies are ordered from left to right based on their stellar-to-halo mass ratios (M_*/M_{halo}) and are classified as classical dwarfs and bright dwarfs. (The ultra-faint dwarf m09 in the suite also has its M_*/M_{halo} value lying in the classical dwarf regime.) The asymptotic behaviors of the slopes at the low mass end are clearly different between different DM models. In low-mass dwarf galaxies, the density profiles in dSIDM models with $(\sigma/m) \geq 1 \text{ cm}^2 \text{ g}^{-1}$ and the velocity-dependent model converge to a slope of ~ -1.5 (indicated by the thick red horizontal line). The slope is steeper than the asymptotic slope -1 of the NFW profile (~ -1.1 at the radii we measure the slope, indicated by the thick black horizontal line). In contrast, the dSIDM model with $(\sigma/m) = 0.1 \text{ cm}^2 \text{ g}^{-1}$ can still produce small cores in some dwarf galaxies with relatively strong baryonic feedback, with $\alpha \sim -1$ at the radius of measurement and becoming even shallower at smaller radii as shown in the right panels of Figure 2.5 and 2.6. In the bright dwarfs, the velocity-dependent dSIDM model produces cored profiles with $\alpha \sim -0.5$. The dSIDM models with constant cross-sections still produce cuspy density profiles with slopes centering around -1.5 but scattering from -2 to -1 . Unlike dSIDM models, density profiles in CDM are shallower than the NFW profile and are shallower in more massive dwarf galaxies, due to stronger baryonic feedback there (indicated by the thick cyan line). The eSIDM model consistently produces cored density profiles with slope ~ -0.2 in most of the dwarf galaxies (indicated by the thick gray horizontal line). We note that all the thick reference lines are meant to label different “tracks” and are rigorous fits to the simulation results. 29

- 2.8 **Top: Slope change versus effective self-interaction cross-section of dwarf galaxies in simulations.** $\Delta\alpha$ is defined as the difference in slopes measured at $0.2 - 0.8\% R_{\text{vir}}^{\text{cdm}}$ between galaxies in dSIDM and CDM. The red dashed line labels the qualitative trend (not rigorous fitting). In the regime where $(\sigma/m)_{\text{eff}} < 1 \text{ cm}^2 \text{ g}^{-1}$, the steepening of central profiles induced by dissipative DM self-interactions becomes progressively stronger in systems with higher effective cross-sections. In the regime where $(\sigma/m)_{\text{eff}} > 1 \text{ cm}^2 \text{ g}^{-1}$, the steepening of central profiles saturates. **Bottom: Slope change versus dissipation time scale at halo center.** When $\log(t_{\text{diss}}^{\text{c}}/t_{\text{h}}) > -1$, the density profiles become steeper as $t_{\text{diss}}^{\text{c}}$ decreases while the steepening saturates when $\log(t_{\text{diss}}^{\text{c}}/t_{\text{h}}) < -1$ 30
- 2.9 **Coherent rotation velocity relative to velocity dispersion of DM in simulations.** The coherent rotation velocities and the velocity dispersions are measured in spherical shells as discussed in the main text. We present the results in CDM and dSIDM with $(\sigma/m) = 1$ and $10 \text{ cm}^2 \text{ g}^{-1}$. For each model, we show the results of five dwarf galaxies: m10q, m10b, m10v, m11a, and m11b. The coherent rotation becomes more prominent inside $\sim 1\% R_{\text{vir}}$ as the self-interaction cross-section increases, but not in every galaxy. The two galaxies that have rotation velocities comparable to velocity dispersions are m10q and m11b. 33
- 2.10 **Velocity anisotropy profiles of DM in simulated dwarf galaxies.** The velocity anisotropies are calculated using Equation 2.13. We present the results in CDM and dSIDM with $(\sigma/m) = 1$ and $10 \text{ cm}^2 \text{ g}^{-1}$. For each model, we show the results of the same five galaxies as in Figure 2.9. The velocity anisotropy decreases as the self-interaction cross-section increases and eventually becomes negative, suggesting that the velocity dispersion is more dominated by the tangential component. This is consistent with more coherent rotation found in Figure 2.9. 33

2.11 **Phase space distribution function of DM in simulated classical dwarfs.** We present the two-dimensional density distribution of DM in the $v_\phi - v_r$ phase space, $d\rho_{\text{dm}}/dv_r dv_\phi$. In the three columns, we show the distribution in three radial bins: central, $r < r_{1/2}^{\text{cdm}}/3$, intermediate, $r_{1/2}^{\text{cdm}}/3 < r < 3r_{1/2}^{\text{cdm}}$, and “outskirt”, $3r_{1/2}^{\text{cdm}} < r < 0.5R_{\text{vir}}^{\text{cdm}}$, respectively. From inside out, each contour is determined such that it encloses a certain percentile of DM particles in the bin. The percentiles range from 10% to 90% with 20% as interval, as labeled on the contours. The dots represent the locations where the velocity distribution function peaks. DM in dSIDM models exhibit positive median v_ϕ while the phase space distribution is almost isotropic in CDM. The differences consistently show up in the three radial bins and suggest a coherent rotation built up in dSIDM halos. The phase space distribution in the dSIDM model is also more peaky than the CDM case, at least for the central and intermediate radial bins. 34

2.12 **Velocity distribution functions of DM in the classical dwarfs.** *Top left:* Velocity distribution function at small galactocentric radii ($r < r_{1/2}^{\text{cdm}}/3$). We show the velocity distributions in CDM and dSIDM with $(\sigma/m) = 1$ and $10 \text{ cm}^2 \text{ g}^{-1}$ (as labeled). As a reference, a Maxwell-Boltzmann distribution is shown with the thick gray line. Compared to CDM, the velocity distribution functions in dSIDM models are more suppressed at the high-velocity tail as the cross-section increases and the peaks of the distributions also decrease systematically. *Top right:* Same velocity distribution functions as the top left panel but in log-log scale to highlight the asymptotic behavior at the low-velocity tail. Both CDM and dSIDM models have velocity distribution functions that decrease slower than the Maxwell-Boltzmann distribution at the low-velocity tail. Dissipation has limited impact at low velocities due to small interaction rates there. *Bottom left:* Velocity distribution function at intermediate galactocentric radii ($r_{1/2}^{\text{cdm}}/3 < r < 3r_{1/2}^{\text{cdm}}$). Similar differences in the velocity distribution of CDM and dSIDM are found compared to the one at small radii. *Bottom right:* The same velocity distribution function as the bottom left panel but in log-log scale. Both CDM and dSIDM models have velocity distributions that overall resemble the Maxwell-Boltzmann distribution at the low-velocity tail. 35

- 2.13 **Top: Axis ratios of DM halos at central kpc in simulations at $z = 0$.** We show the minor/intermediate axis ratio (c/b) versus the intermediate/major axis ratio (c/a) of DM mass distribution in different simulations. The axes are measured iteratively while fixing the volume of an ellipsoid as $4\pi/3 r_{\text{lim}}^3$, where r_{lim} is chosen to be 1 kpc. When c/b (b/a) is close to unity, the system is a prolate (oblate) spheroid. When both c/b and b/a are close to unity, the system is spherically symmetric. In CDM, DM halos are triaxial ellipsoids with a clear hierarchy of minor, intermediate and major axes. The CDM halos lean towards prolate shapes, driven by mild radial dispersion anisotropy. In the dSIDM model with $(\sigma/m) = 1$ and $10 \text{ cm}^2 \text{ g}^{-1}$, DM halos behave as oblate spheroids, driven by the coherent rotation of DM. In the extreme cases (e.g., m10q in dSIDM with $(\sigma/m) = 10 \text{ cm}^2 \text{ g}^{-1}$), c/b drops to as low as ~ 0.5 while b/a stays around unity. At larger radii ($r \gg \text{kpc}$), the qualitative trends are similar but the differences between DM models become rapidly smaller. **Bottom: Evolution of the axis ratios of m10q at central kpc from $z \simeq 2.2$ to $z = 0$.** The markers with darker colors represent measurements at lower redshifts. The CDM halo stays triaxial since $z \simeq 2.2$ while the eSIDM halo becomes more spherical at late times. The halo in dSIDM with $(\sigma/m) = 1 \text{ cm}^2 \text{ g}^{-1}$ is already more spherical than CDM and eSIDM counterparts at $z \simeq 2.2$ and it becomes extremely spherical at $z = 0$. However, the halo in dSIDM with $(\sigma/m) = 10 \text{ cm}^2 \text{ g}^{-1}$ initially follows the track of becoming more spherical but then turns oblate in shape. 38
- 2.14 **DM energy transfer rates via “thermal conduction” (DM collisional energy transfer) versus dissipation energy loss rates, measured in spherical shells, as a function of galactocentric radii.** We show the heat gain or loss of DM via collisions (\dot{E}_{coll} , Equation 2.26) versus the energy dissipation rate (\dot{E}_{diss} , Equation 2.27) in circles (red for $\dot{E}_{\text{coll}} > 0$, blue for $\dot{E}_{\text{coll}} < 0$). We present the results in one of the classical dwarfs m10q and in one of the bright dwarfs m11a. In both galaxies, with $f_{\text{diss}} = 0.5$, the collisional energy transfer rate is always roughly an order of magnitude lower than the energy dissipation rate. 44

- 2.15 *Top left: Total mass density profiles of m09 in dSIDM models with other combinations of f_{diss} and σ/m .* We choose three combinations of f_{diss} and σ/m that give the same dissipation time scale: $f_{\text{diss}} = 0.5$, $\sigma/m = 1 \text{ cm}^2 \text{ g}^{-1}$; $f_{\text{diss}} = 0.1$, $\sigma/m = 5 \text{ cm}^2 \text{ g}^{-1}$; $f_{\text{diss}} = 0.9$, $\sigma/m = 0.56 \text{ cm}^2 \text{ g}^{-1}$. *Other panels: Collisional energy transfer rates versus energy dissipation rate of DM (as Figure 2.14).* The energy transfer rate via collisions is subdominant compare to dissipation in the model with $f_{\text{diss}} = 0.5$ or 0.9 . In the model with $f_{\text{diss}} = 0.1$, collisional heating overtakes dissipation at the center of the galaxy. This model actually produces a denser and cusper central density profile, as the halo experiences the gravothermal collapse and a dense core in the SMFP regime emerges at the center. In all models, at large radii ($\sim 10 \text{ kpc}$), collisional energy transfer rates become comparable to the dissipation rate, but the absolute values of both terms at these radii are too small to make a difference. 46
- 2.16 **A cartoon of the dSIDM parameter space.** The dSIDM model is parameterized with σ/m and f_{diss} . When σ/m is small enough, both elastic and dissipative SIDM models become analogous to CDM in the lifetime of the Universe. When f_{diss} becomes small enough, dSIDM becomes essentially eSIDM-like since collisional energy transfer dominates over dissipation in this regime. When the product of σ/m and f_{diss} becomes large enough, the dissipation time scale could drop below the local dynamical time scale of the system and result in the fragmentation of dSIDM into compact dark objects. Effectively, baryon-like models are located at the low f_{diss} , high σ/m corner of the plot. The dSIDM models studied in this chapter live in the parameter space, which is not immediately ruled out but can still give rise to unique phenomena different from CDM or eSIDM models. 49

- 2.17 **Total mass density profiles of galaxies in DMO simulations and full physics simulations.** We present the density profiles of m10q and m11q in CDM and dSIDM with $(\sigma/m) = 1 \text{ cm}^2 \text{ g}^{-1}$. The results of full physics simulations are shown in solid lines while the results of DMO simulations are shown in dashed lines. The purple dotted vertical line indicates the convergence radius in DMO runs (see Table 2.1). In CDM, the central density profiles in DMO simulations are similar to the NFW profile before reaching the convergence radii. The full physics simulation of m11q produces a kpc size core at the center due to strong baryonic feedback there. However, in the dSIDM model with $(\sigma/m) = 1 \text{ cm}^2 \text{ g}^{-1}$, the DMO and full physics simulations produce almost identical results, indicating that dissipative interactions of DM completely determine the evolution of the DM halo and the impact of baryonic feedback becomes negligible. This is generally true when the dissipation time scale becomes significantly shorter than the Hubble time scale. 50
- 3.1 **Visualizations of two simulated classical dwarfs.** Each column corresponds to one DM model studied. The images are mock *Hubble Space Telescope* composites of u,g,r bands with a logarithmic surface brightness stretch. We use the STARBURST99 model to determine the SED of each stellar particle based on its age and initial metallicity and use ray-tracing [4] to model dust attenuation assuming a Milky Way-like reddening curve and a dust-to-metal ratio of 0.4. The side lengths of the images are chosen to be $8 \times r_{1/2}$ of the CDM run. The dSIDM models with $(\sigma/m) = 1 \text{ cm}^2 \text{ g}^{-1}$ and the velocity-dependent cross-section produce visibly more concentrated stellar content compared to the CDM case (the effective cross-section as defined in Shen et al. [5] of our velocity-dependent model in classical dwarfs is about $0.3 \text{ cm}^2 \text{ g}^{-1}$). However, the model with $(\sigma/m) = 10 \text{ cm}^2 \text{ g}^{-1}$ produces overall fluffier stellar distribution. 56

- 3.2 **Visualizations of three simulated bright dwarfs.** The images are generated in the same way as those in Figure 3.1. Since some of the bright dwarfs develop disk-like structures, we show both face-on and edge-on images here. Compared to the CDM case, the stellar disks in the dSIDM model with $(\sigma/m) = 1 \text{ cm}^2 \text{ g}^{-1}$ are more well-defined and exhibit more concentrated central regions. On the other hand, the velocity-dependent dSIDM model produces galaxies that are visibly similar to the CDM case given its small effective cross-section at this mass scale ($(\sigma_{\text{eff}}/m) \sim 0.01 \text{ cm}^2 \text{ g}^{-1}$). Interestingly, the model with $(\sigma/m) = 10 \text{ cm}^2 \text{ g}^{-1}$ produces stellar disks accompanied by overall fluffier stellar distribution compared to the model with $(\sigma/m) = 1 \text{ cm}^2 \text{ g}^{-1}$ and CDM. 57
- 3.3 **Visualization of the gas content of three simulated bright dwarfs.** The images are logarithmically-weighted gas surface density projections. Each column corresponds to one DM model studied and each row corresponds to one bright dwarf simulated. For each dwarf, both the face-on and edge-on images are shown. The side lengths of the images are chosen as $12 \times r_{1/2}^{\text{cdm}}$. Each image is a composite of gas distribution in three phases characterized by the gas temperature. The magenta color represents the “cold” neutral gas with $T \lesssim 8000 \text{ K}$; the green color represents the “warm” gas with $T \sim 1 - 3 \times 10^4 \text{ K}$; the red color represents the “hot” ionized gas in the CGM with $T \gtrsim 10^5 \text{ K}$. The neutral gas disks are promoted in the dSIDM-c1 and c10 models, even in m11a which is strongly perturbed by supernovae feedback in CDM. 58

- 3.4 **Left column: Stellar density profiles of simulated classical dwarfs.** The density profiles from different DM models are presented as labeled. The short vertical lines indicate the stellar-half-mass-radius of the galaxy in each model. The m10q and m10v halos show different responses to DM dissipation. In m10q (*top*), which forms its stars early, a cuspy stellar profile appears with moderate dSIDM cross-sections accompanied by shrinking galaxy size, and then the profile turns shallower when the cross-section further increases. In m10v (*bottom*), which forms quite late, the profile becomes more concentrated monotonically as the cross-section increases, and the decline of galaxy size is less dramatic. This is related to the distinct star formation histories of the two galaxies as shown on the right. **Right column: Archaeological star formation history of simulated classical dwarfs.** This is computed as the age distribution of stellar particles within $10\% R_{\text{vir}}^{\text{cdm}}$ at $z = 0$. The galaxy m10q has an early star formation history peaked at $z \simeq 3$. The stars have more time to react to the underlying DM distribution. On the other hand, the galaxy m10v with a relative late period of star formation does not exhibit this. The late time star formation and feedback also puffs up the stellar content and make it less dependent on the underlying DM distribution. 62
- 3.5 **Left column: Stellar density profiles of simulated bright dwarfs.** The notation is the same as Figure 3.4. In both m11a and m11b, the stellar density profiles become cuspy in dSIDM models with moderate cross-sections while turning shallower as we further increase the cross-section. This largely reflects similar behavior seen in the DM density profiles in Shen et al. [5] – in particular, at very high cross-sections the central DM profiles are flattened via dark rotation. **Right column: Archaeological star formation history of simulated bright dwarfs.** The notation is the same as Figure 3.4. The galaxy m11a has a relatively flat star formation history and is not significantly affected by the DM physics. However, in m11b, dips in star formation history at low redshifts appear in dSIDM models. 63

- 3.6 **Size-mass relation of simulated (isolated) dwarf galaxies.** The stellar half-mass radius versus stellar masses of simulated dwarfs are shown with open markers (as labeled). We compare them with several observations of dwarf galaxies in the Local Universe: gray points with error bars, the Local Group dSphs compiled in McConnachie [6]; blue contours, the NGFS dwarfs in Eigenthaler et al. [7]; green contours, the SPARC galaxies presented in Lelli et al. [8, 9]; red contours, the UDGs in the Coma and Virgo cluster from van Dokkum et al. [10] and Mihos et al. [11]; purple (red) line, the size-mass relation of the observed “normal” late-type (early-type) galaxies [12, 13]. The simulated dwarfs are consistent with the median size-mass relation of LTGs in observations and its extrapolation. With mild DM self-interaction ($(\sigma/m) \lesssim 1 \text{ cm}^2 \text{ g}^{-1}$), the sizes and masses of galaxies, in general, do not vary much from the CDM case. In some cases, the dSIDM models can produce compact dwarfs at $M_* \sim 10^6 M_\odot$, in better agreement with Local Group observations. However, in the dSIDM-c10 model, dwarf galaxies have apparently more extended stellar content and are located at the diffuse end of the observed distribution. 66

- 3.7 **Circular velocity profiles of simulated classical dwarfs compared with the observed field dwarfs in the Local Group.** *Top left:* Circular velocity profiles of the simulated dwarfs in different DM models. The circular velocities are enhanced at the sub-kpc scale in dSIDM models. In the model with $(\sigma/m) = 10 \text{ cm}^2 \text{ g}^{-1}$, the normalization of the circular velocity profile decreases. *Top right:* We compare the results in CDM and dSIDM models with $(\sigma/m) = 0.1/1 \text{ cm}^2 \text{ g}^{-1}$ with the observed field dwarfs in the Local Group (we show two measurements for Tucana, connected by gray line; see text for details). The $r_{1/2}$ of these galaxies are shown by solid circles. We highlight the observed dwarfs of similar sizes to the simulated one ($0.2 \text{ kpc} \lesssim r_{1/2} \lesssim 0.9 \text{ kpc}$) with the purple shaded region. The CDM results are consistent with the majority of the observed dwarfs, but lower compared to the most compact dwarfs (NGC6822 and the older measurement of Tucana). The $(V_{\text{circ}}(r_{1/2}), r_{1/2})$ of these two dSIDM models are still marginally consistent with the observed dwarfs of similar sizes and improve the agreement for compact dwarfs. The circular velocities in the dSIDM models are about two times higher than the observed ones at small radii $r \lesssim 0.2 \text{ kpc}$. *Bottom left:* We show the results of the velocity-dependent dSIDM model and compare them to the observed dwarfs with $0.1 \text{ kpc} \lesssim r_{1/2} \lesssim 1.2 \text{ kpc}$. *Bottom right:* We show the results of the model with $(\sigma/m) = 10 \text{ cm}^2 \text{ g}^{-1}$ and compare them to the observed dwarfs with $0.7 \text{ kpc} \lesssim r_{1/2} \lesssim 1.5 \text{ kpc}$. The results from these two models are also consistent with observations. 69
- 3.8 **Circular velocity profiles of simulated bright dwarfs compared with observed LSBs in the Local Universe.** *Right:* Circular velocity profiles of the bright dwarf galaxies in simulations. We compare the results with the measured circular velocities of LSBs observed in the field (see Section 3.4 for details of the observed sample and selection criteria). Models with constant σ/m that are consistent with in the classical dwarfs (with low V_c) generally produce too concentrated galaxies at high V_c , but the velocity-dependent model is consistent over the entire range we consider here. 70

3.9 Circular velocity profiles of satellite galaxies of simulated Milky Way-mass galaxies and compared with observations. The circular velocity profiles in each DM model are shown in each column respectively. The solid lines and the shaded regions show the median and the 1.5σ scatter (86% of the sample) of the curves. The dashed lines highlight the three circular velocity profiles with the highest (and the three with the lowest) circular velocities at $r = 1$ kpc. Gray circles with error bars show the $(V_{1/2}, r_{1/2})$ of observed Milky Way and M31 satellites compiled in Section 3.4. The $r_{1/2}$'s of simulated satellites are marked by solid circles. The identified subhalos in simulations are selected as satellites if they have galactocentric distance $20 \text{ kpc} < d < 300 \text{ kpc}$, and with at least 200 DM particles and 10 associated stellar particles (equivalently $M_* \geq 10 m_b$). The selected satellites are in the mass range $M_* \sim 10^5 - 10^8 M_\odot$, in concordance with the observed sample. The circular velocity profiles in different models are almost indistinguishable compared to the scatter among the observed satellites, despite the slightly larger median rotation velocities and upper scatter in the dSIDM-c0.1 model. Circular velocity profiles from all three models are consistent with the bulk of the observed dwarfs, although the predicted galaxy sizes are systematically larger. The smallest $r_{1/2}$ reached in the two dSIDM models is smaller than the CDM case, down to about ~ 500 pc. As indicated by the dashed lines, the most compact satellites in the dSIDM-c0.1 model agree better with the observed compact dwarfs in the Local Group, though the stellar content is still puffier compared to observations. . . 73

3.10 Size-mass relation of satellite galaxies. We show the stellar-half-mass-radius versus the stellar mass of satellites of the simulated Milky Way-mass host(s). Only the high-resolution runs are considered here. The satellites from simulations follow the same selection criteria as in Figure 3.9. The solid points show satellite sizes corrected for the surface brightness limit in observations. The black dotted lines indicate the surface brightness limit $30 \text{ mag arcsec}^{-2}$ for the SDSS surveys and the limit with an order of magnitude increasing sensitivity. For reference, the Local Group dwarfs [6] are shown by gray points and the NGFS dwarfs [7] are shown by the gray shaded contours. The purple dashed line is the extrapolation of the size-mass relation of local late-type galaxies [12]. The left shaded region indicates the mass resolution limit of the simulated satellites. The horizontal cyan dashed line indicates radius limit where the enclosed DM particle number is ≤ 200 for a typical satellite central density $\rho_{\text{dm}} \simeq 10^{7.5} M_{\odot} \text{ kpc}^{-3}$. The markers encircled highlight the three most compact dwarfs (with the highest rotation velocities at $r = 0.5 \text{ kpc}$) in each run. A significant population of low-mass satellites in simulations are not detectable in current observations. For those in the observed regime, no obvious difference is found between CDM and dSIDM models. Massive satellites in dSIDM models are slightly more compact than their CDM counterparts, but they are still systematically puffier than the observed ones. In all the models, the satellites with the most compact DM content (highest circular velocities identified in Figure 3.9) also have the most compact stellar content. However, despite similar stellar masses, they have about three times larger $r_{1/2}$ than the observed compact dwarf elliptical galaxies. For reference, the $(r_{1/2}, M_*)$'s of simulated classical dwarfs (isolated systems) are shown as open stars. With an order-of-magnitude better mass resolution, the isolated dwarfs have slightly more compact stellar content that is in better agreement with the observed samples. This hints the resolution-dependent uncertainties, which will be discussed in Appendix 3.7. . . . 75

- 3.11 **Satellite stellar mass function.** The satellite stellar mass functions of different DM models are shown in solid lines with different colors (as labeled). The purple and orange dashed lines show the satellite stellar mass functions of the Milky Way and M31, respectively. The gray dashed lines with shaded regions show mass function of Milky Way-like systems in the SAGA survey with 1σ scatter. Each panel corresponds to one simulated Milky Way-mass galaxy in the suite. The vertical dotted line indicates the resolution limits of satellite stellar mass (set as 10 times the baryonic mass resolution of the simulation). Strong diversity shows up in the stellar mass function of both observed satellites and the satellites of simulated galaxies. The counts of satellites get enhanced slightly in the dSIDM models, but the differences are still too small compared to the observed scatter to effectively rule out any of the models studied. 78
- 3.12 **Cumulative count of satellites above a given stellar 3-D velocity dispersion.** The notation is the same as Figure 3.11. Similar to the stellar mass function, we find strong diversity here in both observed and simulated systems. The satellite σ_*^{3d} distributions of m12i (l.r.) and m12f are in good agreement with the Milky Way and M31 samples at $\sigma_*^{3d} \lesssim 20 \text{ km s}^{-1}$ but do not produce enough dynamically hot satellites. On the contrary, in m12i (h.r.) and m12m, the high σ_*^{3d} end is in better agreement with the observed sample, but they tend to over-predict the number of satellites with $\sigma_*^{3d} \lesssim 25 \text{ km s}^{-1}$. In terms of the DM physics tested, the dSIDM models (especially the dSIDM-c0.1 model) predict systematically higher velocity dispersions of satellites. 81
- 3.13 We compare satellite circular velocity profiles from the high and low-resolution simulations of m12i. The notation follows the top panel. Although the median circular velocity profile and the scatter do not differ appreciably between high and low-resolution simulations, the $r_{1/2}$'s of satellites in simulations are systematically smaller in the high-resolution simulation. Compared to the observed dwarfs, even the high-resolution simulation produces fluffier stellar content for these satellites. 85

- 3.14 We compare the high- and low-resolution simulations on the plane of the size-mass relation. They are all corrected for the surface brightness limit at $\mu_V = 30 \text{ mag arcsec}^{-2}$. The horizontal lines indicate the radius enclosing 200 DM particles assuming the typical satellite central density $\rho_{\text{dm}} = 10^{7.5} M_{\odot} \text{ kpc}^{-3}$. Satellites in the low-resolution simulations are systematically more diffuse than their high-resolution counterparts. The resolution dependence could explain the discrepancy between the simulations with observations in this plane. . . . 86
- 4.1 Enclosed mass fraction as a function of radius (normalized to the scale radius r_s), for 8 and 7 different 5- and 3- σ halos (upper and lower panels, respectively) including DM dissipation with cross-section $1 \text{ cm}^2 \text{ g}^{-1}$. Different halos are labeled with the mass (in units of $10^{11} M_{\odot}$) and redshift. The high spin curve corresponds to $\lambda = 0.1$ at $z = 10$, while other halos have spin parameter $\lambda = 0.03$. In these figures, the more dense 5- σ halos show core collapse, indicated by the region of constant density at small radii, while 3- σ halos have not been destabilized, consistent with Fig. 4.2. In the collapsed halos, the collapse fraction is found universally to be $\sim 3 \times 10^{-3}$. . . 94

- 4.2 *left panel:* Shown as shaded contours, minimum halo mass M to seed an SMBH (labeled “SMBH seeds”) immediately at redshift of halo formation z_f , for a fixed tdSIDM cross-section (σ/m in units of cm^2/g). The solid curves show the mass of a $\nu = 1, 3, 5$ halo in a spherical collapse model formed at redshift z_f . A halo is available in the cosmological history to seed an SMBH (for a given cross-section) if the shaded region corresponding to that cross-section is above a solid curve. For comparison, we show as dashed curves the cosmological history of the Main Progenitors of a Milky Way Mass and Cluster Mass galaxy, as given in Eq. (4.19). Interestingly, the main progenitor of a $1 - \sigma$ halo at $z = 0$, can be a $3 - \sigma$ halo at $z \sim 10$, which is more likely to form SMBHs. *right panel:* Mass M of a $\nu = 5$ halo, again for fixed cross-section corresponding to colored regions, that may seed an SMBH at a lower redshift $z \leq z_f$. We can see that rare halos that do not seed an SMBH immediately may do so later in the history of the Universe. During the evolution of these halos, we assume the central density and the halo mass are fixed; we will track the assembly history of halos more completely in Sec. 4.3 utilizing merger trees. 97
- 4.3 **Halo mass function.** The reconstructed halo mass functions at $z = 4, 6, 8$ based on the weighted abundance of halos in the merger trees (shown by circles of different colors). They are compared to the halo mass functions determined analytically using the HMF code (shown by dashed lines), which itself is calibrated based on numerical cosmological simulations [14]. The halo mass functions determined by the merger trees agree reasonably well with the analytic ones up to $10^{12} M_\odot$ ($10^{13.5} M_\odot$) at $z = 8$ ($z = 6$), which covers the mass range of quasar host halos of interest. 102

- 4.4 **SMBH mass function.** *Top:* Number density of SMBHs as a function SMBH mass at $z = 6$, calculated from the weighted abundance of SMBHs in the merger trees. The prediction assuming $\sigma/m = 0.1$ (0.05) $\text{cm}^2 \text{g}^{-1}$ and $\Delta M_0 = 0$ is shown and compared to the halo mass function multiplied by the collapse fraction f_{col} . The massive end of the BHMF is coupled with the seeding mechanism, and the shape of the SMBH mass function resembles the exponential cut-off in the halo mass function. Low-mass SMBHs have decoupled from the seeding mechanism and the low-mass end of the mass function deviates from the halo mass function. The choice of self-interaction cross-section does not affect the massive end but changes the characteristic mass where the SMBH mass function deviates from the halo mass function. The shaded region indicates the abundance of observed massive quasars ($M_{\text{BH}} \gtrsim 10^9 M_{\odot}$) at high redshift and the abundance of underlying SMBH population should at least be larger. *Bottom:* We show the SMBH mass functions in the model with $\sigma/m = 0.1 \text{ cm}^2 \text{g}^{-1}$ and $\Delta M_0 = 0$ (10^7) M_{\odot} . The baryonic accretion arguably only has an impact at the low-mass end (shifting the lowest mass of the seeds produced by the mechanism), hardly changing the abundance of the most massive SMBHs. 106
- 4.5 **Bolometric quasar luminosity function at $z = 6$.** *Top:* Model predictions, varying σ/m and ΔM_0 . The predictions are derived by convolving the SMBH mass function with a log-normal ERDF, tuning the duty-cycle to match the abundance of luminous quasars. The solid circles represent observational constraints compiled in [15]. The prediction assuming $\sigma/m = 0.05 \text{ cm}^2 \text{g}^{-1}$ is compatible with the observations and produces the observed abundance of luminous quasars at $z = 6$, assuming a relatively low duty-cycle. On the other hand, the model with $\sigma/m = 0.05 \text{ cm}^2 \text{g}^{-1}$ will overproduce quasars of $L_{\text{bol}} \sim 10^{47} \text{ erg/s}$. *Bottom:* We show the predictions with a cut-off power-law as the ERDF. The duty-cycle is assumed to be unity. The faint-end slope of the ERDF (α) is tuned to make the predicted quasar luminosity function close to observations. Both models can agree well with the luminous quasar abundances in observations. But the model $\sigma/m = 0.05 \text{ cm}^2 \text{g}^{-1}$ does not fit perfectly with the faint end luminosity function regardless of the α adopted. 109

- 4.6 **Mass growth history of SMBHs.** The blue solid lines show the mass of SMBHs as a function of redshift in our model assuming $\sigma/m = 0.1 \text{ cm}^2 \text{ g}^{-1}$. These SMBHs are selected from merger trees with $M_{\text{BH}} \leq 10^{10} M_{\odot}$. The red points are the observed massive quasars at $z \gtrsim 6$ compiled in [16, 17] with the mass estimated using the virial method. The gray points are a more complete set of 196 quasars at $z \gtrsim 6$ compiled in [18], with the mass estimated indirectly from UV luminosity. The red dotted lines indicate the growth history of the observed quasars assuming they exhibit the same Eddington ratio as the measured value at the redshift of discovery. The typical mass and formation redshift of SMBH seeds from classical seeding mechanisms are shown in shaded regions, with the Eddington-limit growth tracks of these seeds in dashed lines for reference. Seeds formed in canonical mechanisms need to accrete at rates near the Eddington limit in order to produce billion solar mass SMBHs at $z \simeq 6 - 8$. This is in tension with the low Eddington ratios of some observed quasars, which require seed masses of $\sim 10^8 M_{\odot}$ implied by their observed Eddington ratio. However, such quasars can be accommodated in our seeding model. 110
- 4.7 **The $M_{\text{BH}} - \sigma_{\text{v}}^*$ relation of high redshift SMBHs.** We show SMBHs in the merger trees selected at $z = 7$ in solid circles, with the marker size scaling with the statistical weight. Red and blue circles correspond to the model with $\sigma/m = 0.1$ and $0.05 \text{ cm}^2 \text{ g}^{-1}$, respectively. The local $M_{\text{BH}} - \sigma_{\text{v}}^*$ relation [19] is shown with the purple dashed line. The orange dashed line shows the relation $M_{\text{BH}} \sim f_{\text{col}} M_{\text{vir}}$, assuming the relation between M_{vir} and σ_{v}^* (Eq. (4.23) and Eq. (4.24)) holds. Observational samples based on the [C II] line observations of the quasar host galaxies compiled in [17] (originally from [20]) are shown in orange circles. 111

- 4.8 **The comoving SMBH mass density in the Universe versus redshift.** The cumulative mass density of SMBHs integrated over the mass function. The results with different model parameters are shown as labeled and compared to the local SMBH mass density, $4.4\text{--}5.9 \times 10^5 M_{\odot} \text{Mpc}^{-3}$ [21], as indicated by the horizontal line. The mass density from the model with $\sigma/m = 0.1 \text{ cm}^2 \text{ g}^{-1}$ approaches the local mass density already at $z \simeq 6$, which is potentially problematic since the integrated quasar luminosity density matches the local SMBH mass density [15] (at 0.5 dex level, assuming $\epsilon_r = 0.1$). Therefore, the mass density at high redshift needs to be significantly lower than the local value in order to be consistent with the observation of quasar luminosity functions, unless ϵ_r is larger (*i.e.* SMBHs are rapidly rotating). 113
- 4.9 *Top: Mass growth history of halo progenitors.* The growth tracks of relatively massive progenitors are color-coded by their concentrations. Low-mass progenitors are shown by the gray cloud. The main progenitor is indicated by the cyan solid line. The green dashed line shows an analytic model for the main progenitor mass growth history [22]. The gray solid lines show the mass of the halo corresponding to a certain rareness of fluctuations. *Bottom: Ratio $t_{\text{diss}}/t_{\text{h}}$ of halo progenitors versus redshift.* The cross-section $(\sigma/m) = 0.05 \text{ cm}^2 \text{ g}^{-1}$ is assumed here. Progenitors that are more massive than $10^{10} M_{\odot}$ are color-coded by their halo masses. The labeling is the same as the top row. The green dashed lines show analytic expectations for the timescales of the low and high redshift branches (as discussed in the main text). The horizontal dashed line indicates the threshold where SMBH seeding will occur assuming $(\sigma/m) = 0.05 \text{ cm}^2 \text{ g}^{-1}$ and $\epsilon = 0.1$ 116
- 4.10 Enclosed mass profile of two $5 - \sigma$ halos at $z = 10$ with the same NFW parameters but different simulation parameters. Solid curves represent the mass profile at different times for the fiducial run, while the dashed curves are for a run with a factor of 4 improved resolution (improving both mass and force resolution accordingly). The vertical dashed lines indicate the gravitational force softening length for both the fiducial run and the high-resolution run. 121

- 4.11 Enclosed mass profile of three collapsed $5 - \sigma$ halos at $z = 10$ with the same NFW profile parameters. The collapse of those halos is simulated with different cross-sections but the same mass and force resolution. The enclosed profiles are flat at small radii, suggesting the formation of SMBHs. Therefore, the universality of the collapse fraction is not violated by changing the cross-section of tdSIDM. . . . 126
- 5.1 Redshift and temperature distributions of the observed clusters and temperature distribution for the simulated clusters. *Left:* Redshift distribution of the observed clusters. The distributions of the “peaky” and “non-peaky” samples are shown in red and blue. For both distributions, most of the clusters fall in the range $0.1 \lesssim z \lesssim 0.5$, with a few outliers out to $z \sim 1$. *Right:* Temperature distribution of the observed (red and blue) and the simulated clusters (green). The median temperature of each sample is shown by a corresponding vertical dashed line. On average, the temperatures of simulated clusters are fairly consistent with the observed samples, despite having a smaller dispersion in temperature. 133
- 5.2 DM mass density profiles of the simulated clusters. For each DM model, we show the median and 1σ dispersion of the density profiles of the simulated clusters. The grey dotted line with a shaded region indicates the conservative estimation of the convergence radii of DM properties with its error. SIDM halos develop thermalized cores with flat central density profiles, in contrast to the cuspy central profile in CDM. The core size increases with greater self-interaction cross-sections. These differences exist outside the convergence radius, but eventually become negligible at the outskirts of the halos ($\gtrsim 5\% R_{200}$). 138

- 5.3 Gas mass density profiles of the simulated clusters. The labeling is the same as in Figure 5.2. The convergence radius for hydrodynamical properties of the gas is ambiguous, so we choose 16 times the hydro spatial resolution h_b as a reference, indicated with the grey dashed line (see Figure 5.4 and the discussion at the end of Section 5.5 for the convergence criterion). The colored short dashed lines show gas density profiles inferred from the gravitational potential of the gas, assuming that the intracluster gas is isothermal and in hydrostatic equilibrium. A zoom-in subplot is included to compare density profiles at the center. Unlike DM, the gas density profiles show little difference between DM models. The central densities are also lower than expected from the hydrostatic equilibrium predictions. 139
- 5.4 *Top:* Gas temperature profiles of the simulated clusters. The labeling is the same as in Figure 5.3. The vertical dashed line shows an estimate of the convergence radius for hydrodynamical properties. The horizontal dashed lines indicate the median virial temperatures of the halos in each DM model. Gas temperatures rise monotonically towards halo centers with the central temperature being slightly lower in SIDM models. *Bottom:* Thermal pressure gradient versus gravitational potential gradient as a function of radius. The thermal pressure support balances the gravitational attraction at $r \gtrsim 10\% R_{200}$, indicating that the hydrostatic equilibrium is perfectly respected. At small radii, the dispersion in $\mathcal{D}P/\mathcal{D}\Phi$ gradually becomes larger. The convergence radius for hydrodynamical properties is estimated as 16 times the hydro spatial resolution h_b and is indicated with the grey vertical dashed line. Within the convergence radius, the median value of $\mathcal{D}P/\mathcal{D}\Phi$ shows order of magnitude fluctuations. 140

- 5.5 Three-dimensional axial ratios of the DM (gas) distribution of the simulated clusters. The left (right) column shows the axial ratios for DM (gas). The top row shows the minor-to-major axial ratio, c/a , and the bottom row shows the intermediate-to-major axial ratio, b/a . The shaded vertical regions on the left and dashed lines on the right indicate the convergence radii for DM and gas properties, respectively. Considerable differences between SIDM and CDM show up in the DM shape out to large radii, while the distinct signature of SIDM in the gas shape is much weaker. Meanwhile, the gas distribution is systematically rounder than the DM one, as a consequence of the X-ray emitting gas tracing more directly the isopotential surface of the matter distribution rather than the mass distribution. 141
- 5.6 Soft X-ray surface brightness profiles of the simulated clusters in different DM models. For each model, we show the median and 1σ dispersion of the surface brightness profiles. A zoom-in subplot of the central surface brightness profiles is included. The hydro convergence radius is shown with the grey vertical dashed line. The surface brightness profile is basically insensitive to DM physics, due to a combination of projection effects and the weak response of the intracluster gas distribution to SIDM physics. 144

- 5.7 Comparisons of the soft X-ray surface brightness profiles of the simulated and observed clusters. *Top*: Surface brightness profiles (with observational error bars) of individual clusters. The observed clusters are grouped as the low-redshift “peaky” and “non-peaky” clusters [23], and the three SPT-selected clusters at $z \gtrsim 1.2$ [24] which do not exhibit cool-cores. The surface brightness profiles are normalized with the units defined in Equation 5.9. The shaded region indicates the radial range of interest, $0.1 - 0.2 R_{200}$. The cuspy central profiles of the low-redshift observed clusters, in particular the “peaky” sample, are not present in the simulated clusters with the absence of cooling processes. The high-redshift SPT-selected clusters appear to agree better with the simulations, due to the different thermodynamical properties compared to the low-redshift clusters. At large radii, including the radial range of interest for shape measurements, we find reasonable agreement in terms of normalization and slope between the simulated and observed profiles. *Bottom*: Median and 1σ dispersion of each group of surface brightness profiles. It is clear that the simulated clusters agree better with the “non-peaky” sample at the outskirts of the clusters. Based on the surface brightness in the radial range of interest ($0.1 - 0.2 R_{200}$, indicated with the shaded region), we pick the flux levels of the isophotes for morphology analysis. They are marked by the purple dashed lines. 145
- 5.8 Ellipticity profiles of the simulated clusters compared to the observational results. We show the ellipticity of the isophotes as a function of the effective radius of the isophote. The median values and 1σ dispersions of the simulated samples are shown as solid lines and shaded regions. The results of the observed “non-peaky” (“peaky”) samples are shown by open black (grey) markers with error bars. The vertical dashed line on the left indicates the hydro convergence radius. The SIDM-c0.5 and SIDM-c1 models predict lower ellipticities and agree better with the observational results. However, the signal is smeared by large statistical uncertainties. 146

- 5.9 *Left:* Cumulative distribution function of the ellipticities of the X-ray isophotes. The fit to the isophotes is performed at $0.1 - 0.2 R_{200}$ for each viewing angle of each simulated halo. In the lower subpanel, we show the median ellipticities and 1σ dispersions for the different DM models and the observed cluster samples. *Top right:* Probability distribution function of the ellipticities. For simplicity, we only show PDFs of the CDM and SIDM-c1 models compared to observations. *Bottom right:* p value of the two-sample KS and AD tests. The tests are performed on the ellipticity distributions of observed and simulated clusters. The p value is the likelihood that the two samples are drawn from the same underlying continuous distribution function. Compared to the “non-peaky” sample, the KS and AD tests reject the CDM and SIDM-c0.1 models at about 90% confidence level. 147
- 5.10 Ellipticity CDFs and statistics from the bootstrapped samples. *Top:* Ellipticity CDFs of the bootstrapped samples for the CDM and SIDM-c1 models and the “non-peaky” sample from observations. The 1σ dispersions of the CDFs are shown by the shaded regions. The discrepancy found between CDM and the observed sample is larger than the statistical uncertainties illustrated here. *Bottom:* The p values of KS and AD tests for the bootstrapped samples. The median p values and the 1σ scatters are shown by solid circles with error bars. The p values from the measurements of the original samples are shown by crosses. Since the numerical implementation of the AD test only covers the p values from 0.1% to 25%, the bootstrapped results are thus capped, as marked by the arrows in the figure. Even taking into account the scatter in p value, the CDM and SIDM-c0.1 models are rejected with a 68% confidence level. 152
- 5.11 *Top:* Ellipticity versus redshift of the observed clusters. The ellipticity does not show any apparent dependence on redshift. Note that these clusters have been pre-selected as dynamically relaxed objects through the SPA criteria. *Bottom:* Ellipticity versus temperature. No apparent dependence on temperature is found either. However, the simulated clusters have a narrower distribution in temperature. 153

- 5.12 *Top:* Ellipticity CDFs when varying the radial aperture of the measurements. The CDF when increasing (decreasing) the radial aperture by 25% is shown as the solid (dotted) lines. The original CDMs are shown as transparent lines. The comparison demonstrates that the results are robust against aperture shifts. *Middle:* Ellipticity CDFs when excluding outliers in the ICM temperature distribution. The CDFs of the temperature-limited samples are presented in dashed lines while those of the original samples are shown in solid lines. The impact of the temperature outliers is small. *Bottom:* The p value of KS and AD tests when varying the radial aperture of the measurements or applying a temperature selection criterion. The conclusion that the CDM and dSIDM-c0.1 models are disfavored at 68% confidence level is not altered by either the aperture shift or the temperature selection criterion. 154

LIST OF TABLES

<i>Number</i>	<i>Page</i>
2.1	
Simulations of the FIRE-2 dSIDM suite.	
The simulated galaxies are labeled and grouped by their halo masses. They are classified into four categories: ultra-faint dwarfs; classical dwarfs, with typical halo mass $\lesssim 10^{10} M_{\odot}$; bright dwarfs, with typical halo mass $\sim 10^{10-11} M_{\odot}$; Milky Way-mass galaxies, with typical halo mass $\sim 10^{12} M_{\odot}$. These halos are randomly picked from the standard FIRE-2 simulation suite [25], sampling various star formation and merger histories. All units are physical.	
(1) Name of the simulation. “l.r.” (“h.r.”) indicates low (high)-resolution version of the simulation.	
(2) $M_{\text{halo}}^{\text{cdm}}$: Virial mass of the halo (definition given in Section 2.4) in the CDM simulation with baryons at $z = 0$.	
(3) $R_{\text{vir}}^{\text{cdm}}$: Virial radius of the halo (definition given in Section 2.4) in the CDM simulation with baryons at $z = 0$.	
(4) M_{*}^{cdm} : Galaxy Stellar mass (see Section 2.4) in the CDM simulation at $z = 0$.	
(5) $r_{1/2}^{\text{cdm}}$: Galaxy stellar half mass radius (see Section 2.4) in the CDM simulation at $z = 0$.	
(6) $r_{\text{dm}}^{\text{conv}}$: Radius of convergence in DM properties at $z = 0$ (calculated for the CDM DMO simulations in the standard FIRE-2 series [25] based on the Power et al. [26] criterion). As shown in Hopkins et al. [25], the convergence radii in simulations with baryons can in fact extend to much smaller radii.	
(7-11) Parameters of the DM models. σ (with the number after it) indicates the self-interaction cross-section, σ/m , in unit of $\text{cm}^2 \text{g}^{-1}$. $\sigma(v)$ denotes the velocity-dependent cross-section, introduced in Section 2.2. f_{diss} indicates the dimensionless degree of dissipation.	
(12) Notes: Additional information of each simulation.	11

5.1 Simulated cluster-mass halos in the suite.

(a) Each halo is simulated in CDM, SIDM-c0.1, SIDM-c0.5, and SIDM-c1. The bulk properties of these halos are indistinguishable in different DM models, so we only list the properties in the CDM simulations here.

(b) The radius of convergence of DM properties (based on the Power et al. 26 criterion discussed in Section 5.2). We present the maximum convergence radius for simulations in all four DM models as a conservative estimate.

(c) Due to a technical issue, the simulation was stopped at $z \simeq 0.18$ instead of $z = 0$. We approximate the $z = 0$ results with this snapshot. 132

Chapter 1

INTRODUCTION

1.1 Motivations for DM alternative to collisionless cold DM

Despite its veiled nature, dark matter (DM) is considered the main driver of structure formation in the Universe. The current paradigm — the cosmological constant plus cold DM (Λ CDM) cosmological model — has been successful in describing the large-scale structures in the Universe [27, 28]. This model assumes that DM is non-relativistic and is effectively collisionless, apart from its gravitational interactions with itself and Standard Model particles. However, in recent decades, evidence from astrophysical observations and the absence of signals from particle physics experiments have motivated conjectures on alternative DM models. On the astrophysics side, the Λ CDM model faces significant challenges in matching observations at small scales [see a recent review 29]. For example, the *core-cusp* problem states that the central profiles of DM-dominated systems, e.g. dwarf spheroidal galaxies (dSphs) and low surface brightness galaxies (LSBs), are cored [e.g., 30–43], in contrast to the universal cuspy central density profile found in DM only (DMO) simulations [44–49]. The *too-big-to-fail* (TBTf) problem states that a substantial population of massive concentrated subhalos appears in DMO simulations, which is incompatible with the stellar kinematics of observed satellite galaxies around the Milky Way or M31 [50–52]. This mismatch has been extended to field dwarf galaxies in the Local Group [53, 54] and beyond [55]. Although the inclusion of bursty star formation and feedback processes has been shown to alleviate the tensions [e.g., 56–62], a population of compact dwarf galaxies in the local Universe are missing in cosmological simulations of CDM (plus baryons) that can produce DM cores [e.g., 62–64]. Related to this, the rotation curves of dwarf galaxies appear to be more diverse than CDM predictions in the field [65] and Milky Way satellites [66]. Therefore, it is important to explore how non-standard DM models — in conjunction with baryonic physics — could help solve the small-scale anomalies. On the particle physics side, one of the most popular candidates for CDM (the class of Weakly Interacting Massive Particles, WIMPs) has not been discovered despite decades of efforts and a significant proportion of its parameter space being ruled out [e.g., 67–69]. The null results in collider production and direct/indirect detection experiments of classical CDM candidates have motivated ideas about al-

ternative DM models [e.g., 70–73] and explorations of the rich phenomenology from potential non-gravitational DM interactions. Many of these alternative DM models could behave dramatically differently from CDM at astrophysical scales and could potentially solve the small-scale problems mentioned above.

1.2 DM with self-interactions

Self-interacting DM (SIDM) is an important category of alternative DM models that have been proposed and discussed in the literature for about three decades [e.g., 71, 74–76]. It is well motivated by hidden dark sectors as extensions to the Standard Model [e.g., 77–85]. The introduction of SIDM could potentially solve some small-scale problems [see the review of 86, and references therein]. DM self-interactions enable effective heat conduction and could result in an isothermal distribution of DM with cores at halo centers, which alleviates the *core-cusp* problem. Meanwhile, it could also make DM halos (subhalos) less dense and alleviate the TBTF problem. Previous DMO simulations have found that a self-interaction cross-section of $\sim 1 \text{ cm}^2 \text{ g}^{-1}$ could solve the *core-cusp* and TBTF problems in dwarf galaxies simultaneously [e.g., 87–90]. In addition, SIDM with comparable cross-sections also has the potential to explain [e.g., 91–93] the diversity of rotation curves of dwarf galaxies [65, 66]. Following studies of galaxy clusters in SIDM suggested a cross-section of $\sim 0.1 \text{ cm}^2 \text{ g}^{-1}$ [e.g., 94, 95], which motivates the velocity-dependence of the self-interaction cross-section.

These previous studies on SIDM focused on elastic DM self-interactions. However, in many particle physics realizations of SIDM, DM particles have inelastic (or specifically dissipative) self-interactions [e.g., 78, 81, 83, 85, 96–106]. The impact of dissipative processes of DM has not yet been explored in the context of cosmological structure formation. In addition, the focus on purely elastic SIDM (eSIDM) in previous studies has been motivated by solving some small-scale problems (making galaxy centers less dense). Since dissipative DM self-interactions tend to make centers of halos denser to first-order consideration, dSIDM was largely omitted in previous studies of SIDM. However, apart from DM physics, some baryonic physics processes, including bursty star formation, stellar/supernovae feedback, and tidal disruption, have also been shown to strongly impact the structure of DM halos and help alleviate some small-scale problems. Specifically, gas outflows driven by stellar/supernovae feedback could create fluctuations in the central potential, which irreversibly transfer energy to CDM particles and generate DM cores [56–58, 107]. Some more recent CDM simulations could resolve the small-scale problems by

more realistic modeling of gas cooling, star formation, and stellar/supernovae feedback [e.g., 59–62, 108–110]. The interplay between baryons and SIDM in galaxy formation has been more carefully considered in subsequent SIDM simulations that include baryonic physics [e.g., 90, 111–116]. The inclusion of baryons substantially reduces the distinct signatures in dwarf galaxies caused by elastic DM self-interactions, especially in bright dwarfs with $r_{1/2} \gtrsim 400$ pc [115]. This could hide DM physics that lead to enhanced central density originally, other than those proposed specifically to lower the central density. The parameter space for dSIDM, as an example of such models, reopens due to these recent developments. The contraction of the halo driven by dSIDM interactions could help produce the compact dwarf galaxies found in the local Universe that are missing in CDM simulations plus baryons [e.g., 62–64] and increase the diversity of dwarf galaxy rotation curves.

A finite self-gravitating system has negative heat capacity and the heat conduction will eventually result in the “gravothermal catastrophe” of the system [e.g., 117, 118]. In the eSIDM case, effective heat conduction is realized by DM self-interactions and the inner cores of isolated eSIDM halos will ultimately experience gravothermal collapse and cuspy density profiles will reappear [e.g., 87, 90, 119–124]. However, for the most favored elastic self-interaction cross-sections $\sim 0.1 - 1 \text{ cm}^2 \text{ g}^{-1}$ (assuming velocity-independent), the “gravothermal catastrophe” would not have enough time to happen in halos within their typical lifetime. In the presence of dissipative self-interactions, the gravothermal evolution of a halo can be accelerated significantly, which affects the structure of dwarf galaxies within a Hubble time. Essig et al. [125] recently used a semi-analytical fluid model to investigate the structure of isolated spherically symmetric halos in dissipative SIDM (dSIDM) and presented the first constraint on the energy loss and cross-section of dSIDM. This work was followed by Huo et al. [126] with non-cosmological N-body simulations of isolated DM halos with the NFW profile [127] initially. Moreover, when the dissipation of DM self-interaction is strong enough, a patch of DM could lose its kinetic energy faster than rebuilding hydrostatic equilibrium with surrounding matter. Substructures of dissipative DM, e.g. dark disks and dark stars, could be generated under this circumstance. For example, DM scenarios with a highly dissipative component (sourced by an $U(1)$ -like hidden sector) have been studied by Foot and Vagnozzi [100], Fan et al. [128, 129, 130], Randall and Scholtz [131], Foot [132], Foot and Vagnozzi [133], Hyeok Chang et al. [134]. Randall and Scholtz [131] claimed that a dark disk composed of highly dissipative DM could appear and help explain the exotic mass-to-light ratios of some Milky Way satellites. However, the analytical or semi-

analytical studies discussed above were limited to isolated DMO halos with various geometrical simplifications. The influences of baryonic physics, hierarchical halo mergers, and deviations from simple fluid approximations in DM halos were not properly captured in these previous studies. In addition, multi-component DM with inelastic interactions has been considered in simulations in Todoroki and Medvedev [135], Vogelsberger et al. [136], but the dominant process is exothermic in these studies.

Meanwhile, continuous improvements in observations of local dwarf galaxies and other small-scale baryonic structures have enabled great opportunities to constrain the nature of DM. For example, the census of ultra-faint satellite galaxies in the Local Group through optical imaging surveys has been boosted in recent years, using the data from the Dark Energy Survey [DES; 137–140], the Panoramic Survey Telescope and Rapid Response System [Pan-STARRS; 141, 142], and others [e.g., 143, 144]. Many of the recently detected ultra-faints appear to be clustered around the Large Magellanic Cloud (LMC; Drlica-Wagner et al. 138, Koposov et al. 145). These candidate LMC satellites are attractive targets for ongoing and future observations to test the Λ CDM model [146]. The structural and dynamical properties of the Local Group satellites with resolved stellar populations have been measured [see for example compilations by 6, 52, and references therein] and play a key role in understanding the TBTF problem [50]. In the near future, the Legacy Survey of Space and Time [LSST, 147] at the Vera Rubin Observatory has the potential to substantially expand the discovery space of faint dwarf galaxies, being sensitive to galaxies one hundred times fainter than Sloan Digital Sky Survey [SDSS, 148] at the same distance [29]. Beyond the Local Group, the Dark Energy Camera [DECam, 149] and Subaru (Hyper) Suprime-Cam [e.g., 150, 151] are being used to search for faint companions of nearby galaxies [e.g., 152–154], as well as the LSBs and ultra-diffuse dwarf galaxies (UDGs) in cluster environment [e.g., 7, 10, 11, 155, 156]. In addition, for relatively massive disk dwarfs (late-type), radio observations have reported the HI rotation curves and mass models of a few hundred of them in the Local Universe [e.g., 8, 39, 41, 157]. The time is therefore ripe to make testable predictions from different DM model parameter space.

In Chapter 2 and Chapter 3 of this thesis, I will present two projects that focus on dSIDM in Local dwarf galaxies and their analogs in simulations. These chapters will explore the impact of dSIDM on galaxy structures and discuss the resulting observational signatures and constraints.

1.3 Beyond Local dwarf galaxies

Historically, the study of SIDM has been primarily focused on Local dwarf galaxies due to their dark matter dominance and the related observational implications. However, assuming a constant self-interaction cross-section, the interaction rate and the resulting signatures of SIDM should be more pronounced in systems with higher densities and velocity dispersions. Such systems include massive galaxy clusters and their host halos in the Local Universe, as well as rare massive halos at high redshift, which could act as the hosts of bright quasars.

Massive halos in the Local Universe

Due to the strong signature of SIDM in high-density and velocity systems, the most stringent constraints on SIDM naturally come from massive galaxy clusters. For instance, constraints around $0.4 - 2 \text{ cm}^2 \text{ g}^{-1}$ (95% confidence level) have been obtained from the lack of a spatial offset between the total mass peak and galaxy centroid [e.g., 158–162] in merging bullet-like clusters, or the strength of wobbles of the bright central galaxy [BCG; 163]. The robustness of these constraints is still under debate due to the difficulty in measuring and interpreting observables given the complexity of the baryonic physics and their interplay with the SIDM physics [e.g., 94, 95, 111, 113, 115, 164].

DM halo shape is a promising avenue to constrain SIDM with several studies made in the past. For example, Miralda-Escudé [165] argued that DM halos should be spherical inside the radius where DM particles would collide with each other once during a Hubble time on average. Based on the shape of the galaxy cluster MS 2137-23 as inferred from strongly gravitationally-lensed arcs, Miralda-Escudé [165] obtained a stringent constraint on the SIDM cross-section, $\sigma/m \lesssim 0.02 \text{ cm}^2 \text{ g}^{-1}$. Such a strong constraint was later shown to be incorrect by Peter et al. [166], by demonstrating that one collision event of DM particles on average is not enough to make halos completely spherical and that projection effects need to be properly considered to interpret observations. As a result, the constraint on SIDM was weakened to $\sigma/m \lesssim 1 \text{ cm}^2 \text{ g}^{-1}$. In recent years, high-resolution X-ray imaging data have provided rich information on the intracluster gas over a large dynamical range and have been used to infer the shapes of matter distributions in galaxy clusters [e.g., 167, 168], which has direct implications for SIDM constraints. In addition, X-ray morphological studies are also a powerful tool to assess the dynamical state of the intracluster medium (ICM). Samples of massive relaxed clusters have been identified through quantitative studies of the morphology of X-ray selected clusters [e.g.,

23, 169–173]. These clusters are ideal to compare to simulated counterparts in near equilibrium states in order to place significant constraints on SIDM based on their shapes.

In Chapter 4 of this thesis, I will present a project that compares the X-ray morphology of observed nearby galaxy clusters with the ones in cosmological hydrodynamical simulations. Through this comparison, we aim to derive constraints on elastic dark matter self-interactions.

Massive halos at high-redshift

The implication of SIDM is not restricted to the Local Universe. Observations of quasars at $z \gtrsim 6$ indicate that SMBHs with masses greater than $\sim 10^9 M_\odot$ formed in the early Universe (e.g. [174–178]). The discovery of such SMBHs is puzzling in the current understanding of SMBHs, *i.e.*, *how did the first SMBHs grow so large so quickly?* One possible scenario is that the SMBHs were seeded by the remnants of the Population III (Pop III) stars, which are expected to form in $\sim 10^{5-6} M_\odot$ DM minihalos through primordial gas undergoing molecular hydrogen cooling. Since the primordial gas is significantly warmer than the usual star-forming molecular clouds at low redshift, the cooling is less efficient, leading to inefficient fragmentation [179–186]. Therefore, Pop III stars are expected to be more massive than stars in the Local Universe, and simulations have suggested a mass range of $10 \lesssim M_\star/M_\odot \lesssim 10^3$ [187]. If SMBH growth is dominated by Eddington-limited accretion, SMBH seeds will grow exponentially within an e -folding time $t_{\text{edd}} \approx 50$ Myr, assuming a radiative efficiency $\epsilon_r \approx 10\%$. In the Eddington-limit, a $100 M_\odot$ Pop III seed will need ≈ 0.8 Gyr to reach a billion solar mass, a time greater than the age of the universe at $z = 7$ even assuming a duty-cycle $D \approx 1$ over eight orders of magnitude growth in mass, making it impossible to explain the mass growth of SMBHs with masses $10^9 M_\odot$ at $z = 7$. A high duty-cycle ($D \approx 1$) is also disfavored by the feedback effects from accretion onto the SMBH, as well as displacement of the gas reservoir by UV radiation and supernovae explosions of the Pop III stars in the shallow gravitational potential of minihalos [188–191].

Several different scenarios have been proposed to ease the timescale constraints (see [18] for a review of the assembly of SMBHs at high redshift). Generally, one can increase either the SMBH seed mass or the growth rate. One possibility is that a small fraction of SMBH seeds in rare massive halos may be able to sustain Eddington accretion over most of the history of the Universe or even grow at a super-Eddington

rate [192]. Super-Eddington accretion at a few times the Eddington-limited rate could be maintained with duty-cycles $\sim 20 - 30\%$ in some accretion disk models (e.g. [193]), which could explain the existence of billion solar mass SMBHs at $z \gtrsim 7$. Another popular scenario relies on the formation of massive SMBH seeds with mass $\approx 10^{4-6} M_{\odot}$ formed through collapse of chemically pristine primordial gas in so-called “atomic cooling halos” with virial temperature $T_{\text{vir}} \sim 10^4$ k at $z \simeq 15 - 20$ [186, 194–199]. However, even in these models, an Eddington-limit accretion has to be sustained for most of the lifetime of the seeds, which implies a very high duty-cycle of SMBHs in the early Universe. Thus, such a scenario is hard to reconcile with some of the massive quasars at $z \gtrsim 6$ with low measured Eddington ratios [200, 201] as well as the short quasar lifetimes ($\sim 10^{4-5}$ yr) found in observations of quasar proximity zones at $z \sim 6$ [202–206].

SIDM halos have the potential to seed massive SMBHs in a much more accelerated way through the “gravothermal catastrophe” [123, 207–210]. Finite self-gravitating systems (e.g. DM halos, globular clusters) have a negative heat capacity and the heat conduction will eventually lead to the “gravothermal catastrophe” of the system (e.g. [117, 118]). In a halo with elastic DM self-interactions, effective heat conduction is realized by collisions between DM particles and the SIDM halo cores could ultimately experience run-away collapse into compact objects (e.g. [87, 119, 120, 122, 123, 207]). However, such eSIDM requires a cross-section $\sigma/m = 5 \text{ cm}^2 \text{ g}^{-1}$ to seed SMBHs with masses $10^6 M_{\odot}$ at $z \sim 10$ [207], which is now ruled out by observations of galaxy cluster collisions [159]. Those constraints are derived at relative velocities 1000-2000 km/s, while the DM halos we are interested in have virial velocities 200-2000 km/s. If the cross-section is velocity dependent, those constraints might be avoided and a large cross-section that can seed SMBHs efficiently is allowed, which we have not studied quantitatively. To accelerate the “gravothermal catastrophe”, hybrid DM models were proposed where the bulk of DM does not have any self-interaction, but a small fraction is SIDM with a large cross-section [208, 211]. Alternatively, the presence of baryons in protogalaxies has also been shown to accelerate the gravothermal collapse of eSIDM halos [16] with a smaller cross-section.

If the self-interaction is totally inelastic (hit-and-stick), the collapse timescale can be two orders of magnitude shorter than the prediction in elastic SIDM [125, 211, 212]. Therefore, totally dissipative self-interacting DM (tdSIDM) can greatly accelerate the catastrophic collapse of halos, which leads to the formation of SMBHs in the

early universe. Our study is motivated by the analysis of dark nuggets in Refs. [213–215], based on the model of Refs. [216, 217] featuring hit-and-stick interactions that are crucial for accelerating the catastrophic collapse of SIDM halos. Other dissipative DM models, such as atomic DM, exciting DM, and composite strongly interacting DM [98, 218–228], feature a constant kinetic energy loss in the center-of-momentum frame, which needs to be tuned to accelerate the catastrophic collapse efficiently. The proposal of Gresham et al. [213] was to consider *rare, high density* fluctuations of dissipative DM which features hit-and-stick interactions as the seeds of SMBHs at high redshift.

In Chapter 5 of this thesis, I will introduce a project aiming at testing this hypothesis in detail using a combination of numeric simulations and semi-analytical models. Though the timescale of seeding SMBHs in an isolated tdSIDM halo was well-studied [211, 212], the cosmological abundance of SMBHs in the early Universe has never been calculated. We want to determine whether a hit-and-stick dissipative DM model that produces SMBHs through this mechanism can explain the SMBH abundance in the early Universe while remaining consistent with observations of DM halos (and their SMBHs) in the late Universe.

Chapter 2

DISSIPATIVE DM – SIMULATIONS

Xuejian Shen, Philip F. Hopkins, Lina Necib, Fangzhou Jiang, Michael Boylan-Kolchin, and Andrew Wetzel. Dissipative dark matter on FIRE - I. Structural and kinematic properties of dwarf galaxies. *MNRAS*, 506(3):4421–4445, September 2021. doi: 10.1093/mnras/stab2042.

2.1 Abstract of the chapter

In this chapter, we present the first set of cosmological baryonic zoom-in simulations of galaxies including dSIDM. These simulations utilize the Feedback In Realistic Environments (FIRE-2) galaxy formation physics, but allow the dark matter to have dissipative self-interactions analogous to Standard Model forces, parameterized by the self-interaction cross-section per unit mass, (σ/m) , and the dimensionless degree of dissipation, $0 < f_{\text{diss}} < 1$. We survey this parameter space, including constant and velocity-dependent cross-sections, and focus on structural and kinematic properties of dwarf galaxies with $M_{\text{halo}} \sim 10^{10-11} M_{\odot}$ and $M_{*} \sim 10^{5-8} M_{\odot}$. Central density profiles (parameterized as $\rho \propto r^{\alpha}$) of simulated dwarfs become cuspy when $(\sigma/m)_{\text{eff}} \gtrsim 0.1 \text{ cm}^2 \text{ g}^{-1}$ (and $f_{\text{diss}} = 0.5$ as fiducial). The power-law slopes asymptote to $\alpha \approx -1.5$ in low-mass dwarfs independent of cross-section, which arises from a dark matter “cooling flow”. Through comparisons with DM-only simulations, we find the profile in this regime is insensitive to the inclusion of baryons. However, when $(\sigma/m)_{\text{eff}} \ll 0.1 \text{ cm}^2 \text{ g}^{-1}$, baryonic effects can produce cored density profiles comparable to non-dissipative CDM runs but at smaller radii. Simulated galaxies with $(\sigma/m) \gtrsim 10 \text{ cm}^2 \text{ g}^{-1}$ and the fiducial f_{diss} develop a significant coherent rotation of dark matter, accompanied by halo deformation, but this is unlike the well-defined thin “dark disks” often attributed to baryon-like dSIDM. The density profiles in this high cross-section model exhibit lower normalizations given the onset of halo deformation. For our surveyed dSIDM parameters, halo masses, and galaxy stellar masses do not show appreciable differences from CDM, but dark matter kinematics and halo concentrations/shapes can differ.

The chapter is arranged as follows: In Section 2.2, we discuss the details of the simulations and briefly introduce the dSIDM models we study. We derive relevant time scales for dSIDM halos analytically in Section 2.3 and study the stellar masses

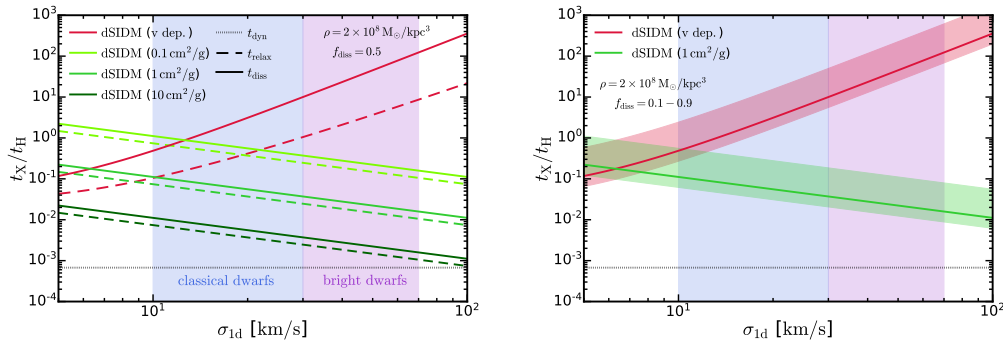


Figure 2.1: *Top: Relevant time scales of the physical processes involved in dSIDM halos versus one-dimensional velocity dispersion of the system.* We have assumed that the local DM density is $\rho_{\text{dm}} = 2 \times 10^8 M_\odot/\text{kpc}^3$, a typical value at dwarf galaxy centers. We show the collision time scale (t_{coll}) and dissipation time scales (t_{diss}) of all the dSIDM models studied in this chapter as well as the dynamical time scale (t_{dyn}). All the time scales are normalized by the Hubble time scale at $z = 0$ ($t_{\text{h}} \equiv 1/h_0$). The dissipation time scales are calculated assuming $f_{\text{diss}} = 0.5$. The shaded regions show the typical one-dimensional velocity dispersions in the classical (e.g. Milky Way satellites) and bright dwarf galaxies (e.g. LSB galaxies). In dwarf galaxies, dissipation and collision time scales are much larger than the dynamical time scale, but can become considerably shorter than the Hubble time scale. The velocity-dependent model becomes less dissipative ($t_{\text{diss}}/t_{\text{h}}$ becomes larger) in more massive galaxies (with larger velocity dispersion) while models with constant cross-sections become more dissipative. *Bottom: Dissipation time scales versus one-dimensional velocity dispersion of the system with f_{diss} varying from 0.1 to 0.9.* The symbols are the same as the top panel. For each model, the upper boundary of the shaded region corresponds to the case $f_{\text{diss}} = 0.1$ and the lower boundary corresponds to the case $f_{\text{diss}} = 0.9$.

and host halo masses of simulated dwarf galaxies in Section 2.4. Then we present the mass density profiles of simulated dwarf galaxies and quantitatively study the impact of dissipation on galaxy structure in Section 2.4. We study the kinematic properties of DM and the shapes of halos in simulations in Section 2.4 and Section 2.5. Subsequently, in Section 2.6, we use analytical methods to explain the phenomena in dSIDM simulations and summarize the evolution pattern of dSIDM halos in different regimes. In Section 2.7, we explore the results of simulations with other choices of f_{diss} as well as the DMO simulations and compare their differences from the fiducial simulations. The summary and conclusion of the chapter are presented in Section 2.8.

Simulation name	$M_{\text{halo}}^{\text{cdm}}$ [M_{\odot}]	$R_{\text{vir}}^{\text{cdm}}$ [kpc]	M_{*}^{cdm} [M_{\odot}]	$r_{1/2}^{\text{cdm}}$ [kpc]	$r_{\text{dm}}^{\text{conv}}$ [pc]	Notes
ultra-faint dwarf						
m09	2.5e9	35.6	7.0e4	0.46	65	par choices explored
Classical dwarfs						
m10b	9.4e9	55.2	5.8e5	0.36	77	late-forming
m10q	7.5e9	51.1	1.7e6	0.72	73	isolated, early-forming
m10v	8.5e9	53.5	1.4e5	0.32	65	isolated, late-forming
Bright dwarfs						
m11a	3.6e10	86.7	3.7e7	1.2	310	diffuse, cored
m11b	4.2e10	90.7	4.2e7	1.7	250	intermediate-forming
m11q	1.5e11	138.7	2.9e8	3.1	240	early-forming, cored
Milky Way-mass galaxies						
m11f	4.5e11	200.2	1.0e10	2.9	280	quiescent late history
m12i l.r.	1.1e12	272.3	1.1e11	2.0	290	Milky Way like
m12f l.r.	1.5e12	302.8	1.3e11	4.1	310	Milky Way like
m12m l.r.	1.5e12	299.3	1.4e11	6.1	360	early-forming
m12i h.r.	9.8e11	259.9	2.4e10	3.7	150	Milky Way like

Table 2.1: **Simulations of the FIRE-2 dSIDM suite.** The simulated galaxies are labeled and grouped by their halo masses. They are classified into four categories: ultra-faint dwarfs; classical dwarfs, with typical halo mass $\lesssim 10^{10} M_{\odot}$; bright dwarfs, with typical halo mass $\sim 10^{10-11} M_{\odot}$; Milky Way-mass galaxies, with typical halo mass $\sim 10^{12} M_{\odot}$. These halos are randomly picked from the standard FIRE-2 simulation suite [25], sampling various star formation and merger histories. All units are physical.

(1) Name of the simulation. “l.r.” (“h.r.”) indicates low (high)-resolution version of the simulation.

(2) $M_{\text{halo}}^{\text{cdm}}$: Virial mass of the halo (definition given in Section 2.4) in the CDM simulation with baryons at $z = 0$.

(3) $R_{\text{vir}}^{\text{cdm}}$: Virial radius of the halo (definition given in Section 2.4) in the CDM simulation with baryons at $z = 0$.

(4) M_{*}^{cdm} : Galaxy Stellar mass (see Section 2.4) in the CDM simulation at $z = 0$.

(5) $r_{1/2}^{\text{cdm}}$: Galaxy stellar half mass radius (see Section 2.4) in the CDM simulation at $z = 0$.

(6) $r_{\text{dm}}^{\text{conv}}$: Radius of convergence in DM properties at $z = 0$ (calculated for the CDM DMO simulations in the standard FIRE-2 series [25] based on the Power et al. [26] criterion). As shown in Hopkins et al. [25], the convergence radii in simulations with baryons can in fact extend to much smaller radii.

(7-11) Parameters of the DM models. σ (with the number after it) indicates the self-interaction cross-section, σ/m , in unit of $\text{cm}^2 \text{g}^{-1}$. $\sigma(v)$ denotes the velocity-dependent cross-section, introduced in Section 2.2. f_{diss} indicates the dimensionless degree of dissipation.

(12) Notes: Additional information of each simulation.

2.2 Simulations

Overview of the simulation suite

We present the new FIRE-2 dSIDM simulation suite, which consists of ~ 45 cosmological hydrodynamical zoom-in simulations of galaxies chosen at representative mass scales with CDM, eSIDM, and dSIDM models. The simulations here are part of the Feedback In Realistic Environments project [FIRE, 229], specifically the ‘‘FIRE-2’’ version of the code with details described in Hopkins et al. [25]. The simulations adopt the code Gizmo [230], with hydrodynamics solved using the mesh-free Lagrangian Godunov ‘‘MFM’’ method. The simulations include heating and cooling from a meta-galactic radiation background and stellar sources in the galaxies, star formation in self-gravitating molecular, Jeans-unstable gas, and stellar/supernovae/radiation feedback. The FIRE physics, source code, and numerical parameters are identical to those described in Hopkins et al. [25], Garrison-Kimmel et al. [231]. For dwarf galaxies, the baryonic particle masses of simulations are $m_b \simeq 250 - 2000 M_\odot$. For Milky Way-mass galaxies, the high-resolution ‘latte’ runs have $m_b = 7000 M_\odot$ while the low-resolution runs have $m_b = 56000 M_\odot$. In all simulations, the DM particle masses are roughly five times larger, according to the universal baryon fraction. For dwarf galaxies, the minimum gravitational force softening length reached by gas in the simulations is $h_b \simeq 0.5 - 2$ pc. For Milky Way-mass galaxies, the value is $h_b \simeq 0.3 - 0.5$ pc (1.4 pc) for high-resolution (low-resolution) runs. The physical DM force resolution of the simulations of dwarf (Milky Way-mass) galaxies is $\epsilon_{\text{dm}} = 40$ pc (30 pc). Force softening for gas uses the fully conservative adaptive algorithm from Price and Monaghan [232], meaning that the gravitational force assumes the identical mass distribution as the hydrodynamic equations (resulting in identical hydrodynamic and gravitational resolution). The simulations are identified with the main ‘‘target’’ halo around which the high-resolution zoom-in region is centered. In post-processing, we identify subhalos (of the main ‘‘target’’ halo) with the ROCKSTAR [233] halo finder and create merger trees of halos (subhalos) with the code CONSISTENT TREES [234, 235]. As shown in Table 2.1, the simulation suite consists of one ultra-faint dwarf (m09), three classical dwarf galaxies (m10q, m10b, m10v), three bright dwarf galaxies (m11a, m11b, m11q) and four Milky Way-mass galaxies (m11f, m12i, m12f, m12m). The analysis in this chapter will primarily focus on the classical and bright dwarf galaxies and we defer analysis on Milky Way-mass galaxies to a follow-up work.

Dissipative DM parameterization

DM self-interactions are simulated in a Monte-Carlo fashion following the implementation in Rocha et al. [88] and the scattering process is assumed to be isotropic. In this chapter, we study a simplified empirical dSIDM model: two DM particles lose a constant fraction, f_{diss} , of their kinetic energy in the center of momentum frame when they collide with each other. The extreme version of this type of interaction is the fusion process ($f_{\text{diss}} = 1$) of DM composites. Such a model has been discussed in the context of self-interacting asymmetric DM [e.g., 99, 106, 236–238]. Self-interaction mediated by a scalar mediator can give rise to strong attractive forces, and large bound states of DM (“nuggets”) can form in the absence of competing repulsive forces [99, 106]. These dark nuggets are the smoking gun signature of fermionic asymmetric DM [see 239, for a review]. The residual self-interaction between nuggets is highly dissipative and mimics the fusion process of nucleons.

Beyond this, dissipative portals present in other SIDM models as well. For strongly-interacting dark composites in a hidden non-Abelian sector [e.g., 85, 96, 98], DM will consist of dark baryons/mesons and glueballs (or glueballinos if incorporating super-symmetry). For example, inelastic scattering to excited state(s) and glueball emission will be possible when glueballinos have mass $m_\chi \gg \Lambda$ [98]. Hyperfine-transitions of dark mesons/baryons have been suggested in Alves et al. [96, 240] and the late time up-scattering to excited states can induce dissipation. Excited states and dissipative (endothermic) processes are also ubiquitous in generic SIDM models [e.g., 78, 81], models featuring a dark SU(2)-like sector [e.g., 241, 242] or a dark U(1)-like sector [e.g., 97, 101, 128, 243]. However, the exact behavior of dissipation is model-dependent and could be quite different from what we are modeling here.

For each galaxy, we run simulations with a default dissipation fraction $f_{\text{diss}} = 0.5$ ¹ and with constant self-interaction cross-sections $(\sigma/m) = 0.1/1/10 \text{ cm}^2 \text{ g}^{-1}$ or a velocity-dependent cross-section model

$$\frac{\sigma(v)}{m} = \frac{(\sigma/m)_0}{1 + (v/v_0)^4}, \quad (2.1)$$

where the fiducial choice of parameters is $(\sigma/m)_0 = 10 \text{ cm}^2 \text{ g}^{-1}$ and $v_0 = 10 \text{ km s}^{-1}$. The velocity dependence of the self-interaction cross-section is empirically motivated by the relatively tight constraints on SIDM at galaxy cluster scale [e.g., 94, 159, 244] and the relatively high cross-section needed to solve some small-scale

¹Other choices of f_{diss} are explored with m09 in Section 2.7.

problems [e.g., 87–90, 94]. Meanwhile, velocity dependence is a generic feature of many particle physics realizations of DM. The asymptotic $(v/v_0)^{-4}$ velocity dependence we adopt is motivated by particle physics models featuring DM self-interactions mediated by light gauge bosons [e.g., 79, 83, 97, 102, 104]. The sharp decline in cross-section could also appear in some models of strongly interacting composites. In these models, when the de Broglie wavelength of the particle becomes smaller than the characteristic length scale of the interaction, $\sim 1/\Lambda_{\text{dm}}$, the self-interaction cross-section is expected to drop significantly [e.g., 85, 86, 98].

2.3 Relevant time scales

In this section, we derive analytical formulae for relevant time scales in dSIDM halos, including the dynamical time scale, the collision time scale, and the dissipation time scale. These analytical formulae can be used to understand the influence of dissipation on galaxy structures in different circumstances. We will present results for models with constant and velocity-dependent cross-sections, respectively.

Dynamical time scale

The local dynamical time scale in a system is defined as

$$\begin{aligned} t_{\text{dyn}} &\equiv \sqrt{\frac{1}{4\pi G \rho}} \\ &= 0.0042 \text{ Gyr} \left(\frac{\rho}{10^9 M_{\odot} / \text{kpc}^3} \right)^{-1/2}, \end{aligned} \quad (2.2)$$

where G is the gravitational constant and ρ is the local matter density. At the centers of dwarf galaxies, the mass density is dominated by DM, so ρ is simply the local DM mass density.

Collision time scale

The collision time scale of DM self-interaction is

$$t_{\text{coll}} \equiv \frac{1}{\langle \rho v_{\text{rel}} \frac{\sigma}{m} \rangle}, \quad (2.3)$$

where ρ is local DM mass density, v_{rel} is the relative velocity between DM particles and $\langle \dots \rangle$ denotes the average over all possible encounters. This measures the time scale that one DM particle is expected to have one self-interaction with any other DM particles. For simplicity, we assume that the velocities of DM particles locally obey the Maxwell-Boltzmann distribution. Therefore, the average can be treated as

a thermal average

$$\langle X \rangle = \frac{1}{2\sqrt{\pi}\sigma_{1d}^3} \int_0^\infty dv_{\text{rel}} v_{\text{rel}}^2 e^{-v_{\text{rel}}^2/4\sigma_{1d}^2} X, \quad (2.4)$$

where σ_{1d} is the local one-dimensional velocity dispersion of DM. After taking the thermal average, the collision time scale is

$$\begin{aligned} t_{\text{coll}} &= 0.206 \text{ Gyr} \left(\frac{\rho}{10^9 M_\odot / \text{kpc}^3} \right)^{-1} \left(\frac{(\sigma/m)}{1 \text{ cm}^2 \text{ g}^{-1}} \right)^{-1} \left(\frac{\sigma_{1d}}{10 \text{ km s}^{-1}} \right)^{-1} \\ &\quad \text{[constant cross-section];} \\ t_{\text{coll}} &= 0.661 \text{ Gyr} \left(\frac{\rho}{10^9 M_\odot / \text{kpc}^3} \right)^{-1} \left(\frac{(\sigma/m)_0}{10 \text{ cm}^2 \text{ g}^{-1}} \right)^{-1} \left(\frac{\sigma_{1d}}{10 \text{ km s}^{-1}} \right)^{-1} \\ &\quad \left(\frac{\sigma_{1d}}{v_0} \right)^4 \left[-2\text{Ci}\left(\frac{v_0^2}{4\sigma_{1d}^2}\right) \cos\left(\frac{v_0^2}{4\sigma_{1d}^2}\right) + \sin\left(\frac{v_0^2}{4\sigma_{1d}^2}\right) \left(\pi - 2\text{Si}\left(\frac{v_0^2}{4\sigma_{1d}^2}\right) \right) \right]^{-1} \\ &\quad \simeq 0.165 \text{ Gyr} \left(\frac{\rho}{10^9 M_\odot / \text{kpc}^3} \right)^{-1} \left(\frac{(\sigma/m)_0}{10 \text{ cm}^2 \text{ g}^{-1}} \right)^{-1} \left(\frac{\sigma_{1d}}{10 \text{ km s}^{-1}} \right)^{-1} \\ &\quad \left(\frac{\sigma_{1d}}{v_0} \right)^4 \ln \left(\frac{\sigma_{1d}}{v_0} \right)^{-1} \quad [\sigma_{1d} \gg v_0] \\ &\quad \text{[velocity-dependent cross-section],} \end{aligned} \quad (2.5)$$

where $\text{Si}(x) = \int_0^x dt \sin(t)/t$ and $\text{Ci}(x) = -\int_x^\infty dt \cos(t)/t$ are sine and cosine integrals, $(\sigma/m)_0$ and v_0 are parameters of the velocity-dependent cross-section. For our fiducial choice of $v_0 = 10 \text{ km s}^{-1}$, galaxies of masses $\gtrsim 10^{11} M_\odot$ (massive dwarfs/Milky Way-mass galaxies) will have velocity dispersions in the limit $\sigma_{1d} \gg v_0$. We can see that the collision time scale of the velocity-dependent model is usually much larger than the constant cross-section model after the thermal average. This is due to the velocity suppression of collisions between particles with high relative velocities, which contribute more to the total interaction rate. In addition, the collision time scale in different models scales with velocity dispersion in opposite ways. For the models with *constant* cross-sections, the collision time scale is *shorter* in systems with higher densities or higher velocity dispersions, which indicates that *self-interaction has a stronger impact in more massive systems*. On the other hand, for the *velocity-dependent* model, the collision time scale sharply *increases* in systems with higher velocity dispersions, which indicates that *self-interaction has a weaker impact in more massive systems*.

Dissipation time scale

The dissipation time scale here is defined as the time scale for an order-unity fraction of local DM kinetic energy to be dissipated away through DM self-interactions

$$t_{\text{diss}} \equiv \frac{3}{2} \rho \sigma_{1d}^2 / C, \quad (2.6)$$

where σ_{1d} is the one-dimensional velocity dispersion and C is the effective cooling rate defined as

$$C \equiv \left\langle n(\rho v_{\text{rel}} \frac{\sigma}{m}) E_{\text{loss}} \right\rangle = \left\langle \rho^2 \frac{\sigma}{m} v_{\text{rel}} \frac{E_{\text{loss}}}{m} \right\rangle, \quad (2.7)$$

where n is the local number density of DM particles, E_{loss} is the kinetic energy loss per collision in the center of momentum frame, and $\langle \dots \rangle$ again denotes the thermal average. For the fractional dissipation model we study in this chapter, $E_{\text{loss}}/m = (1/4) f_{\text{diss}} v_{\text{rel}}^2$. The dissipation time scale measures how fast the kinetic energy is dissipated away from the system and, after order one dissipation time scale, the local DM structure is expected to be dramatically affected.

After taking the thermal average, the dissipation time scale is

$$\begin{aligned} t_{\text{diss}} &= \frac{3}{4 f_{\text{diss}}} t_{\text{coll}} \\ &= 0.310 \text{ Gyr} \left(\frac{f_{\text{diss}}}{0.5} \right)^{-1} \left(\frac{\rho}{10^9 \text{ M}_{\odot} / \text{kpc}^3} \right)^{-1} \left(\frac{\sigma/m}{1 \text{ cm}^2 \text{ g}^{-1}} \right)^{-1} \\ &\quad \left(\frac{\sigma_{1d}}{10 \text{ km s}^{-1}} \right)^{-1} \\ &\quad \text{[constant cross-section];} \\ t_{\text{diss}} &= 7.926 \text{ Gyr} \left(\frac{f_{\text{diss}}}{0.5} \right)^{-1} \left(\frac{\rho}{10^9 \text{ M}_{\odot} / \text{kpc}^3} \right)^{-1} \left(\frac{(\sigma/m)_0}{10 \text{ cm}^2 \text{ g}^{-1}} \right)^{-1} \\ &\quad \left(\frac{\sigma_{1d}}{10 \text{ km s}^{-1}} \right)^{-1} \left(\frac{\sigma_{1d}}{v_0} \right)^6 \left[8 \left(\frac{\sigma_{1d}}{v_0} \right)^2 - 2 \text{Ci} \left(\frac{v_0^2}{4\sigma_{1d}^2} \right) \sin \left(\frac{v_0^2}{4\sigma_{1d}^2} \right) \right. \\ &\quad \left. - \cos \left(\frac{v_0^2}{4\sigma_{1d}^2} \right) \left(\pi - 2 \text{Si} \left(\frac{v_0^2}{4\sigma_{1d}^2} \right) \right) \right]^{-1} \\ &\approx 0.991 \text{ Gyr} \left(\frac{f_{\text{diss}}}{0.5} \right)^{-1} \left(\frac{\rho}{10^9 \text{ M}_{\odot} / \text{kpc}^3} \right)^{-1} \left(\frac{(\sigma/m)_0}{10 \text{ cm}^2 \text{ g}^{-1}} \right)^{-1} \\ &\quad \left(\frac{\sigma_{1d}}{10 \text{ km s}^{-1}} \right)^{-1} \left(\frac{\sigma_{1d}}{v_0} \right)^4, \quad [\sigma_{1d} \gg v_0] \\ &\quad \text{[velocity dependent model]}. \end{aligned} \quad (2.8)$$

In the model with a constant cross-section, the dissipation time scale has the same scaling behavior as the collision time scale defined in Equation 2.5 and differs only

by a factor of $0.75/f_{\text{diss}}$. In the velocity-dependent model, the scaling behaviors of the dissipation and collision time scales are also quite similar when $\sigma_{1d} \gg v_0$. The dissipation time scale of the velocity-dependent model is usually much larger than the constant cross-section model after thermal average. This again can be attributed to the velocity suppression of collisions between particles with high relative velocities, which not only contribute more to the total collision rate but also induce higher energy loss per collision. Similar to what has been found for the collision time scale, dissipation is *more significant in more massive systems* in the models with *constant* cross-sections. Dissipation, however, is *less significant in more massive systems* in the *velocity-dependent* model.

In Figure 2.1, we show the relevant time scales discussed above as a function of the one-dimensional velocity dispersion of the system; in particular, we show the collision and dissipation time scales of the dSIDM models studied in this chapter as well as the dynamical time scale, assuming that the local DM mass density is $\rho = 2 \times 10^8 \text{ M}_\odot/\text{kpc}^3$, which is a typical value at dwarf galaxy centers. The time scales are all normalized by the Hubble time scale at $z = 0$, roughly representing the lifetime of the system. In the top panel, the dissipation time scales are calculated assuming $f_{\text{diss}} = 0.5$ while, in the bottom panel, the shaded regions indicate the variation of t_{diss} with $f_{\text{diss}} = 0.1 - 0.9$. With the vertical shaded regions in both panels, we show the typical ranges of one-dimensional velocity dispersions of the classical (e.g., Milky Way satellites) and bright dwarf galaxies (e.g., LSB galaxies). For the dSIDM models with constant cross-sections, the collision time scales are always proportional to the dissipation time scales and, they are order of magnitude comparable to each other. Both of them are shorter than the Hubble time scale but larger than the dynamical time scale in dwarf galaxies. The dissipation time scale decreases in systems with higher velocity dispersions, so we expect these constant cross-section models to become more dissipative in more massive dwarfs. For the velocity-dependent dSIDM model, the collision and dissipation time scales are no longer proportional to each other, and they both increase as the velocity dispersion increases, opposite to the behavior of models with constant cross-sections. The dissipation time scale of the velocity-dependent model is comparable to the Hubble time scale in the classical dwarfs but becomes at least an order of magnitude larger than the Hubble time scale in the bright dwarfs, suggesting negligible effects of dissipation in this case.

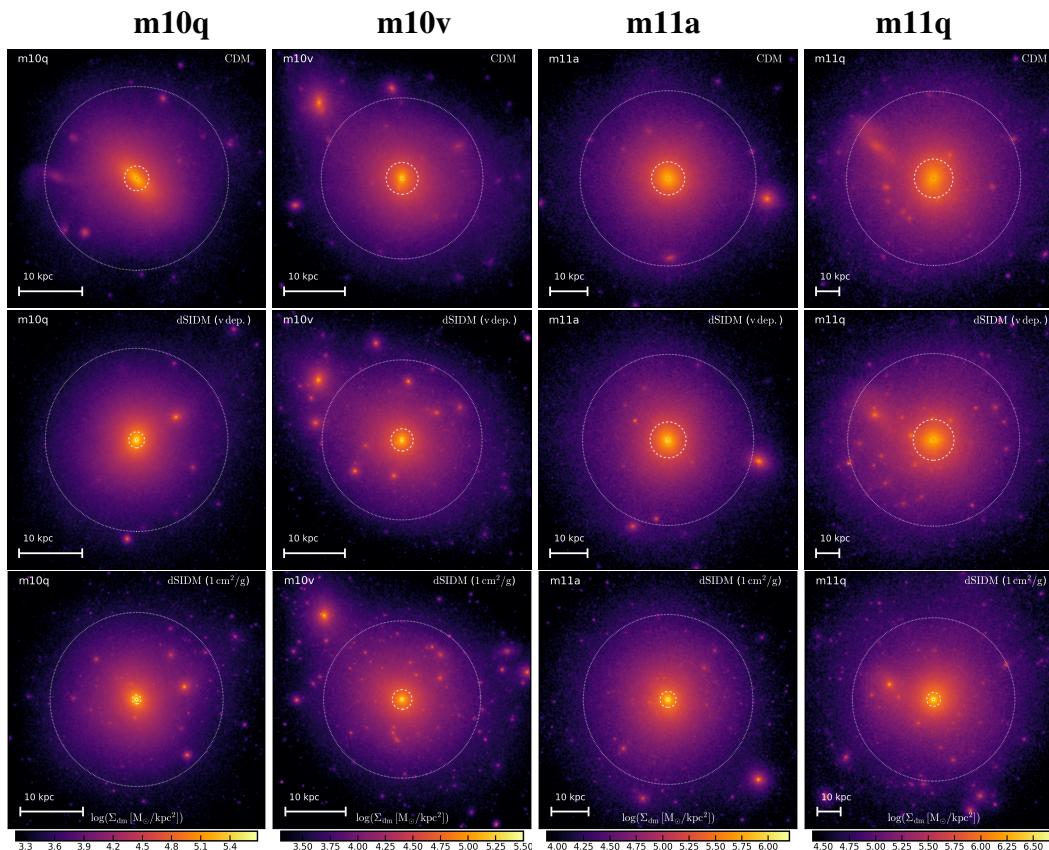


Figure 2.2: **Visualizations of four DM halos in simulations with CDM versus dSIDM.** The images are DM surface density maps, projected along the z -direction of simulation coordinates, at $z = 0$ with a logarithmic stretch. The dynamical ranges are adjusted based on the maximum/median intensities of the pixels (but remain the same for the same halo). The side lengths of the images are all chosen to be $0.8 \times R_{\text{vir}}$ of the CDM run. In the first row, we show the halos in the CDM. In the second row, we show the halos in the velocity-dependent dSIDM model. In the third row, we show halos in the dSIDM model with constant cross-section $1 \text{ cm}^2 \text{ g}^{-1}$. The halos are ordered from left to right by their virial masses. In each image, the outer dotted circle indicates the radius R_{500} (the density enclosed is 500 times the critical density at $z = 0$) which represents the overall size of the halo. The inner dashed circle indicates the radius $R_{\text{core}} \equiv 10 \times R_{0.1\%}$ (the mass enclosed in a sphere of radius $R_{0.1\%}$ is 0.1% the virial mass of the halo) which represents the core size of the halo. Comparing the core sizes, the halos in the dSIDM model are visibly more concentrated than their CDM counterparts. For the velocity-dependent dSIDM model, since the self-interaction cross-section decreases in more massive halos, the increased concentration of halo is less apparent in more massive halos. For the dSIDM with constant cross-section, halos of all masses are consistently more concentrated than their CDM counterparts.

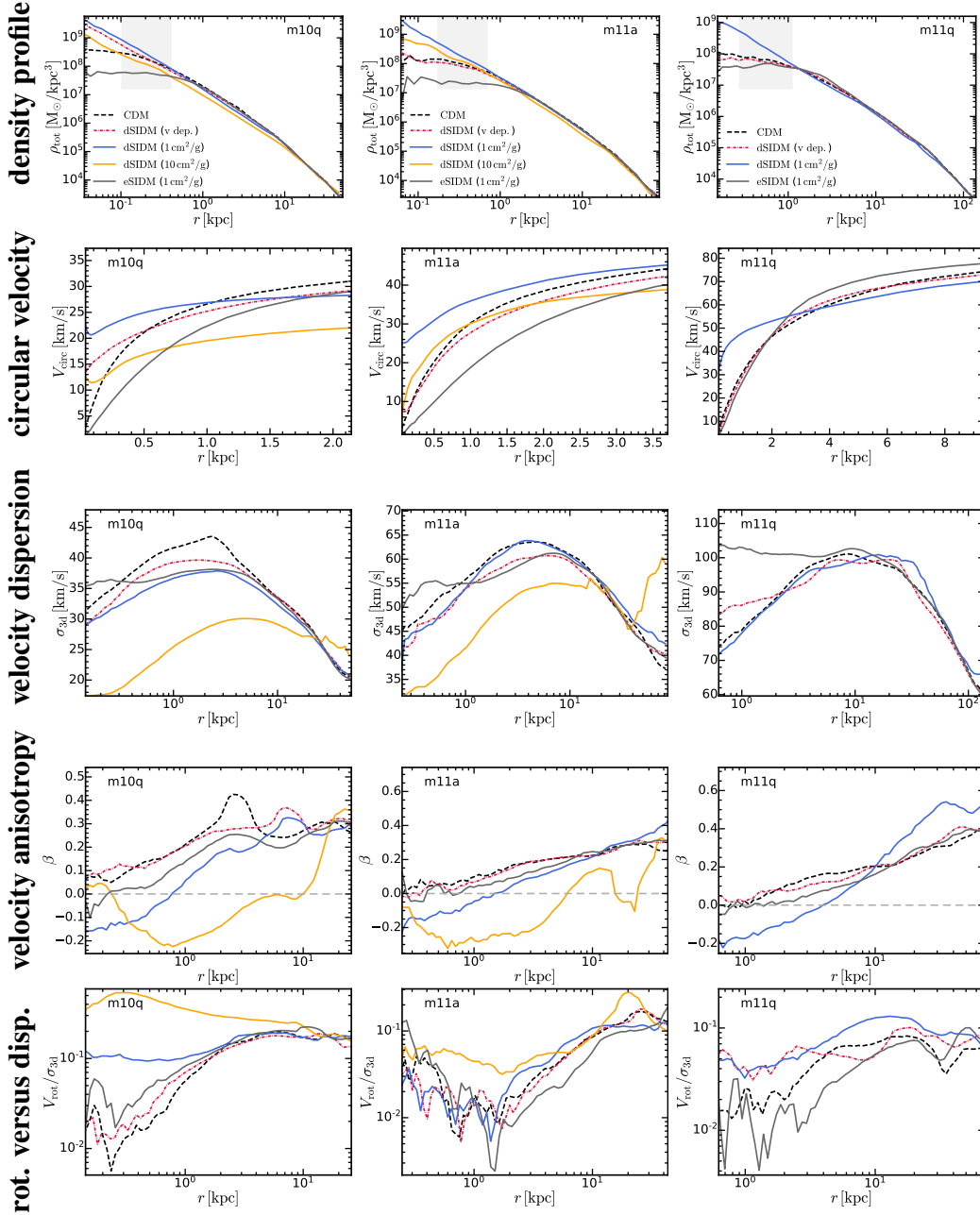


Figure 2.3: A gallery view of the structural and kinematic properties of dwarf galaxies in simulations. From top to bottom, in each row, we show the three-dimensional total mass density ($\rho_{\text{tot}} = \rho_{\text{dm}} + \rho_{\text{star}} + \rho_{\text{gas}}$), circular velocity ($V_{\text{circ}} \equiv \sqrt{GM_{\text{enc}}^{\text{tot}}(r)/r}$), the three-dimensional velocity dispersion of DM ($\sigma_{3d} \equiv \sqrt{\sigma_r^2 + \sigma_\theta^2 + \sigma_\phi^2}$), velocity anisotropy of DM ($\beta \equiv 1 - (\sigma_\theta^2 + \sigma_\phi^2)/2\sigma_r^2$), and rotation velocity versus velocity dispersion of DM ($V_{\text{rot}}/\sigma_{3d}$) averaged in spherical shells as a function of galactocentric distance for three simulated galaxies. We compare three categories of DM models: CDM, eSIDM (elastic SIDM model with a constant cross-section $1 \text{ cm}^2 \text{ g}^{-1}$), and dSIDM (dissipative SIDM models with various cross-sections, as defined in Table 2.1). The gray shaded regions in the first row of plots indicate $0.2\% - 0.8\% R_{\text{vir}}^{\text{cdm}}$, which is the aperture we will later use to measure the slopes of the density profiles (see Section 2.4 and Figure 2.5-2.7). The gray dashed horizontal line in the fourth row is a reference line, indicating isotropic velocity dispersion ($\beta=0$). In general, dSIDM models produce cuspy central density profiles in the simulated dwarf galaxies, as opposed to the cored central density profile in CDM and eSIDM models. As a consequence, the circular velocities at the center of the galaxies increase. In dSIDM models with $(\sigma/m) \geq 1 \text{ cm}^2 \text{ g}^{-1}$, coherent rotation of DM becomes prominent, and random velocity dispersion is suppressed.

Comparison to the cooling of baryons

The cooling induced by dissipative DM self-interactions can be compared to the cooling of baryons, which is usually described by the cooling function Λ . For dSIDM, the effective cooling function is

$$\begin{aligned} \Lambda_{\text{eff}} &\sim \frac{T}{nt_{\text{diss}}} \sim (\sigma/m) f_{\text{diss}} \sigma_{\text{1d}}^3 \\ &\sim \begin{cases} \sigma_{\text{1d}}^3 \sim T^{3/2} & \text{[constant cross-section]} \\ \sigma_{\text{1d}}^{-1} \sim T^{-1/2} & \text{[velocity dependent model]} \end{cases} \end{aligned} \quad (2.9)$$

where T is $m\sigma_{\text{1d}}^2/k_{\text{b}}$ for weakly collisional DM. The cooling function in the constant cross-section model is similar to the cooling curve of gas below $\sim 10^4$ K while the cooling function in the velocity-dependent model is similar to the $10^4 - 10^7$ K gas cooling curve. Other behaviors are possible if a velocity-dependence of f_{diss} is introduced, e.g. Λ_{eff} would be a constant if $f_{\text{diss}} \sim T^{1/2}$ with the same velocity-dependent cross-section. However, the most important qualitative difference between the dSIDM studied here and baryons is not the behavior of the cooling curve but the fact that baryons (gas) are effectively in the $f_{\text{diss}} \rightarrow 0$ and $(\sigma/m) \rightarrow \infty$ regime. The effective interaction cross-section of gas is enormous compared to favored SIDM interaction cross-sections and the energy loss per ‘‘collision’’ is small. Gas cooling is the result of a large number of particle interactions in a locally thermalized region. On the contrary, dSIDM with t_{coll} order of magnitude comparable to t_{diss} cannot achieve local thermalization effectively when cools down.

Effective cross-section

It is useful to define an ‘‘effective cross-section’’ for the velocity-dependent dSIDM model

$$\left(\frac{\sigma}{m}\right)_{\text{eff}} = \left\langle \frac{\sigma}{m} v_{\text{rel}} \right\rangle / \langle v_{\text{rel}} \rangle, \quad (2.10)$$

where v_{rel} is the relative velocity between encountering particles and $\langle \dots \rangle$ is a thermal average as discussed in Section 2.3. This definition ensures that a dSIDM model with a constant cross-section taking the value of this ‘‘effective cross-section’’ will result in the identical rate of DM self-interaction, assuming that DM particles are in thermal equilibrium. This definition allows a proper comparison between

velocity-dependent and independent SIDM models. Using Equation 2.4, we find

$$\left(\frac{\sigma}{m}\right)_{\text{eff}} = \frac{(\sigma/m)_0}{32} \left(\frac{v_0}{\sigma_{1d}}\right)^4 \left[-2\text{Ci}\left(\frac{v_0^2}{4\sigma_{1d}^2}\right) \cos\left(\frac{v_0^2}{4\sigma_{1d}^2}\right) + \sin\left(\frac{v_0^2}{4\sigma_{1d}^2}\right) \left(\pi - 2\text{Si}\left(\frac{v_0^2}{4\sigma_{1d}^2}\right)\right) \right], \quad (2.11)$$

where the notation is the same as Equation 2.5. The asymptotic behavior of $(\sigma/m)_{\text{eff}}$ is dominated by the σ_{1d}^{-4} term, which is similar to the velocity-dependent cross-section defined in Equation 2.1. The factor 32 in the denominator comes from the thermal average and indicates that dSIDM models with velocity-dependent cross-sections are not as efficient as those with constant cross-sections, owing again to the velocity suppression.

2.4 Simulation Results

In this section, we present the structural and kinematic properties of simulated dwarf galaxies in different DM models and study the impact of dissipation on galaxy structures.

Overview

In Figure 2.2, we show images of four DM halos in our simulation suite at $z = 0$. Each image is a two-dimensional surface density map of DM, projected along the z -direction of simulation coordinates, with a logarithmic stretch. The dynamical ranges are adjusted based on the maximum and median intensities of pixels. The halos are ordered from left to right by their halo masses (see Section 2.4 for the definition). We show the images in CDM, the dSIDM with constant cross-section ($\sigma/m = 1 \text{ cm}^2 \text{ g}^{-1}$), and the velocity-dependent dSIDM model for comparison. The halos in dSIDM models are visibly more concentrated than their CDM counterparts when comparing their core sizes (dashed circles). For the velocity-dependent dSIDM model, since the self-interaction cross-section decreases in more massive halos which typically have higher velocity dispersions, the increased concentration of the halo becomes less apparent. On the contrary, in dSIDM models with constant cross-sections, halos of all masses are consistently more concentrated than their CDM counterparts. Meanwhile, the substructures also appear to be more abundant and concentrated in dSIDM models. For example, in m10q, the number of subhalos (within the virial radius) with $M > 10^6 M_\odot$ increases by about 20%, and the median concentration increases by about 25% in the dSIDM model with

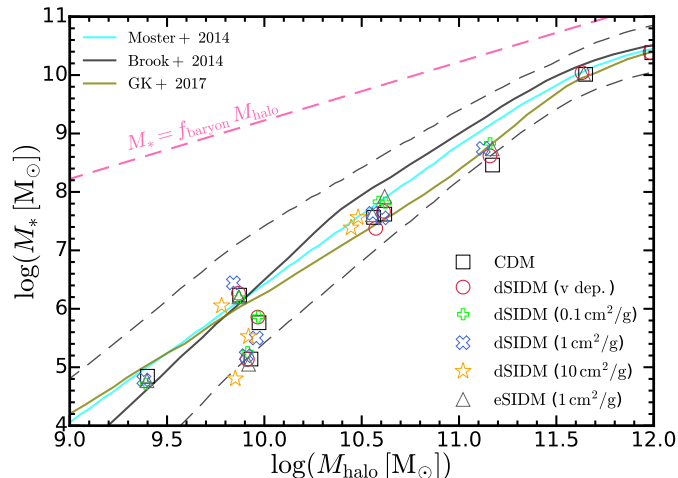


Figure 2.4: **Stellar mass versus halo mass relation of galaxies in simulations.** The stellar masses and halo masses of simulated dwarf galaxies are presented with open markers (as labeled). We compare them with the observational results derived through abundance matching from Moster et al. [1], Brook et al. [2], Garrison-Kimmel et al. [3]. The black dashed lines show $\sim 95\%$ inclusion contour assuming the scatter of the relation estimated in Garrison-Kimmel et al. [3]. Regardless of the DM model, the simulated galaxies are consistent with the observational relation.

$(\sigma/m) = 1 \text{ cm}^2 \text{ g}^{-1}$. But we will focus on the main halo in this chapter and defer the analysis of substructures to follow-up work.

In Figure 2.3, we present a gallery view of the total mass density, circular velocity, three-dimensional velocity dispersion of DM, velocity anisotropy of DM, rotation velocity versus velocity dispersion of DM, averaged in spherical shells as a function galactocentric distance for three simulated galaxies. Details of the measurements of the kinematic properties and relevant definitions are introduced in Section 2.4. Under the influence of baryonic feedback, the density profiles in CDM are generally shallower than the cuspy NFW profiles at galaxy centers, which is expected for these galaxies for their M_*/M_{halo} values [e.g., 42, 245–248]. In the eSIDM model, due to effective heat conduction, the profiles are even flatter at galaxy centers compared to the CDM case, but the difference becomes less apparent in the bright dwarf (m11q) where thermal conduction through self-interactions is subdominant compared to baryonic feedback. In dSIDM models, when the effective self-interaction cross-section is large (and equivalently dissipation is efficient assuming a fixed f_{diss}), the central density profiles are cuspy and power-law like. For the velocity-dependent dSIDM model, in the classical dwarf galaxies like m10q, the velocity-dependent cross-section is high and a cuspy central profile emerges. In more massive galax-

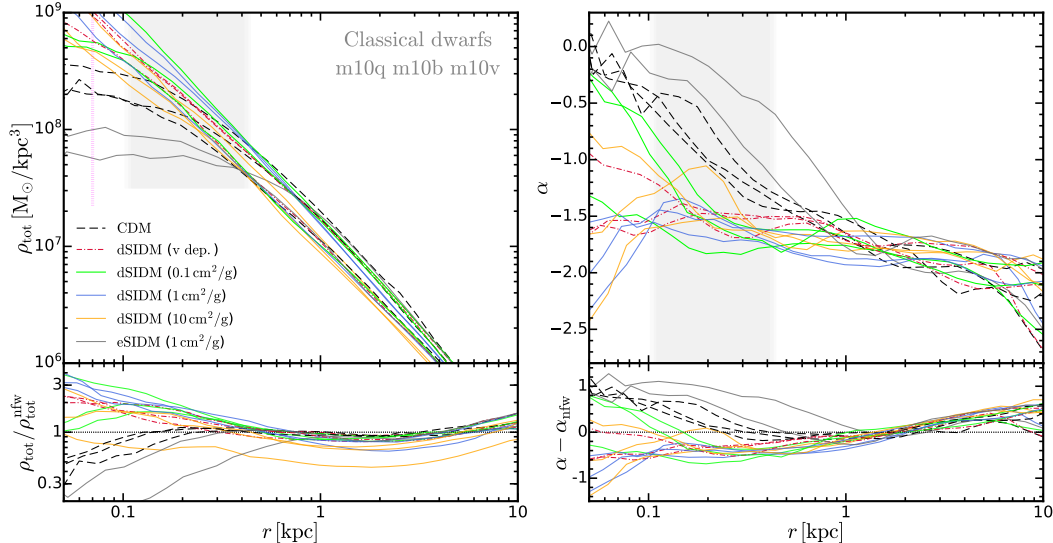


Figure 2.5: *Left: Total mass density profiles of the classical dwarf galaxies in simulations.* The three classical dwarfs presented here are m10q, m10b and m10v. The total mass density profiles in different DM models are shown (as labeled). They can be compared to the NFW profiles derived by fitting the density profiles at large radii of the halos ($0.5 r_{1/2}^{\text{cdm}} < r < 20 r_{1/2}^{\text{cdm}}$), and the ratios of the density profiles to the NFW fits are shown in the lower sub-panel. The gray shaded region denotes the range of radii where we measure the slopes of the density profiles below. The purple dotted vertical line indicates the average convergence radius (~ 70 pc) of the classical dwarfs (see Table 2.1). *Right: Local power-law slopes of density profiles of the classical dwarf galaxies.* The slopes are derived by fitting the nearby density profile with the power-law. In these classical dwarfs, the CDM model predicts cored central density profiles due to baryonic feedback. The eSIDM model produces cores of slightly bigger sizes and shallower slopes. The dSIDM model with $(\sigma/m) = 0.1 \text{ cm}^2 \text{ g}^{-1}$ still produces cored profiles but with higher central densities and steeper slopes than their CDM counterparts. The dSIDM models with effective cross-section $> 0.1 \text{ cm}^2 \text{ g}^{-1}$ all produce cuspy central density profiles with power-law slopes centering around -1.5 . These profiles are even steeper than the NFW profiles.

ies like m11a and m11q, the velocity-dependent cross-section there becomes much smaller, accompanied by stronger baryonic feedback. As a consequence, the profiles in these systems become cored again though the central mass density is still higher than the CDM case. An interesting outlier here is the dSIDM model with constant $(\sigma/m) = 10 \text{ cm}^2 \text{ g}^{-1}$, exhibiting a cuspy central density profile but with lower normalization, which is likely due to the deformed shape of the halo (see Section 2.5). A more detailed discussion on the mass density profiles will be presented in Section 2.4.

In addition to the density profile, the kinematic properties of halos are also quite different in different DM models. Despite some variations, there are some important features shared by the simulations of different halos. When the cross-section is high, the rotation curves of dwarf galaxies in dSIDM models are significantly higher at small radii compared to their CDM counterparts. The differences are consistent with the findings in density profiles. Again, an outlier is the dSIDM model with $(\sigma/m) = 10 \text{ cm}^2 \text{ g}^{-1}$, with the normalization of rotation velocities lower than other models. For the velocity dispersion profile, the ones in eSIDM are flat at halo centers indicating an isothermal distribution of DM particles. The velocity dispersions in dSIDM models in general decrease towards halo centers. Particularly, the dSIDM model with $(\sigma/m) = 10 \text{ cm}^2 \text{ g}^{-1}$ shows a dramatic decrease in velocity dispersion at $r \lesssim 10 \text{ kpc}$. This indicates a more coherent motion of DM particles and a decreasing support from random velocity dispersion. For the velocity anisotropy profile, the dSIDM models with $(\sigma/m) \geq 1 \text{ cm}^2 \text{ g}^{-1}$ have lower velocity anisotropies than their CDM counterparts at halo centers, indicating that the velocity dispersions are more dominated by the tangential component. At the same time, the coherent rotation is also stronger in these dSIDM models. An extreme case is the dSIDM model with $(\sigma/m) = 10 \text{ cm}^2 \text{ g}^{-1}$ where the sub-kpc structure is clearly in transition from dispersion supported to coherent rotation supported. The ratio between coherent circular velocity and velocity dispersion is significantly higher than others. In Section 2.4, the kinematic properties of simulated galaxies will be investigated in detail.

Halo mass and galaxy stellar mass

We measure the bulk properties of the DM halos and galaxies in simulations following what has been done for the standard FIRE-2 simulations as described in Hopkins et al. [25]. We define the halo mass M_{halo} and the halo virial radius R_{vir} using the overdensity criterion introduced in Bryan and Norman [249]. We define the stellar mass M_* as the total mass of all the stellar particles within an aperture of $0.1 R_{\text{vir}}$ and correspondingly define the stellar half-mass radius $r_{1/2}$ as the radius that encloses half of the total stellar mass. For the isolated dwarf galaxies in simulations, these definitions of the stellar mass and the stellar half-mass radius give similar results to what was derived using the iterative approach described in Hopkins et al. [25].

In Figure 2.4, we compare the stellar mass versus halo mass of simulated dwarf galaxies with the scaling relations derived based on observations [1, 3, 59]. The black dashed lines show 95% inclusion contour assuming the scatter estimated in

Garrison-Kimmel et al. [3]. The simulated dwarfs are consistent with observations in the stellar mass versus halo mass relation and the galaxies we sampled in the simulation suite well represent the "median" galaxies in the real Universe. With mild DM self-interaction ($(\sigma/m) \lesssim 1 \text{ cm}^2 \text{ g}^{-1}$), the halo and stellar masses of galaxies are not significantly affected compared to their CDM counterparts, in agreement with previous studies of eSIDM [e.g., 111, 113, 115]. However, in the dSIDM model with $(\sigma/m) = 10 \text{ cm}^2 \text{ g}^{-1}$, both the halo masses and the stellar masses decrease for about 0.1 - 0.2 dex (compared to CDM) in dwarf galaxies with $M_{\text{halo}} \lesssim 10^{11} M_{\odot}$. Although this level of difference is still minor compared to the scatter of the relation, it is worth noting that the model with $(\sigma/m) = 10 \text{ cm}^2 \text{ g}^{-1}$ behaves qualitatively differently from other models explored. This aspect will be discussed in Section 2.4 and Section 2.4 in the following.

Total mass density profiles

In this section, we present the total mass density profiles (including the contribution from DM, stars, and gas) of simulated dwarf galaxies in dSIDM models with different parameters and compare them with the CDM predictions. We note that, for the dwarf galaxies in simulations, the mass density profiles are dominated by DM. We divide the simulated dwarf galaxies into two categories: (1) classical dwarfs, e.g. the m10's, with typical halo mass of $\lesssim 10^{10} M_{\odot}$ and sub-kpc stellar half-mass radius; (2) bright dwarfs, e.g. the m11's, with typical halo mass of $\gtrsim 10^{10} M_{\odot}$ and stellar half-mass radius of several kpc. We will investigate the extent to which the dissipative DM self-interactions affect the structure of these dwarfs.

In the left panel of Figure 2.5, we show the total mass density profiles of the classical dwarf galaxies in simulations with CDM, eSIDM, and dSIDM models at $z = 0$ ². The effective cross-section $(\sigma/m)_{\text{eff}}$ of the velocity-dependent dSIDM model in these classical dwarfs is $\sim 0.3 \text{ cm}^2 \text{ g}^{-1}$ calculated using Equation 2.11, plugging in the density and one-dimensional velocity dispersion of DM particles enclosed in a sphere of radius $1/3 r_{1/2}^{\text{cdm}}$, where $r_{1/2}^{\text{cdm}}$ is the stellar half-mass radius in the CDM model. We fit the density profiles at large radii of the halos ($0.5 r_{1/2}^{\text{cdm}} < r < 20 r_{1/2}^{\text{cdm}}$) with the NFW profile. In the lower sub-panel, we show the ratios between the density profiles in different models and the NFW fits. In the right panel of Figure 2.5, we show the local power-law slopes of the density profiles. In the lower sub-panel, we

²The bursty star formation history in dwarf galaxies could create fluctuations in density profiles, which leads to uncertainties in the profile measured at the $z = 0$ snapshot. But we have explicitly checked that the difference between the density profiles at $z = 0$ and the other four latest snapshots are minimal.

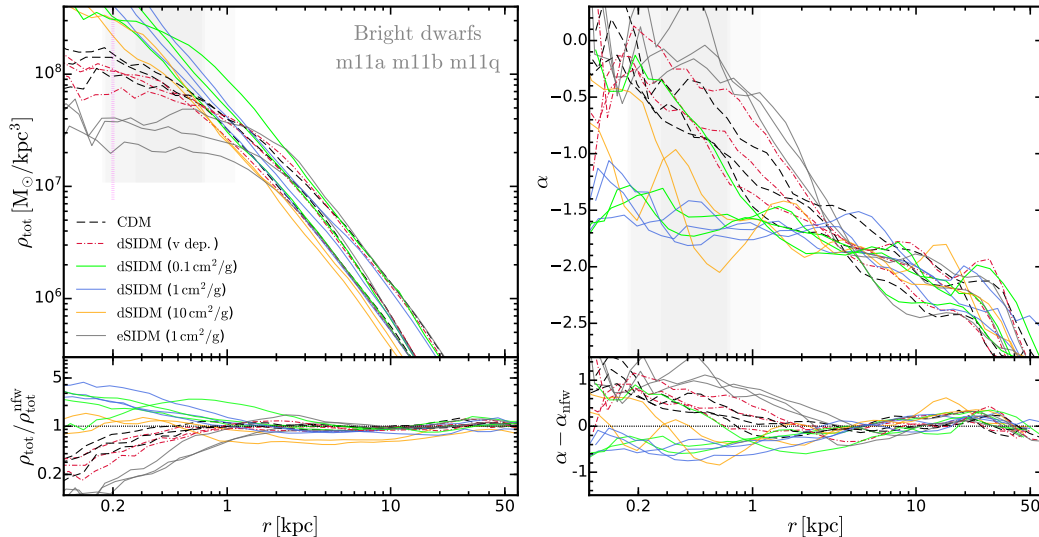


Figure 2.6: **Left: Total mass density profiles of the bright dwarf galaxies in simulations.** The three bright dwarfs presented here are m11a, m11b, and m11q. The notation is the same as Figure 2.5. The purple dotted vertical line here indicates the average convergence radius (~ 200 pc) of the bright dwarfs (see Table 2.1). **Right: Local power-law slopes of the density profiles of the bright dwarf galaxies.** In these bright dwarfs, the CDM model again predicts cored central density profiles with even larger cores (\sim kpc) than the classical dwarfs due to stronger baryonic feedback. The eSIDM model produces cores of similar sizes and slopes. The velocity-dependent dSIDM model has relatively low effective cross-sections ($\sim 0.01 \text{ cm}^2 \text{ g}^{-1}$) in these dwarfs. This model still produces cores but with slightly higher central densities than their CDM counterparts. The dSIDM models with relatively high effective cross-sections ($\gg 0.01 \text{ cm}^2 \text{ g}^{-1}$) still produce cuspy and power-law-like central density profiles. The power-law slopes center around -1.5 with a scatter from -2 to -1 .

show the differences in the slopes versus the NFW fits. In the classical dwarfs, the central density profiles are cored in the CDM case due to baryonic feedback. The eSIDM model produces profiles with much larger cores and shallower slopes than CDM. However, the dSIDM models all predict cuspy and power-law-like central density profiles at the sub-kpc scale, except for the one with low self-interaction cross-section $0.1 \text{ cm}^2 \text{ g}^{-1}$. These profiles are even steeper than the NFW profiles, with power-law slopes ~ -1.5 compared to the -1 asymptotic power-law slope of the NFW profile at the sub-kpc scale. The dSIDM model with a low cross-section of $0.1 \text{ cm}^2 \text{ g}^{-1}$ still produces cored central profiles in two galaxies, but the central densities are higher, and the core sizes are smaller than their CDM counterparts. The profiles in the velocity-dependent dSIDM model lie between the profiles in

the dSIDM models with $(\sigma/m) = 0.1$ and $1 \text{ cm}^2 \text{ g}^{-1}$, which is consistent with the estimate of $(\sigma/m)_{\text{eff}}$ in these systems. Surprisingly, increasing the self-interaction cross-section to $10 \text{ cm}^2 \text{ g}^{-1}$ does not lead to further contraction of the halos. Instead, the density profiles in the model have lower normalization out to $\sim 10 \text{ kpc}$, although the profiles still have cuspy shapes at galaxy centers. The classical dwarf galaxy that exhibits the strongest decrease in density profile normalization in this model is m10q. This decreased normalization of density profiles measured in spherical shells is likely related to the deformation of halos (e.g. with the same energy budget, a disk-like structure will have a lower spherically averaged density than a spherical structure). Assuming that the radial contraction is adiabatic which preserves specific angular momentum, the radial contraction of dSIDM halos will eventually be halted by the growing centrifugal force from coherent DM rotation. This will also make dSIDM halos deform from spherical to oblate in shape and the density profiles will appear with lower normalization. In subsequent sections, we will see more evidence for this phenomenon from the analysis of kinematic properties (Section 2.4) and shapes (Section 2.5) of DM halos.

In the left panel of Figure 2.6, we show the total mass density profiles of the bright dwarf galaxies in simulations with CDM, eSIDM, and dSIDM models. The $(\sigma/m)_{\text{eff}}$ of the velocity-dependent dSIDM model in these bright dwarfs is $\sim 0.01 \text{ cm}^2 \text{ g}^{-1}$. In the right panel of Figure 2.6, we show the local power-law slopes of the density profiles of the bright dwarfs. The phenomena in the bright dwarfs are qualitatively consistent with those in the classical dwarfs shown above. In the bright dwarfs, the central density profiles are cored in the CDM case. The decrease of the central density compared to the NFW profile is stronger than that in the classical dwarfs, due to stronger baryonic feedback in the bright dwarfs. The eSIDM model again produces larger cores and shallower slopes in these galaxies compared to the CDM case. In dSIDM models, the shapes of the density profiles vary with the self-interaction cross-section (or equivalently the efficiency of dissipation, assuming fixed f_{diss}). The velocity-dependent dSIDM model has a relatively low effective cross-section in the bright dwarfs and thus the central density profiles are still cored, similar to the CDM case. However, in the dSIDM model with $(\sigma/m) = 0.1 \text{ cm}^2 \text{ g}^{-1}$, cuspy and power-law-like central profiles show up in two out of the three bright dwarfs and the only cored one shows enhanced central densities at $r \lesssim \text{kpc}$. In the dSIDM model with $(\sigma/m) = 1 \text{ cm}^2 \text{ g}^{-1}$, the central profiles of all three bright dwarfs are cuspy with power-law slopes centering around -1.5 at the sub-kpc scale. In the dSIDM model with $(\sigma/m) = 10 \text{ cm}^2 \text{ g}^{-1}$, the density profiles have lower

normalization although they are still cuspy, similar to the phenomenon we found in the classical dwarfs. Here, the bright dwarf galaxy that exhibits the strongest decrease in density profile normalization in this model is m11b.

Comparing the density profiles of the classical dwarfs and bright dwarfs, we find that the dSIDM model with the same constant cross-section can behave qualitatively differently in galaxies of different masses. For example, the model with $(\sigma/m) = 0.1 \text{ cm}^2 \text{ g}^{-1}$ produces cored central profiles in two of the classical dwarfs but produces cuspy central profiles in two of the bright dwarfs. As discussed in Section 2.3, the dissipation time scale of models with constant cross-section inversely depends on the density and velocity dispersion of the system. The bright dwarfs typically have much higher velocity dispersion at their centers than the classical dwarfs while the central densities are comparable to the classical dwarfs. As expected, dissipation has a stronger impact on the bright dwarfs. On the other hand, the velocity-dependent dSIDM model produces cuspy central profiles in the classical dwarfs but produces cored central profiles in the bright dwarfs. The dissipation time scale of the velocity-dependent model inversely depends on density but exhibits a v^3 asymptotic dependence on velocity dispersion. The opposite dependence on velocity dispersion makes the impact of dissipation stronger in the classical dwarfs.

To quantify the impact of dissipation on galaxy structures, we measure the slopes of the total mass density profiles at galaxy centers. The aperture we choose for this measurement is $0.2 - 0.8\% R_{\text{vir}}^{\text{cdm}}$ (as indicated by the gray bands in Figure 2.5 and 2.6), where $R_{\text{vir}}^{\text{cdm}}$ is the virial radius of the halo in the CDM model.³ This has been chosen since it is an appropriate aperture to illustrate the impact of dissipation at small radii while remaining larger than the convergence radii of DM profiles in these runs (rather conservative estimates, see Table 2.1). In Figure 2.7, we show the power-law slopes of the density profiles (measured at $0.2 - 0.8\% R_{\text{vir}}^{\text{cdm}}$) of simulated dwarf galaxies versus their stellar-to-halo mass ratios (M_*/M_{halo}). The slopes of the density profiles in different models show four different “tracks”:

- The NFW profile has an asymptotic -1.4 power-law slope at galaxy centers.
- In CDM, baryonic feedback drives gas outflow and creates fluctuations in the central gravitational potential which significantly affects the distribution of

³The virial radius does not vary much in simulations with different DM models. Using the virial radius in the CDM run is simply to ensure that the aperture is identical for different DM models.

⁴The slope of the NFW profile varies with radius. At the radii we measure the slopes, the NFW profile has a slope of ~ -1.1 .

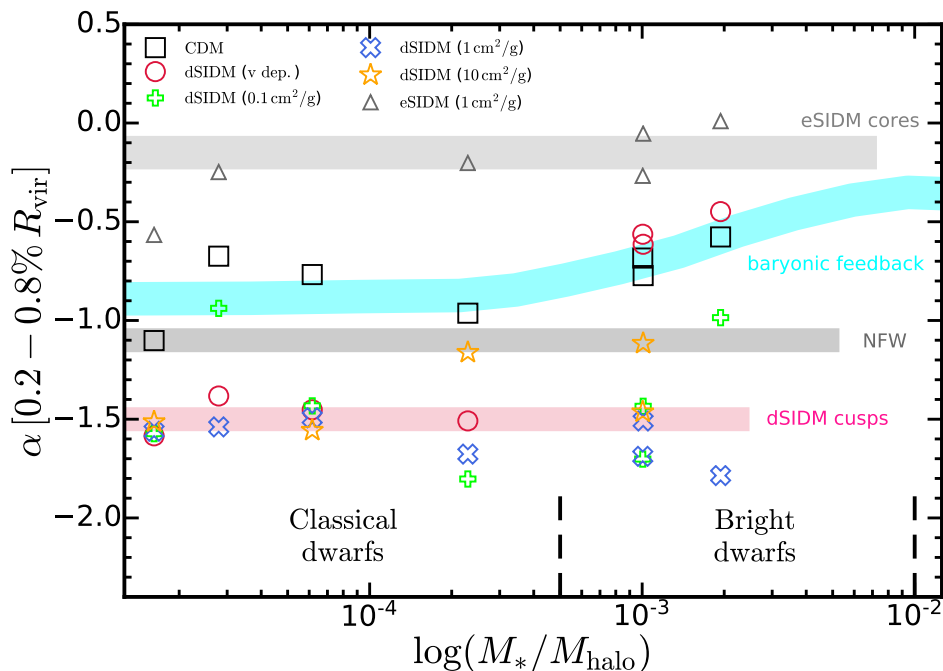


Figure 2.7: **Slopes of the central density profiles of dwarf galaxies in the simulation suite.** The slopes are measured at $0.2 - 0.8\% R_{\text{vir}}^{\text{cdm}}$. The slopes measured in simulations with different DM models are shown in open markers (as labeled). Galaxies are ordered from left to right based on their stellar-to-halo mass ratios (M_*/M_{halo}) and are classified as classical dwarfs and bright dwarfs. (The ultra-faint dwarf m09 in the suite also has its M_*/M_{halo} value lying in the classical dwarf regime.) The asymptotic behaviors of the slopes at the low mass end are clearly different between different DM models. In low-mass dwarf galaxies, the density profiles in dSIDM models with $(\sigma/m) \geq 1 \text{ cm}^2 \text{ g}^{-1}$ and the velocity-dependent model converge to a slope of ~ -1.5 (indicated by the thick red horizontal line). The slope is steeper than the asymptotic slope -1 of the NFW profile (~ -1.1 at the radii we measure the slope, indicated by the thick black horizontal line). In contrast, the dSIDM model with $(\sigma/m) = 0.1 \text{ cm}^2 \text{ g}^{-1}$ can still produce small cores in some dwarf galaxies with relatively strong baryonic feedback, with $\alpha \sim -1$ at the radius of measurement and becoming even shallower at smaller radii as shown in the right panels of Figure 2.5 and 2.6. In the bright dwarfs, the velocity-dependent dSIDM model produces cored profiles with $\alpha \sim -0.5$. The dSIDM models with constant cross-sections still produce cuspy density profiles with slopes centering around -1.5 but scattering from -2 to -1 . Unlike dSIDM models, density profiles in CDM are shallower than the NFW profile and are shallower in more massive dwarf galaxies, due to stronger baryonic feedback there (indicated by the thick cyan line). The eSIDM model consistently produces cored density profiles with slope ~ -0.2 in most of the dwarf galaxies (indicated by the thick gray horizontal line). We note that all the thick reference lines are meant to label different “tracks” and are rigorous fits to the simulation results.

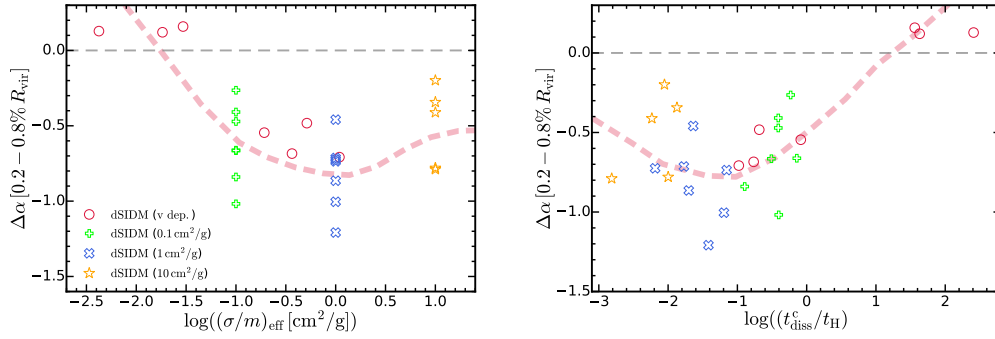


Figure 2.8: *Top: Slope change versus effective self-interaction cross-section of dwarf galaxies in simulations.* $\Delta\alpha$ is defined as the difference in slopes measured at $0.2-0.8\%R_{\text{vir}}^{\text{cdm}}$ between galaxies in dSIDM and CDM. The red dashed line labels the qualitative trend (not rigorous fitting). In the regime where $(\sigma/m)_{\text{eff}} < 1 \text{ cm}^2 \text{ g}^{-1}$, the steepening of central profiles induced by dissipative DM self-interactions becomes progressively stronger in systems with higher effective cross-sections. In the regime where $(\sigma/m)_{\text{eff}} > 1 \text{ cm}^2 \text{ g}^{-1}$, the steepening of central profiles saturates. *Bottom: Slope change versus dissipation time scale at halo center.* When $\log(t_{\text{diss}}^c/t_h) > -1$, the density profiles become steeper as t_{diss}^c decreases while the steepening saturates when $\log(t_{\text{diss}}^c/t_h) < -1$.

DM. Dwarf galaxies have shallower density profiles than the NFW profile. The difference in slope peaks in most massive bright dwarfs where baryonic feedback is most efficient in perturbing galaxy structures, as has been found in previous studies [e.g., 42, 245–248].

- In eSIDM, elastic DM self-interaction drives the halo to thermal equilibrium and produces an isothermal density profile with a core at the center. The power-law slopes of the central profiles are close to zero in most of the simulated dwarf galaxies, regardless of their mass.
- In dSIDM, dissipative DM self-interaction is a competing factor against baryonic feedback in shaping the central density profile. When $(\sigma/m)_{\text{eff}} > 0.1 \text{ cm}^2 \text{ g}^{-1}$, DM dissipation becomes dominant and the central density profiles in dwarf galaxies are steeper than the ones in the CDM model.⁵ In the classical dwarfs, the power-law slopes are steeper than the -1 of NFW profiles and asymptote to ~ -1.5 . In the bright dwarfs, the power-law slopes have a larger scatter, ranging from -2 to -1 . When the $(\sigma/m)_{\text{eff}}$ is relatively low (e.g. the model with $(\sigma/m) = 0.1 \text{ cm}^2 \text{ g}^{-1}$ in the classical dwarfs and the

⁵We verify that the impact of baryonic feedback becomes negligible in this regime through the comparison with DMO simulations in Section 2.7.

velocity-dependent model in the bright dwarfs), the central density profiles are affected by a mixture of DM dissipation and baryonic feedback, which compete with each other. In some dwarfs with relatively strong feedback effects, the slopes become shallower than the ~ -1.5 value at the radius of measurement. They could even develop a core ($\alpha \gtrsim -0.5$) at smaller radii as shown in the right panels of Figure 2.5 and 2.6.

To demonstrate the net impact of dissipation, in the top panel of Figure 2.8, we show the slope change $\Delta\alpha$ versus the effective self-interaction cross-section $(\sigma/m)_{\text{eff}}$. $\Delta\alpha$ is defined as the difference in slopes measured at $0.2 - 0.8\% R_{\text{vir}}^{\text{cdm}}$ between galaxies in dSIDM and CDM, $\Delta\alpha = \alpha^{\text{dsidm}} - \alpha^{\text{cdm}}$. More negative $\Delta\alpha$ indicates a stronger impact of dissipation on the steepness of the density profile. The effective self-interaction cross-section is calculated using Equation 2.11, plugging in the density and one-dimensional velocity dispersion of DM particles enclosed in a sphere of radius $1/3 r_{1/2}^{\text{cdm}}$. The red dashed line shows the qualitative trend (not rigorous fitting) of $\Delta\alpha$ versus $(\sigma/m)_{\text{eff}}$. When $(\sigma/m)_{\text{eff}} \lesssim 1 \text{ cm}^2 \text{ g}^{-1}$, the steepening of the central density profiles induced by dissipation becomes progressively stronger in systems with higher effective cross-sections. The change of the power-law slope scales roughly linearly as the logarithm of the effective cross-section. When $(\sigma/m)_{\text{eff}}$ is larger than $1 \text{ cm}^2 \text{ g}^{-1}$, the steepening of the central density profiles saturates. The $\Delta\alpha$ when $(\sigma/m)_{\text{eff}} \simeq 10 \text{ cm}^2 \text{ g}^{-1}$ is comparable to the $(\sigma/m)_{\text{eff}} \simeq 0.1 \text{ cm}^2 \text{ g}^{-1}$ case. In the bottom panel of Figure 2.8, we show the slope change $\Delta\alpha$ versus the dissipation time scale at halo center $t_{\text{diss}}^{\text{c}}$, calculated using Equation 2.8. The steepening of the central density profiles occurs when $t_{\text{diss}}^{\text{c}}$ becomes comparable to t_{h} . The slope difference becomes larger as $t_{\text{diss}}^{\text{c}}$ decreases when $t_{\text{diss}}^{\text{c}} \gtrsim 0.1 t_{\text{h}}$. When $t_{\text{diss}}^{\text{c}} \lesssim 0.1 t_{\text{h}}$, the steepening of the central profile saturates, similar to the trend in the top panel. This is likely related to the increasing rotation support of DM when $(\sigma/m)_{\text{eff}} \gtrsim 1 \text{ cm}^2 \text{ g}^{-1}$, which will be shown in the following section.

Kinematic properties

In this section, we will explore the kinematic properties of DM particles in the simulated dwarf galaxies. These properties include velocity dispersion, coherent rotation velocity, velocity anisotropy and the velocity distribution function of DM.

To evaluate these properties, we first divide a simulated halo into spherical shells with respect to the halo center. In each shell, we measure the total angular momentum of DM particles and align the z-axis of the coordinate system with the direction of

the angular momentum. This helps us define the azimuthal and zenith directions (note that different shells could have different directions of angular momentum and thus different definitions of the z-axis). The velocities of DM particles are decomposed to the radial, zenith, and azimuthal components (v_r , v_θ , and v_ϕ) in spherical galactocentric coordinates. The coherent rotation velocity V_{rot} of particles in the shell is calculated as

$$V_{\text{rot}} = \frac{J_{\text{dm}}}{I_{\text{shell}}} R_{\text{shell}},$$

$$I_{\text{shell}} = \frac{2}{5} M_{\text{dm}} \frac{r_o^5 - r_i^5}{r_o^3 - r_i^3}, \quad R_{\text{shell}} = \frac{r_o + r_i}{2}, \quad (2.12)$$

where J_{dm} is the total angular momentum of DM particles in the shell, M_{dm} is the total mass of DM in the shell, I_{shell} is the moment of inertia of the shell, r_o and r_i are the outer and inner radii of the shell, and R_{shell} is the median radius of the shell. Here, we have assumed that the mass is uniformly distributed in the shell in the calculation of moment of inertia. We also measure the mean inflow/outflow velocity ($\overline{v_r}$) of DM particles in the shell. We subtract both the coherent rotation velocity and the mean inflow/outflow velocity before measuring the velocity dispersion σ_r , σ_θ and σ_ϕ corresponding to the radial direction, and the azimuthal and zenith angles, respectively. Finally, the three-dimensional velocity dispersion is calculated as $\sigma_{3d} = \sqrt{\sigma_r^2 + \sigma_\theta^2 + \sigma_\phi^2}$. The one-dimensional velocity dispersion is estimated as $\sigma_{1d} = \sqrt{(\sigma_r^2 + \sigma_\theta^2 + \sigma_\phi^2)/3}$. The degree of velocity anisotropy is calculated as

$$\beta = 1 - \frac{\sigma_\phi^2 + \sigma_\theta^2}{2\sigma_r^2}. \quad (2.13)$$

Under this definition, $\beta = 0$ corresponds to an isotropic velocity dispersion, $\beta = 1$ to a velocity dispersion purely dominated by the radial component, and negative β to a velocity dispersion dominated by the tangential component.

Coherent rotation: A natural consequence of dissipative interactions is that particles tend to move in a more coherent fashion, rather than in random dispersion. If the energy dissipation is faster than the relaxation processes (either through DM self-interactions or gravitational interactions), the coherent rotation would gradually become prominent in the system if angular momentum is conserved. In Figure 2.9, we show the ratio between coherent rotation velocity and three-dimensional velocity dispersion of DM measured in spherical shells in CDM and dSIDM with $(\sigma/m) = 1$ and $10 \text{ cm}^2 \text{ g}^{-1}$. For each model, each line corresponds to one of the simulated dwarf

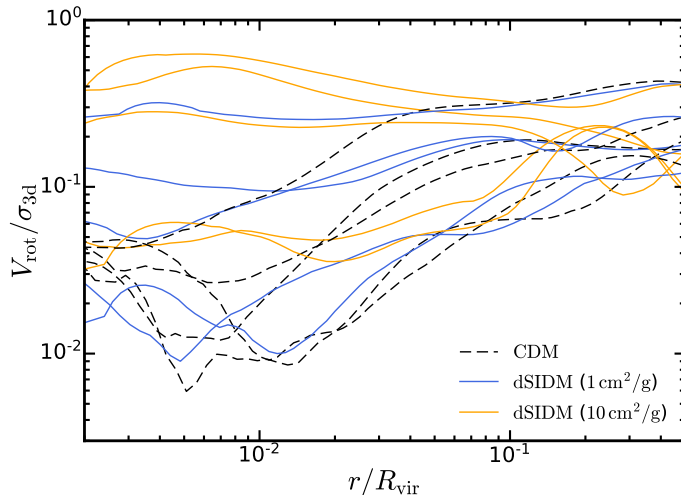


Figure 2.9: **Coherent rotation velocity relative to velocity dispersion of DM in simulations.** The coherent rotation velocities and the velocity dispersions are measured in spherical shells as discussed in the main text. We present the results in CDM and dSIDM with $(\sigma/m) = 1$ and $10 \text{ cm}^2 \text{ g}^{-1}$. For each model, we show the results of five dwarf galaxies: m10q, m10b, m10v, m11a, and m11b. The coherent rotation becomes more prominent inside $\sim 1\% R_{\text{vir}}$ as the self-interaction cross-section increases, but not in every galaxy. The two galaxies that have rotation velocities comparable to velocity dispersions are m10q and m11b.

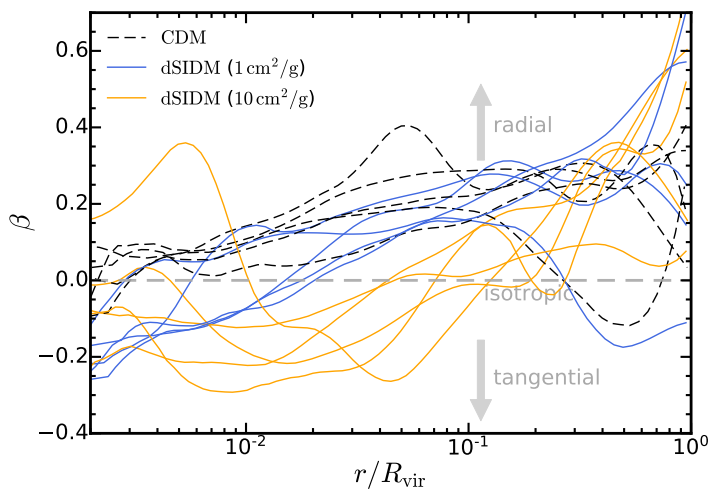


Figure 2.10: **Velocity anisotropy profiles of DM in simulated dwarf galaxies.** The velocity anisotropies are calculated using Equation 2.13. We present the results in CDM and dSIDM with $(\sigma/m) = 1$ and $10 \text{ cm}^2 \text{ g}^{-1}$. For each model, we show the results of the same five galaxies as in Figure 2.9. The velocity anisotropy decreases as the self-interaction cross-section increases and eventually becomes negative, suggesting that the velocity dispersion is more dominated by the tangential component. This is consistent with more coherent rotation found in Figure 2.9.

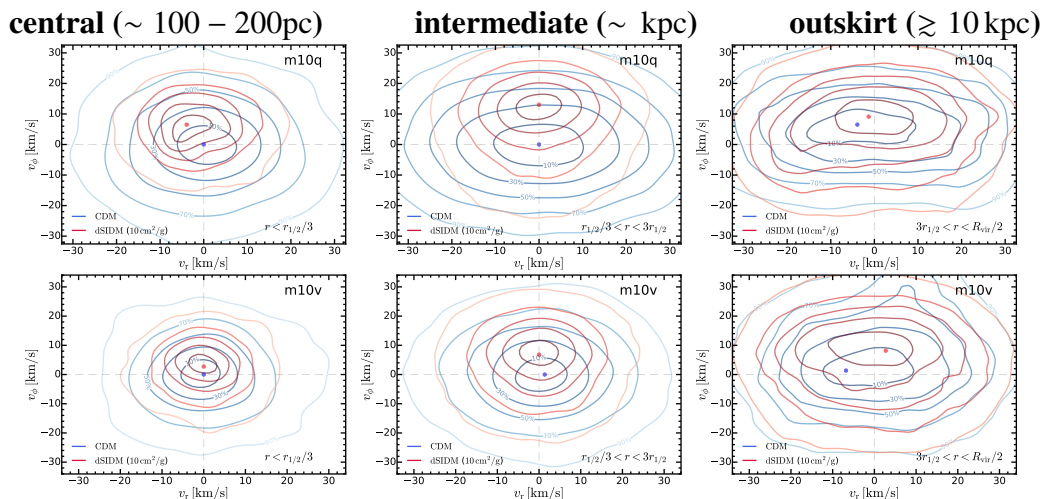


Figure 2.11: **Phase space distribution function of DM in simulated classical dwarfs.** We present the two-dimensional density distribution of DM in the $v_\phi - v_r$ phase space, $d\rho_{\text{dm}}/dv_r dv_\phi$. In the three columns, we show the distribution in three radial bins: central, $r < r_{1/2}^{\text{cdm}}/3$, intermediate, $r_{1/2}^{\text{cdm}}/3 < r < 3r_{1/2}^{\text{cdm}}$, and “outskirt”, $3r_{1/2}^{\text{cdm}} < r < 0.5R_{\text{vir}}^{\text{cdm}}$, respectively. From inside out, each contour is determined such that it encloses a certain percentile of DM particles in the bin. The percentiles range from 10% to 90% with 20% as interval, as labeled on the contours. The dots represent the locations where the velocity distribution function peaks. DM in dSIDM models exhibit positive median v_ϕ while the phase space distribution is almost isotropic in CDM. The differences consistently show up in the three radial bins and suggest a coherent rotation built up in dSIDM halos. The phase space distribution in the dSIDM model is also more peaky than the CDM case, at least for the central and intermediate radial bins.

galaxies: m10q, m10b, m10v, m11a and m11b. Qualitatively, the coherent rotation velocity at small galactocentric radii becomes progressively more prominent as the self-interaction cross-section becomes higher (and dissipation becomes more efficient). At large radii, the systematic difference becomes negligible. Quantitatively, there are apparent galaxy-to-galaxy variations. The ratio can reach ~ 0.5 inside $\sim 1\% R_{\text{vir}}$ (roughly sub-kpc scale in dwarfs) in m10q and m11b in dSIDM with $(\sigma/m) = 10 \text{ cm}^2 \text{ g}^{-1}$, while in m11a and m10b, the ratio remains $\lesssim 0.1$ inside $\sim 1\% R_{\text{vir}}$ in any models. These evidences suggest that, at the centers of galaxies, some dSIDM realizations are in a transition from a pure dispersion-supported system to a system supported by a mixture of random velocity dispersion and coherent rotation. The radial scale for this transition to take place is a few percent of the virial radius. Such scale is quite consistent with the centrifugal barrier $\sim sR_{\text{vir}}$ (s is the halo spin parameter with typical value $\sim 0.01 - 0.1$) found for dissipative gas in

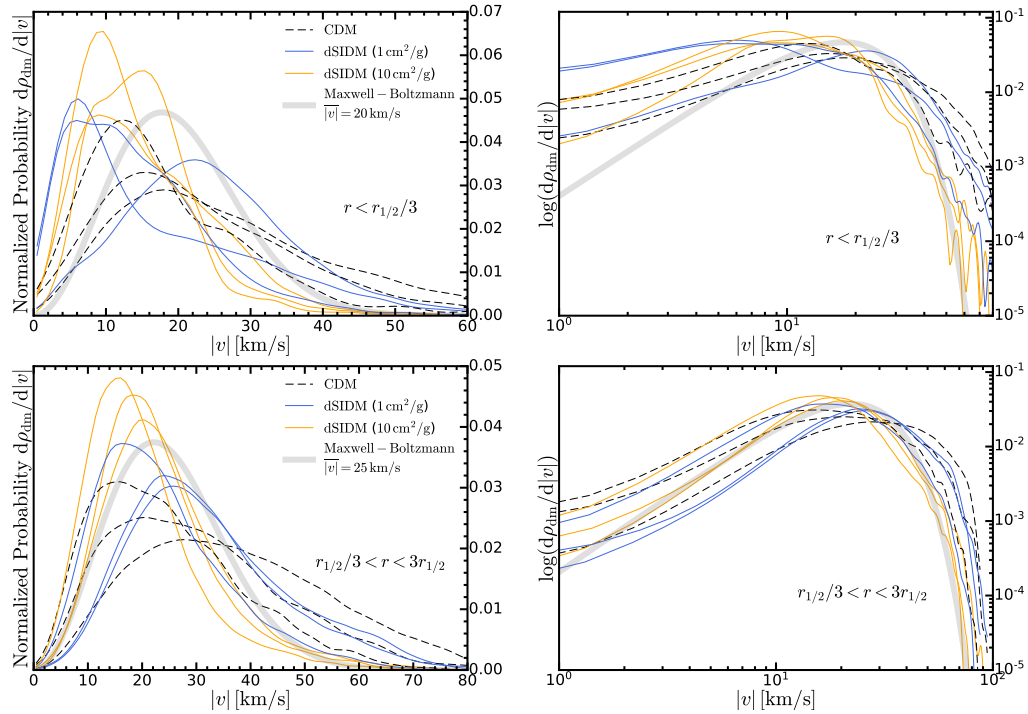


Figure 2.12: **Velocity distribution functions of DM in the classical dwarfs.** *Top left:* Velocity distribution function at small galactocentric radii ($r < r_{1/2}^{\text{cdm}}/3$). We show the velocity distributions in CDM and dSIDM with $(\sigma/m) = 1$ and $10 \text{ cm}^2 \text{ g}^{-1}$ (as labeled). As a reference, a Maxwell-Boltzmann distribution is shown with the thick gray line. Compared to CDM, the velocity distribution functions in dSIDM models are more suppressed at the high-velocity tail as the cross-section increases and the peaks of the distributions also decrease systematically. *Top right:* Same velocity distribution functions as the top left panel but in log-log scale to highlight the asymptotic behavior at the low-velocity tail. Both CDM and dSIDM models have velocity distribution functions that decrease slower than the Maxwell-Boltzmann distribution at the low-velocity tail. Dissipation has limited impact at low velocities due to small interaction rates there. *Bottom left:* Velocity distribution function at intermediate galactocentric radii ($r_{1/2}^{\text{cdm}}/3 < r < 3r_{1/2}^{\text{cdm}}$). Similar differences in the velocity distribution of CDM and dSIDM are found compared to the one at small radii. *Bottom right:* The same velocity distribution function as the bottom left panel but in log-log scale. Both CDM and dSIDM models have velocity distributions that overall resemble the Maxwell-Boltzmann distribution at the low-velocity tail.

CDM halos [e.g., 250].

Velocity anisotropy: In Figure 2.10, we show the velocity anisotropy of DM measured in spherical shells in CDM and dSIDM with $(\sigma/m) = 1$ and $10 \text{ cm}^2 \text{ g}^{-1}$. The velocity anisotropies are calculated using Equation 2.13. The measured anisotropy is not sensitive to the bulk motion of DM in the shell since we have subtracted the mean rotation/inflow/outflow velocities. For each model, we show the results of the same five galaxies as in Figure 2.9. CDM halos are almost isotropic at the centers with mild radial velocity dispersion anisotropy at the outskirts, which is consistent with previous studies [e.g, 251–253]. In dSIDM models, it is similar to the CDM case in that the velocity anisotropy increases towards larger galactocentric radii. However, as dissipation becomes more efficient, the normalization of the velocity anisotropy decreases and eventually becomes negative at small radii. In the dSIDM model with $(\sigma/m) = 10 \text{ cm}^2 \text{ g}^{-1}$, the velocity anisotropy drops to ~ -0.2 at $r \sim 1\% R_{\text{vir}}$, suggesting that the tangential component of the velocity dispersion is relatively stronger there. This phenomenon is inline with the more prominent coherent rotation developed in dSIDM halos.

Phase space distribution: In Figure 2.11, we present the density distribution function of DM in the $v_\phi - v_r$ phase space, $d\rho_{\text{dm}}/dv_r dv_\phi$, of m10q and m10v. We compare the results in CDM and dSIDM with $(\sigma/m) = 10 \text{ cm}^2 \text{ g}^{-1}$ to better illustrate the contrast. The phase space distributions are measured in three radial bins: central, $r < r_{1/2}^{\text{cdm}}/3$ (~ 100 - 200 pc); intermediate, $r_{1/2}^{\text{cdm}}/3 < r < 3r_{1/2}^{\text{cdm}}$ (\sim kpc) and “outskirt”, $3r_{1/2}^{\text{cdm}} < r < 0.5R_{\text{vir}}^{\text{cdm}}$ ($\gtrsim 10$ kpc). The azimuthal and zenith directions are defined based on the direction of the total angular momentum of DM in each radial bin respectively. From inside out, each contour is determined such that it encloses a certain percentile (as labeled on the contour line) of DM particles in the bin. We note that, different from the measurement of velocity dispersions, the coherent rotation or inflow/outflow velocity has not been subtracted when determining v_r and v_ϕ . DM at small and intermediate radii in the dSIDM model with $(\sigma/m) = 10 \text{ cm}^2 \text{ g}^{-1}$ exhibits a median $v_\phi \simeq 5 - 10 \text{ km s}^{-1}$ contrary to the almost zero median v_ϕ in the CDM case. The distribution in the dSIDM model is also more peaky than in the CDM case. The differences here are consistent with the coherent rotation of DM in dSIDM found above. At the outskirts of the galaxy, the increase in the median of v_ϕ is still visible but the scatter in the phase space also becomes larger.

In Figure 2.12, we show the velocity ($|v|$) distribution functions of DM in the classical

dwarfs in CDM and dSIDM with $(\sigma/m) = 1$ and $10 \text{ cm}^2 \text{ g}^{-1}$. We present the results at small ($r < r_{1/2}^{\text{cdm}}/3$) and intermediate galactocentric radii ($r_{1/2}^{\text{cdm}}/3 < r < 3r_{1/2}^{\text{cdm}}$), respectively. We also show the distribution function in log-log scale to emphasize the low-velocity tail. Compared to the CDM case, the velocity distributions in dSIDM models show apparent suppression at the high-velocity tail and bumps at lower velocities, due to relatively high interaction rates of particles with high absolute velocities. The low-velocity tail is less affected by dissipation due to relatively low interaction rates there. The peak velocity decreases as the self-interaction cross-section becomes larger. The phenomenon is actually opposite to the prediction of the “gravothermal collapse” in SIDM halos [e.g., 121, 125]. The difference reflects the deviation of dSIDM halos from both dynamical and thermal equilibrium in the phase of radial contraction, as well as the fact that one cannot assume velocity distributions as purely isotropic in relaxed dSIDM halos. Compared with the Maxwell-Boltzmann distribution, the velocity distributions in CDM have extended tails at both the low and high-velocity tails, since CDM particles are collisionless and are not locally thermalized. The distributions in the dSIDM models are suppressed in the high-velocity tail. At small galactocentric radii, the asymptotic behavior of the velocity distribution function in CDM and dSIDM is quite different from the Maxwell-Boltzmann distribution, decreasing slower towards lower velocities. However, at intermediate radii, both CDM and dSIDM have distributions that resemble the Maxwell-Boltzmann distribution at the low-velocity tail.

2.5 Halo shape

The change in halo shape is another important signature for alternative DM physics. This aspect has been explored in detail for the eSIDM case [e.g., 113, 166, 254–256]. In dSIDM halos, morphological changes in response to the energy dissipation are also expected, inline with the steepening of the density profile and the increased rotation support found in previous sections.

To measure the shape of DM halos, we determine the orientation and magnitude of the principal axes of DM distribution by computing the eigenvectors and eigenvalues of the shape tensor of DM mass distribution, defined as

$$\mathbf{S} = \frac{\int_V \rho(\mathbf{r}) \mathbf{r} \mathbf{r}^T dV}{\int_V \rho(\mathbf{r}) dV}, \quad (2.14)$$

where $\rho(\mathbf{r})$ is the DM mass density at position \mathbf{r} with respect to halo center. In

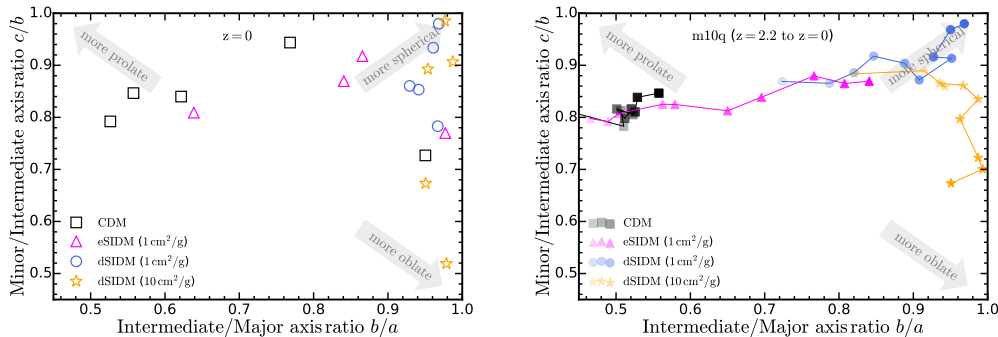


Figure 2.13: **Top: Axis ratios of DM halos at central kpc in simulations at $z = 0$.** We show the minor/intermediate axis ratio (c/b) versus the intermediate/major axis ratio (b/a) of DM mass distribution in different simulations. The axes are measured iteratively while fixing the volume of an ellipsoid as $4\pi/3 r_{\text{lim}}^3$, where r_{lim} is chosen to be 1 kpc. When c/b (b/a) is close to unity, the system is a prolate (oblate) spheroid. When both c/b and b/a are close to unity, the system is spherically symmetric. In CDM, DM halos are triaxial ellipsoids with a clear hierarchy of minor, intermediate and major axes. The CDM halos lean towards prolate shapes, driven by mild radial dispersion anisotropy. In the dSIDM model with $(\sigma/m) = 1$ and $10 \text{ cm}^2 \text{ g}^{-1}$, DM halos behave as oblate spheroids, driven by the coherent rotation of DM. In the extreme cases (e.g., m10q in dSIDM with $(\sigma/m) = 10 \text{ cm}^2 \text{ g}^{-1}$), c/b drops to as low as ~ 0.5 while b/a stays around unity. At larger radii ($r \gg \text{kpc}$), the qualitative trends are similar but the differences between DM models become rapidly smaller. **Bottom: Evolution of the axis ratios of m10q at central kpc from $z \simeq 2.2$ to $z = 0$.** The markers with darker colors represent measurements at lower redshifts. The CDM halo stays triaxial since $z \simeq 2.2$ while the eSIDM halo becomes more spherical at late times. The halo in dSIDM with $(\sigma/m) = 1 \text{ cm}^2 \text{ g}^{-1}$ is already more spherical than CDM and eSIDM counterparts at $z \simeq 2.2$ and it becomes extremely spherical at $z = 0$. However, the halo in dSIDM with $(\sigma/m) = 10 \text{ cm}^2 \text{ g}^{-1}$ initially follows the track of becoming more spherical but then turns oblate in shape.

terms of discrete DM particles, each element of the tensor is calculated as

$$S_{ij} = \frac{\sum_{\mathbf{k}} m_{\mathbf{k}} (r_{\mathbf{k}})_i (r_{\mathbf{k}})_j}{\sum_{\mathbf{k}} m_{\mathbf{k}}}, \quad (2.15)$$

where $m_{\mathbf{k}}$ is the mass of the \mathbf{k} -th DM particle and $(r_{\mathbf{k}})_i$ is the spatial coordinate of the \mathbf{k} -th particle. The three eigenvectors of the shape tensor give the three axes of the mass distribution. Specifically, the major, intermediate, and minor axes will be denoted as a , b , and c , respectively. The ratios between the eigenvalues of the shape tensor give the axis ratios of the mass distribution.

For the simulated DM halos, we perform this measurement in a fixed volume of $V = 4\pi r_{\text{lim}}^3/3$, where r_{lim} is chosen to be 1 kpc. The volume is an ellipsoid

with its major, intermediate, and minor axes (a , b , and c are set to r_{lim} initially) updated iteratively until convergence is reached. This gives an estimation of the shape of the DM halo at kpc scale. In the top panel of Figure 2.13, we show the minor/intermediate axis ratio (c/b) versus the intermediate/major axis ratio (b/a) of DM mass distribution at $z = 0$ in simulations. Most of the CDM halos are triaxial, with a clear hierarchy of minor, intermediate and major axes, and lean towards prolate shapes likely driven by mild radial velocity dispersion anisotropy [e.g., 257–259]. The eSIDM halos overall become more spherical than CDM halos. Despite some galaxy-to-galaxy variations, it is clear that halos in the dSIDM models behave as oblate or spherical spheroids, with the intermediate axes always comparable to the major axes. In the model with $(\sigma/m) = 1 \text{ cm}^2 \text{ g}^{-1}$, halos are quite spherical with $b/a \gtrsim 0.9$ and $c/b \gtrsim 0.8$. The radial contraction washes the initial triaxiality of the halos and the increased central force makes halos more spherical. However, in the model with $(\sigma/m) = 10 \text{ cm}^2 \text{ g}^{-1}$, two of the halos become oblate in shape, with c/b drops to around 0.5 and 0.7, while the other three are still quite spherical in the end.

In the bottom panel of Figure 2.13, we show the evolution of the axis ratios of m10q from $z \simeq 2.2$ to $z = 0$ as an example. The halo shape is again measured at the central kpc scale, an invariant of redshift. We choose m10q as an example since it has dramatic changes in its shape in dSIDM models. The markers with darker colors represent measurements at lower redshifts. The CDM halo stays triaxial since $z \simeq 2.2$ with little change in its shape subsequently. The eSIDM halo is initially triaxial but becomes progressively more spherical at late times due to the elastic scattering of DM. The halo in dSIDM with $(\sigma/m) = 1 \text{ cm}^2 \text{ g}^{-1}$ is already more spherical than CDM and eSIDM counterparts at $z \simeq 2.2$ and it becomes extremely spherical ($c/b, b/a > 0.95$) at $z = 0$. However, the halo in dSIDM with $(\sigma/m) = 10 \text{ cm}^2 \text{ g}^{-1}$ initially follows the track of becoming more spherical but then turns oblate in shape. We note that, though not shown explicitly here, the other halo (m11b) which ends up oblate ($c/b \sim 0.5$ at $z = 0$) in the model with $(\sigma/m) = 10 \text{ cm}^2 \text{ g}^{-1}$ has a similar evolutionary track in the axis ratio plane. However, the three halos (m10b, m10v, m11a) that end up spherical ($c/b, b/a \gtrsim 0.9$ at $z = 0$) are still in the phase of turning spherical.

The morphological differences found here are consistent with our findings in the previous sections that coherent rotation develops in dSIDM halos with $(\sigma/m) = 10 \text{ cm}^2 \text{ g}^{-1}$ and could also result in the lower normalization of the density profiles

(measured in spherical shells) found in Section 2.4. In the model with $(\sigma/m) = 10 \text{ cm}^2 \text{ g}^{-1}$, the two halos that become oblate in shape at $z = 0$ (m10q and m11b) are the halos with the most significant coherent rotation (as presented in Section 2.4) and also with the most significant decrease in density profile normalization (as presented in Section 2.4). When the coherent rotation velocity becomes comparable to the velocity dispersion, a self-gravitating spheroidal system consisting of collisionless particles flattens. This is a well-known behavior in the stellar distribution of elliptical galaxies [e.g., 260, 261] and models of isotropic oblate rotating spheroids [262–264]. Similar to these previous studies, the response of the ellipticity of the spheroid to $V_{\text{rot}}/\sigma_{3d}$ is weak. In the simulated dwarfs m10q and m11b, significant coherent rotation of $V_{\text{rot}}/\sigma_{3d} \sim 0.5$ results in only modest ellipticity of the halo (c/b , $c/a \sim 0.5 - 0.7$ at $r \lesssim \text{kpc}$). However, the coherent rotation and halo deformation are weaker in other simulated dwarfs and this is likely related to the differences in the mass assembly history of the dwarfs.

We note that, for the oblate spheroids we found here, the minor and major axes are still comparable to each other. The shape is qualitatively different from the thin "dark disk" discussed in the literature (albeit for Milky Way-sized galaxies) regarding dissipative DM [100, 128–133]. The dissipation time scale in the model studied here is still orders of magnitude longer than the dynamical time scale of the system, which prevents fragmentation of the DM into e.g., "dark stars" and other compact structures [e.g., 265–267]. This is qualitatively different from baryon-like dissipative DM models. In addition, unlike those models that assume dissipative DM is a sub-component of all the DM, the model studied here assumes that all the DM are dissipative. In our case, there would be no external gravitational force that can suppress the growth of secular gravitational instabilities [e.g., 268, 269], which prevents the formation of a cold and thin "dark disk" completely supported by rotation.

2.6 Discussion

In previous sections, we have presented several signatures of dSIDM models in dwarf galaxies that differ from their CDM counterparts. In this section, we discuss these phenomena in more detail and provide some physical explanations for the behaviors using simple analytical arguments.

Slope of the density profile

When σ/m becomes large enough such that the dissipation time scale is comparable or lower than the Hubble time scale ($1/H_0$), all the dSIDM halos in simulations first undergo radial contraction, accompanied by the steepening of the central density profiles. It is surprising that, during this phase, the asymptotic power-law slopes of the central density profiles of dwarf galaxies converge to ~ -1.5 (though with significant scatter ~ 0.5 in the bright dwarfs), insensitive to the detailed value of effective cross-section.

The cooling and contraction of dSIDM halos here share some similarities with the cooling and collapse of gas clouds in the baryonic sector, which have been well-studied in the context of star formation. However, compared to dSIDM halos studied here, there are notable differences in the hierarchy of relevant time scales, which result in different evolution patterns. Gas clouds exhibit much higher particle scattering rates and less energy dissipation per scattering, so the collisional relaxation time scale is orders of magnitude shorter than the cooling time scale, which means that global thermal equilibrium is easier to be established in gas clouds. During the early contraction of gas clouds, it is often assumed that the compressional heating will offset the radiative loss of thermal energy and keep the cloud nearly isothermal [e.g., 270, 271]. However, in dSIDM halos, since the dissipation time scale is comparable to the collision time scale (see Section 2.3), the dSIDM fluid cannot adjust itself to global thermal equilibrium during the contraction of the system, which is qualitatively different from the isothermal contraction of gas clouds. This is supported by the fact that the velocity dispersion profiles (shown in Figure 2.3) at the centers of simulated dwarfs in are never flat in dSIDM models, contrary to the isothermal profiles in eSIDM cases.

For gas clouds, the isothermal contraction will gradually increase the imbalance of gravitational forces over thermal pressure forces, which eventually results in the free-fall collapse of the central part of the cloud [e.g., 271–277]. In terms of time scales, the free-fall collapse will happen when the cooling time scale becomes shorter than the dynamical time scale of the cloud. However, in dSIDM halos, this is also prohibited, since the dissipation time scale (in the surveyed parameter space) is orders of magnitude larger than the dynamical time scale of the system. As the dissipation of thermal/kinetic energy drives the contraction of the halo on the dynamical time scale, DM particles could be gravitationally accelerated again, which would effectively increase the thermal pressure and slow down the collapse.

Moreover, on the dynamical time scale, DM particles from different radii can “mix” because they are only weakly collisional as opposed to gas. As a consequence, even though the global thermal equilibrium of the system is broken, the contraction would still be much slower than the free-fall collapse of gas clouds (as found in Figure 2.11).

We find the behavior of our systems can be reasonably described by the solution for a “slow” quasi-equilibrium cooling flow (with negligible thermal conduction) rather than isothermal or rapid free-fall “collapse”. Following Stern et al. [278], the continuity equation of a steady slow-cooling halo, that is spherically symmetric, isotropic, and pressure supported, can be written as

$$\frac{d \ln \rho}{d \ln r} + \frac{d \ln v_r}{d \ln r} = -2, \quad (2.16)$$

where ρ is the density of the fluid and v_r is the radial inflow velocity. The momentum equation and the entropy equation of the system can be reduced to [278]

$$\frac{d \ln v_r}{d \ln r} \left(\frac{v_r^2}{c_s^2} - 1 \right) = 2 - \frac{v_c^2}{c_s^2} - \frac{r/v_r}{\gamma t_{\text{cool}}}, \quad (2.17)$$

where v_c is the circular velocity, c_s is the adiabatic sound speed, γ is the adiabatic index and t_{cool} is the cooling time scale of the fluid. Applying the solution to the cooling flow of DM, we replace the sound speed c_s with the one-dimensional velocity dispersion of DM σ_{1d} and the cooling time scale t_{cool} with the dissipation time scale t_{diss} of DM self-interactions. In the “subsonic” limit ($v_r \ll \sigma_{1d}$), the second equation becomes

$$-\frac{d \ln v_r}{d \ln r} = 2 - \frac{v_c^2}{\sigma_{1d}^2} - \frac{r/v_r}{\gamma t_{\text{diss}}}. \quad (2.18)$$

A simple self-similar solution exists by requiring that all the logarithmic derivatives of DM properties are constants. Then v_c^2/σ_{1d}^2 and $(r/v_r)/t_{\text{diss}}$ also need to be constants. If we assume $\rho \sim r^\alpha$, we obtain the scaling of the one-dimensional velocity dispersion as

$$\sigma_{1d} \sim v_c \sim \sqrt{GM_{\text{enc}}(r)/r} \sim r^{1+\alpha/2}. \quad (2.19)$$

In the meantime, Equation 2.16 implies that $v_r \sim r^{-\alpha-2}$. According to Equation 2.8, the dissipation time scale t_{diss} scales with density and velocity dispersion as $\rho^{-1}\sigma_{1d}^{-1} \sim r^{-(1+3\alpha/2)}$. If we plug in the scaling of v_r and t_{diss} to the term $(r/v_r)/t_{\text{diss}}$, we obtain

$$\frac{r/v_r}{t_{\text{diss}}} \sim \frac{r r^{\alpha+2}}{r^{-(1+3\alpha/2)}} \sim r^{4+5\alpha/2}. \quad (2.20)$$

So the power-law solution (which requires the term to be a constant at all radii) has $\alpha = -8/5$. Quantitatively, the slope of the density profile given by this “dark cooling flow” solution is consistent with the finding in dSIDM simulations that the asymptotic slopes of the density profiles converge to around -1.5 . It also predicts $\sigma_{1d} \sim r^{0.2}$, which is consistent with the central velocity dispersions of simulated dwarfs that mildly increase with radii.

A similar solution for self-gravitating gaseous spheres with a polytropic equation of state has been presented in Suto and Silk [279], as a generic study of the solution proposed in Shu [271]. They considered spherical gaseous systems with the same equations for mass and momentum conservation. Purely aiming at finding self-similar solutions and without involving a detailed description of cooling/heating, they derived an asymptotic self-similar density profile $\rho \sim r^{-1.5}$ that is independent of the assumed polytropic index of gas. The solution is not restricted to a steady-state, subsonic inflow of gas and still holds even when there is no cooling term.

DM energy transfer in dSIDM

In general, “thermal conduction” and dissipation are the two main mechanisms in SIDM halos to transfer the kinetic energy of DM. “Thermal conduction” is DM collisional energy transfer. The detailed form of the heat conductivity depends on the nature of the heat conduction. In the theory of thermal conductivity of an ideal fluid, the heat flux is the averaged one-way flux of particles across an imaginary surface multiplied by the difference in energy per particle between the starting and ending points. Up to order-unity corrections, this gives

$$\kappa \simeq \frac{3}{2} \frac{k_b}{m} \rho \frac{l^2}{\tau}, \quad (2.21)$$

where k_b is the Boltzmann constant, l is the characteristic distance between the starting and ending points and τ is the time between collisions. In SIDM halos, the collision (or close encounters) between particles is governed by DM self-interactions since the collision time scale of DM self-interaction is significantly lower than the two-body gravitational relaxation time scale. Thus, we have $\tau = t_{\text{coll}}$. If the mean free path between collisions is significantly shorter than the physical size of the system (referred to as the Short Mean Free Path (SMFP) regime), DM will behave like a fluid and the heat conductivity is fully regulated by the mean free path of DM particles ($l = \lambda = 1/(\rho\sigma/m)$). Therefore, in this regime, the thermal conductivity is

$$\kappa = \frac{3}{2} \frac{k_b}{m} C_1 \rho \frac{\lambda^2}{t_{\text{coll}}}, \quad (2.22)$$

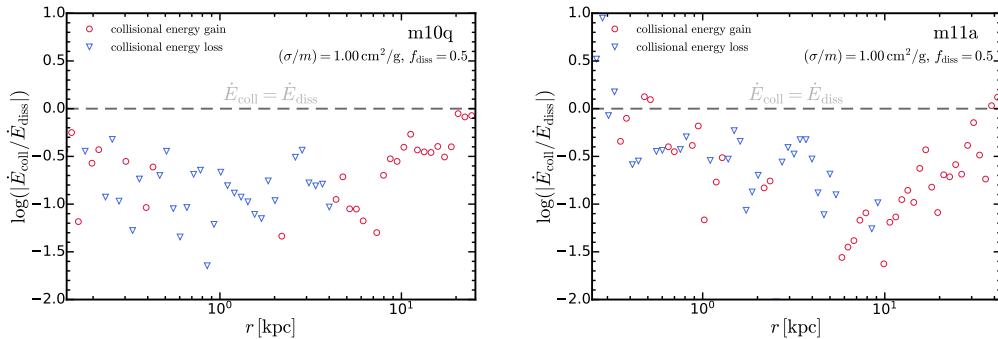


Figure 2.14: **DM energy transfer rates via “thermal conduction” (DM collisional energy transfer) versus dissipation energy loss rates, measured in spherical shells, as a function of galactocentric radii.** We show the heat gain or loss of DM via collisions (\dot{E}_{coll} , Equation 2.26) versus the energy dissipation rate (\dot{E}_{diss} , Equation 2.27) in circles (red for $\dot{E}_{\text{coll}} > 0$, blue for $\dot{E}_{\text{coll}} < 0$). We present the results in one of the classical dwarfs m10q and in one of the bright dwarfs m11a. In both galaxies, with $f_{\text{diss}} = 0.5$, the collisional energy transfer rate is always roughly an order of magnitude lower than the energy dissipation rate.

where C_1 is an order-unity constant and has been found to be $(25\sqrt{\pi}/32)/(4/\sqrt{\pi})$ in the Chapman-Enskog theory [e.g., 280, 281] and $0.25/(4/\sqrt{\pi})$ in numerical simulations [123].

On the other hand, this picture is not valid when the mean free path between collisions is much larger than the gravitational scale height H of the system (referred to as the Long Mean Free Path (LMFP) regime), defined as

$$H = \sqrt{\frac{\sigma_{\text{1d}}^2}{4\pi G\rho}}. \quad (2.23)$$

In this regime, particles can travel several orbits before experiencing a collision. Lynden-Bell and Eggleton [118] found that the characteristic distance between encounters in this limit (for weakly collisional fluid) can be roughly described by the gravitational scale height ($l = H$). In this case, the thermal conductivity is

$$\kappa = \frac{3}{2} \frac{k_b}{m} C_2 \rho \frac{H^2}{t_{\text{coll}}}, \quad (2.24)$$

where C_2 is an order-unity constant and has been found to be 0.75 in numerical simulations [123]. For the fiducial model studied in the paper, the mean free path of DM self-interaction is always orders of magnitudes larger than the gravitational scale height of the systems (or translated to time scale, the collision time scale of DM self-interaction is orders of magnitudes larger than the dynamical time scale of the system). So, these halos all stay in the LMFP regime.

The flux of thermal energy transferred outward through a sphere of radius r can be calculated as

$$j_{\text{coll}}(r) = -\kappa \frac{\partial T(r)}{\partial r} = -\kappa \frac{m}{k_b} \frac{\partial \sigma_{\text{ld}}^2(r)}{\partial r}, \quad (2.25)$$

where κ takes the conductivity in the LMFP regime defined in Equation 2.24. The net collisional energy gain per unit volume in a spherical shell can be calculated as

$$\dot{E}_{\text{coll}}(r) = -\frac{1}{4\pi r^2} \frac{\partial(4\pi r^2 j_{\text{coll}}(r))}{\partial r}. \quad (2.26)$$

The second mechanism of energy transfer is energy dissipation due to DM self-interactions. Different from “thermal conduction”, the dissipation we modeled here is not regulated by any characteristic length scale, since the dissipated energy will not be reabsorbed and effectively has an infinite mean free path. The dissipation energy loss per unit volume in a spherical shell is the volumetric cooling rate

$$\dot{E}_{\text{diss}}(r) = C(r) = \frac{3}{2} \rho(r) \sigma_{\text{ld}}^2(r) / t_{\text{diss}}(r). \quad (2.27)$$

The relative importance of collisional energy transfer and dissipation is determined by the comparison between t_{coll} and t_{diss} . For the dSIDM model studied in this chapter, t_{coll} and t_{diss} always have a similar dependence on density and velocity dispersion. Thus, their ratio is almost constant over the evolution of the halo and only depends on f_{diss} . For the fiducial model with $f_{\text{diss}} = 0.5$, t_{diss} is of the same order of magnitude as t_{coll} (e.g., $t_{\text{diss}} = 0.75 t_{\text{coll}} / f_{\text{diss}}$ for the models with constant cross-sections). In this regime, dissipation is always the dominant mechanism for energy transfer and is responsible for triggering the contraction of the halo. Collisional energy transfer is negligible. Therefore, the evolution pattern of dSIDM halos in this regime will be qualitatively different from the canonical gravothermal collapse of eSIDM halos.

In Figure 2.14, we demonstrate the dominance of dissipation over collisional energy transfer in simulations. We show the collisional energy transfer rate, \dot{E}_{coll} , relative to the energy loss rate due to dissipation, \dot{E}_{diss} , of spherical shells as a function of galactocentric radii. In the classical and bright dwarfs, assuming the fiducial choice of f_{diss} , the rate of energy transfer via collisions is always roughly an order of magnitude lower than the energy dissipation rate.

Evolution of a dSIDM halo

When dissipation dominates over collisional energy transfer of DM, the evolution track of an isolated dSIDM halo can be divided into four regimes, depending on the dissipation time scale t_{diss}

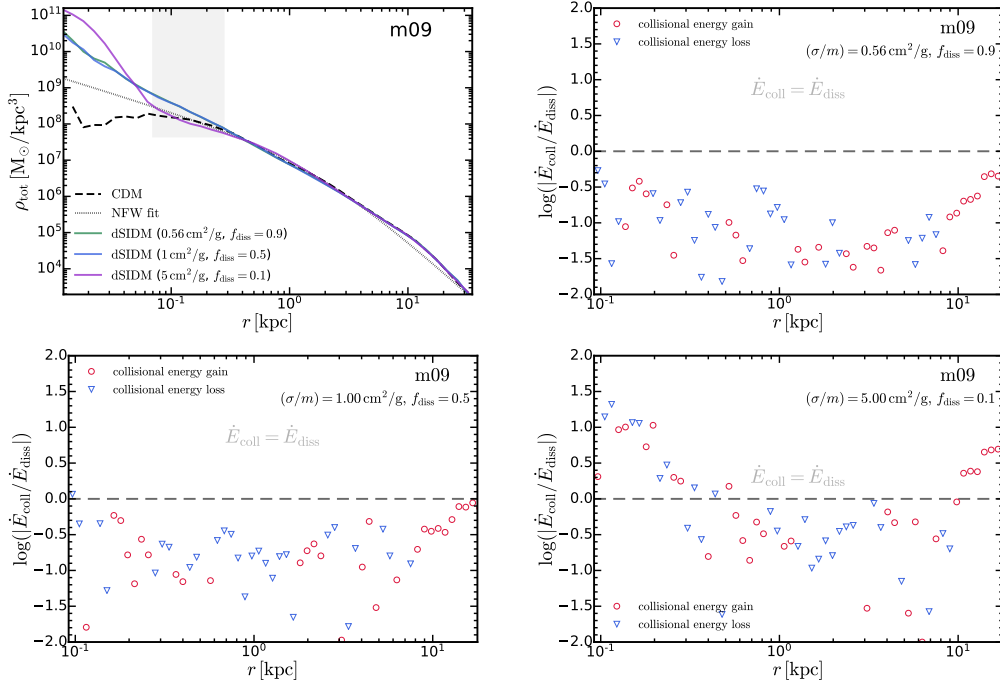


Figure 2.15: *Top left: Total mass density profiles of m09 in dSIDM models with other combinations of f_{diss} and σ/m . We choose three combinations of f_{diss} and σ/m that give the same dissipation time scale: $f_{\text{diss}} = 0.5$, $\sigma/m = 1 \text{ cm}^2 \text{ g}^{-1}$; $f_{\text{diss}} = 0.1$, $\sigma/m = 5 \text{ cm}^2 \text{ g}^{-1}$; $f_{\text{diss}} = 0.9$, $\sigma/m = 0.56 \text{ cm}^2 \text{ g}^{-1}$. Other panels: Collisional energy transfer rates versus energy dissipation rate of DM (as Figure 2.14). The energy transfer rate via collisions is subdominant compare to dissipation in the model with $f_{\text{diss}} = 0.5$ or 0.9 . In the model with $f_{\text{diss}} = 0.1$, collisional heating overtakes dissipation at the center of the galaxy. This model actually produces a denser and cuspier central density profile, as the halo experiences the gravothermal collapse and a dense core in the SMFP regime emerges at the center. In all models, at large radii ($\sim 10 \text{ kpc}$), collisional energy transfer rates become comparable to the dissipation rate, but the absolute values of both terms at these radii are too small to make a difference.*

- Regime A ($t_{\text{diss}} \gg t_{\text{h}}$): The halo evolves in the same way as analogous CDM halo since both t_{diss} and t_{coll} are significantly longer than the lifetime of the system.
- Regime B ($t_{\text{h}} \gtrsim t_{\text{diss}} \gtrsim 0.1 t_{\text{h}}$): The halo undergoes radial contraction. The density profile within the radius where $t_{\text{h}} \gtrsim t_{\text{diss}}$ steepens and becomes cuspy with power-law slopes asymptoting to ~ -1.5 . The shape of the halo becomes more spherical in this phase.
- Regime C ($0.1 t_{\text{h}} \gtrsim t_{\text{diss}} \gg t_{\text{dyn}}$ at the halo center): At a certain stage of the radial contraction, prominent coherent rotation of DM will develop in the system. The system is in a transition from purely dispersion supported to being supported by a mixture of random velocity dispersion and coherent rotation. During this transition, the radial contraction of the halo and the steepening of the density profile are stopped by centrifugal forces. The halo becomes oblate in shape during this phase and the normalization of the density profile measured in spherical shells decreases.
- Regime D ($t_{\text{dyn}} \gtrsim t_{\text{diss}}$): Local instability starts to build up and results in fragmentation of the halo. Numbers of dark "clumps" would start to form within the local free-fall time scale. None of our simulations has reached this regime and it would require order-of-magnitude larger self-interaction cross-sections to test.

2.7 Comparison with other simulation physics

Varying the energy dissipation fraction

We note that the specific simulations studied in this chapter have assumed that the dimensionless degree of dissipation is $f_{\text{diss}} = 0.5$. However, the results can be extrapolated to other slices of the dSIDM parameter space based a simple time scale argument. In Section 2.3, we show that the energy dissipation time scale only depends on the product of f_{diss} and σ/m . Therefore, when dissipation is the dominant mechanism for energy transfer, different combinations of f_{diss} and σ/m should give rise to similar predictions as long as the dissipation time scale is the same. In this section, we vary the dissipation fraction f_{diss} and test how the results are affected in explicit simulations.

We use the ultra-faint dwarf m09 as the test halo. The halo is ideal for the test since the density profile is DM dominated and baryonic feedback is weak considering its

$M_*/M_{\text{halo}} \lesssim 3 \times 10^{-5}$. We choose three combinations of f_{diss} and σ/m that give the same dissipation time scale: $f_{\text{diss}} = 0.5$, $\sigma/m = 1 \text{ cm}^2 \text{ g}^{-1}$; $f_{\text{diss}} = 0.1$, $\sigma/m = 5 \text{ cm}^2 \text{ g}^{-1}$; $f_{\text{diss}} = 0.9$, $\sigma/m = 0.56 \text{ cm}^2 \text{ g}^{-1}$. In Figure 2.15, we show the total mass density profile of m09 in these three models compared with the CDM counterpart and the NFW profile. The models with $f_{\text{diss}} = 0.5$ and $f_{\text{diss}} = 0.9$ produce exactly the same density profile, which justifies that, when dissipation dominates energy transfer, the evolution of the halo is determined by the dissipation time scale and is independent of the detailed combination of parameters. However, we find the model with $f_{\text{diss}} = 0.1$ (and a large cross-section of $\sigma/m = 5 \text{ cm}^2 \text{ g}^{-1}$) produces a qualitatively different profile from the other two models. The density follows the NFW profile at $\gtrsim 100 \text{ pc}$ while getting enhanced by about two orders of magnitude at the scale $\lesssim 100 \text{ pc}$ compared to the extrapolation of the NFW profile, and is even denser than the cuspy profile in the other two models. It is counterintuitive that the model with a lower degree of dissipation gives rise to higher central densities. The phenomenon can be explained by the increased importance of collisional energy transfer in this model. When $f_{\text{diss}} = 0.1$, the collision time scale becomes an order of magnitude lower than the dissipation time scale and the halo is no longer purely dominated by dissipation. Under the influence of collisional energy transfer, the evolution track of the halo resembles the “gravothermal catastrophe” of eSIDM halos, where “thermal conduction” is responsible for energy transfer. The analytical model of the “gravothermal catastrophe” of SIDM halos [e.g., 121] predicts that a halo initially in the LMFP regime will contract while maintaining a cored, self-similar density profile until the central part of the halo reaches the SMFP regime. Subsequently, a dense, optical thick core (in the SMFP regime) will form while the outskirts of the halo stays in the LMFP regime. In the simulation with $f_{\text{diss}} = 0.1$, at the center of m09, the density reaches $10^{11} \text{ M}_{\odot}/\text{kpc}^3$ and the collision time scale there is comparable to the dynamical time scale (assuming a typical one-dimensional velocity dispersion $\sim 10 \text{ km s}^{-1}$) which indicates that the center of the halo is indeed in the SMFP regime. It is striking that the enhanced central density due to the gravothermal evolution is even higher than that produced by models with a higher degree of dissipation.

We verify that the phenomenon discussed above is indeed caused by the increased importance of “thermal conduction” by showing the collisional energy transfer rates versus dissipation rates in simulations in Figure 2.15. In the model with $f_{\text{diss}} = 0.9$, $\sigma/m = 0.56 \text{ cm}^2 \text{ g}^{-1}$ or $f_{\text{diss}} = 0.5$, $\sigma/m = 1 \text{ cm}^2 \text{ g}^{-1}$, the collisional energy transfer rate is always subdominant compared to dissipation. However, in

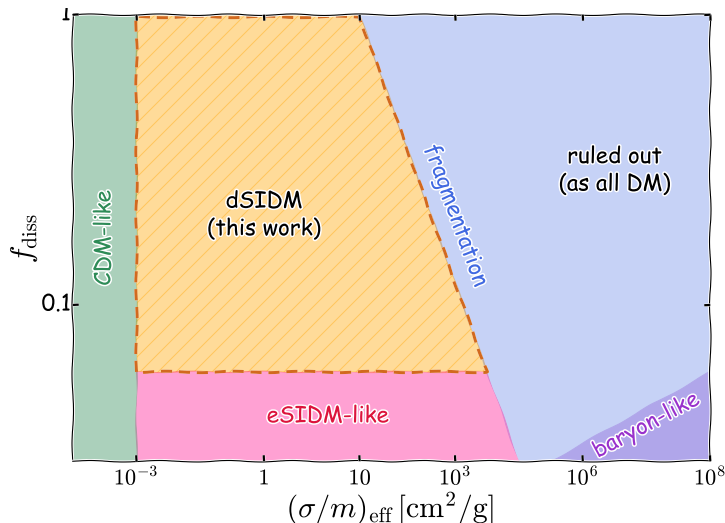


Figure 2.16: **A cartoon of the dSIDM parameter space.** The dSIDM model is parameterized with σ/m and f_{diss} . When σ/m is small enough, both elastic and dissipative SIDM models become analogous to CDM in the lifetime of the Universe. When f_{diss} becomes small enough, dSIDM becomes essentially eSIDM-like since collisional energy transfer dominates over dissipation in this regime. When the product of σ/m and f_{diss} becomes large enough, the dissipation time scale could drop below the local dynamical time scale of the system and result in the fragmentation of dSIDM into compact dark objects. Effectively, baryon-like models are located at the low f_{diss} , high σ/m corner of the plot. The dSIDM models studied in this chapter live in the parameter space, which is not immediately ruled out but can still give rise to unique phenomena different from CDM or eSIDM models.

the model with $f_{\text{diss}} = 0.1$, $\sigma/m = 5 \text{ cm}^2 \text{ g}^{-1}$, the collisional energy transfer rate overtakes dissipation at small radii ($\lesssim 0.2 \text{ kpc}$). This is in very good agreement with the radii where we find the differences in density profiles between the two models. In summary, when $|\dot{E}_{\text{coll}}| \gg |\dot{E}_{\text{diss}}|$ at halo centers, which occurs for $f_{\text{diss}} \lesssim 0.1$, the halo behaves more like an eSIDM halo and the higher central density is primarily due to the gravothermal evolution driven by collisional energy transfer (but potentially accelerated by dissipation).

To better illustrate the parameter space of dSIDM (including the space that has not been explored in this chapter), we create a cartoon image (Figure 2.16) which qualitatively divides the dSIDM parameter space into several regions. The dSIDM models are parameterized with σ/m and f_{diss} . Both eSIDM and dSIDM models become CDM-like when σ/m is small enough such that the collision time scale becomes much longer than the lifetime of the Universe. dSIDM becomes essentially eSIDM-like when f_{diss} becomes small enough since collisional energy transfer dominates

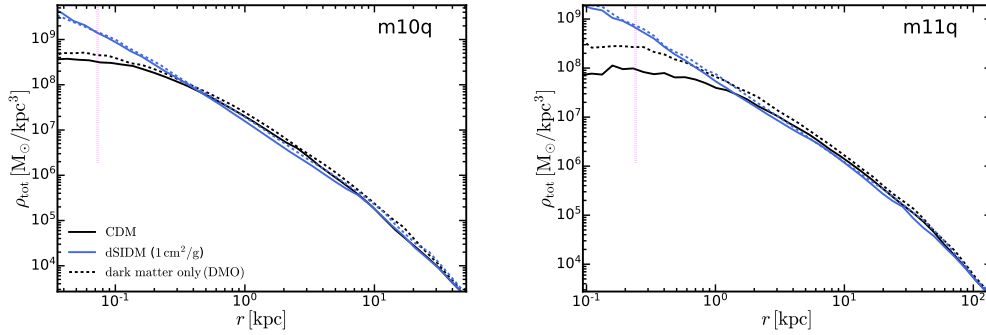


Figure 2.17: Total mass density profiles of galaxies in DMO simulations and full physics simulations. We present the density profiles of m10q and m11q in CDM and dSIDM with $(\sigma/m) = 1 \text{ cm}^2 \text{ g}^{-1}$. The results of full physics simulations are shown in solid lines while the results of DMO simulations are shown in dashed lines. The purple dotted vertical line indicates the convergence radius in DMO runs (see Table 2.1). In CDM, the central density profiles in DMO simulations are similar to the NFW profile before reaching the convergence radii. The full physics simulation of m11q produces a kpc size core at the center due to strong baryonic feedback there. However, in the dSIDM model with $(\sigma/m) = 1 \text{ cm}^2 \text{ g}^{-1}$, the DMO and full physics simulations produce almost identical results, indicating that dissipative interactions of DM completely determine the evolution of the DM halo and the impact of baryonic feedback becomes negligible. This is generally true when the dissipation time scale becomes significantly shorter than the Hubble time scale.

over dissipation in this regime. When the product of σ/m and f_{diss} becomes large enough, the dissipation time scale could drop below the local dynamical time scale of the system and result in the fragmentation of dSIDM into compact dark objects. For a higher value of f_{diss} and σ/m , the scenario that all dark is dissipative would be ruled out by observations (e.g., constraints from merger clusters [159, 244]; lensing constraints on compact DM substructures). If we put baryons (and baryon-copy dSIDM models) in this space effectively, they will be located at the low f_{diss} , high σ/m corner of the plot. Thus the interesting dSIDM parameter space that gives unique phenomena but is not immediately ruled out is roughly around $f_{\text{diss}} \simeq 0.1 - 1$, $(\sigma/m) \simeq 0.01 - 100 \text{ cm}^2 \text{ g}^{-1}$.

DM only versus full physics simulations

The analysis and discussion in the main chapter revolve around the impact of dissipative DM interactions on galaxy structures. However, baryonic physics could also impact galaxy structures in various ways. For instance, the gas outflow driven by stellar/supernovae feedback could irreversibly transfer energy to DM and in-

duce cores at galaxy centers [e.g., 56–58]; the gravitational influence of baryons condensed at galaxy centers could induce adiabatic contraction of DM halos [e.g., 282, 283]. The contamination of baryonic physics processes is an important factor when studying the influence of alternative DM physics.

We explore this aspect by performing DMO simulations of the same halos in the simulation suite and comparing the results. In Figure 2.17, we compare the total mass density profiles of dwarf galaxies m10q and m11q in DMO simulations and full physics simulations. It is not surprising that, in the CDM case, the density profiles produced by DMO simulations are cuspy and NFW-like before reaching the convergence radii. In full physics simulations, m11q exhibits a kpc size core while m10q still exhibits a cuspy profile like its DMO counterpart. The difference results from the different level of baryonic feedback in the two galaxies. However, in the dSIDM model with $(\sigma/m) = 1 \text{ cm}^2 \text{ g}^{-1}$, the DMO and full physics simulations produce almost the same density profiles, indicating that *baryonic physics no longer affect the density profiles of dwarf galaxies once dissipation is strong enough*. This check also validates the results presented in this chapter against uncertainties in modeling the baryonic physics processes in simulations.

2.8 Summary of the chapter

In this chapter, we present the first suite of cosmological baryonic (hydrodynamical) zoom-in simulations of galaxies in dSIDM. We adopt a dSIDM model where a constant fraction f_{diss} of the kinetic energy is lost during DM self-interaction. We sample models with different constant self-interaction cross-sections as well as a model with velocity-dependent cross-section. The dSIDM models explored here are weakly collisional ($\sigma/m \lesssim 10 \text{ cm}^2 \text{ g}^{-1}$) but strongly dissipative ($f_{\text{diss}} \gtrsim 0.1$) and are qualitatively different from some previously proposed baryon-like dSIDM models [e.g., 128, 131, 132], which are limited to explain a subset of all DM in the Universe. The simulations utilize the FIRE-2 model for hydrodynamics and galaxy formation physics, which allows for realistic predictions on the structural and kinematic properties of galaxies. This simulation suite consists of various galaxies, from ultra-faint dwarfs to Milky Way-mass galaxies. In this chapter, we primarily focus on the analysis of dwarf galaxies in dSIDM and explore galaxy/halo’s response to dissipative self-interactions of DM. The following signatures of dSIDM models in dwarf galaxies are identified and explored:

- The DM halo masses and galaxy stellar masses are not significantly affected

in dSIDM models with $(\sigma/m) \lesssim 1 \text{ cm}^2 \text{ g}^{-1}$ compared to the CDM case (see Figure 2.4). The dwarf galaxies in the dSIDM model with $(\sigma/m) = 10 \text{ cm}^2 \text{ g}^{-1}$ have slightly lower (0.1 - 0.2 dex) halo/galaxy stellar masses. But the results of this model are still within the scatter of the relation constrained in observations as well as the stochastic run-to-run scatter of simulations of different dwarf galaxies.

- Energy dissipation due to DM self-interactions induces radial contraction of DM halo. This mechanism competes with baryonic feedback in shaping the central profiles of dwarf galaxies (see Figure 2.5 and 2.6). When the effective self-interaction cross-section is low, the central profiles are still cored despite higher densities and smaller core sizes. When the effective self-interaction cross-section is larger than $\sim 0.1 \text{ cm}^2 \text{ g}^{-1}$, assuming $f_{\text{diss}} = 0.5$, the central density profiles of dwarf galaxies become cuspy and power-law like. The resulting asymptotic power-law profile is steeper than the NFW profile. The power-law slopes asymptote to ~ -1.5 in the classical dwarfs and range from -2 to -1 in the bright dwarfs (see Figure 2.7). The slope of the profile can be well explained by the steady-state solution of a “dark cooling flow” (see Section 2.6), which predicts a density profile with power-law slope -1.6 .
- Interestingly, further increasing the effective cross-section to $10 \text{ cm}^2 \text{ g}^{-1}$ does not lead to further contraction of the halo or steepening of the density profile. Instead, the normalization of the density profiles drops. A likely explanation is that the centrifugal force increases faster than the gravitational attraction as the halo contracts with specific angular momentum conserved. This eventually halts the contraction, increases the rotation support of the halo, and drives the halo deformation (to oblate), which makes the density measured in spherical shell decreased.
- Through time scale analysis (Section 2.3), we show that the dSIDM models with constant cross-sections will have stronger impact in more massive galaxies while the velocity-dependent model has the opposite dependence. This is demonstrated by the simulations of classical dwarfs and bright dwarfs with the same DM model (see Figure 2.5 and 2.6). The dSIDM model with $(\sigma/m) = 0.1 \text{ cm}^2 \text{ g}^{-1}$ produces small cores in two of the classical dwarfs but produces cuspy profiles in two of the bright dwarfs. The velocity-dependent dSIDM model produces cuspy profiles in all the classical dwarfs while pro-

ducing cored profiles in the bright dwarfs that are almost identical to the CDM case.

- The kinematic properties of the DM change in parallel to the contraction of DM halo (see Section 2.4). As the self-interaction cross-section of dSIDM increases, the coherent rotation becomes more prominent compared to random velocity dispersion. In the meantime, the velocity dispersions are more dominated by the tangential component than the radial component, reflected by the negative velocity anisotropies in dSIDM halos. The central parts of the galaxies are in transition from dispersion supported to rotation supported. Meanwhile, the velocity distribution function is suppressed at high velocities while it increases at low velocities in dSIDM models. As the cross-section increases, the median velocity is also shifted lower.
- The shape of the halo is affected by dissipation (see Figure 2.13). In the dSIDM model with $(\sigma/m) = 1 \text{ cm}^2 \text{ g}^{-1}$, the halo becomes more spherical towards lower redshifts, contrary to the triaxial shape of CDM halos. The spherical “dark cooling flow” washes out the initial triaxiality of the halo and makes the halo compact and spherical in the end. However, in the dSIDM model with $(\sigma/m) = 10 \text{ cm}^2 \text{ g}^{-1}$, the halo shape shows a response to the more prominent coherent rotation of DM. Halos are initially on the track of becoming more spherical, but later turn oblate in shape due to the halt of spherical contraction and increased rotation support.
- As shown in Section 2.6, the energy transfer in dSIDM halos (with the degree of dissipation $f_{\text{diss}} = 0.5$) is dominated by dissipation rather than “thermal conduction” (collisional energy transfer). When we vary f_{diss} to $\lesssim 0.1$, collisional energy transfer becomes important and the density at small radii ($r \lesssim 100 \text{ pc}$) is significantly enhanced (see Figure 2.15), which resembles the gravothermal collapse of eSIDM halos. This gives the counterintuitive prediction that a model with a lower degree of dissipation (but higher cross-section to make the dissipation time scale invariant) can produce even denser halos than models with higher degrees of dissipation.
- The density profiles in full physics simulations of CDM are more cored than the ones in DMO simulations, caused by the inclusion of baryonic physics. However, the DMO simulations of dSIDM models show little difference from the full physics simulations (see Figure 2.17), likely due to the dominance

of DM energy dissipation over perturbations from baryonic feedback. This shows that the structural properties of dSIDM halos is insensitive to baryonic physics in this regime and demonstrates the robustness of our results against various uncertainties in the baryonic sector in simulations.

In this chapter, we present the first study of dwarf galaxies in dSIDM models using cosmological hydrodynamical simulations. We find several observable signatures of dSIDM models in dwarf galaxies and systematically study the evolution patterns of dSIDM halos, which differs from canonical astrophysical systems. Analytical explanations are provided to explain the phenomena found in simulations. The findings in this chapter could serve as effective channels to constrain dSIDM models when compared to observations. This aspect will be considered in follow-up work in this series.

DISSIPATIVE DM – OBSERVATIONAL CONSTRAINTS

Xuejian Shen, Philip F. Hopkins, Lina Necib, Fangzhou Jiang, Michael Boylan-Kolchin, and Andrew Wetzel. Dissipative Dark Matter on FIRE: II. Observational signatures and constraints from local dwarf galaxies. *arXiv e-prints*, art. arXiv:2206.05327, June 2022. doi: 10.48550/arXiv.2206.05327.

3.1 Abstract of the chapter

We analyze the first set of cosmological baryonic zoom-in simulations of galaxies in dSIDM introduced in the previous chapter. The simulations utilize the FIRE-2 galaxy formation physics with the inclusion of dissipative dark matter self-interactions modeled as a constant fractional energy dissipation ($f_{\text{diss}} = 0.75$). In this chapter, we examine the properties of dwarf galaxies with $M_* \sim 10^5 - 10^9 M_\odot$ in both isolation and within Milky Way-mass hosts. For isolated dwarfs, we find more compact galaxy sizes and promotion of disk formation in dSIDM with $(\sigma/m) \leq 1 \text{ cm}^2 \text{ g}^{-1}$, but they are still consistent with observed galaxy sizes and masses. On the contrary, models with $(\sigma/m) = 10 \text{ cm}^2 \text{ g}^{-1}$ produce puffier stellar distributions that lie in the diffuse end of the observed size-mass relation. In addition, owing to the steeper central density profiles in dSIDM, the sub-kpc circular velocities of isolated dwarfs when $(\sigma/m) \geq 0.1 \text{ cm}^2 \text{ g}^{-1}$ are enhanced by about a factor of two, which are still consistent with the measured stellar velocity dispersions of Local Group dwarfs but in tension with the HI rotation curves of more massive field dwarfs. Meanwhile, for satellites of Milky Way-mass hosts, the median circular velocity profiles are marginally affected by dSIDM physics, but dSIDM may help address the missing compact dwarf satellites in CDM. The number of satellites is slightly enhanced in dSIDM, but the differences are small compared with the large host-to-host variations. In conclusion, the dSIDM models with constant cross-section $(\sigma/m) \gtrsim 0.1 \text{ cm}^2 \text{ g}^{-1}$ (assuming $f_{\text{diss}} = 0.75$) are in tension in bright dwarfs ($M_{\text{halo}} \sim 10^{11} M_\odot$) due to circular velocity constraints. However, models with lower effective cross-sections (at this halo mass/velocity scale) are still viable and can produce non-trivial observable signatures.

In this chapter, we make predictions for various observed properties of galaxies in dSIDM and compare them to the observed dwarf satellite galaxies in the Local

Classical dwarfs

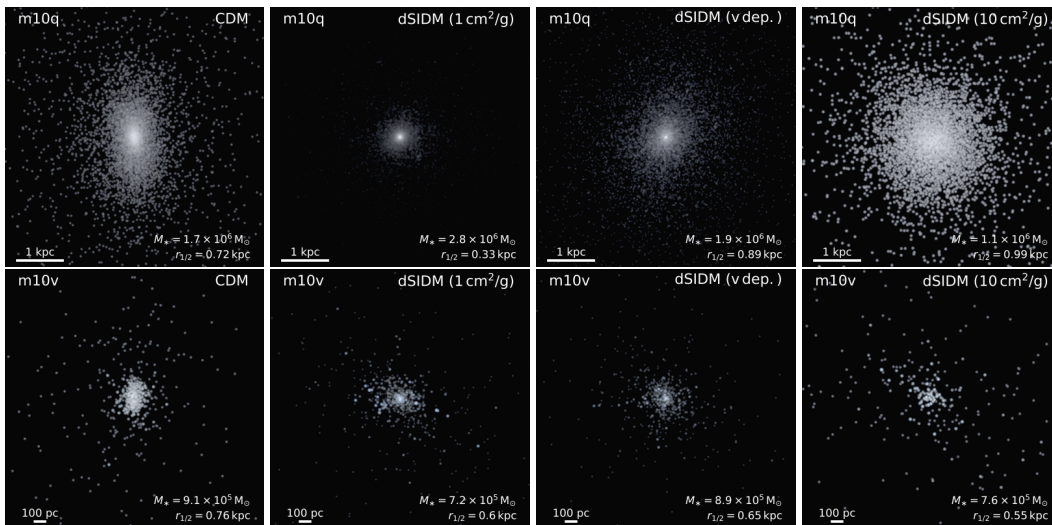


Figure 3.1: **Visualizations of two simulated classical dwarfs.** Each column corresponds to one DM model studied. The images are mock *Hubble Space Telescope* composites of u,g,r bands with a logarithmic surface brightness stretch. We use the STARBURST99 model to determine the SED of each stellar particle based on its age and initial metallicity and use ray-tracing [4] to model dust attenuation assuming a Milky Way-like reddening curve and a dust-to-metal ratio of 0.4. The side lengths of the images are chosen to be $8 \times r_{1/2}$ of the CDM run. The dSIDM models with $(\sigma/m) = 1 \text{ cm}^2 \text{ g}^{-1}$ and the velocity-dependent cross-section produce visibly more concentrated stellar content compared to the CDM case (the effective cross-section as defined in Shen et al. [5] of our velocity-dependent model in classical dwarfs is about $0.3 \text{ cm}^2 \text{ g}^{-1}$). However, the model with $(\sigma/m) = 10 \text{ cm}^2 \text{ g}^{-1}$ produces overall fluffier stellar distribution.

Group or LSBs in the field. The chapter will be organized as follows: In Section 3.2, we briefly review the simulation setup and the DM models studied. In Section 3.3, we present predictions for the stellar content of the simulated dwarfs, including density profiles, size and mock optical images. Then in Section 3.4, the circular velocity profiles of the simulated dwarfs (or satellites of Milky Way-mass hosts) will be compared with their observational counterparts specifically. In Section 3.5, the satellite counts of simulated Milky Way-mass hosts will be studied. Finally, in Section 3.6, the summary and conclusions will be presented.

3.2 Simulations

Overview of the simulation suite

The analysis in this chapter is based on the FIRE-2 dSIDM simulation suite introduced in Shen et al. [5], which consists of ~ 40 cosmological hydrodynamical

Bright dwarfs

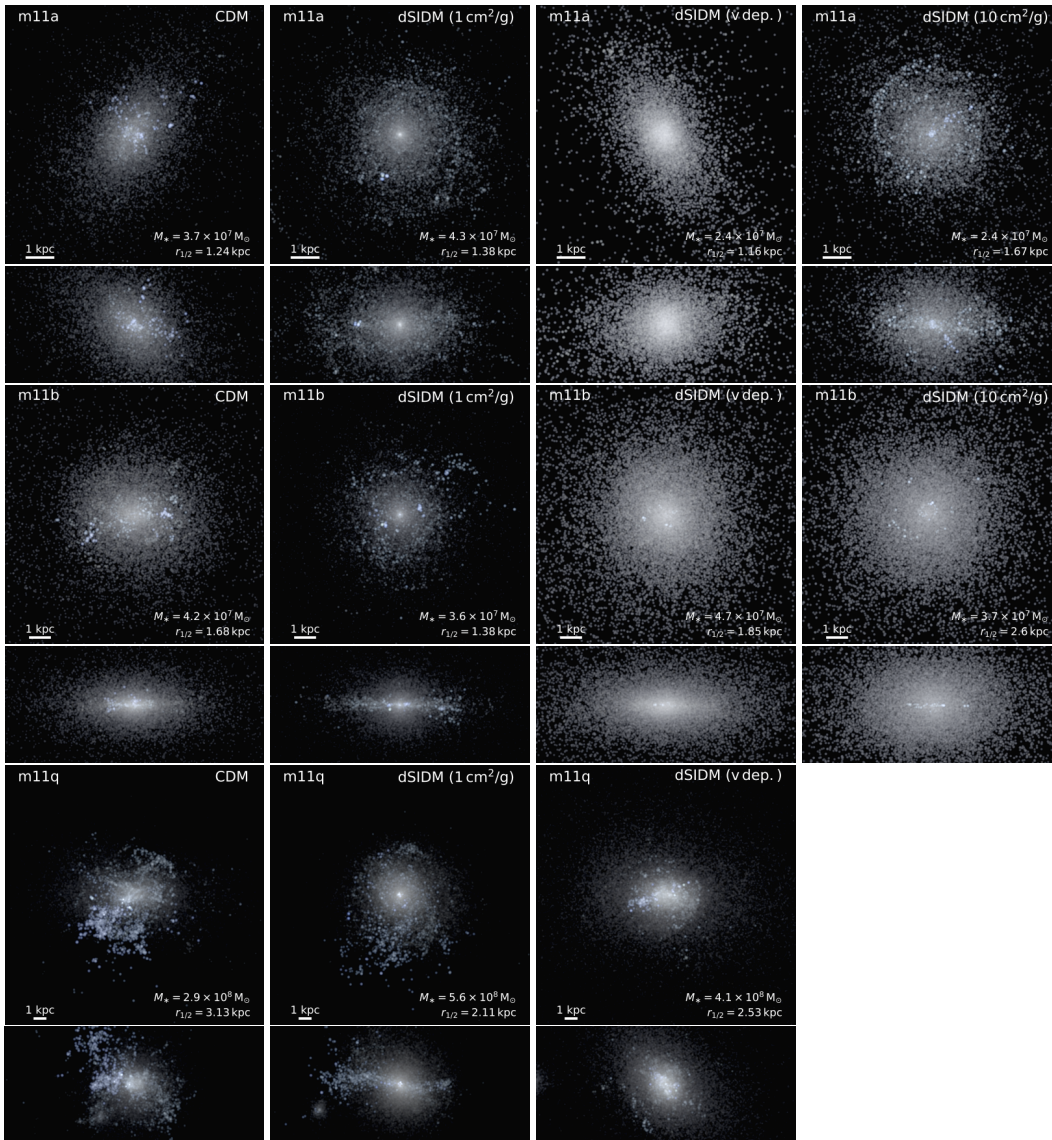


Figure 3.2: **Visualizations of three simulated bright dwarfs.** The images are generated in the same way as those in Figure 3.1. Since some of the bright dwarfs develop disk-like structures, we show both face-on and edge-on images here. Compared to the CDM case, the stellar disks in the dSIDM model with $(\sigma/m) = 1 \text{ cm}^2 \text{ g}^{-1}$ are more well-defined and exhibit more concentrated central regions. On the other hand, the velocity-dependent dSIDM model produces galaxies that are visibly similar to the CDM case given its small effective cross-section at this mass scale ($(\sigma_{\text{eff}}/m) \sim 0.01 \text{ cm}^2 \text{ g}^{-1}$). Interestingly, the model with $(\sigma/m) = 10 \text{ cm}^2 \text{ g}^{-1}$ produces stellar disks accompanied by overall fluffier stellar distribution compared to the model with $(\sigma/m) = 1 \text{ cm}^2 \text{ g}^{-1}$ and CDM.

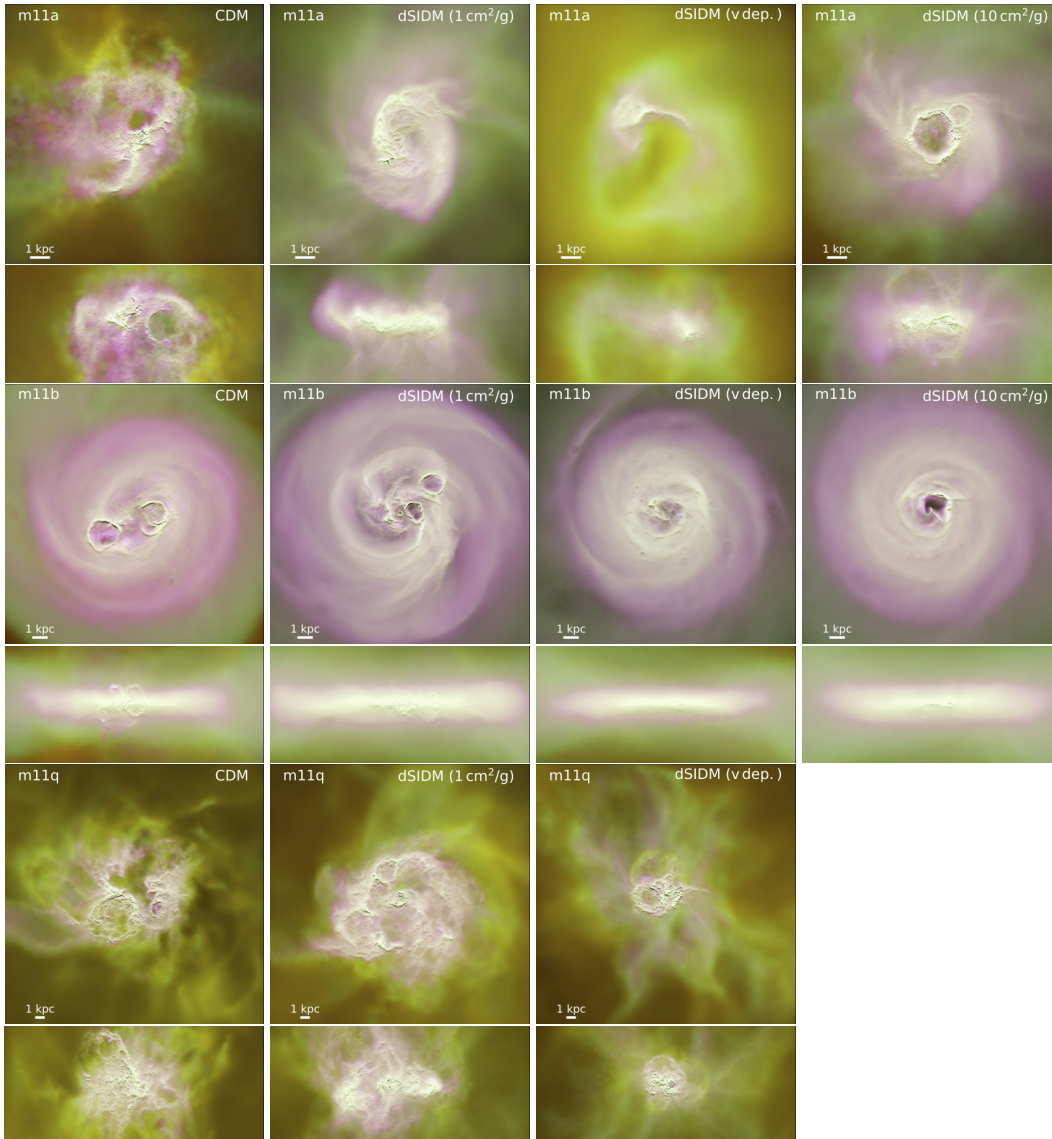


Figure 3.3: **Visualization of the gas content of three simulated bright dwarfs.** The images are logarithmically-weighted gas surface density projections. Each column corresponds to one DM model studied and each row corresponds to one bright dwarf simulated. For each dwarf, both the face-on and edge-on images are shown. The side lengths of the images are chosen as $12 \times r_{1/2}^{\text{cdm}}$. Each image is a composite of gas distribution in three phases characterized by the gas temperature. The magenta color represents the “cold” neutral gas with $T \lesssim 8000$ K; the green color represents the “warm” gas with $T \sim 1 - 3 \times 10^4$ K; the red color represents the “hot” ionized gas in the CGM with $T \gtrsim 10^5$ K. The neutral gas disks are promoted in the dSIDM-c1 and c10 models, even in m11a which is strongly perturbed by supernovae feedback in CDM.

zoom-in simulations of galaxies chosen at representative mass scales with CDM, eSIDM, and dSIDM models. Below we will give a brief introduction of the simulations and refer the readers to Shen et al. [5] for more details. The simulations are part of the Feedback In Realistic Environments project [FIRE, 229], specifically the “FIRE-2” version described in Hopkins et al. [25]. The simulations adopt the code GIZMO [230], with gravity solved using the Tree-PM method [284] and hydrodynamics solved using the mesh-free Lagrangian Godunov “MFM” method. The FIRE galaxy formation physics and numerical parameters are identical to those described in Hopkins et al. [25], Garrison-Kimmel et al. [231]¹. A full list of the galaxies simulated and relevant parameters are shown in Table 2.1.

DM self-interactions are simulated in a Monte-Carlo fashion following the implementation in Rocha et al. [88]. A simplified, empirical dissipation model is employed: two interacting DM particles lose a constant fraction (the dissipation factor f_{diss}) of their kinetic energy in the center-of-momentum frame when they collide with each other. The extreme version of this type of interaction is the fusion process (i.e. $f_{\text{diss}} = 1$) of DM composites discussed in the context of self-interacting asymmetric DM [e.g., 99, 106, 236–238] and specifically the dark “nuggets” model [99, 106]. It is worth noting that there are other particle physics models for dSIDM [e.g., 85, 96–98, 101, 128, 243] with potentially different behaviors on cosmological scales that are not captured by this simplified parameterization. However, it is a reasonable starting point to study the phenomenology of dissipative DM in cosmic structural formation.

The simulations employed a fiducial dissipation factor $f_{\text{diss}} = 0.75$ and we explore models with constant self-interaction cross-section² $(\sigma/m) = 0.1, 1, 10 \text{ cm}^2 \text{ g}^{-1}$ ³, or a velocity-dependent cross-section model

$$\frac{\sigma(v)}{m} = \frac{(\sigma/m)_0}{1 + (v/v_0)^4}, \quad (3.1)$$

where the fiducial choice is $(\sigma/m)_0 = 10 \text{ cm}^2 \text{ g}^{-1}$ and $v_0 = 10 \text{ km s}^{-1}$. The velocity dependence of the self-interaction cross-section is empirically motivated by the relatively tight constraints on SIDM at galaxy cluster scale [e.g., 94, 159, 244]

¹We note that the CDM runs are rerun to exactly match the configuration of dSIDM runs, so galaxy properties are not expected to be “identical” to the original FIRE-2 results.

²The self-interaction cross-section is the total cross-section, $\int (d\sigma/d\Omega) d\Omega$, throughout this chapter.

³The galaxy m11q does not have the $(\sigma/m) = 10 \text{ cm}^2 \text{ g}^{-1}$ simulation since it stalls at fairly high redshift due to formation of dense DM clumps (see Table 1 in Shen et al. [5]).

and the relatively high cross-section needed to strongly influence some small-scale galaxy properties [e.g., 87–90, 94]. The velocity dependence is also a generic feature of many particle physics models for SIDM [e.g., 79, 83, 85, 86, 97, 98, 102, 104]. In this work, we assume scatterings to be isotropic. Angular dependence can arise when the force mediator is light or massless [e.g., 79, 83, 102] but the effects are limited for isolated halos [e.g. 285].

Given the choices of cross-section and dissipation factor, the typical collision and energy dissipation time scale of DM will be smaller than the Hubble time scale but still larger than the free-fall time scale (see Shen et al. [5] for details). In this regime, the dissipative DM is weakly-collisional and weakly-dissipative compared to the baryonic gas and will not fragment or form “compact” dark objects. In this chapter, we will refer to the dSIDM model with constant cross-section $(\sigma/m) = 0.1, 1, 10 \text{ cm}^2 \text{ g}^{-1}$ as “dSIDM-c0.1,1,10” for simplicity. For comparison, a subset of the galaxies in the suite are also simulated with the eSIDM model with constant cross-section $(\sigma/m) = 1 \text{ cm}^2 \text{ g}^{-1}$.

Host halo and substructures

The simulations in this suite are all identified with the main “target” halo around which the high-resolution zoom-in region is centered. The central position and velocity of this main halo are defined by the center of mass (of DM particles) and are calculated via an iterative zoom-in approach. However, specifically for the measurements of stellar density profiles and galaxy visible sizes, we use stellar particles for the center identification. The bulk properties of the halo and the galaxy it hosts are calculated following the practice of the standard FIRE-2 simulations, as described in Hopkins et al. [25]. We define the halo mass M_{halo} and the halo virial radius R_{vir} using the redshift-dependent overdensity criterion in Bryan and Norman [249]. We define the stellar mass M_* as the total mass of all the stellar particles within an aperture of $0.1 R_{\text{vir}}$ and correspondingly define the stellar half-mass radius $r_{1/2}$ as the radius that encloses half of the total stellar mass.

To identify substructures in post-processing, we take two steps following Wetzel et al. [60], Garrison-Kimmel et al. [62], Necib et al. [286] and Samuel et al. [287]. We first identify bound DM subhalos (of the main “target” halo) using the ROCKSTAR [233] halo finder, based only on DM particles. The force resolution of ROCKSTAR is conservatively set to be the same as the softening length of DM particles in simulations. To exclude misidentified subhalos with a limited number

of particles, we only keep subhalos with mass $M_{200,m} > 3 \times 10^6 M_\odot$ ⁴ and maximum circular velocity $V_{\text{circ}}^{\text{max}} > 5 \text{ km s}^{-1}$ from the output ROCKSTAR halo catalogs. In the second step, stellar particles are assigned to the identified dark subhalos through an iterative method [60, 62, 287, 288]. Initially, stellar particles are assigned to a DM subhalo with a generous cut on their distances to the subhalo center ($r \leq 0.8R_{200,m}$ and $r \leq 30 \text{ kpc}$) and velocities with respect to the subhalo center ($v \leq 2V_{\text{circ}}^{\text{max}}$ and $v \leq 2\sigma_{v,\text{dm}}^{3\text{d}}$). Subsequently, stellar particles are iteratively removed if $r < 1.5 r_{90}$, where r_{90} is the radius that enclose 90% of the stellar mass currently associated to the subhalo, or if $v < 2\sigma_{v,*}^{3\text{d}}$, where $\sigma_{v,*}^{3\text{d}}$ is the three-dimensional velocity dispersion of stars currently associated to the subhalo, until the number of stellar particles selected stabilizes at one percent level. Finally, we define M_* of the subhalo as the mass sum of all the stellar particles that remain assigned to each galaxy in this way and correspondingly define $r_{1/2}$ as the radius within which the enclosed mass is $M_*/2$. The mass density profiles will be calculated in spherical shells centering on each subhalo, using all relevant types of particles in those shells. The circular velocity will be calculated based on the total mass enclosed by each shell.

3.3 Galaxy baryonic content

Galaxy morphology

In Figure 3.1 and Figure 3.2, we show mock images of simulated dwarf galaxies at $z = 0$, grouped as classical and bright dwarfs. Each image is a mock *Hubble Space Telescope* composite of u,g,r bands with a logarithmic stretch of the surface brightness. We use the STARBURST99 model [289] to determine the spectral energy distribution (SED) of each stellar particle based on its age and initial metallicity, and use the ray-tracing method [4] to model dust attenuation, assuming a Milky Way-like reddening curve and a dust-to-metal ratio of 0.4. For the classical dwarfs (m10 galaxies) in Figure 3.1, the dSIDM-c1 and the velocity-dependent model produce visibly more concentrated stellar content than the CDM case. The contraction of the stellar content is likely related to the contraction of the underlying DM distribution. On the other hand, the dSIDM-c10 model produces fluffier stellar content in m10q. This phenomenon is likely related to the lowered normalization of the central DM density profile, and thus shallower gravitational potential, in this model as found and described in Shen et al. [5]. However, in the same model, the stellar content of m10v is still compact, which demonstrates the large galaxy-to-galaxy variations of

⁴ $M_{200,m}$ and $R_{200,m}$ are defined for the subhalo with the density criterion 200 times the mean matter density of the Universe at $z = 0$ calculated by ROCKSTAR. Note that this is different from the virial mass definition of the main “target” halo, and is used only for selection purpose.

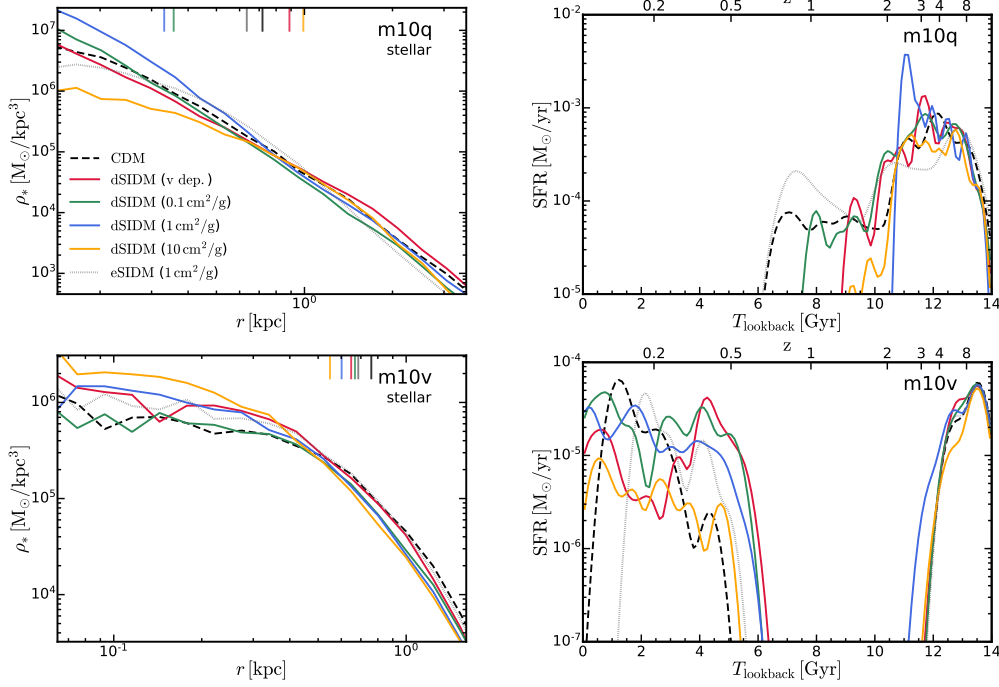


Figure 3.4: *Left column: Stellar density profiles of simulated classical dwarfs.* The density profiles from different DM models are presented as labeled. The short vertical lines indicate the stellar-half-mass-radius of the galaxy in each model. The m10q and m10v halos show different responses to DM dissipation. In m10q (*top*), which forms its stars early, a cuspy stellar profile appears with moderate dSIDM cross-sections accompanied by shrinking galaxy size, and then the profile turns shallower when the cross-section further increases. In m10v (*bottom*), which forms quite late, the profile becomes more concentrated monotonically as the cross-section increases, and the decline of galaxy size is less dramatic. This is related to the distinct star formation histories of the two galaxies as shown on the right. *Right column: Archaeological star formation history of simulated classical dwarfs.* This is computed as the age distribution of stellar particles within $10\sigma_{\text{vir}}^{\text{cdm}}$ at $z = 0$. The galaxy m10q has an early star formation history peaked at $z \approx 3$. The stars have more time to react to the underlying DM distribution. On the other hand, the galaxy m10v with a relative late period of star formation does not exhibit this. The late time star formation and feedback also puffs up the stellar content and make it less dependent on the underlying DM distribution.

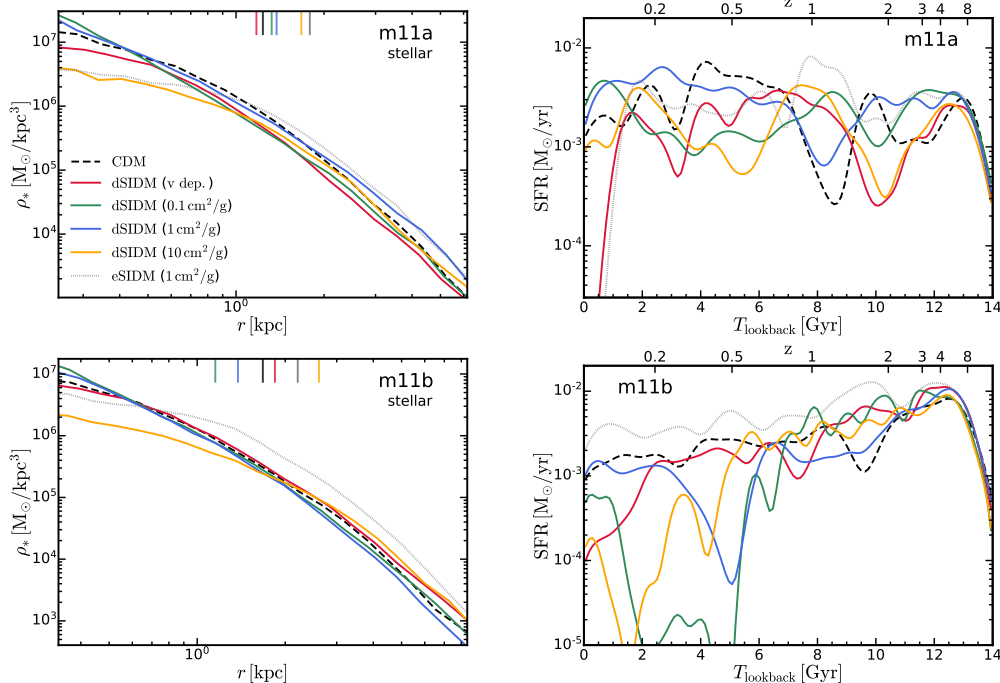


Figure 3.5: *Left column: Stellar density profiles of simulated bright dwarfs.* The notation is the same as Figure 3.4. In both m11a and m11b, the stellar density profiles become cuspy in dSIDM models with moderate cross-sections while turning shallower as we further increase the cross-section. This largely reflects similar behavior seen in the DM density profiles in Shen et al. [5] – in particular, at very high cross-sections the central DM profiles are flattened via dark rotation. *Right column: Archaeological star formation history of simulated bright dwarfs.* The notation is the same as Figure 3.4. The galaxy m11a has a relatively flat star formation history and is not significantly affected by the DM physics. However, in m11b, dips in star formation history at low redshifts appear in dSIDM models.

the star formation and corresponding DM and galaxy dynamics in classical dwarfs. This variation mainly comes from the distinct star formation histories of the two dwarfs. As will be shown in the following section (see also Hopkins et al. [25]), m10q is an early-forming galaxy with half of its stellar mass formed at $z \gtrsim 4$ while m10v is late-forming with most of its stellar mass formed at $z \lesssim 0.4$, dominated by a few starburst events within the recent 4 Gyr. Therefore, the early-formed stars in m10q would have enough time to relax and respond to the change of the underlying DM structure, while m10v is still strongly affected by its very recent star formation and feedback. Similar phenomena are found in the stellar density profiles of the two classical dwarfs presented in Figure 3.4, which will be discussed in Section 3.3.

For the bright dwarfs (m11 galaxies) in Figure 3.2, we show both face-on and edge-

on images because stellar disks start to show up in some simulated galaxies. The viewing angles are determined by the total angular momentum of the stellar particles within half of the field of view. Compared to its CDM counterpart, the dSIDM-c1 model gives rise to thinner and more well-defined stellar disks and meanwhile more concentrated central cusps. This again is in line with the more concentrated underlying DM distribution. The morphological transition is caused by the stronger central attraction forces provided by the compact cusps formed in dSIDM halos. The central dSIDM cusp provides a well-defined “center” of the galaxy for star-forming gas to coherently rotate around and also stabilize the thin stellar disk formed. For the velocity-dependent model, the compactness of the stellar content is close to the CDM case because the effective cross-section (at the mass scale of bright dwarfs) decreases to $\sim 0.01 \text{ cm}^2 \text{ g}^{-1}$ which is much smaller than that in the classical dwarfs. Nevertheless, the stellar distribution in this model is more extended and the on-going star formation is also suppressed (see the lack of blue star-forming clouds in the images). For the dSIDM-c10 model, stellar disks are produced but accompanied by apparently fluffier stellar distributions, which is similar to what we described in classical dwarfs.

An important feature of the bright dwarfs is the formation of co-rotating baryonic structures, e.g. the stellar disks in some of the m11 galaxies, which is absent in lower mass dwarfs. The larger halo mass and the presence of dense central baryonic components make these galaxies more stable against the energy/momentum injection from feedback, and therefore more able to sustain a rotationally supported gaseous disk [e.g., 290, 291]. In observations, a highly-rotating subset of disk dwarf galaxies (late-type) have been found in HI surveys at similar mass scale [e.g., 8, 39, 41]. In Figure 3.3, we show the gas surface density projections of the simulated dwarfs in the face-on and edge-on direction (determined by the angular momentum of the gas). The images are composites of the gas surface density in three phases, with the magenta/green/red color representing the “cold” neutral gas with $T \lesssim 8000 \text{ K}$, the “warm” gas with $T \sim 1 - 3 \times 10^4 \text{ K}$ and the “hot” ionized gas with $T \gtrsim 10^5 \text{ K}$, respectively. The cold neutral gas in these dwarf galaxies is confined by the hot CGM gas, and star formation takes place in dense molecular clouds embedded in the gas disks, and perturbations from subsequent stellar/supernovae feedback manifest as “super bubbles” in the ISM. The feedback heats up the gas at the shock front of “super bubbles” and creates a warm layer in the gas disk. Among all three m11 galaxies simulated in CDM, only m11b develops a well-defined rotating disk consists of cold neutral gas while the other two dwarfs are severely perturbed by

feedback. However, in dSIDM-c1, all three dwarfs show signatures of a co-rotating gaseous disk, with obvious diskness in the edge-on projection and spiral arms visible in the face-on projection. Similar to what we found for the stellar disk, the compact cusps of dSIDM halos provide stronger central attraction forces to stabilize and promote the formation of thin gaseous disks. The role of modified gravitational potential/acceleration on disk formation in dwarf galaxies will be studied in detail in Hopkins et al. 2023 (in prep).

Stellar density profiles and star formation history

In Figure 3.4 and Figure 3.5, we show the stellar density profiles of simulated classical and bright dwarfs, respectively. Each stellar density profile plot is paired with the plot of the archaeological star formation history of the galaxy. The star formation history is computed as the age distribution of stellar particles selected at $r \leq 10\% R_{\text{vir}}^{\text{cdm}}$ at $z = 0$. In both classical and bright dwarfs, dSIDM with moderate cross-sections give rise to central stellar density profiles that are cuspier than the NFW profile and the galaxy stellar-half-mass-radii decrease correspondingly. These phenomena are likely caused by the more concentrated DM content in these dSIDM models. Similarly, the stellar profiles in eSIDM are cored due to the gravitational impact of thermalized DM cores. In the dSIDM-c10 model, the stellar distribution becomes cored and more extended, which is also related to the decreased normalization of DM density profiles in this model. Specifically, in Shen et al. [5], coherent rotation of DM was found in the highly-dissipative models (including dSIDM-c10) and we showed that this drives halo deformation to oblate shapes. This combination of rotational support and change in shape actually leads to a *decline* in the central spherically-measured DM density, which we see here is reflected in the stellar distribution. In general, the compactness of the DM distribution appears to strongly influence the stellar density profile of dwarf galaxies. The star formation efficiency is regulated by the competition between feedback-driven ejection versus the gravitational attraction from DM [e.g., 292]. In equilibrium states (or after numerous cycles of star formation events), star formation is promoted (inhibited) in compact (diffuse) DM halos. Stars formed before their DM halo is structurally modified (e.g. before a dark disk structure or a strong cusp owing to dissipation can form) can still relax with respect to the modified halo potential within a few dynamical time scales. One galaxy in this suite that deviates from the picture above is the classical dwarf m10v. In all DM models for this particular galaxy, cored stellar density profiles are developed at the galaxy center, while the central stellar density

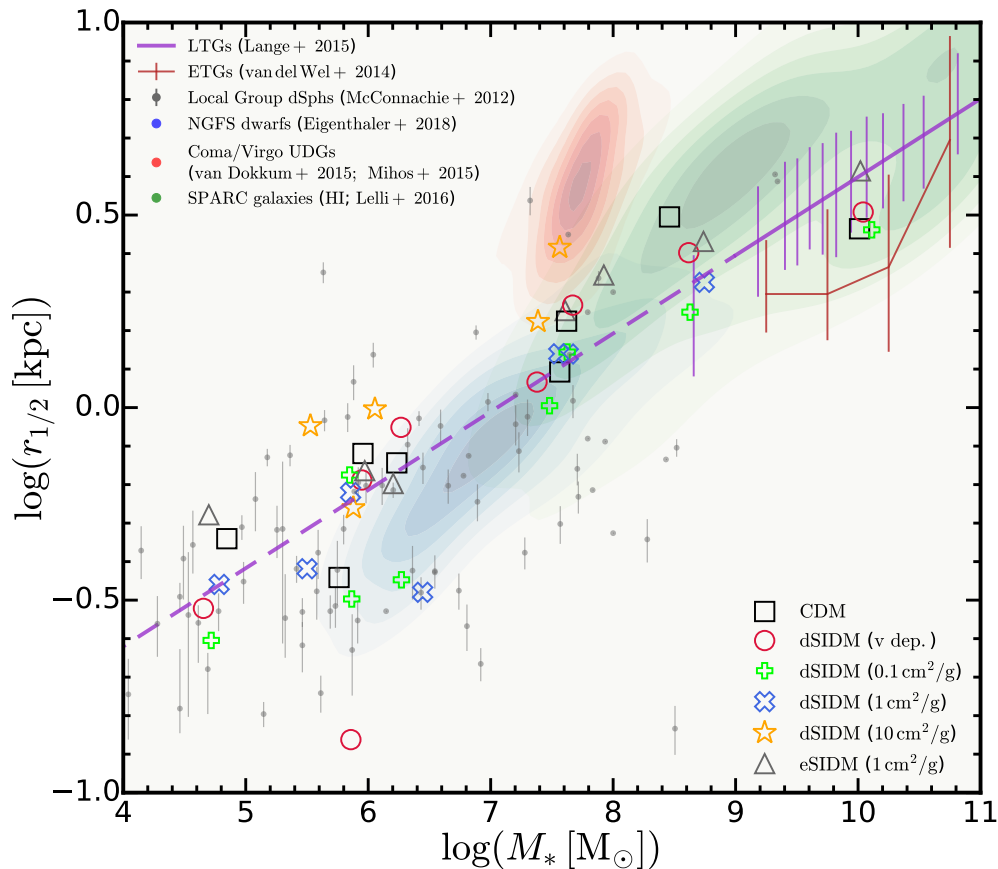


Figure 3.6: Size-mass relation of simulated (isolated) dwarf galaxies. The stellar half-mass radius versus stellar masses of simulated dwarfs are shown with open markers (as labeled). We compare them with several observations of dwarf galaxies in the Local Universe: gray points with error bars, the Local Group dSphs compiled in McConnachie [6]; blue contours, the NGFS dwarfs in Eigenthaler et al. [7]; green contours, the SPARC galaxies presented in Lelli et al. [8, 9]; red contours, the UDGs in the Coma and Virgo cluster from van Dokkum et al. [10] and Mihos et al. [11]; purple (red) line, the size-mass relation of the observed “normal” late-type (early-type) galaxies [12, 13]. The simulated dwarfs are consistent with the median size-mass relation of LTGs in observations and its extrapolation. With mild DM self-interaction ($(\sigma/m) \lesssim 1 \text{ cm}^2 \text{ g}^{-1}$), the sizes and masses of galaxies, in general, do not vary much from the CDM case. In some cases, the dSIDM models can produce compact dwarfs at $M_* \sim 10^6 M_\odot$, in better agreement with Local Group observations. However, in the dSIDM-c10 model, dwarf galaxies have apparently more extended stellar content and are located at the diffuse end of the observed distribution.

increases monotonously with dSIDM cross-section. The unique stellar content of m10v could be a result of its distinct star formation history (bottom right panel of Figure 3.4), which is dominated by several recent (very low-redshift) starburst events. The system has therefore not yet relaxed from the perturbations of the recent star formation and feedback.

In terms of the star formation history, as shown in Figure 3.4, m10q is clearly an early-forming dwarf with most of the star formation taking place at $z \gtrsim 2$ and a tail extended to $z \sim 0.7$. In dSIDM models with increasing effective cross-sections, this tail of star formation ceases earlier which is likely due to the faster depletion of star-forming gas in the more compact dSIDM halos. In m10v, despite drastically different star formation history from m10q, the recent period of star formation also takes place earlier in dSIDM runs. On the other hand, for the bright dwarfs shown in Figure 3.5, we do not see an apparent shift in the halt/onset of star formation. The star formation histories in these dwarfs are continuous but fairly bursty in all the models. In m11a, the star formation histories in different DM models do not exhibit significant differences. However, the star formation history of m11b shows apparent dips at low redshifts ($z \lesssim 0.5$) in dSIDM models, which never occur in CDM or eSIDM runs. This again could be related to the faster depletion of star-forming gas in deeper gravitational potentials of dSIDM halos.

Galaxy size-mass relation

In Figure 3.6, we compare the stellar-half-mass radii (as a function of stellar mass) of simulated dwarf galaxies (isolated ones only, do not include satellites of Milky Way-mass hosts) with observations of dwarf galaxies in the local Universe. These observations include the Local Group dwarf spheroidal galaxies (dSphs) compiled in McConnachie [6], dwarf galaxies from the Next Generation Fornax Survey [NGFS, 7], galaxies measured in the *Spitzer* Photometry and Accurate Rotation Curves [SPARC, 8, 9] project, and the ultra-diffuse galaxies (UDGs) in the Coma and Virgo cluster from van Dokkum et al. [10] and Mihos et al. [11]. The quoted effective radius (half-light radius) in literature has been converted to the half-mass radius assuming $r_{1/2} \simeq 4/3 R_{\text{eff}}$ [293]. The purple solid line shows the galaxy size-mass relation of “normal” late-type galaxies [LTGs; 12] and its extrapolation (purple dashed line) while the red solid line shows that of early-type galaxies [ETGs; 13].

In general, despite some random galaxy-to-galaxy variations, the simulated dwarfs agree well with the observed dwarf population in the Local Universe and follow the

extrapolated size-mass relation of LTGs. The diversity of dwarfs is manifest as the distinction between LTGs and ETGs in massive sub-Milky Way-mass galaxies, the existence of UDGs, and the large scatter in galaxy size at $M_* \sim 10^8 M_\odot$ as well as the population of compact Local Group dwarfs that fall significantly lower than the median relation. With mild DM self-interaction ($(\sigma/m) \lesssim 1 \text{ cm}^2 \text{ g}^{-1}$), galaxy sizes and masses in dSIDM or eSIDM do not vary much from the CDM case. This is consistent with previous FIRE-2 studies of dwarf galaxies in eSIDM [113, 115]. Some compact dwarfs at $M_* \lesssim 10^7 M_\odot$ are found in dSIDM models, which are in better agreement with the observed compact dwarfs in the Local Group. However, the compact dwarf elliptical galaxies with large stellar masses ($M_* \gtrsim 10^7 M_\odot$) in the Local Group [e.g., 52, 62] are still hard to produce in these isolated dwarf simulations, no matter which DM model is employed. This point will be revisited when we study the satellite galaxies of simulated Milky Way-mass hosts. Notably in the dSIDM-c10 model, simulated dwarfs exhibit systematically more extended stellar content and shift from the median relation. In this model, the bright dwarfs become more like analogs to UDGs, and the classical dwarfs are located at the diffuse end of the observed distribution. The dSIDM-c10 model is therefore perhaps disfavored due to this systematic shift. However, we caution that, as many of the observational studies above have noted, there could well exist a substantial population of even-lower-surface-brightness galaxies in nature which would simply not be detected given the present state-of-the-art surface brightness limits [see 294]. The number of dwarfs in the simulation suite is too limited to tell if dSIDM with lower cross-sections are ruled out or are more consistent with the observed sample (in terms of the diversity of the stellar content).

3.4 Galaxy circular velocity profiles

In this section, we will compare the circular velocity profiles of the simulated dwarfs with observations and attempt to derive constraints for dSIDM. First, we will analyze the isolated dwarfs (main “target” halos in simulations). The ideal observational counterparts for the simulated classical dwarfs (m10 galaxies, see Table 2.1) are the observed field dwarfs in the Local Group (with distances to the Milky Way and M31 $d > 300 \text{ kpc}$). These field dwarfs typically have sub-kpc $r_{1/2}$ and $M_* \lesssim 10^7 M_\odot$, which are comparable to the m10 galaxies. The observational counterparts for the simulated bright dwarfs (m11 galaxies) are the LSBs in the Local Universe, usually with $r_{1/2}$ of several kpc and $10^7 M_\odot \lesssim M_* \lesssim 10^9 M_\odot$. In addition to the isolated dwarfs, we will analyze the subhalos (and the satellite galaxies they host) of the

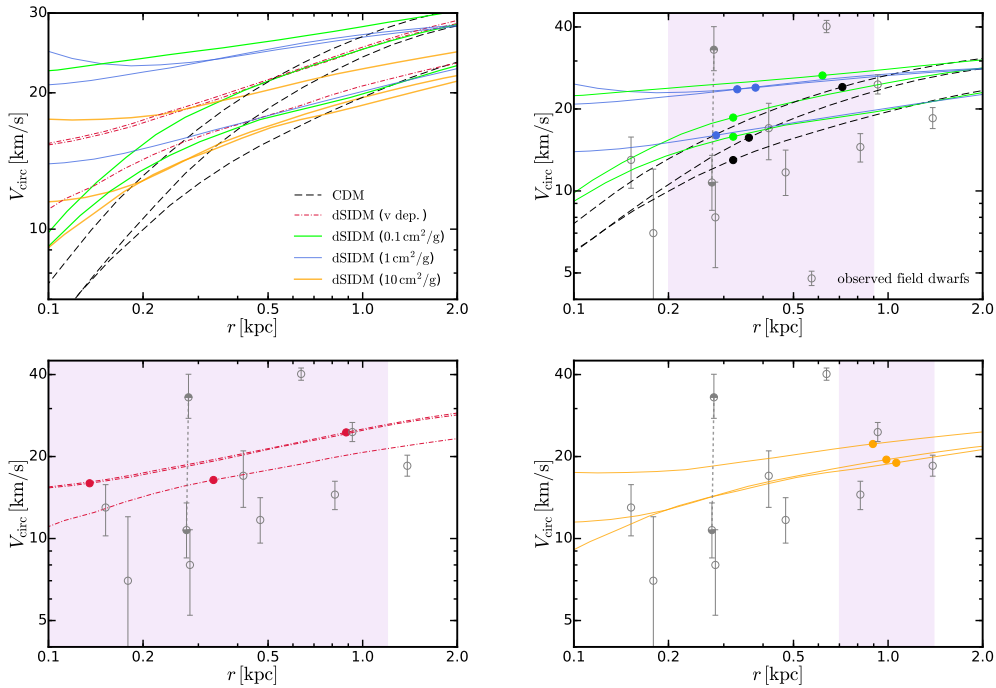


Figure 3.7: **Circular velocity profiles of simulated classical dwarfs compared with the observed field dwarfs in the Local Group.** *Top left:* Circular velocity profiles of the simulated dwarfs in different DM models. The circular velocities are enhanced at the sub-kpc scale in dSIDM models. In the model with $(\sigma/m) = 10 \text{ cm}^2 \text{ g}^{-1}$, the normalization of the circular velocity profile decreases. *Top right:* We compare the results in CDM and dSIDM models with $(\sigma/m) = 0.1/1 \text{ cm}^2 \text{ g}^{-1}$ with the observed field dwarfs in the Local Group (we show two measurements for Tucana, connected by gray line; see text for details). The $r_{1/2}$ of these galaxies are shown by solid circles. We highlight the observed dwarfs of similar sizes to the simulated one ($0.2 \text{ kpc} \lesssim r_{1/2} \lesssim 0.9 \text{ kpc}$) with the purple shaded region. The CDM results are consistent with the majority of the observed dwarfs, but lower compared to the most compact dwarfs (NGC6822 and the older measurement of Tucana). The $(V_{\text{circ}}(r_{1/2}), r_{1/2})$ of these two dSIDM models are still marginally consistent with the observed dwarfs of similar sizes and improve the agreement for compact dwarfs. The circular velocities in the dSIDM models are about two times higher than the observed ones at small radii $r \lesssim 0.2 \text{ kpc}$. *Bottom left:* We show the results of the velocity-dependent dSIDM model and compare them to the observed dwarfs with $0.1 \text{ kpc} \lesssim r_{1/2} \lesssim 1.2 \text{ kpc}$. *Bottom right:* We show the results of the model with $(\sigma/m) = 10 \text{ cm}^2 \text{ g}^{-1}$ and compare them to the observed dwarfs with $0.7 \text{ kpc} \lesssim r_{1/2} \lesssim 1.5 \text{ kpc}$. The results from these two models are also consistent with observations.

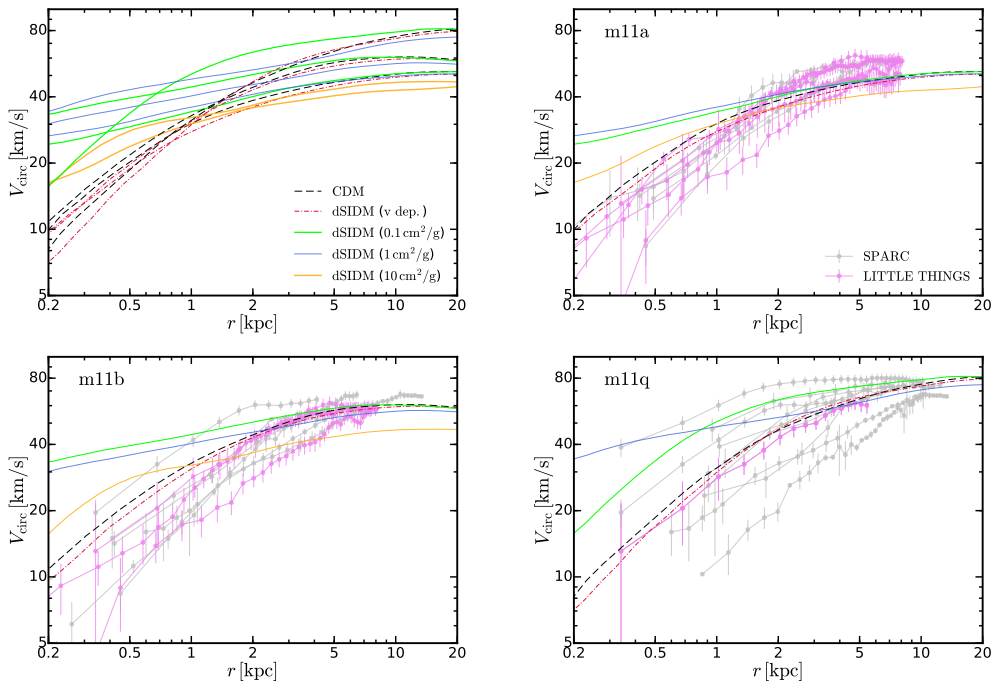


Figure 3.8: **Circular velocity profiles of simulated bright dwarfs compared with observed LSBs in the Local Universe.** *Right:* Circular velocity profiles of the bright dwarf galaxies in simulations. We compare the results with the measured circular velocities of LSBs observed in the field (see Section 3.4 for details of the observed sample and selection criteria). Models with constant σ/m that are consistent with in the classical dwarfs (with low V_c) generally produce too concentrated galaxies at high V_c , but the velocity-dependent model is consistent over the entire range we consider here.

simulated Milky Way-mass hosts (m12 galaxies) and compare them to the observed satellites of the Milky Way and M31.

Observational samples

For satellite galaxies, we adopt the Milky Way and M31 satellites compiled in Garrison-Kimmel et al. [62], which was updated based on the McConnachie [6] compilation. These dwarf galaxies were classified as satellites with their distances to the Milky Way or M31 smaller than 300 kpc (following the criterion adopted in Wetzel et al. [60] and Garrison-Kimmel et al. [62]). For the Milky Way satellites, the dSphs presented in Wolf et al. [293] were included and the implied circular velocity at the three-dimensional (de-projected) half-mass radius, $V_{1/2} = V_{\text{circ}}(r_{1/2})$, has been calculated using their formula based on the average velocity dispersion of stars. In addition, the HI-based circular velocity measurement of the Small Magellanic

Cloud (SMC) from Stanimirović et al. [295] and the proper motion-based circular velocity measurement of the Large Magellanic Cloud (LMC) from van der Marel and Kallivayalil [296] was included. For the satellites of M31, the compilation included the $r_{1/2}$ and $V_{1/2}$ measurements from Tollerud et al. [52]. For the dwarfs in the Local Field (with distances to hosts larger than 300 kpc), the compilation included the $r_{1/2}$, $V_{1/2}$ and $\sigma_{v,*}$ from Kirby et al. [54] where possible, though with modifications to the three galaxies with evidence of rotation [53]. A recent measurement [297] on the field dwarf ‘‘Tucana’’ obtained a much lower dynamical mass of the system than the previous measurements [298, 299], so we update the compilation correspondingly.

For the LSBs, we adopt the HI rotation curves and mass models from the ‘‘Local Irregulars That Trace Luminosity Extremes, The HI Nearby Galaxy Survey’’ [LITTLE THINGS, 41]. The mass modeling results in Oh et al. [41] showed that the selected galaxies have a typical halo mass of $\sim 10^{10-11} M_{\odot}$ and stellar mass of $\sim 10^{7-9} M_{\odot}$, which are in good agreement with the simulated bright dwarfs. In addition, we include the HI/H α rotation curves and mass models from the ‘‘*Spitzer* Photometry and Accurate Rotation Curves’’ [SPARC, 8] project. Given the limited statistics provided by only three simulated bright dwarfs, we will do a case-by-case comparison by selecting observed galaxies based on their maximum circular velocities, effective radii, and inferred stellar masses.

Circular velocity profiles of isolated dwarfs

In the top left panel of Figure 3.7, we show the circular velocity profiles of the simulated classical dwarfs in different DM models. In general, the circular velocities at $r \lesssim 1$ kpc increase in dSIDM models with $0.1 \text{ cm}^2 \text{ g}^{-1} \lesssim (\sigma/m)_{\text{eff}} \lesssim 1 \text{ cm}^2 \text{ g}^{-1}$ ⁵ and the circular velocity profiles are almost flat at the center. For example, the circular velocities at $r \simeq 0.2$ kpc are enhanced by about a factor of two in the dSIDM-c1 model compared to the CDM case. This is a direct consequence of the cuspy central density profiles in dSIDM models, as detailed in Shen et al. [5]. In the dSIDM-c10 model, circular velocity profiles have similar flat shapes but with systematically lower normalizations than the dSIDM-c1 model, which is likely related to the coherent rotation and halo deformation in the strong dissipation limit.

In the other three panels of Figure 3.7, we show specifically the $(V_{1/2}, r_{1/2})$ of the simulated dwarfs and compare them to the circular velocities of 10 observed Local Group field dwarfs (compiled in Section 3.4). For Tucana, both the recent

⁵At the mass scale of classical dwarfs, the effective cross-section $(\sigma/m)_{\text{eff}}$ is about $0.3 \text{ cm}^2 \text{ g}^{-1}$, where $(\sigma/m)_{\text{eff}}$ follows the definition in Shen et al. [5].

measurement [297], which attempts to subtract a potential correction (still somewhat uncertain) for unresolved stellar binaries and an older measurement [298] without such a correction are shown and linked by a gray dashed line in the figure. The circular velocity profiles in CDM are consistent with the bulk of the observed dwarfs, except two dense outliers (Tucana, if we take the older measurement and NGC6822) with $V_{1/2} \sim 30 - 40 \text{ km s}^{-1}$. The dSIDM-c0.1 and dSIDM-c1 models are marginally consistent with observations: the $V_{1/2}$ of some simulated dwarfs are slightly higher than the observed dwarfs of similar $r_{1/2}$ except for NGC6822 (if we adopt the new measurement of Tucana) but the differences at this level are not enough to rule out these models given the limited statistics. For the velocity-dependent dSIDM model, the simulated dwarfs are consistent with the relatively compact observed dwarfs but may be in tension with the six diffuse ones. Again the limited statistics prevent us from drawing any conclusions about the model. For the dSIDM-c10 model, although the circular velocities at small radii appear higher than the observed ones, the $V_{1/2}$ are still consistent with the observed dwarfs with comparable sizes. The potential problem with this model is that the stellar content of all simulated dwarfs is relatively diffuse, and the range of galaxy stellar effective radii may not be diverse enough to match observations. We also note that there is one observed galaxy (NGC6822, or two if the older Tucana measurement is used) lying above the circular velocity profiles of any simulated galaxies regardless of the DM model employed. Even the model with the highest degree of dissipation used here cannot produce analogs of these compact systems. If the discrepancy is real (not the result of e.g. unresolved binaries or other sources of dispersion), the physical origin of these systems in the field is still a challenge to existing cosmological simulations [e.g., 60–62, 108, 109].

In the top left panel of Figure 3.8, we show the circular velocity profiles of the simulated bright dwarf galaxies in different DM models. Circular velocities in the dSIDM-c0.1 and dSIDM-c1 models are enhanced to about $30 - 40 \text{ km s}^{-1}$ at $r \lesssim 1 \text{ kpc}$. The circular velocity profiles in the dSIDM-c10 model have similar shapes but lower normalizations. Those in the velocity-dependent dSIDM model are almost indistinguishable from the CDM case, due to the limited effective cross-sections in the bright dwarfs. In the other three panels, we compare the circular velocity profiles of each simulated dwarf with the HI-based measurements from the LITTLE THINGS survey [41] and the SPARC survey [8] as introduced in Section 3.4. For m11a, we select observed galaxies with maximum circular velocities $40 \text{ km s}^{-1} \lesssim V_{\text{circ}}^{\text{max}} \lesssim 60 \text{ km s}^{-1}$ and, for m11b, we select observed galaxies with $50 \text{ km s}^{-1} \lesssim V_{\text{circ}}^{\text{max}} \lesssim 70 \text{ km s}^{-1}$. In addition, for both galaxies, we require the observed sample to have

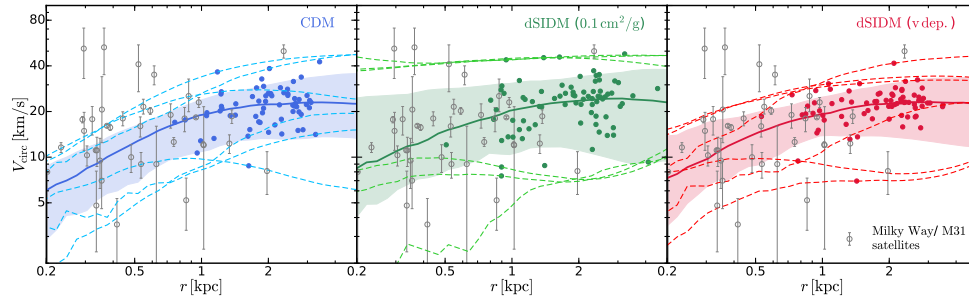


Figure 3.9: Circular velocity profiles of satellite galaxies of simulated Milky Way-mass galaxies and compared with observations. The circular velocity profiles in each DM model are shown in each column respectively. The solid lines and the shaded regions show the median and the 1.5σ scatter (86% of the sample) of the curves. The dashed lines highlight the three circular velocity profiles with the highest (and the three with the lowest) circular velocities at $r = 1$ kpc. Gray circles with error bars show the $(V_{1/2}, r_{1/2})$ of observed Milky Way and M31 satellites compiled in Section 3.4. The $r_{1/2}$'s of simulated satellites are marked by solid circles. The identified subhalos in simulations are selected as satellites if they have galactocentric distance $20 \text{ kpc} < d < 300 \text{ kpc}$, and with at least 200 DM particles and 10 associated stellar particles (equivalently $M_* \geq 10 m_b$). The selected satellites are in the mass range $M_* \sim 10^5 - 10^8 M_\odot$, in concordance with the observed sample. The circular velocity profiles in different models are almost indistinguishable compared to the scatter among the observed satellites, despite the slightly larger median rotation velocities and upper scatter in the dSIDM-c0.1 model. Circular velocity profiles from all three models are consistent with the bulk of the observed dwarfs, although the predicted galaxy sizes are systematically larger. The smallest $r_{1/2}$ reached in the two dSIDM models is smaller than the CDM case, down to about ~ 500 pc. As indicated by the dashed lines, the most compact satellites in the dSIDM-c0.1 model agree better with the observed compact dwarfs in the Local Group, though the stellar content is still puffier compared to observations.

$0.5 \text{ kpc} \lesssim r_{1/2} \lesssim 3 \text{ kpc}$ and $10^7 M_\odot \lesssim M_* \lesssim 10^{8.5} M_\odot$. From these comparisons, we find that the CDM and the velocity-dependent dSIDM model are fully consistent with observations at these mass scales. However, the circular velocities in the dSIDM-c0.1 and dSIDM-c1 models are about two times higher than the observed values at the sub-kpc scale, and the discrepancy appears to be larger than both the observational uncertainties as well as the galaxy-to-galaxy scatter.

For the massive dwarf m11q, we select observed galaxies with $60 \text{ km s}^{-1} \lesssim V_{\text{circ}}^{\text{max}} \lesssim 80 \text{ km s}^{-1}$, $1 \text{ kpc} \lesssim r_{1/2} \lesssim 5 \text{ kpc}$ and $10^8 M_\odot \lesssim M_* \lesssim 10^9 M_\odot$. The CDM and the velocity-dependent dSIDM models are again consistent with the median circular velocity profiles of the observed dwarfs. However, due to the prominent diversity

of the observed circular velocity profiles at the mass scale, the dSIDM-c0.1 and dSIDM-c1 models are still marginally consistent with observations.

In conclusion, the comparisons of the three bright dwarfs with observations appear to disfavor both the constant cross-section dSIDM models with $(\sigma/m) \gtrsim 0.1 \text{ cm}^2 \text{ g}^{-1}$. However, a velocity-dependent model is still viable to produce unique phenomena in lower mass dwarfs while maintaining consistency with the HI-based observations of bright dwarfs.

One important caveat we note is that the measurements here all adopt HI as the kinematic tracer of the gravitational potential. This certainly involves an additional layer of uncertainties in fitting the HI velocity field and asymmetric drift corrections. In addition, the galaxies selected in the observational sample all are chosen to exhibit cold dense gas disks. Most galaxies so selected are morphologically spiral or irregular galaxies, and the observed samples by construction will miss elliptical or spheroidal dwarf galaxies lacking a dense HI disk, which some authors have argued may be more compact than the late-type disk galaxies of similar stellar masses [e.g., 7, 13]. This could potentially bias the comparison here and naively might loosen the constraints on dSIDM models. However, as shown in Figure 3.3, disk-like structures of cold neutral gas are indeed prominent in m11a and m11b and are promoted in dSIDM models. Therefore, compared to the CDM case, galaxies in dSIDM models would be more likely to appear in HI-selected samples in observations but actually match less well with the measured circular velocity profiles of those samples.

Circular velocity profiles of satellites of Milky Way-mass hosts

The comparisons above focus on isolated systems to avoid contamination with environmental effects, but the derived constraints are subjected to galaxy-to-galaxy statistical variations given the limited number of isolated dwarfs in the simulation suite. An alternative way to constrain the dSIDM models is to compare satellite galaxies of more massive hosts to improve the statistics. For this purpose, we analyze the three low-resolution runs of Milky Way-mass hosts (m12i, m12m, and m12f) and a high-resolution run for m12i (details listed in Table 2.1). Their subhalos (as well as the associated stellar content) are identified with the procedure introduced in Section 3.2.

In Figure 3.9, we show the circular velocity profiles of satellite galaxies of simulated Milky Way-mass galaxies (the median curve, the 1.5σ scatter and the three satellites with the maximum/minimum rotation velocities at $r = 1 \text{ kpc}$) and compare them

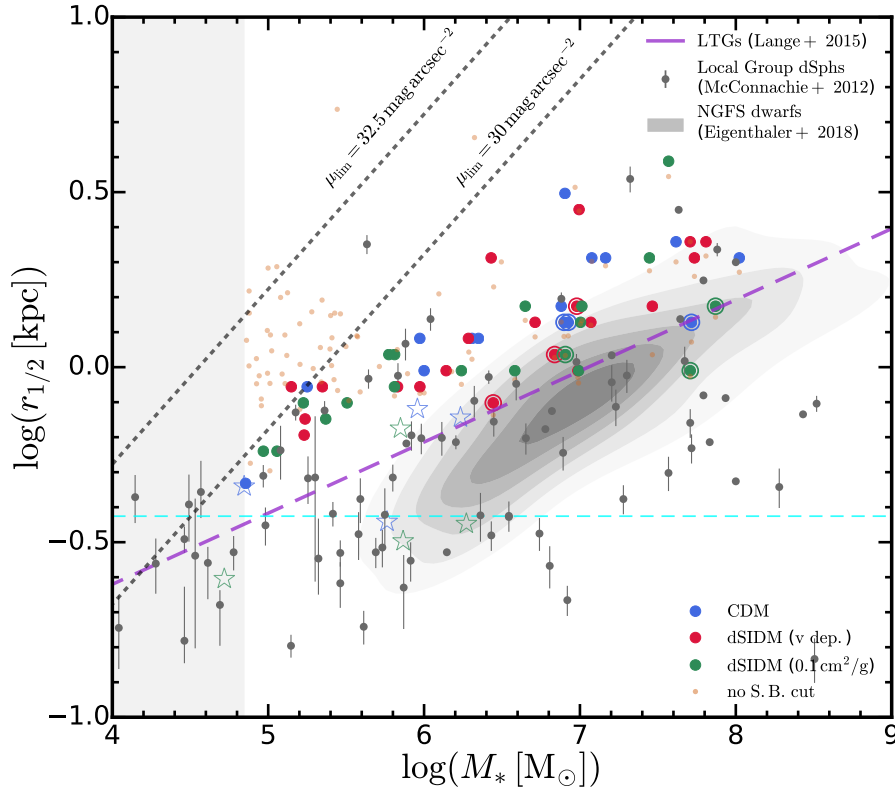


Figure 3.10: Size-mass relation of satellite galaxies. We show the stellar-half-mass-radius versus the stellar mass of satellites of the simulated Milky Way-mass host(s). Only the high-resolution runs are considered here. The satellites from simulations follow the same selection criteria as in Figure 3.9. The solid points show satellite sizes corrected for the surface brightness limit in observations. The black dotted lines indicate the surface brightness limit $30 \text{ mag arcsec}^{-2}$ for the SDSS surveys and the limit with an order of magnitude increasing sensitivity. For reference, the Local Group dwarfs [6] are shown by gray points and the NGFS dwarfs [7] are shown by the gray shaded contours. The purple dashed line is the extrapolation of the size-mass relation of local late-type galaxies [12]. The left shaded region indicates the mass resolution limit of the simulated satellites. The horizontal cyan dashed line indicates radius limit where the enclosed DM particle number is ≤ 200 for a typical satellite central density $\rho_{\text{dm}} \approx 10^{7.5} \text{ M}_{\odot} \text{ kpc}^{-3}$. The markers encircled highlight the three most compact dwarfs (with the highest rotation velocities at $r = 0.5 \text{ kpc}$) in each run. A significant population of low-mass satellites in simulations are not detectable in current observations. For those in the observed regime, no obvious difference is found between CDM and dSIDM models. Massive satellites in dSIDM models are slightly more compact than their CDM counterparts, but they are still systematically puffier than the observed ones. In all the models, the satellites with the most compact DM content (highest circular velocities identified in Figure 3.9) also have the most compact stellar content. However, despite similar stellar masses, they have about three times larger $r_{1/2}$ than the observed compact dwarf elliptical galaxies. For reference, the $(r_{1/2}, M_*)$'s of simulated classical dwarfs (isolated systems) are shown as open stars. With an order-of-magnitude better mass resolution, the isolated dwarfs have slightly more compact stellar content that is in better agreement with the observed samples. This hints the resolution-dependent uncertainties, which will be discussed in Appendix 3.7.

with the observed satellites of the Milky Way and M31 compiled in Garrison-Kimmel et al. [62] as introduced in Section 3.4. For simulations, the identified subhalos are classified as “satellites” if their distance from the center of the Milky Way or M31-analog is $20 \text{ kpc} \leq d \leq 300 \text{ kpc}$. We only keep satellites with DM particle number $N_{\text{dm}} \geq 200$ and associated stellar particle number $N_* \geq 10$, which roughly corresponds to a stellar-mass cut of $M_* \geq 7 \times 10^4$ (5.6×10^5) M_\odot for high-(low-)resolution simulations. For reference, the minimum stellar mass of the observed sample we select is $7.3 \times 10^4 M_\odot$ ($3 \times 10^5 M_\odot$) for M31 (Milky Way). As shown in Figure 3.9, circular velocities in dSIDM models are slightly higher than their CDM counterparts (both the median and upper scatter), but the differences are subdominant compared to the intrinsic scatter of the observed satellites. Despite the fact that the circular velocity profiles in all the models are consistent with the majority of the observed dwarfs, the stellar-half-mass radii are systematically larger than the observed values. This will be discussed in more detail in the comparison of the size-mass relation below. In addition, the CDM and the velocity-dependent dSIDM model fail to produce the most compact dwarf with $r_{1/2} \lesssim 1 \text{ kpc}$ and $V_{1/2} \sim 40 \text{ km s}^{-1}$, which are typically elliptical or irregular galaxies in the M31 subgroup with stellar masses $\gtrsim 10^8 M_\odot$. However, the dSIDM-c0.1 model gives a larger scatter in the rotation velocities at the sub-kpc scale and can produce analogs of those galaxies. But we need to note that the presence of compact satellite analogs in the dSIDM run (while not in CDM) needs further validation with improved statistics of the host systems simulated (at this point, it is difficult to say how significant the result is). It is worth mentioning that the difference is smaller compared to isolated halos. This could be caused by various heating from environmental effects, e.g. evaporation and tidal heating balancing the cooling of DM and suppressing cusp formation [e.g. 300].

The typical mass and size of the satellites studied here are similar to the isolated classical dwarfs studied in Section 3.4. However, the differences between DM models found in these satellites are smaller than what we found for field dwarfs. First, this could be related to additional factors that affect galaxy structure in a group environment, such as dynamical friction, tidal and ram pressure stripping [e.g., 301–306]. But a more plausible explanation would be resolution effects. The Milky Way-mass host simulations are about 30 times poorer in mass resolution (i.e. $m_b = 7000 M_\odot$ for m12i versus $250 M_\odot$ for m10q) than the isolated dwarf simulations. Since the impact of dSIDM typically shows up at very small radii $r \lesssim 500 \text{ pc}$, this could be challenging to resolve in $m_b = 7000 M_\odot$ runs (see the

convergence plots of m_{10q} and m_{10v} in Hopkins et al. 25).

In Figure 3.10, we show the size-mass relation for selected satellite galaxies from simulations and compare them to observations. The Local Group dSphs and the NGFS dwarfs compiled for Figure 3.6 are shown here again for reference. The galaxy size measurements are often affected by the surface brightness detection limit in observations. Following Wheeler et al. [294], this is estimated to be $\mu_V = 30 \text{ mag arcsec}^{-2}$ for SDSS, which corresponds to a physical stellar surface density limit $\Sigma_*^{\text{lim}} = 0.036 M_\odot \text{ pc}^{-2}$ assuming solar absolute magnitude $M_{\odot,V} = 4.83$ and a stellar mass-to-light ratio of $M_*/L \approx 1 M_\odot/L_\odot$. The limit is indicated with the black dotted line in Figure 3.10 when $\Sigma_{1/2} \equiv M_*/\pi r_{1/2}^2 = \Sigma_*^{\text{lim}}$. We also show the surface density limit with an order of magnitude increasing sensitivity at $\mu_V = 32.5 \text{ mag arcsec}^{-2}$ for future surveys. In simulations, a significant population of low-mass satellites has surface brightness close to or below the observational detection limit, the majority of which will not be detected in current surveys. Even the bright ones are potentially affected by the surface brightness cut in size/mass measurements. To correct for this effect, we measure the stellar surface density profile and truncate it where the average enclosed stellar surface density drop below Σ_*^{lim} . The stellar mass is then corrected to the enclosed stellar mass within the cut-off radius and the $r_{1/2}$ is also corrected correspondingly. If the stellar surface density of the satellite is too low to identify the cut-off radius, the satellite is removed from the sample. After this correction, most of the satellites eventually reside in the detectable region on the size-mass plane. However, compared to the observed satellites, they are systematically more diffuse which is consistent with what we found in Figure 3.9. No obvious difference between DM models is found, despite the fact that satellites at the massive end in the dSIDM-c0.1 model are more compact than the CDM counterparts. It is usually the satellites with the most compact DM content (highest circular velocities at the sub-kpc scale) that also exhibit the most compact stellar content. In Figure 3.9, we found that the most compact satellites in the dSIDM-c0.1 model are better counterparts to the observed compact dwarf elliptical galaxies in the Local Group, in terms of their circular velocities. However, in the size-mass plane, it is clear that these satellites found in simulations still do not have compact enough stellar content to match the most compact observed systems. This discrepancy could owe to observational effects (e.g. selection effects making it much easier to identify high-surface-brightness objects or the fact that observations often use the light-weighted, Sersic-estimated profiles rather than the mass-weighted $r_{1/2}$ we measure here), or to the fact that some ‘‘satellites’’ may

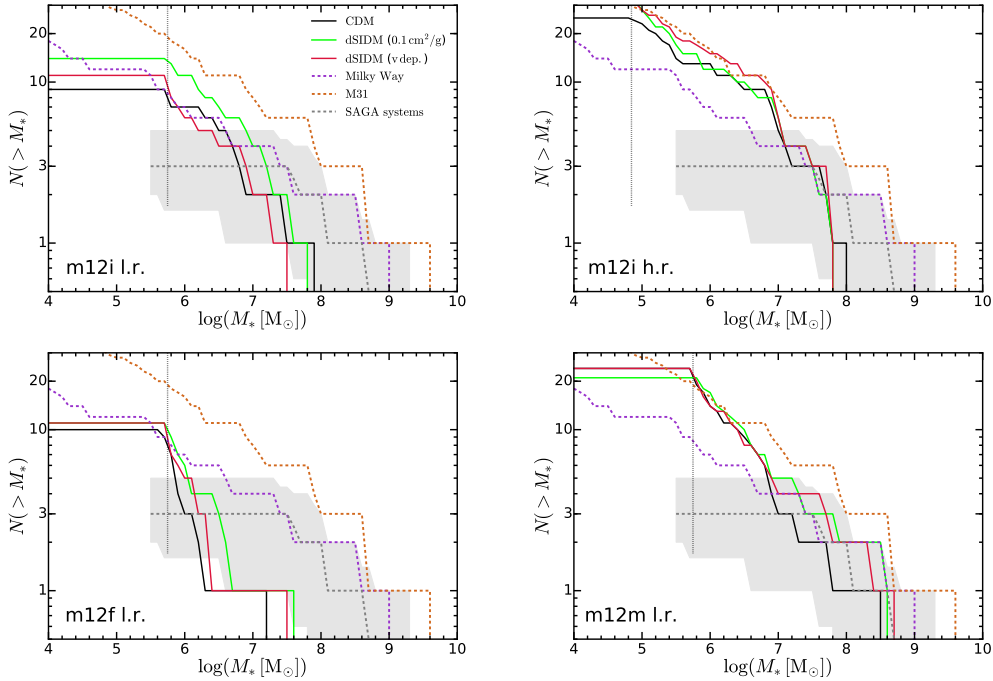


Figure 3.11: **Satellite stellar mass function.** The satellite stellar mass functions of different DM models are shown in solid lines with different colors (as labeled). The purple and orange dashed lines show the satellite stellar mass functions of the Milky Way and M31, respectively. The gray dashed lines with shaded regions show mass function of Milky Way-like systems in the SAGA survey with 1σ scatter. Each panel corresponds to one simulated Milky Way-mass galaxy in the suite. The vertical dotted line indicates the resolution limits of satellite stellar mass (set as 10 times the baryonic mass resolution of the simulation). Strong diversity shows up in the stellar mass function of both observed satellites and the satellites of simulated galaxies. The counts of satellites get enhanced slightly in the dSIDM models, but the differences are still too small compared to the observed scatter to effectively rule out any of the models studied.

have their light profiles dominated by a single, massive/compact star cluster (or even themselves be a star cluster entirely rather than a true dwarf galaxy) as shown in some very high-resolution simulations in Ma et al. [307]. Exploring these possibilities will require more detailed forward modeling in future work. Similar to the point we made above about the circular velocity profiles of satellites, we caution that this discrepancy could also be a resolution effect. Specifically, with about an order-of-magnitude better mass resolution, the simulated isolate dwarfs at a similar mass scale are in better agreement with the observed samples. The potential resolution effects will be discussed in detail in Appendix 3.7.

3.5 Satellite counts

In addition to the internal structure of satellites, the number counts of satellites could also serve as a channel to constrain alternative DM models. For example, the most well-known small-scale issue is the “missing satellite” (MS) problem [46, 308], which states that the DM subhalos around Milky Way-mass hosts in DMO simulations outnumber the observed satellites in the actual Milky Way. The problem has been alleviated by the growing number of observed satellites in the Local Group and more realistic modeling of the baryonic physics in CDM simulations [e.g., 60, 62, 287]. In some cases, the observed satellite statistics and distribution can be used to constrain alternative DM theories. For example, Nadler et al. [309] used observational data from the Dark Energy Survey and Pan-STARRS1 to constrain several alternative DM models that suppress the linear matter power spectrum at small scales. Specifically for SIDM, the properties of satellites can be changed in non-trivial ways. Thermalized cores generated by elastic SIDM can make satellites prone to tidal stripping. Ram pressure stripping resulting from self-interactions between satellite and host halo particles can drive material out of subhalos. The relative importance of ram pressure stripping can also vary as cross-section has velocity dependence. For instance, in Banerjee et al. [310], Nadler et al. [311], the evolution of satellite pre- and post-infall have been systematically studied for the elastic SIDM models with various velocity-dependence. Different types of SIDM can also give rise to very different satellite responses. In Vogelsberger et al. [136], they studied a multi-state SIDM model featuring inelastic (mainly exothermic) interactions and found that this type of interaction suppresses the abundance of substructures in Milky Way-mass halos considerably. In Fischer et al. [312], they studied highly anisotropic DM self-interactions with large scattering rates but low momentum transfer efficiency per scattering. They found larger suppression of satellite abundance in this model compared to the isotropic model. Satellite statistics and evolution in dSIDM have not yet been studied in previous works. In the regime where $t_{\text{diss}} \ll t_{\text{h}}$, dark cusps can develop in dwarf galaxies prior to infall, making them more sustainable against tidal stripping and having higher chances to penetrate deeper in the host halo.

In Figure 3.11, we show the satellite stellar mass functions from simulated Milky Way-mass galaxies and compare them to the observed mass functions of the Milky Way, M31 and 36 Milky Way-like systems from the Exploring Satellites Around Galactic Analogs [SAGA, 313, 314] Survey Stage II ⁶. Each panel corresponds to

⁶We acknowledge potential inconsistency in the selection criteria used between satellites in

one of the simulations of Milky Way-mass galaxies. Following the convention in the previous section, we only select satellites with a stellar mass larger than 10 times the baryonic mass resolution of the simulations. This limit is indicated by the vertical dotted lines. For the observations, the Milky Way and M31 satellites extend to stellar mass below $10^5 M_\odot$. All 36 complete systems in SAGA reach 100% spectroscopic coverage within the primary targeting region for galaxies brighter than $M_r = -15.5$. For galaxies fainter than $M_r = -15.5$, the survey maintains a $\sim 90\%$ spectroscopic coverage down to $M_r = -12.3$, with completeness slightly decreasing towards fainter magnitudes. Using the color-dependent stellar mass estimates in Mao et al. [314] [modified based on 315], the limit $M_r = -12.3$ can be translated to the stellar mass of $M_* \sim 10^{6.4-7}$ assuming the typical color $0.2 \lesssim (g-r)_0 \lesssim 0.7$ of the confirmed satellites. This forms an estimate of the completeness limit of the SAGA surveys. The satellite mass function of simulated galaxies shows significant diversity, with m12m and m12i (h.r.) hosting ~ 10 satellites with $M_* \gtrsim 10^{6.5} M_\odot$ while m12f hosts only one such satellite. This level of diversity is consistent with the scatter in mass functions revealed by the SAGA surveys. Except for m12f, which shows an apparent deficiency of massive satellites, the satellite mass functions of simulated galaxies are generally consistent with observations. There are slight differences between different DM models. The dSIDM models with either constant or velocity-dependent cross-sections do produce slightly more satellites at a given mass than CDM (i.e. slightly more-massive satellites by stellar mass, for a given halo mass, on average). In the case of m12i, the total amount of resolved satellites increases by about 50% in dSIDM-c0.1 compared to CDM. In m12f and m12m, although the total number of resolved satellites does not differ significantly, massive satellites are still systematically more abundant in dSIDM models. This is likely due to suppressed tidal stripping for satellites with dark cusps built prior to infall. However, the difference is subdominant compared to the scatter found in observations and none of the models tested is in tension with observations here.

In Figure 3.12, we show the cumulative number counts of satellites above a given stellar 3-D velocity dispersion, σ_*^{3d} . For satellites in simulations, σ_*^{3d} is measured at $r_{1/2}$, where it is expected to reflect the total dynamical mass [316]. For the observed sample, we convert the observed line-of-sight velocity dispersion to 3-D via $\sigma_*^{3d} = \sqrt{3} \sigma_*^{1d}$ [e.g. 293]. The σ_*^{3d} distributions of m12i (l.r.) and m12f are consistent with the Milky Way and M31 satellites at $\sigma_*^{3d} \lesssim 20 \text{ km s}^{-1}$ until

simulations and the SAGA satellites, which are selected within a line-of-sight aperture and within a line-of-sight velocity cut.

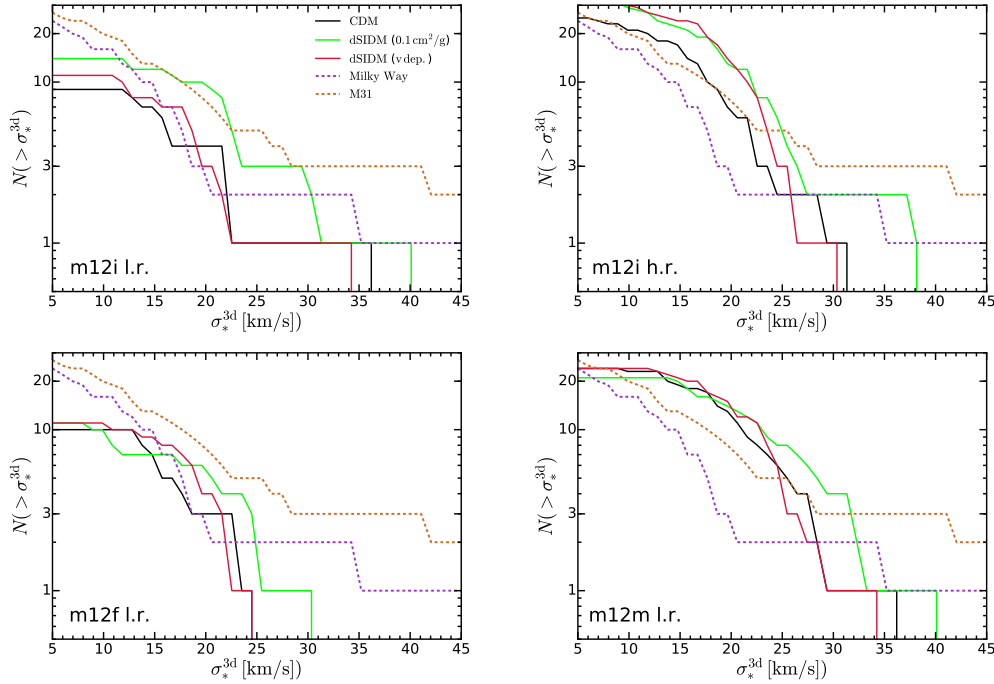


Figure 3.12: **Cumulative count of satellites above a given stellar 3-D velocity dispersion.** The notation is the same as Figure 3.11. Similar to the stellar mass function, we find strong diversity here in both observed and simulated systems. The satellite σ_*^{3d} distributions of m12i (l.r.) and m12f are in good agreement with the Milky Way and M31 samples at $\sigma_*^{3d} \lesssim 20 \text{ km s}^{-1}$ but do not produce enough dynamically hot satellites. On the contrary, in m12i (h.r.) and m12m, the high σ_*^{3d} end is in better agreement with the observed sample, but they tend to overpredict the number of satellites with $\sigma_*^{3d} \lesssim 25 \text{ km s}^{-1}$. In terms of the DM physics tested, the dSIDM models (especially the dSIDM-c0.1 model) predict systematically higher velocity dispersions of satellites.

reaching the resolution limit at low velocities. However, they do not contain as many dynamically hot satellites as the observed sample. In m12i (h.r.) and m12m, satellites exhibit systematically higher velocity dispersions (or equivalently more satellites above a given σ_*^{3d}) than m12i (l.r.) and m12f, and match better the high σ_*^{3d} end of the observed sample. But they tend to overpredict the number of satellites with $\sigma_*^{3d} \lesssim 25 \text{ km s}^{-1}$. The dSIDM models, especially the dSIDM-c0.1 model, produce more dynamically hot satellites in all the four Milky Way-mass galaxies simulated. This is likely caused by larger dynamical masses of the satellites at $r_{1/2}$ on average and also a few compact outliers in dSIDM-c0.1 as shown in Figure 3.9. Although the comparisons here do not necessarily imply a particular model is favored or in tension with observations (given limited statistics of the host systems studied), it

points to an interesting channel to study dissipative DM models.

In addition to the number count, the spatial distribution of satellites is also crucial in understanding the evolution of substructures in the Local Group environment. In particular, astrometric measurements have revealed that most of the Milky Way satellites orbit coherently within a spatially thin plane [e.g., 317–319] affirmed by the recent *Gaia* measurements [320, 321]. The mass and spatial distribution of satellites have been studied using FIRE-2 simulations [287, 322] in Λ CDM. The dSIDM counterpart would be particularly interesting to explore since dissipation promotes coherent dark rotation and triggers halo deformation as found in Shen et al. 5. This aspect along with the physical evolution of subhalos in dSIDM will be investigated in future works.

3.6 Summary of the chapter

This chapter is the second in a series studying galaxy formation in dissipative self-interacting DM. In Shen et al. [5], a suite of cosmological hydrodynamical zoom-in simulations of galaxies with dSIDM was introduced. As the starting point to study structure formation in dissipative DM, a simplified empirical model featuring a constant fractional energy dissipation was chosen, motivated by interactions of DM composites (for example, confined particles in a non-Abelian hidden sector or large stable bound states (dark “nuggets”) of asymmetric DM). Several interesting phenomena and physics on the DM side, related to dSIDM, were identified in Shen et al. [5].

In this chapter, we attempt to compare predictions to basic galaxy observables affected by the underlying structural changes of DM halos induced by dissipative interactions. The stellar morphology, the size-mass relation and the circular velocity profiles of both field and satellite dwarf galaxies are studied, and first constraints on the dSIDM model are obtained through comparisons with observations of local dwarf galaxies.

We first study the observed morphology of the stellar component and quantitatively the size-mass relation of isolated dwarf galaxies. With moderate but not negligible interaction cross-sections ($(\sigma/m) \sim 1 \text{ cm}^2 \text{ g}^{-1}$), dSIDM makes the stellar content more concentrated and promotes the formation of thin stellar disks as well as neutral gas disks in massive bright dwarfs. The simulated galaxies in these models are still consistent with observations in the plane of the galaxy size-mass relation. However, perhaps surprisingly, when the cross-section becomes large enough

($\sigma/m \sim 10 \text{ cm}^2 \text{ g}^{-1}$), the stellar content of simulated dwarfs becomes fluffier even than the CDM case, owing to rotation and other emergent properties of the DM cusp. The dwarfs in this model lie systematically at the most diffuse observed end of the size-mass relation and thus this model faces strong constraints.

In terms of the circular velocity profiles of simulated dwarfs, we separately consider the isolated classical and bright dwarfs in the suite as well as the satellites in the simulations of Milky Way-mass galaxies. The isolated classical dwarfs are compared to the field dwarf galaxies in the Local Group and we find all of the dSIDM models studied survive this comparison. The isolated bright dwarfs are compared to the LSBs with HI-based circular velocity measurements. We find that the dSIDM models with $(\sigma/m) \gtrsim 0.1 \text{ cm}^2 \text{ g}^{-1}$ are in tension with observations and the velocity-dependent model is favored. The satellites in simulated Milky Way-mass galaxies are compared to the Local Group satellites. Though we find little differences in the median and scatter of the circular velocity profiles between DM models, dSIDM models with $(\sigma/m) = 0.1 \text{ cm}^2 \text{ g}^{-1}$ produce outliers that agree better with the compact elliptical satellites in observations, whose analogs are missing in CDM. Although the circular velocity profiles of satellites in simulations are consistent with the observationally inferred velocity dispersions of these systems, the size of the simulated satellites are systematically larger. However, this is potentially subjected to selection bias in observations and also could be a resolution effect. Further high-resolution simulations are required to resolve the central kinematic structure of satellites to give more robust predictions. Meanwhile, the stellar mass function and velocity dispersion function of satellites are studied. In dSIDM models, the number count of satellite galaxies is slightly enhanced and the satellites are dynamically hotter, but the difference is too small to infer valid constraints on the models.

In conclusion, it is at the mass scale of isolated bright dwarfs that the dSIDM models with constant cross-sections face the most stringent constraint and models with $(\sigma/m) \gtrsim 0.1 \text{ cm}^2 \text{ g}^{-1}$ are in tension with HI-based circular velocity measurements. The constraint is much weaker in lower-mass isolated dwarfs or in satellites of Milky Way-mass hosts. Since as shown in Shen et al. [5] the dSIDM-related phenomena strictly depend on the dissipation time scale, which is inversely proportional to the product of f_{diss} and (σ/m) , the constraints derive here can be translated to other f_{diss} values giving the combined constraints: $f_{\text{diss}} (\sigma/m) \lesssim 0.075 \text{ cm}^2 \text{ g}^{-1}$. The constraints here should be treated with caution since we are limited by the number of simulated isolated halos at each representative mass scale. In addition, the systemat-

ical uncertainties in interpreting rotation curve measurements in observations [e.g. 323] and the potential bias of HI-selected galaxies are still open questions in the field. In future work, it would be helpful to improve the robustness of the constraints here with better statistics of simulations (simulating a greater variety and unbiased sample of dwarf galaxies). Meanwhile, the improved resolution would help to resolve the central structure of satellite galaxies, and in particular to investigate the implication of dSIDM in explaining the diversity of dwarf compactness in the Local Group.

3.7 Resolution dependence of satellite properties

The analysis above utilizes both low and high-resolution Milky Way-mass galaxies in the simulation suite. However, the satellite structure could be resolution-dependent. This can arise from two primary causes: (1) the N-body relaxation of collisionless particles and (2) the artificial burstiness of the star formation history due to limited mass resolution (discreteness effects). Both can puff up the DM and the stellar content of low-mass galaxies artificially. For example, in Fitts et al. [115], the test on the isolated classical dwarf m10b has shown that the $r_{1/2}$ shrinks by about a factor of two (despite minimal changes of the overall halo properties) when increasing the mass resolution from $m_b = 4000 M_\odot$ to $m_b = 62.5 M_\odot$. Similar resolution effects manifested in the comparison of the observed ultra-faint dwarfs with high-resolution dwarf simulations in Wheeler et al. [294].

In Figure 3.13, we compare the satellite circular velocity profiles from the high and low-resolution simulations of m12i (listed in Table 2.1). Aside from the median and scatter of circular velocity profiles, we also show the $(V_{1/2}, r_{1/2})$ of these satellites. The median circular velocity profile is converged and the 1.5σ (7% to 93% inclusion) contour moves up slightly. This indicates that the underlying DM structure of these satellites is converged at the resolution level. However, the $r_{1/2}$'s are systematically smaller in the high-resolution run and the factor of by which they change is consistent with the enhancement in spatial resolution (two times higher spatial resolution and eight times better mass resolution). Even in the high-resolution run (the mass resolution of which is still at least an order of magnitude poorer than that of isolated dwarf galaxy simulations), the stellar content of satellites can only be resolved to about 1 kpc scale, and so the simulated small satellites are more extended than the observed satellites.

In Figure 3.14, we show the size-mass relations of satellites from the high- and

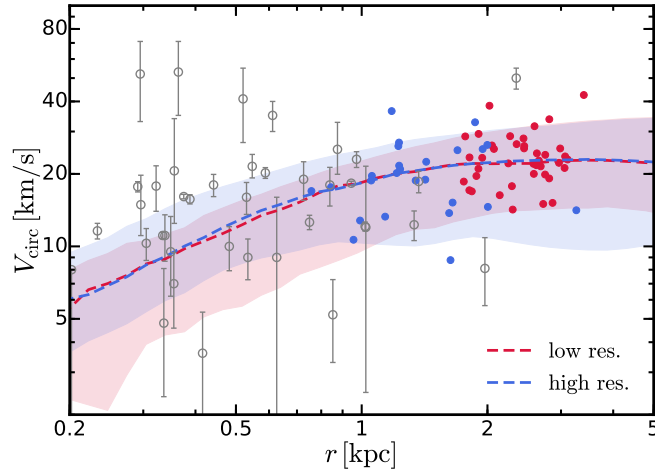


Figure 3.13: We compare satellite circular velocity profiles from the high and low-resolution simulations of m12i. The notation follows the top panel. Although the median circular velocity profile and the scatter do not differ appreciably between high and low-resolution simulations, the $r_{1/2}$'s of satellites in simulations are systematically smaller in the high-resolution simulation. Compared to the observed dwarfs, even the high-resolution simulation produces fluffier stellar content for these satellites.

low-resolution simulations. The satellite stellar mass and size have been corrected for the surface brightness cut-off at $\mu_V = 30 \text{ mag arcsec}^{-2}$. The satellite sizes in the low-resolution runs are systematically higher than the high-resolution ones. The horizontal lines indicate the radius enclosing 200 DM particles assuming the typical satellite central density $\rho_{\text{dm}} = 10^{7.5} \text{ M}_{\odot} \text{ kpc}^{-3}$. The number 200 is suggested in Hopkins et al. [25] as the convergence criterion in DM properties for FIRE-2 simulations. This limit roughly gives the minimum $r_{1/2}$ that the simulation can resolve. Certainly, we cannot conclude that the satellite sizes are fully resolved even in the high-resolution runs, and it is likely that increasing the resolution will give better agreement with the observed satellites. This is supported by that the simulated isolated dwarfs in the mass range $10^5 - 10^6 \text{ M}_{\odot}$ (with baryonic mass resolution $\sim 250 - 500 \text{ M}_{\odot}$) agree well with the observations on the size-mass plane as shown in Figure 3.6 and Figure 3.10. The impact of resolution on satellite properties of Milky Way-mass hosts will be explored more in the upcoming Triple *Latte* simulations (with baryonic mass resolution $\sim 880 \text{ M}_{\odot}$) (Wetzel et al. in prep).

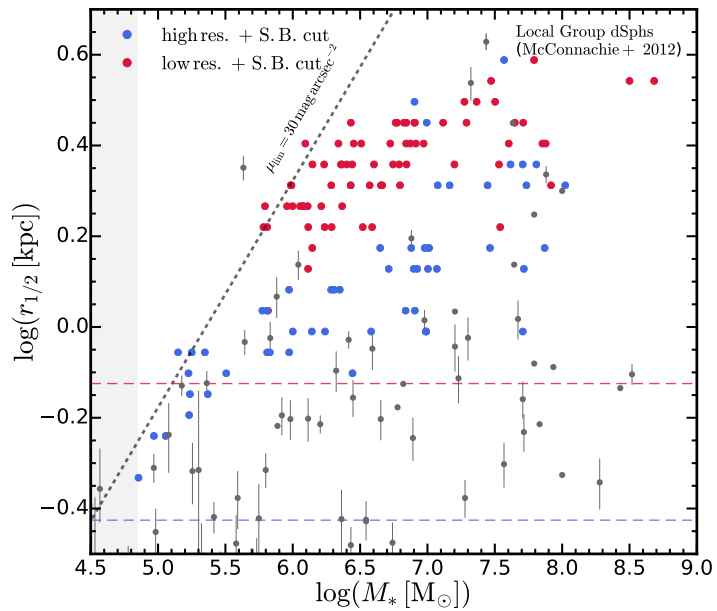


Figure 3.14: We compare the high- and low-resolution simulations on the plane of the size-mass relation. They are all corrected for the surface brightness limit at $\mu_V = 30 \text{ mag arcsec}^{-2}$. The horizontal lines indicate the radius enclosing 200 DM particles assuming the typical satellite central density $\rho_{\text{dm}} = 10^{7.5} \text{ M}_{\odot} \text{ kpc}^{-3}$. Satellites in the low-resolution simulations are systematically more diffuse than their high-resolution counterparts. The resolution dependence could explain the discrepancy between the simulations with observations in this plane.

Chapter 4

DISSIPATIVE DM – SMBH SEEDING

Huangyu Xiao, Xuejian Shen, Philip F. Hopkins, and Kathryn M. Zurek. SMBH seeds from dissipative dark matter. *J. Cosmol. Astropart. Phys.*, 2021(7):039, July 2021. doi: 10.1088/1475-7516/2021/07/039.

4.1 Abstract of the chapter

The existence of SMBHs with masses greater than $\sim 10^9 M_\odot$ at high redshift ($z \gtrsim 7$) is difficult to accommodate in standard astrophysical scenarios. We study the possibility that (nearly) totally dissipative self-interacting dark matter (tdSIDM)—in rare, high-density dark matter fluctuations in the early Universe—produces SMBH seeds through catastrophic collapse. We use a semi-analytic model, tested and calibrated by a series of N-body simulations of isolated dark matter halos, to compute the collapse criteria and timescale of tdSIDM halos, where dark matter loses nearly all of its kinetic energy in a single collision in the center-of-momentum frame. Applying this model to halo merger trees, we empirically assign SMBH seeds to halos and trace the formation and evolution history of SMBHs. We make predictions for the quasar luminosity function, the $M_{\text{BH}}-\sigma_v^*$ relation, and cosmic SMBH mass density at high redshift and compare them to observations. We find that a dissipative dark matter interaction cross-section of $\sigma/m \sim 0.05 \text{ cm}^2 \text{ g}^{-1}$ is sufficient to produce the SMBHs observed in the early Universe while remaining consistent with ordinary SMBHs in the late Universe.

This chapter is organized as follows. In Sec. 4.2, we discuss our semi-analytical model of the dissipation timescale and calibrate it with a series of N-body simulations in isolated NFW halos. In Sec. 4.3, we generate the merger trees of halos and track the cosmological evolution of SMBH seeds in those halo progenitors, allowing us to compute the mass function of SMBHs and compare it with observables. In Sec. 4.4, we show our tdSIDM model will not cause the formation of overly massive SMBHs at low redshift, remaining consistent with low redshift observations.

4.2 Simulating black hole formation in isolated halos

We performed N-body simulations of DM halos with the NFW density profile as the initial condition, using the code GIZMO [324]. The initial condition is generated

using the code `pyICs` which was first used in [325]. 15 N-body simulations are performed for 15 different NFW halos with a mass range $\sim 10^9 - 10^{13} M_\odot$ which are completely isolated in each simulation box. There are 6×10^6 particles in each simulation box and the gravitational softening length is taken to be $2d_0$ where d_0 is the particle mean separation within $0.07r_s$ at the beginning of the simulation. r_s is the scale radius of different NFW halos and $0.07r_s$, as we will show later, is the universal collapsed radius. `GIZMO` is a multi-method gravity plus hydrodynamics code and is capable of simulating both gas and dissipative DM. Baryonic simulations are much more computationally expensive, however, and the formation of SMBH seeds in our model is mainly driven by the dissipation in the dark sector. Therefore, we run DMO simulations to study the formation of SMBH seeds from the catastrophic collapse of halos. The gravity of DM is solved with an improved version of the Tree-PM solver from `GADGET-3` [284]. DM self-interactions are simulated in a Monte-Carlo fashion with the implementation in [88]. In the tdSIDM model, when two DM particles collide with each other, they lose a fraction f of their kinetic energy in the center-of-momentum frame. We focus on the case that nearly all the kinetic energy is dissipated in the interaction, $f \approx 1$. This is a particular feature of the nugget fusion model presented in Refs. [213–217], not shared in general by other dissipative DM models.

As explained in the introduction, we are interested in SMBH seed formation in massive, rare halos in the mass range $10^9 - 10^{13} M_\odot$, which can produce SMBH seeds in the mass range $10^6 - 10^{10} M_\odot$ (if the SMBH-to-halo mass ratio is about 10^{-3} as we will show later in the simulation results). In order to sample such rare structures in cosmological simulations, a comoving boxsize of order Gpc^3 is required. Meanwhile, the physical size of the collapsed region is about $0.07r_s$, as we will show later in the simulation results, where r_s is the scale radius. This poses a challenge to cosmological simulations due to limitations on mass and spatial resolution. For example, if we are interested in SMBH formation in a rare DM halo at high redshift with mass $10^{12} M_\odot$, the particle number in the central region within $0.07r_s$ has to be larger than ~ 200 [26] to resolve the dense core. Assuming the virial radius is $4r_s$, the particle number in this halo is $\sim 2 \times 10^4$, which requires a mass resolution of $5 \times 10^7 M_\odot$ in the simulation box. However, we need a boxsize of $\gtrsim \text{Gpc}^3$ to simulate the structure formation from extremely rare fluctuations. Therefore, the particle number in the simulation box has to be $\sim 10^{12}$, which is at least 100 times larger than the particle number $\lesssim 10^{10}$ in state-of-the-art cosmological simulations (e.g. [25, 326–328]). Therefore, it is very challenging to simulate the formation of

SMBH seeds with cosmological simulations, even employing a zoom-in technique. An alternative strategy is to simulate individual isolated halos with various halo parameters and test the formation of SMBH seeds separately. Large-scale structure with moderate DM self-interactions will not differ significantly from the CDM case [e.g., 87, 88, 329, 330]. The calibration from the isolated halo simulations can then be used to study the cosmological population of SMBHs with semi-analytic approaches.

Semi-Analytic Model

Before introducing simulations, it is useful to develop an analytic model that can predict the collapse timescale of the dissipative DM model. The analytic predictions can then be compared to and calibrated by the simulation results. In this section, we will discuss the analytic model that predicts the collapse timescale and show that it agrees well with our simulation results after calibrating the result by a universal $\mathcal{O}(1)$ prefactor in the formula. We focus on SMBH seed formation in rare, massive halos at high redshift with high central DM density and thus high dissipative DM self-interaction rates, following Ref. [213]. DM halos formed from rare fluctuations are the ideal environments for seeding SMBHs, as such halos form at higher redshift relative to typical halos, where the background density of the universe is larger, implying a higher halo central density. The collapse rate of tdSIDM halos is characterized by $\rho v \sigma / m$, where ρ is the average density, v is the velocity dispersion, and σ is the cross-section of DM self-interaction. Thus higher densities shorten the dissipation timescale, as we will discuss in detail in Eq. (4.14). We will take the average density and velocity dispersion to be those in the collapsing central region of the halo, characterized by a collapse radius r_0 determined by our N-body simulations.

Because of our reliance on high-density DM fluctuations to seed SMBHs, we must quantify the rareness of halos, which can be explicitly defined through the variance of density fluctuation

$$\sigma_h(M, z) = \nu_h \sigma_0(M, z), \quad (4.1)$$

where $\sigma_0(M, z)$ is the variance in the density fluctuation field smoothed over a top-hat filter of scale $R_s = (3M/4\pi\bar{\rho})^{1/3}$, $\bar{\rho}$ is the average comoving background density and $\sigma_h(M, z)$ is the variance of a local density fluctuation that can differ from the average fluctuation. Clearly ν_h defines the rareness of the fluctuation and the halo that just formed from this fluctuation. One can also define the peak height

ν

$$\nu(M, z) \equiv \frac{\delta_c}{\sigma_0(M, z)} = \frac{\delta_c}{\sigma_0(M, z=0) D(z)}, \quad (4.2)$$

where $\delta_c = 1.686$ is the critical overdensity for collapsed halos derived from the spherical top-hat model and $D(z)$ is the growth factor normalized to unity at $z = 0$. In the spherical collapse model, a halo forms when the variance in the density fluctuation field satisfies $\sigma = \delta_c$, corresponding to when typical halos with $\nu = 1$ collapse. However, rare, high-variance halos may collapse earlier than typical halos, when $\nu = \nu_h$. In what follows, $5 - \sigma$ ($3 - \sigma$) halos are defined by $\nu(M, z) = 5$ ($\nu(M, z) = 3$) at $z = z_f$, where z_f is determined by when a density perturbation reaches $\sigma(M, z_f) = \delta_c$. Note that different halos with different peak heights ν may collapse at the same redshift, though rare fluctuations correspond to more massive halos.

We use the model of [331], which is a modification of the Bullock model [332], to define the halo parameters such as characteristic density ρ_0 , halo concentration c_{vir} and halo mass M_{vir} and their evolution with redshift. The density profile of virialized DM halos is well described by the Navarro–Frenk–White profile [333]

$$\rho(r) = \frac{\rho_0}{\frac{r}{r_s} \left(1 + \frac{r}{r_s}\right)^2}, \quad (4.3)$$

where ρ_0 is the scale density of the halo and r_s is the scale radius. ρ_0 characterizes the central density of a DM halo. As is typical in a halo formation model, we can link the central density of a halo formed at redshift z_f to that of the critical density of the universe at z_f . Therefore we define the mass of the halo at the formation redshift z_f via

$$M_f = \frac{4}{3} \pi c_0^3 r_s^3 \Delta(z_f) \rho_{\text{crit}}(z_f), \quad (4.4)$$

where c_0 is the halo concentration at the formation time, $\rho_{\text{crit}}(z)$ is the critical density of the universe at redshift z , and $\Delta(z)$ is the overdensity of the halo with respect to the critical density. One common choice is to set $\Delta(z_f) = 200$, which is motivated by the spherical collapse model. The only dependence on cosmology in this mass definition comes from $\rho_{\text{crit}}(z)$. It has been universally found that the initial halo concentration at the moment of the first collapse satisfies $c_0 \approx 4$ [334]. Therefore the halo central density is $\rho_0 \approx 200 c_0^3 \rho_{\text{crit}}(z_f)$, suggesting that a halo formed at high z_f has a large central density. The scale radius r_s is determined at the time of formation and does not evolve with time

$$r_s = \left(\frac{3M_f}{4\pi c_0^3 \Delta(z_f) \rho_{\text{crit}}(z_f)} \right)^{1/3}. \quad (4.5)$$

The NFW profile is truncated at a virial radius that depends on redshift, which is defined as $R_{\text{vir}}(z) \equiv c_{\text{vir}}(z)r_s$, where $c_{\text{vir}}(z)$ is a redshift dependent concentration number. As the universe expands, the background density drops but the halo central density ρ_s should remain the same, leading to a larger concentration number and a larger virial radius. Therefore the mass within the virial radius for an NFW profile should grow (logarithmically) as the universe evolves, which can be represented as

$$M_{\text{vir}}(z) = 4\pi\rho_0r_s^3f(c_{\text{vir}}(z)) = M_f\frac{f(c_{\text{vir}}(z))}{f(c_0)}, \quad (4.6)$$

where $f(c) = \ln(1+c) - c/(c+1)$. This equation is obtained by integrating the NFW profile truncated at the virial radius. The redshift dependence of the halo concentration is thus defined by

$$\frac{c_{\text{vir}}(z)^3}{f(c_{\text{vir}}(z))} = \frac{c_0^3}{f(c_0)} \frac{\Delta(z_f)\rho_{\text{col}}(z_f)}{\Delta(z)\rho_{\text{crit}}(z)}, \quad (4.7)$$

such that we see that $c_{\text{vir}}(z) \propto 1+z$ in the limit of large concentration parameters and $\Delta(z) = \Delta(z_f)$. Equivalently, we have a generalized form of Eq. (4.4)

$$M_{\text{vir}}(z) = \frac{4}{3}\pi c_{\text{vir}}(z)^3 r_s^3 \Delta(z)\rho_{\text{crit}}(z), \quad (4.8)$$

where we assume $\Delta(z) = \Delta(z_f)$. From these relations, one finds the characteristic density of DM halos

$$\rho_0 = \frac{M_{\text{vir}}(z)}{4\pi r_s^3(z)f(c_{\text{vir}}(z))} = \frac{c_0^3}{3f(c_0)}\Delta(z_f)\rho_{\text{crit}}(z_f). \quad (4.9)$$

This expression clearly states that the halo central density is directly determined by the background density of the universe at the redshift of formation. The invariance of ρ_0 and r_s indicates that the inner profiles of DM halos do not change over time. The boundary of a halo, described by R_{vir} , must move outwards owing to the decreasing background density $\rho_{\text{crit}}(z)$, which is known as the ‘‘pseudo-growth’’ of DM halos [335].

Now that we know how to determine the halo parameters from the halo mass and concentration number at the observation redshift, we can further study the behavior of halos that are made of dissipative self-interacting DM at high redshift. DM particles dissipate their kinetic energy through self-interactions (referred to as ‘‘collisions’’). The average timescale for a particle to encounter one such collision in radius r can be estimated as

$$t_{\text{relax}}(r) = \frac{1}{\alpha\rho(r)\sigma_v(r)} \frac{1}{\sigma/m}, \quad (4.10)$$

where $\rho(r)$ and $\sigma_v(r)$ are the DM mass density and one-dimensional velocity dispersion at radius r , $\alpha = \sqrt{16/\pi}$ is a constant factor assuming hard-sphere-like scattering and a Maxwell-Boltzmann velocity distribution and σ/m is the dissipative interaction cross-section per particle mass. If the velocity field of DM is isotropic (as found in [251–253]), $\sigma_v(r)$ can be obtained by solving the spherical Jeans equation [336]

$$\begin{aligned}\sigma_v(r) &= \sqrt{4\pi G \rho_0 r_s^2 F(r/r_s)}, \\ F(x) &= \frac{1}{2}x(1+x)^2 \left[\pi^2 - \ln(x) - \frac{1}{x} \right. \\ &\quad \left. - \frac{1}{(1+x)^2} - \frac{6}{1+x} + \left(1 + \frac{1}{x^2} - \frac{4}{x} - \frac{2}{1+x} \right) \right. \\ &\quad \left. \times \ln(1+x) + 3 \ln^2(1+x) - 2\text{Li}_2(-x) \right],\end{aligned}\quad (4.11)$$

where $\text{Li}_2(x)$ is the dilogarithm. The timescale for local kinetic energy to dissipate through such collisions is

$$\begin{aligned}t_{\text{diss}}(r) &= \frac{3\rho(r)\sigma_v^2/2}{Cf\rho^2(r)\sigma_v^3(r)} \frac{1}{\sigma/m} \\ &= \frac{1}{\beta f\rho(r)\sigma_v(r)} \frac{1}{\sigma/m},\end{aligned}\quad (4.12)$$

where f is the fraction of kinetic energy loss in the center-of-mass frame per collision, C is a constant factor and $\beta = 4\alpha/3$ [5], assuming a Maxwell-Boltzmann velocity distribution, a velocity independent cross-section and all the kinetic energy in the center-of-momentum frame is dissipated during a collision.

Rapid kinetic (thermal) energy dissipation will inevitably result in the gravitational collapse of the central halo. The collapse timescale should be on the same order as the dissipation time, $t_{\text{col}} = At_{\text{diss}}$, where the order one factor A is determined by our simulations of isolated halos. Collapse is expected to happen at radii where $t_{\text{col}}(r) \ll t_{\text{life}}$, where t_{life} is the lifetime of the system. It is hard to determine the collapse radius analytically, but our N-body simulations can give us the desired information. The details of our simulation results shall be discussed in the next subsection but we can briefly describe the findings. We run a series of dark-matter-only simulations for isolated NFW halos to study the evolution of their density profiles. We show the final stage of the cumulative mass profile $M(r)/M$ in Fig. 4.1, where $M(r)/M$ is roughly a constant in the central region, indicating the formation of SMBHs. We studied the collapse of DM halos with different masses, all of which formed an SMBH with mass $\sim 3 \times 10^{-3}M$, where M is the halo mass. If an NFW

halo within some radius r_0 collapses to an SMBH seed, the fraction of the initial mass in the seed is

$$f_{\text{col}} = \frac{\ln(1 + r_0/r_s) - r_0/(r_s + r_0)}{\ln(1 + c) - c/(c + 1)}. \quad (4.13)$$

Furthermore, if we take a collapse radius $r_0 = 0.07r_s$ and a concentration $c = c_0 = 4$ at formation time, this equation gives a collapse fraction $f_{\text{col}} \approx 3 \times 10^{-3}$. Note that $c_0 = 4$ is a universal prediction for halos at formation [337], independent of their rarity ν . A higher ν halo, of a given mass, will simply form at a higher redshift z_f relative to typical halos and hence will have a higher concentration at lower redshift z , according to Eq. (4.7). A large central density, as shown in Eq. (4.12), corresponds to a smaller dissipation time.

As we will discuss in the next subsection, the simulation results, as shown in Fig. 4.1, indicate that the collapse fraction of tdSIDM halos is universally 3×10^{-3} independent of halo mass and redshift. Therefore, we conclude that the collapse radius (the radius where DM particles will fall into the halo center and collapse) is about $0.07r_s$ independent of halo mass and redshift, corresponding to a collapse fraction of 3×10^{-3} . In Appendix 4.9, we further confirm that the collapse fraction is independent of the cross-section and provide a theoretical explanation for the universality of the collapse fraction. We thus evaluate the collapse time within a collapse radius $0.07r_s$, which gives the timescale of SMBH formation at the halo center. The corresponding collapse timescale $t_{\text{col}}(0.07r_s)$ is

$$t_{\text{col}} = \frac{A}{f} 1.29 \times 10^{11} \text{yr} \left(c_{\text{vir}}(z)^3 \frac{\Delta(z)}{200} \frac{\rho_{\text{crit}}(z)}{\Omega_m \rho_{\text{crit}}(0)} \right)^{-7/6} \times [f(c_{\text{vir}}(z))]^{3/2} \left(\frac{1 \text{ cm}^2 \text{ g}^{-1}}{\sigma/m} \right) \left(\frac{10^{15} M_{\odot}}{M_{\text{vir}}} \right)^{1/3}, \quad (4.14)$$

where Ω_m is the matter density today.

Simulations of halo collapse and black hole formation

We ran a series of DMO simulations with different initial conditions to calibrate the collapse timescale and determine the SMBH-to-halo mass ratio. The initial conditions are characterized by the NFW profile parameters ρ_0 and r_s , which can be determined by the concentration number c_{vir} , halo mass M_{vir} and the observation redshift z by using Eq. (4.9) and Eq. (4.5). We simulate the evolution of $5 - \sigma$ and $3 - \sigma$ rare halos whose mass can be determined from $\nu = 5, 3$. The concentration of those halos can be determined from the models that give the relation between halo mass M and peak height ν [337–340], though for large ν , the halo concentration is

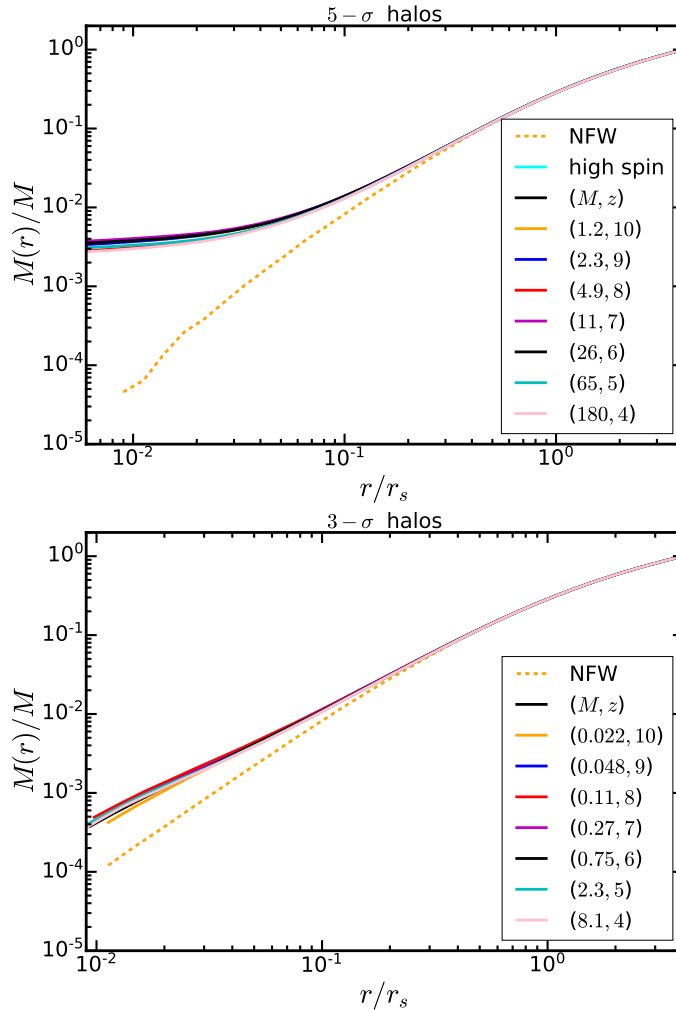


Figure 4.1: Enclosed mass fraction as a function of radius (normalized to the scale radius r_s), for 8 and 7 different 5- and 3- σ halos (upper and lower panels, respectively) including DM dissipation with cross-section $1 \text{ cm}^2 \text{ g}^{-1}$. Different halos are labeled with the mass (in units of $10^{11} M_\odot$) and redshift. The high spin curve corresponds to $\lambda = 0.1$ at $z = 10$, while other halos have spin parameter $\lambda = 0.03$. In these figures, the more dense 5- σ halos show core collapse, indicated by the region of constant density at small radii, while 3- σ halos have not been destabilized, consistent with Fig. 4.2. In the collapsed halos, the collapse fraction is found universally to be $\sim 3 \times 10^{-3}$.

roughly 4, with the exact value weakly depending on redshift. Therefore we assume those halos have a concentration of 4 in our simulations. Selecting an observation redshift z for $5 - \sigma$ or $3 - \sigma$ halos, we obtain the halo mass and concentration, from which we determine ρ_0 , r_s needed to create initial conditions for our N-body simulations.

We expect the most massive halos at high redshift, corresponding to rare fluctuations, will have higher central DM density and thus smaller collapse timescales. The DM self-interaction cross-sections in our simulation is taken to be $\sigma_0/m = 1 \text{ cm}^2 \text{ g}^{-1}$. The analytic formula in Eq. (4.14) suggests that the collapse timescale is inversely proportional to the cross-section. Therefore we can easily apply the simulation results to other cross-sections. The gravitational softening length is chosen to be $2d_0$ where d_0 is the mean separation for particles within radius $0.07 r_s$. The particle number in the whole simulation box is 6×10^6 .

As the tdSIDM halo evolves, dissipation will drive radial contraction of the halo as well as a “dark cooling flow” found in recent cosmological simulations of tdSIDM [5]. The contraction at a certain stage could be halted by centrifugal forces. However, if DM substructure torque, created by global gravitational instability or DM viscosity, efficiently transports angular momentum, the run-away collapse of the halo into an SMBH may occur. During this process, the central DM density is expected to very rapidly increase, causing the integration time step to approach zero. GIZMO uses adaptive time-stepping, which allows us to study the halo profiles at the moment of collapse. In the extreme case, we expect DM particles to lose all of their kinetic energy in the center-of-mass frame, typical in the dark nugget model [213]. In the simulation, we choose $f = 0.8$ to avoid numerical difficulties (e.g. particles cluster in the same position in phase space and blow out the integration time) but the results are nearly identical for $f \approx 1$ (if we correct for the dependence of t_{diss} on f). After the catastrophic collapse, the enclosed mass $M(r)$ is expected to be flat at the halo center, which agrees well with what we found in simulations of isolated $5 - \sigma$ halos, as shown in Fig. 4.1. The NFW parameters of $5 - \sigma$ halos are $r_s = 39.1, 23.2, 14.6, 9.6, 6.5, 4.6, 3.3 \text{ kpc}$, and $\rho_0 = 0.030, 0.051, 0.081, 0.121, 0.173, 0.237, 0.316 M_\odot \text{pc}^{-3}$ for redshift $z = 4 - 10$. The NFW parameters ρ_0 and r_s can be obtained from Eqs. (4.9) and (4.5) once we fix the halo mass M_{vir} and the concentration number c_{vir} at a given observation redshift. The halo spin parameter is taken to be $\lambda = 0.03$. For comparison, we also run a simulation with high spin parameter $\lambda = 0.1$. The halo collapses within the same timescale, suggesting that the centrifugal barrier discussed

in Appendix 4.8 is not important, such that we expect SMBHs to form if the halo mass is above the threshold.

After running simulations for isolated NFW halos, we calibrated our semi-analytic model and found the timescale for SMBH formation is

$$t_{\text{col}} = 1.06t_{\text{diss}}. \quad (4.15)$$

Therefore the collapse timescale can be determined from our analytic prediction of the dissipation timescale, after adding a calibration factor of 1.06. The collapse radius is universally found to be $\sim 0.07 r_s$ for $5\text{-}\sigma$ halos at different redshift, corresponding to a collapse fraction $\sim 3 \times 10^{-3}$, independent of halo mass. Different mass halos have slightly different calibration factors, which are found to be 1.02, 1.05, 1.05, 1.15, 1.12, 1.05, 1.01 for $5\text{-}\sigma$ halos at redshift $z = 4 - 10$. Even though there are some uncertainties, our semi-analytic formula in Eq. (4.14) agrees well with the simulation results after adding a calibration factor. To confirm that less rare halos will not collapse, we also run simulations with $3\text{-}\sigma$ halos and stop the evolution at time $\sigma/\sigma_0\epsilon t_H$, where σ is the cross-section that will be appropriate for seeding SMBHs, $\sigma_0 = 1 \text{ cm}^2 \text{ g}^{-1}$ is the cross-section we are using in our simulation and ϵ is the parameter of seeding criterion discussed in Eq. (4.17). We will show later in Sec. 4.3 that $\sigma \sim 0.1 \text{ cm}^2 \text{ g}^{-1}$ is appropriate for seeding the high mass SMBHs at high redshift while not causing inconsistencies at low redshift.

Mass Threshold of Black Hole Seeding

In this subsection, we discuss the collapse criterion of DM halos analytically based on the collapse timescale calibrated by our simulations. Other criteria related to the halo spin parameter and halo dynamical timescale are discussed in Appendix 4.8, where we will show they are not relevant to the problem at hand. We also study the halo masses that lead to SMBH formation at different redshifts, assuming a median mass-concentration relation discussed in [337]. There will, however, always be a scatter in the halo concentration, which is related to the halo assembly history. The complication is that halos may form early, but not merge until late. Such halos will have a very large central density, corresponding to scatter above the median mass-concentration relation. Another complication is that even though a certain halo is not massive or concentrated enough to seed an SMBH, one of its halo progenitors may have seeded an SMBH which subsequently falls to the halo center. We will fully address those questions in Sec. 4.3 with a merger tree. In this section, we only discuss SMBH formation based on median mass-concentration relations for a

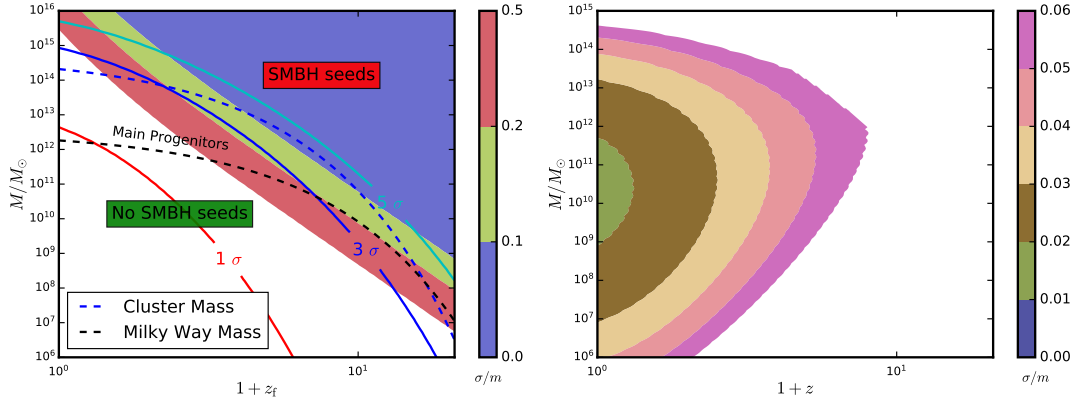


Figure 4.2: *left panel*: Shown as shaded contours, minimum halo mass M to seed an SMBH (labeled “SMBH seeds”) immediately at redshift of halo formation z_f , for a fixed tdSIDM cross-section (σ/m in units of cm^2/g). The solid curves show the mass of a $\nu = 1, 3, 5$ halo in a spherical collapse model formed at redshift z_f . A halo is available in the cosmological history to seed an SMBH (for a given cross-section) if the shaded region corresponding to that cross-section is above a solid curve. For comparison, we show as dashed curves the cosmological history of the Main Progenitors of a Milky Way Mass and Cluster Mass galaxy, as given in Eq. (4.19). Interestingly, the main progenitor of a $1 - \sigma$ halo at $z = 0$, can be a $3 - \sigma$ halo at $z \sim 10$, which is more likely to form SMBHs. *right panel*: Mass M of a $\nu = 5$ halo, again for fixed cross-section corresponding to colored regions, that may seed an SMBH at a lower redshift $z \leq z_f$. We can see that rare halos that do not seed an SMBH immediately may do so later in the history of the Universe. During the evolution of these halos, we assume the central density and the halo mass are fixed; we will track the assembly history of halos more completely in Sec. 4.3 utilizing merger trees.

given halo mass M_{vir} and redshift z . This works well for rare halos that have large masses at high redshift because we do not expect much scatter in their concentration. Therefore the production of high-mass SMBHs is well predicted in this section with purely analytic formulae.

For a halo with mass $M_{\text{vir}}(z)$, the criterion that an SMBH seed form in the halo at redshift z is approximately given by

$$t_{\text{col}}(M_{\text{vir}}(z), \sigma/m, z) \ll t_{\text{h}}(z), \quad (4.16)$$

where $t_{\text{h}}(z)$ is the Hubble time at z . This indicates that seeding happens when the collapse time is significantly shorter than the lifetime of the system. Practically, we determine that an SMBH seed would form when

$$t_{\text{col}}(M_{\text{vir}}(z), \sigma/m, z) = \epsilon t_{\text{h}}(z), \quad (4.17)$$

where ϵ is set to be 0.1; this parameter is somewhat arbitrary, but also degenerates with a rescaling of the cross-section, such that ϵ can be viewed as the uncertainty on the cross-section. Therefore the only parameter that will determine the seeding of SMBHs is $\epsilon\sigma/m$. The choice of $\epsilon = 0.1$ is reasonable because the time threshold of collapse and the Hubble time is expected to be roughly within the same order of magnitude. In our seeding model, the collapse timescale is greater than the halo dynamical timescale as discussed in Appendix 4.8 to avoid local fragmentation. An extremely small collapse timescale is disfavored if an SMBH is seeded in a halo instead of forming many local dark stars. The fraction of a DM halo that eventually collapses into a black hole is crucial for determining the mass function of the SMBH seeds. From the simulation, we know this collapsing fraction is about 3×10^{-3} . Eq. (4.16) gives the lower bound of the halo mass that would lead to a collapsing halo. For high redshift where the cosmological constant is not important and the universe is dominated by matter, the critical density scales like $\rho_{\text{crit}} \propto (1+z)^{3/2}$. We can further assume $\Delta(z) = 200$ regardless of redshift and the mass threshold for collapsed halos can be determined by combining Eq. (4.14) and Eq. (4.17)

$$\begin{aligned}
M &> M_0(c_{\text{vir}}(z), z) \\
&= 1.63 \times 10^{17} M_{\odot} \left[\ln(1 + c_{\text{vir}}(z)) - \frac{c_{\text{vir}}(z)}{c_{\text{vir}}(z) + 1} \right]^{9/2} \\
&\times \frac{1}{(c_{\text{vir}}(z)/4)^{21/2}} \left(\frac{\Omega_m \rho_{\text{crit}}(0)}{\rho_{\text{crit}}(z)} \right)^2 \left(\frac{0.01 \text{ cm}^2 \text{ g}^{-1}}{\epsilon\sigma/m} \right)^3.
\end{aligned} \tag{4.18}$$

For a given DM halo with mass M at z , it has an SMBH seed with mass fM in the halo center if $M > M_0(c, z)$, where $f \sim 3 \times 10^{-3}$ is the collapse fraction of the dissipative DM halo.

Eq. (4.18) suggests that the minimum halo mass to seed an SMBH is much smaller at higher redshift, and furthermore, high concentration (rare) halos are more likely to form an SMBH at higher redshift. This is shown in Fig. 4.2, similar to the proposal and discussion in Ref. [213]. In the left panel of Fig. 4.2, the minimum mass halo to form an SMBH is shown in shaded regions for different cross-sections. To determine whether a halo is available in the cosmological history that meets this minimum mass requirement, these colored regions are compared against the solid lines corresponding to a $\nu = 1, 3, 5$ halo of mass M formed at redshift z_f , using Eq. (4.18). When a colored region is above a solid line of fixed ν , halos of a given cosmological rarity ν are available to make SMBH seeds via dissipation at redshift z . We can thus see that rare halos can seed SMBHs at high redshift.

In the right panel of Fig. 4.2, we track the $5 - \sigma$ halos to lower redshift z to determine if these rare halos of mass M can seed a black hole later in the history of the Universe. The shaded contours, with the colors corresponding again to different cross-sections, indicate where SMBH seeds can form at lower redshifts. Note that we assume the halo mass and central density remain fixed, while the concentration is given by Eq. (4.7); this assumption is idealized since halos will accrete and merge with other halos. Nevertheless, fixing the tdSIDM cross-section, this demonstrates how rare halos that cannot form an SMBH seed immediately may form one at lower redshift.

Furthermore, if the halo is not massive enough to seed an SMBH at high redshift, it may still have lighter SMBH seeds because its progenitors may have formed black holes at higher redshift.

We can thus see that the assembly history has to be determined to fully study SMBH formation at low redshift. This will be discussed in detail in Sec. 4.3 using Monte Carlo simulations to generate the merger tree. However, there is still an analytic shortcut to describe the evolution of the most massive progenitors, known as main progenitors, during the assembly history. Empirically, the mass accretion histories for main progenitors, as observed at $z = 0$, can be characterized by a simple function [22]

$$M(z) = M_0 e^{-\alpha z}, \quad (4.19)$$

where M_0 is the halo mass at $z = 0$ and $M(z)$ is the most massive progenitor in the merger tree. Although the mass accretion history of individual halos may deviate from this form, it provides a good characterization of the range of halo mass accretion trajectories, as we will show later in Sec. 4.3. α is related to the halo mass at the observed time. The average α is ≈ 0.6 for a typical halo with mass $M = 10^{12} M_\odot$ at $z = 0$, and ≈ 0.9 for a rarer halo with mass $M = 10^{14} M_\odot$ at $z = 0$. We show two halo trajectories in Fig. 4.2 for masses $M = 10^{12}$ and $M = 10^{14} M_\odot$. We can see from Fig. 4.2 that the most massive progenitor of a typical $(1 - \sigma)$ halo at low redshift may instead be a rare $3 - \sigma$ halo at high redshift. The rare progenitors, which formed relatively early, have a large central density even at low redshift before merging, and they can potentially seed an SMBH at the halo center. Thus, while the dissipative nature of DM helps us explain the most massive SMBHs at high redshift, one must further examine the merger history of halos to check consistency with observations of SMBHs at low- z in Milky Way-like galaxies. We will show in Sec. 4.3 and Sec. 4.4 that this suggests a range of cross-sections where high

redshift SMBH formation could occur, while simultaneously remaining consistent with low- z observations.

4.3 Cosmological evolution and abundance of SMBHs

In this section, we aim to make predictions for the cosmological abundance of SMBHs formed via the direct collapse of tdSIDM halos and the observed luminosity functions of quasars formed via this mechanism. In contrast to the canonical seeding mechanisms for smaller SMBH seeds (e.g., remnants of Pop III stars with typical mass of $\sim 10 - 10^3 M_\odot$ [179–186] or directly collapsed pristine gas clouds of mass $\sim 10^4 - 10^6 M_\odot$ [186, 194–199]), the mechanism in this chapter could naturally explain the existence of massive quasars ($M_{\text{BH}} \gtrsim 10^9 M_\odot$) at $z \gtrsim 6$ discovered in recent years [200, 201, 341–347]. According to the mass criterion for seeding in Eq. (4.18) and the seed-to-host mass ratio f_{col} discussed in Sec. 4.2, $M_{\text{BH}} \gtrsim 10^9 M_\odot$ SMBHs at $z \sim 7$ will form in $M \gtrsim 10^{12} M_\odot$ halos with normal concentrations. However, it is still an open question whether this model can produce the correct cosmic abundance of the SMBHs and observed quasars at high redshift.

To investigate this aspect, the cosmological evolution of SMBH seeds and their host halos need to be tracked. In this model, halos with different masses and concentrations could be coupled to the seeding mechanism at very different cosmic times. The seeding should be considered as a continuous process rather than happening only in a short period of time. In addition, the decoupled seeds could further increase their masses through the accretion of baryonic matter, and the amount of such accretion depends on the evolutionary history of halos (e.g. a major galaxy merger could trigger such accretion). Furthermore, the seeding criterion has a strong dependence on the concentration of the halo, which in turn depends on the assembly history of the halo [e.g., 348], and is subject to various biases (e.g. environment of formation). A simple median mass-concentration relation may not be accurate enough to describe the seeding process of the entire cosmological population of DM halos.

Given the physical processes and uncertainties involved in the evolution of SMBH seeds, we employ halo merger trees to trace the merger history of halos and SMBH seeds and to evolve SMBHs using empirical prescriptions. The halo merger trees are generated using the SATGEN¹ code [349], which is based on the Extended Press-Schechter (EPS) formalism [350] and the algorithm introduced in Refs. [351, 352].

¹<https://github.com/shergreen/SatGen>

The virial mass and radius of halos in the merger trees are defined with the redshift-dependent Δ_{vir} in Ref. [249]. When creating the merger trees, we uniformly sample 10 halos per dex of halo mass ranging from 10^8 to $10^{16.4} M_{\odot}$ at $z = 4$ and trace their progenitors up to $z \simeq 20$, with a progenitor mass resolution 5 (6 for trees more massive than $10^{15} M_{\odot}$) orders of magnitude lower than the final halo mass at $z = 4$. The merger tree traces the mass and concentration of each halo from the time when it enters the tree (becomes more massive than the mass resolution of the tree) to the time when it merges into a more massive halo. The halo concentration is obtained from an empirical relation calibrated via simulations [348], which relates the main branch (the branch that tracks the most massive progenitor) merging history to the concentration parameter by

$$c_{\text{vir}}(M_{\text{vir}}, z) = [4^8 + (t(z)/t_{0.04}(M_{\text{vir}}, z))^{8.4}]^{1/8}, \quad (4.20)$$

where $t(z)$ is the cosmic time at redshift z and $t_{0.04}$ is the cosmic time when the host halo has assembled 4% of its instantaneous mass, $M_{\text{vir}}(z)$. In principle, the gravitational impact of baryonic matter (e.g. adiabatic contraction of DM [282, 353]), star formation and subsequent feedback processes could potentially affect the structure of high redshift halos. However, self-consistently modeling the baryonic content of high redshift galaxies is beyond the scope of this chapter, and we defer a detailed analysis of this aspect to follow-up work.

All the progenitors of one merger tree are weighted by the number density of the final halo sampled at $z = 4$, determined analytically by the halo mass function from the HMF code [354], which itself is calibrated based on numerical cosmological simulations [14]. In Fig. 4.3, we show the halo mass functions at $z = 4, 6, 8$ reproduced with the weighted abundance of halos in the merger trees. They are in agreement with the halo mass functions determined analytically up to $10^{12} M_{\odot}$ ($10^{13.5} M_{\odot}$) at $z = 8$ ($z = 6$), which covers the mass range of quasar host halos of interest. In the subsequent analysis, we will use the weighted results for any predictions in the cosmological context.

SMBH seeding and growth

Based on the halo merger trees, we initialize and evolve the SMBH seeds with the following empirical prescriptions. An SMBH seed is initialized when the halo meets the seeding criterion introduced in Eq. (4.18). The initial mass of the seed is set as a constant fraction, $f_{\text{col}} = 3 \times 10^{-3}$, of the instantaneous mass of the host halo, motivated by the simulation results in Sec. 4.2. Subsequently, as long as

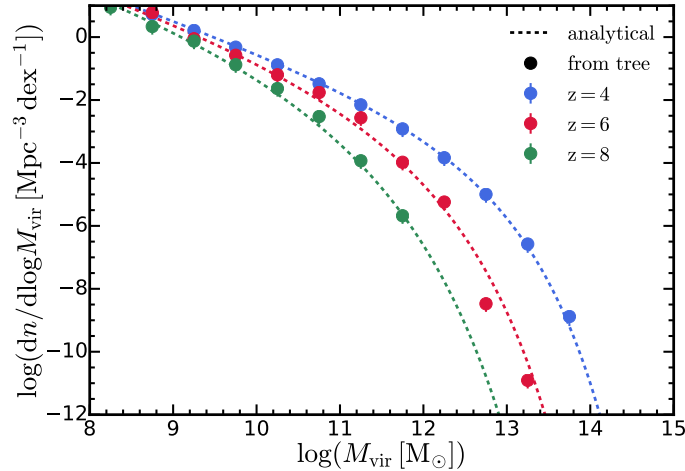


Figure 4.3: **Halo mass function.** The reconstructed halo mass functions at $z = 4, 6, 8$ based on the weighted abundance of halos in the merger trees (shown by circles of different colors). They are compared to the halo mass functions determined analytically using the `HMF` code (shown by dashed lines), which itself is calibrated based on numerical cosmological simulations [14]. The halo mass functions determined by the merger trees agree reasonably well with the analytic ones up to $10^{12} M_{\odot}$ ($10^{13.5} M_{\odot}$) at $z = 8$ ($z = 6$), which covers the mass range of quasar host halos of interest.

the host halo still meets the seeding criterion, we maintain the seed-to-host mass ratio as f_{col} (referred to as the *reseeding mechanism*). The treatment relies on the assumption that, after the initial collapse of the DM halo, the accretion of DM onto the central SMBH seed will continue until a dynamical equilibrium between the SMBH seed and the host halo is reached. This dynamical equilibrium results in the roughly constant seeding fraction found in the simulations, and should hold as long as DM can still be efficiently fed to the halo center via dissipative self-interactions. For halos that are coupled to the seeding mechanism, the *reseeding* would effectively erase the unique growth history of the SMBHs and set a tight correlation between host halo mass and SMBH mass. However, for halos that no longer meet the seeding criterion, the subsequent growth of SMBHs they host will no longer be affected by DM physics but by hierarchical mergers of SMBHs during halo mergers and accretion of baryonic matter. During the merger of host halos, the dynamical friction against the DM background could drag the satellite SMBH towards the primary SMBH and a bound SMBH binary will form. We assume that this happens when the mass ratio of the two SMBH-plus-halo systems is larger than 0.3, as suggested in Ref. [355]. For simplicity, we do not model the subsequent

evolution of the binary and treat the bound binary as a single SMBH right after the merger. The typical timescale for a billion solar mass SMBH binary to go through the hardening stage to the final coalesce is of ~ 1 Gyr (e.g. [355]). Therefore, in the early Universe, it is likely that binary SMBHs seeded through this mechanism are common. These binaries could have different accretion (quasar) activities from low redshift AGNs. In addition, SMBH triplets will likely form through hierarchical merger as well. The intruding SMBH can facilitate the coalesce of the binary through close three-body interactions and Kozai-Lidov oscillations (e.g. [356, 357]). The lightest SMBHs are expected to be ejected from the galaxy center in about 40% of the cases (e.g. [356, 357]). Moreover, the recoil due to the gravitational wave emission after the binary merger (e.g. [358]) could also lead to the ejection of the remnant SMBH. These processes could introduce order-unity correction factors to the SMBH occupation fractions and SMBH masses. Self-consistently modeling these processes is beyond the scope of this chapter, thus our results should be treated as upper limits.

For the accretion of baryonic matter, we model the “merger driven” accretion of SMBHs, which has been adopted in previous studies of the cosmic evolution of SMBHs [355, 359–361]. The efficient gas inflow triggered by galaxy mergers feeds both the accretion of SMBHs and the star-formation in galaxy bulges. We assume this feeding happens when the mass ratio between the two progenitor halos is larger than 0.1 (defined as a “major merger”). The stellar/supernovae feedback from rapid star-formation and potential active galactic nucleus (AGN) feedback will eventually quench the gas inflow as well as further growth of the SMBH. The total amount of mass accreted during each major merger event is related to the complicated gas dynamics and feedback processes in the galaxy bulge. Hypothetically, it manifests as the observed statistical correlation between the SMBH mass and bulge velocity dispersion of its host galaxy (the $M_{\text{BH}} - \sigma_{\text{v}}^*$ relation [19, 362])

$$M_{\text{BH}} = (4.4 \pm 0.9) \times 10^7 M_{\odot} (\sigma_{\text{v}}^*/150 \text{ km s}^{-1})^{4.58 \pm 0.52}. \quad (4.21)$$

This motivates us to set the mass gain of an SMBH through the accretion of baryonic matter during each merger event as

$$\Delta M_{\text{BH}} = \Delta M_0 (1 - \epsilon_{\text{r}}) (\sigma_{\text{v}}^*/150 \text{ km s}^{-1})^{4.58}, \quad (4.22)$$

where σ_{v}^* is the bulge velocity dispersion of the merged galaxy, ϵ_{r} is the radiative efficiency (assumed to be the canonical value 0.1) and ΔM_0 is a free normalization parameter, which has been set to $\sim 10^4 - 10^7 M_{\odot}$ in previous studies of low-mass

seeds [355, 359, 361]. In observations, the bulge velocity dispersion is found to correlate with the asymptotic value of the halo circular velocity as [362]

$$\log V_c = (0.892 \pm 0.041) \log \sigma_v^* + (0.44 \pm 0.09). \quad (4.23)$$

And for the NFW profile, the maximum circular velocity of the host halo is related to the halo mass as [47, 327]

$$V_c = \left[G \frac{f(x_{\max})}{f(c_{\text{vir}})} \frac{c_{\text{vir}}}{x_{\max}} \left(\frac{4\pi}{3} \Delta(z) \rho_{\text{crit}}(z) \right)^{1/3} \right]^{1/2} M_{\text{vir}}^{1/3},$$

$$f(x) = \ln(1+x) - \frac{x}{1+x}, \quad x_{\max} = 2.15. \quad (4.24)$$

Combining Eqs. (4.22), (4.23) and (4.24) above results in a link between ΔM_{BH} and host halo parameters ($M_{\text{vir}}, c_{\text{vir}}$) at a given redshift. This forms an empirical prescription to model the mass growth of SMBHs during galaxy mergers tracked by halo merger trees, with the assumption that the statistical correlations between SMBHs and their host galaxies (halos) are maintained throughout cosmic time. Overall, the two free parameters of the SMBH catalog are the self-interaction cross-section per unit mass, σ/m , and the baryonic mass accretion constant, ΔM_0 . Similar to the host halos, the SMBHs are assigned with statistical weights corresponding to the number density of the final halo of the merger tree at its sampling redshift. For our fiducial model, we set $\Delta M_0 = 0$ to study the pure impact of DM physics and hierarchical mergers of SMBH seeds. In addition, we will try varying ΔM_0 to $10^7 M_\odot$ to study the “maximum” effect (since $10^7 M_\odot$ is already close to the normalization of the local $M_{\text{BH}} - \sigma_v^*$ relation) that baryonic accretion can have on this population of SMBHs at high redshift.

Predictions for high redshift quasars

In this section, we aim to make predictions for the abundance of luminous quasars at high redshift and explain the unexpectedly large masses of these quasars with the seeding model discussed in this chapter. We will first derive predictions for the mass function of SMBHs seeded by tdSIDM, and then link it to the luminosity function of quasars. Binned estimations of SMBH mass functions are derived based on the weighted abundance of SMBHs in the merger trees and the results are shown in Fig. 4.4. At the massive end, the shape of the SMBH mass function resembles the halo mass function with an exponential decrease, since the massive SMBHs are still coupled to the seeding mechanism with mass proportional to the host halo mass. At the low-mass end, SMBHs start to decouple from the seeding mechanism, so the

SMBH mass function turns over and starts to decrease with lower M_{BH} , as opposed to the behavior of the halo mass function. Varying the self-interaction cross-section has almost no effects at the massive end while changing the characteristic lower mass when the SMBH mass function turns over. The model with $\sigma/m = 0.1 \text{ cm}^2 \text{ g}^{-1}$ predicts a more extended tail of SMBHs at the low-mass end, compared to the model with $\sigma/m = 0.05 \text{ cm}^2 \text{ g}^{-1}$, with no apparent mass cut-off. This is because the redshift range of seeding in the model with $\sigma/m = 0.1 \text{ cm}^2 \text{ g}^{-1}$ is broader than the model with $\sigma/m = 0.05 \text{ cm}^2 \text{ g}^{-1}$, as illustrated in the left panel of Fig.4.2. SMBHs seeded and decoupled at higher redshift can populate the low-mass end of the SMBH mass function. Quasar surveys and theoretical modeling indicate that the number density of luminous high redshift quasars with $M_{\text{BH}} \gtrsim 10^9 M_{\odot}$ and $L_{\text{bol}} \gtrsim 10^{46} \text{ erg/s}$ is $10^{-9} \lesssim \Phi \lesssim 10^{-7} [\text{Mpc}^{-3} \text{ dex}^{-1}]$ [15, 18, 363], which sets a lower limit of the abundance of underlying SMBH population ². The predictions here are consistent with this limit. In the lower panel of Fig. 4.4, we compare the model predictions with $\Delta M_0 = 0$ and $\Delta M_0 = 10^7$. Baryonic accretion during major mergers only has a weak impact at the low-mass end (shifting the lowest mass of the seeds produced by the mechanism) and can hardly affect the mass of the most massive SMBHs seeded through this mechanism.

In order to relate the SMBH mass function to the quasar luminosity function, the fraction of SMBHs that are active (the duty-cycle D) and the luminosity of active quasars are required. The bolometric luminosity (luminosity integrated over the entire quasar spectrum and free from extinction) of a quasar, L_{bol} , is often described as its ratio to the Eddington luminosity

$$\begin{aligned} L_{\text{bol}} &= \lambda_{\text{edd}} L_{\text{edd}} = \lambda_{\text{edd}} \frac{4\pi G m_{\text{p}} c}{\sigma_{\text{T}}} M_{\text{BH}} \\ &= 1.26 \times 10^{47} \text{ erg/s} \left(\frac{\lambda_{\text{edd}}}{1} \right) \left(\frac{M_{\text{BH}}}{10^9 M_{\odot}} \right), \end{aligned} \quad (4.25)$$

where m_{p} is the proton mass and σ_{T} is the Thomson scattering cross-section for the electron. The ratio λ_{edd} is referred to as the Eddington ratio. For simplicity, we first adopt a log-normal Eddington ratio distribution function (ERDF)

$$P_1(\log \lambda_{\text{edd}}) = \frac{1}{\sqrt{2\pi}\sigma_{\text{edd}}} e^{-(\log \lambda_{\text{edd}} - \log \lambda_{\text{c}})^2 / 2\sigma_{\text{edd}}^2}, \quad (4.26)$$

²The estimation is done using the bright UV-selected quasars at $z \gtrsim 6$. If actively accreting at (sub-)Eddington rate, a billion solar mass SMBH roughly gives bolometric radiation output $L_{\text{bol}} \sim 10^{46-47} \text{ erg/s}$, which corresponds to $M_{\text{UV}} \sim -24$ after applying the bolometric corrections (e.g. [15]). The number density of bright UV-selected quasar with such luminosities is roughly the range quoted in the main text (e.g. [15, 364, 365]). Similar number density estimations were given in [16, 363].

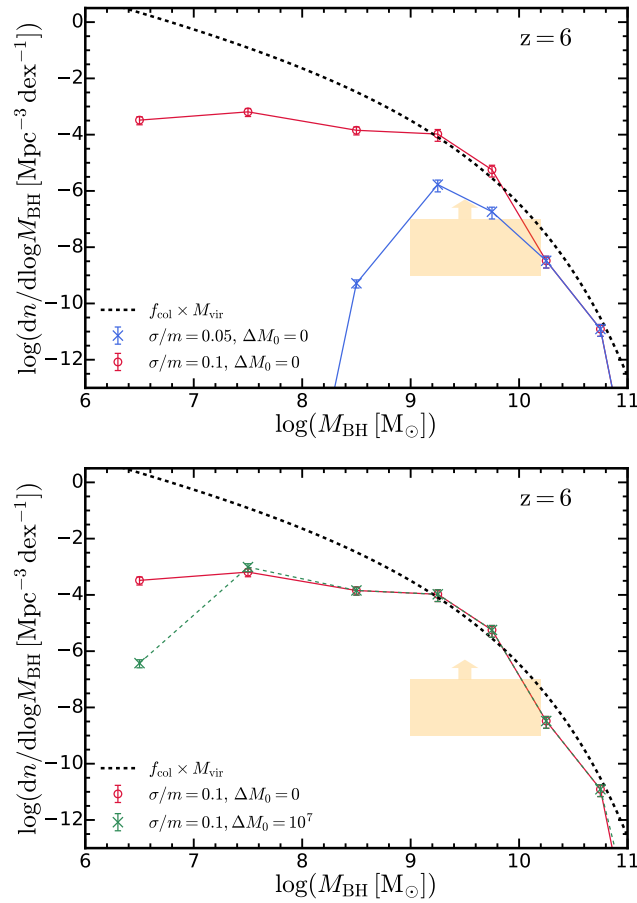


Figure 4.4: **SMBH mass function.** *Top:* Number density of SMBHs as a function SMBH mass at $z = 6$, calculated from the weighted abundance of SMBHs in the merger trees. The prediction assuming $\sigma/m = 0.1$ (0.05) $\text{cm}^2 \text{g}^{-1}$ and $\Delta M_0 = 0$ is shown and compared to the halo mass function multiplied by the collapse fraction f_{col} . The massive end of the BHMF is coupled with the seeding mechanism, and the shape of the SMBH mass function resembles the exponential cut-off in the halo mass function. Low-mass SMBHs have decoupled from the seeding mechanism and the low-mass end of the mass function deviates from the halo mass function. The choice of self-interaction cross-section does not affect the massive end but changes the characteristic mass where the SMBH mass function deviates from the halo mass function. The shaded region indicates the abundance of observed massive quasars ($M_{\text{BH}} \gtrsim 10^9 M_{\odot}$) at high redshift and the abundance of underlying SMBH population should at least be larger. *Bottom:* We show the SMBH mass functions in the model with $\sigma/m = 0.1 \text{ cm}^2 \text{g}^{-1}$ and $\Delta M_0 = 0$ (10^7) M_{\odot} . The baryonic accretion arguably only has an impact at the low-mass end (shifting the lowest mass of the seeds produced by the mechanism), hardly changing the abundance of the most massive SMBHs.

with $\lambda_c = 0.6$ and $\sigma_{\text{edd}} = 0.3$, motivated by observational constraints of $z \sim 6$ quasars [366], as well as the extrapolation of models constrained at lower redshift [e.g., 367, 368]. Such a log-normal ERDF implies that active SMBHs accrete at close to the Eddington limit. However, it is still possible that a substantial fraction of active SMBHs accrete at much lower rates and the observed massive quasars are only tip-of-the-iceberg of the SMBH population. Therefore, in addition to the log-normal ERDF, we also try using a cut-off power-law ERDF that extends to $\lambda_{\text{edd}} = 10^{-4}$

$$P_2(\log \lambda_{\text{edd}}) = N \left(\frac{\lambda_{\text{edd}}}{\lambda_c} \right)^\alpha e^{-\lambda_{\text{edd}}/\lambda_c}, \quad (4.27)$$

where N is a normalization factor to keep the integrated probability at unity, $\lambda_c = 1.5$ [368] sets a cut-off in the super Eddington regime and α is the faint-end slope, which is free and can be tuned to match the prediction with the observed bolometric quasar luminosity function. The SMBH mass function can then be mapped to the bolometric quasar luminosity function through the convolution

$$\phi_L(\log L_{\text{bol}}) = D \int_{-4}^{\infty} \phi_M(\log L_{\text{bol}} - \log \lambda_{\text{edd}} - \log C) P(\log \lambda_{\text{edd}}) d \log \lambda_{\text{edd}}, \quad (4.28)$$

where C is $4\pi G m_p c / \sigma_T$ (as in Eq. (4.25)) and we have assumed that SMBHs with $\log \lambda_{\text{edd}} > -4$ are active (which also defines the duty-cycle). The duty-cycle can be determined by making the normalization of the predicted luminosity function consistent with observations at the bright end. We note that the parameterization of the ERDF and the simple constant duty-cycle assumed here are purely for “a proof of concept”, with the intention to check whether predictions from the seeding model can be reconciled with observations with some level of tuning of the model for SMBH growth. We do not try to argue for a specific model of SMBH growth through the study here.

The bolometric luminosity of quasars is the integrated luminosity over the entire spectrum, representing the total energy output. However, in observations, the luminosity function measurements are performed in certain photometric bands (commonly far-UV and X-ray for quasars at high redshift) covering restricted parts of the quasar spectral energy distribution and are subject to corrections for dust and neutral hydrogen extinction, survey completeness, and selection biases. Ref. [15] has updated the constraints on the bolometric quasar luminosity function at high redshift based on the latest compilation of observations in far-UV, X-ray, and infrared. The

observational binned estimations from compiled observations are converted onto the bolometric plane, taking account of the extinction and bolometric corrections.

In the top panel of Fig. 4.5, we show the predicted bolometric quasar luminosity function at $z = 6$ from the merger trees, assuming a log-normal ERDF. The results are compared to the observational constraints compiled in [15]. With a duty-cycle of 3×10^{-3} (6×10^{-4}), the predicted abundance of the most luminous quasars in the model with $\sigma/m = 0.05$ (0.1) $\text{cm}^2 \text{g}^{-1}$ can match the observed abundances. The prediction assuming $\sigma/m = 0.1 \text{ cm}^2 \text{g}^{-1}$ gives better agreement at faint luminosities ($L_{\text{bol}} \lesssim 10^{46.5} \text{ erg/s}$) but over-predicts the quasars at intermediate luminosities ($L_{\text{bol}} \sim 10^{47} \text{ erg/s}$). The prediction with $\sigma/m = 0.05 \text{ cm}^2 \text{g}^{-1}$ agrees with observations at the luminous end ($L_{\text{bol}} \gtrsim 10^{47.5} \text{ erg/s}$) and is not in tension with observations at intermediate and faint luminosities. Acknowledging that other seeding mechanisms could still be responsible for the formation of low-mass and faint quasars, the prediction with $\sigma/m = 0.05 \text{ cm}^2 \text{g}^{-1}$ is compatible with observations. In terms of the duty-cycle, some observational studies of quasar clustering [369–371] have suggested that the duty-cycle of high redshift AGNs in the most massive halos may approach unity at $z \simeq 6$. That duty-cycle is much larger than the median value required for our models, especially for the $\sigma/m = 0.1 \text{ cm}^2 \text{g}^{-1}$ case, to not overproduce the abundance of luminous quasars. However, if the Eddington ratio of SMBH has a strong positive dependence on the host halo mass or environment, the averaged duty-cycle of all SMBHs could be much smaller than inferred from the clustering of currently observed luminous quasars. It is still debated observationally whether high redshift quasars have order-unity duty-cycles, or we are observing the tip-of-the-iceberg of the SMBH population. Some studies [368, 372] have instead argued for a low duty-cycle of the quasar population at $z \gtrsim 6$. We examine this possibility by using the cut-off power-law function defined in Eq. (4.27) as the ERDF, which essentially includes a power-law tail of SMBHs with low Eddington ratios. The quasar luminosity functions predicted from this ERDF are shown in the lower panel of Fig. 4.5. We have set $D = 1$ (since we have already considered quasars with low activity with this ERDF) and tuned α in order to best match the observational constraints. The model with $\sigma/m = 0.1 \text{ cm}^2 \text{g}^{-1}$ and $\alpha = -1.1$ is in perfect agreement with observations at all luminosities. The model with $\sigma/m = 0.05 \text{ cm}^2 \text{g}^{-1}$ with $\alpha = -0.6$ can produce the correct abundance of bright quasars but predicts a shallower faint-end slope. We note that this discrepancy cannot be alleviated by tuning α and D , since further decreasing α will decrease the normalization at the bright end and require an unphysical value $D > 1$ to match observations. The com-

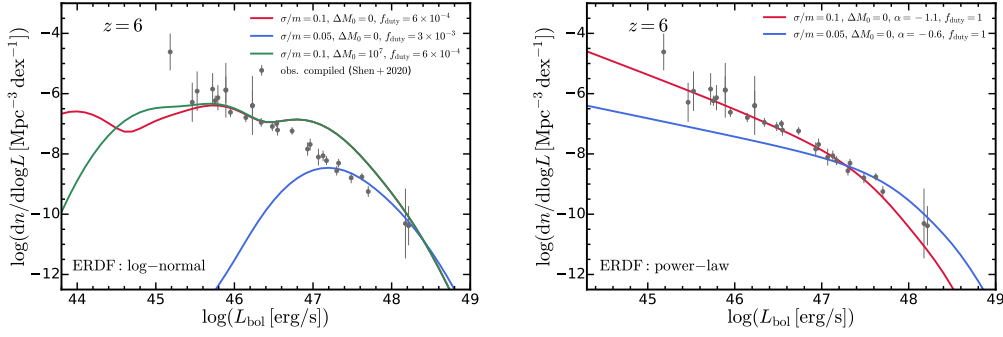


Figure 4.5: **Bolometric quasar luminosity function at $z = 6$.** *Top:* Model predictions, varying σ/m and ΔM_0 . The predictions are derived by convolving the SMBH mass function with a log-normal ERDF, tuning the duty-cycle to match the abundance of luminous quasars. The solid circles represent observational constraints compiled in [15]. The prediction assuming $\sigma/m = 0.05 \text{ cm}^2 \text{ g}^{-1}$ is compatible with the observations and produces the observed abundance of luminous quasars at $z = 6$, assuming a relatively low duty-cycle. On the other hand, the model with $\sigma/m = 0.05 \text{ cm}^2 \text{ g}^{-1}$ will overproduce quasars of $L_{\text{bol}} \sim 10^{47} \text{ erg/s}$. *Bottom:* We show the predictions with a cut-off power-law as the ERDF. The duty-cycle is assumed to be unity. The faint-end slope of the ERDF (α) is tuned to make the predicted quasar luminosity function close to observations. Both models can agree well with the luminous quasar abundances in observations. But the model $\sigma/m = 0.05 \text{ cm}^2 \text{ g}^{-1}$ does not fit perfectly with the faint end luminosity function regardless of the α adopted.

parisons here demonstrate that with a little tuning of parameters of the ERDF, the model can reproduce the observed quasar luminosity function. Meanwhile, despite the detailed functional form we use for the ERDF, our results suggest that if the collapse of dissipative DM halo is the dominant seeding mechanism for SMBHs at high redshift, a significant fraction of non-active SMBHs or SMBHs with low Eddington ratios would be expected. Such a feature can be tested with future surveys of high redshift quasars with improved completeness.

Since the most important implication of the model is the existence of extremely massive SMBHs, we explicitly track the mass growth history of ~ 300 randomly selected massive SMBHs with $\log M_{\text{BH}} \leq 10$ at $z = 7$ in the merger trees. The results of the model with $\sigma/m = 0.1 \text{ cm}^2 \text{ g}^{-1}$ are shown in Fig. 4.6 and compared to the mass measurements of high redshift quasars in the Ref. [16] compilation, including observations from Refs. [200, 201, 341, 343, 345–347]. The masses were measured using the virial method based on the broad line emission from quasars. The recent measurement of a $z \sim 7$ quasar [373] is added to this compilation. For

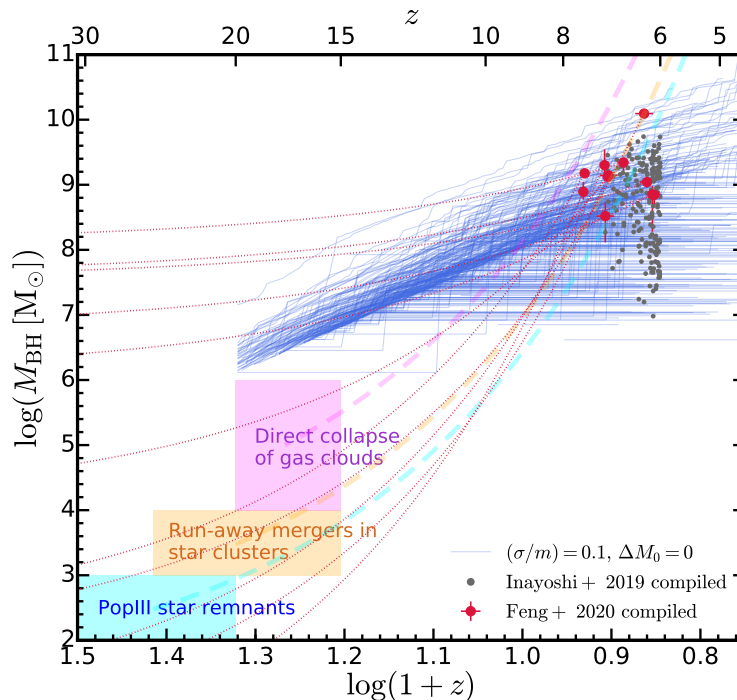


Figure 4.6: **Mass growth history of SMBHs.** The blue solid lines show the mass of SMBHs as a function of redshift in our model assuming $\sigma/m = 0.1 \text{ cm}^2 \text{ g}^{-1}$. These SMBHs are selected from merger trees with $M_{\text{BH}} \leq 10^{10} M_{\odot}$. The red points are the observed massive quasars at $z \gtrsim 6$ compiled in [16, 17] with the mass estimated using the virial method. The gray points are a more complete set of 196 quasars at $z \gtrsim 6$ compiled in [18], with the mass estimated indirectly from UV luminosity. The red dotted lines indicate the growth history of the observed quasars assuming they exhibit the same Eddington ratio as the measured value at the redshift of discovery. The typical mass and formation redshift of SMBH seeds from classical seeding mechanisms are shown in shaded regions, with the Eddington-limit growth tracks of these seeds in dashed lines for reference. Seeds formed in canonical mechanisms need to accrete at rates near the Eddington limit in order to produce billion solar mass SMBHs at $z \simeq 6 - 8$. This is in tension with the low Eddington ratios of some observed quasars, which require seed masses of $\sim 10^8 M_{\odot}$ implied by their observed Eddington ratio. However, such quasars can be accommodated in our seeding model.

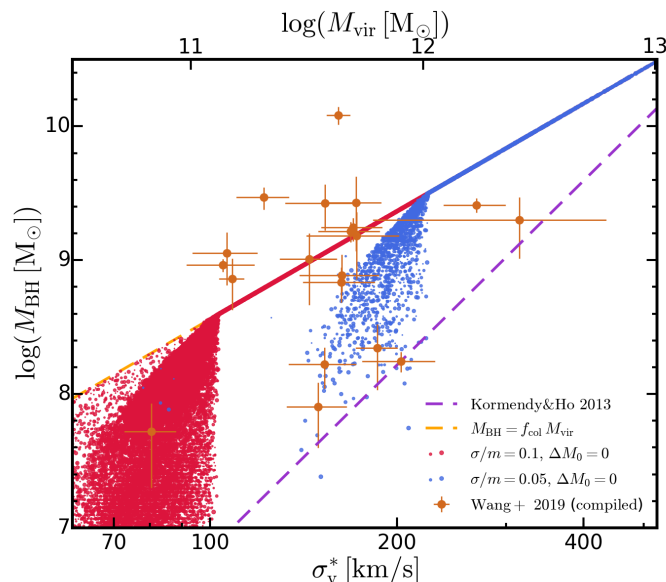


Figure 4.7: **The $M_{\text{BH}} - \sigma_v^*$ relation of high redshift SMBHs.** We show SMBHs in the merger trees selected at $z = 7$ in solid circles, with the marker size scaling with the statistical weight. Red and blue circles correspond to the model with $\sigma/m = 0.1$ and $0.05 \text{ cm}^2 \text{ g}^{-1}$, respectively. The local $M_{\text{BH}} - \sigma_v^*$ relation [19] is shown with the purple dashed line. The orange dashed line shows the relation $M_{\text{BH}} \sim f_{\text{col}} M_{\text{vir}}$, assuming the relation between M_{vir} and σ_v^* (Eq. (4.23) and Eq. (4.24)) holds. Observational samples based on the [C II] line observations of the quasar host galaxies compiled in [17] (originally from [20]) are shown in orange circles.

these quasars, we show their mass growth history assuming they have the same Eddington ratio as the measured value at the redshift of discovery. In addition, we show a more complete set of 196 quasars at $z \gtrsim 6$ compiled by [18], where the SMBH mass was inferred from the UV luminosity with bolometric corrections and assuming $\lambda_{\text{edd}} = 1$. The massive quasars observed at $z \simeq 6 - 8$ with relatively low measured Eddington ratios are hard to reconcile with the canonical seeding mechanisms since the seeds need to continuously accrete at the Eddington limit to reach more than a billion solar mass at the redshift of discovery. On the other hand, in our model, the masses of selected SMBH seeds are in agreement with the massive quasars revealed by observations at $z \simeq 6 - 8$. Among these seeds, the relatively massive ones are still coupled to the seeding mechanism down to $z \simeq 6$ and have their mass growth following the growth of host halo mass. These seeds are already very massive ($M_{\text{BH}} \gtrsim 10^6 M_{\odot}$) when initially seeded at $z \gtrsim 15$ and the mass growth is dominated by the accretion of dissipative DM, so the observed low Eddington ratios can be tolerated. Such a picture is consistent with the large fraction of in-

active quasars constrained above in the discussion of quasar luminosity functions. In addition, recent observational studies found that a few objects have extremely small proximity zone sizes that imply UV-luminous quasar lifetimes of $\lesssim 100,000$ yr [202]. The short lifetimes of these quasars also pose challenges to canonical black hole formation models which require a much longer period of seed accretion to reach the SMBH mass at the redshift of discovery. However, these young quasars can be accommodated in our seeding model, where the mass growth of SMBHs is dominated by dissipative DM accretion with no impact on the ambient intergalactic medium.

In Fig. 4.7, we show the $M_{\text{BH}} - \sigma_v^*$ relation of $z \gtrsim 6$ quasars. The SMBHs in the merger trees at $z = 7$ are shown in this plane for comparison to observational results. We convert the host halo mass to the bulge velocity dispersion using Eq. (4.23) and Eq. (4.24), assuming that the locally observed scaling relations can be applied to high redshift galaxies. The SMBHs in the merger trees tightly follow the $M_{\text{BH}} \sim f_{\text{col}} M_{\text{vir}}$ relation in massive host galaxies, and start to scatter toward lower M_{BH} at the mass when the halo decouples from the seeding mechanism. We compare our results with the observational constraints compiled in Ref. [17], based on the [C II] line observations of the quasar host galaxies compiled in Ref. [20]. Observations [17, 20, 374] indicate that the host galaxies of massive, luminous quasars at $z \gtrsim 6$ have halo dynamical masses and velocity dispersions at least an order of magnitude lower than expected from the local $M_{\text{BH}} - M_{\text{bulge}}$ and $M_{\text{BH}} - \sigma_v^*$ relations. However, as shown in Fig. 4.7, SMBHs seeded by tdSIDM, which exhibit a much larger SMBH-to-halo mass ratio than local constraints, are in better agreement with these measurements. At the massive end, SMBHs in this model cluster around a straight line fixed by the $V_c - \sigma_v^*$ relation (Eq. (4.23)) we assumed. The statistical scatter of the relation is not reflected here. The typical uncertainty of the normalization of the relation measured at low redshift is $\sim 0.1 - 0.2$ dex in $V_c(\sigma_v^*)$ [362], which roughly corresponds to $\sim 0.2 - 0.6$ dex in M_{vir} . At the low-mass end, SMBHs decouple from the linear relation and the scatter at the tail is due to variations in the merger histories of host halos. Such an $M_{\text{BH}} - \sigma_v^*$ relation predicted at high redshift will still be consistent with the relation measured at low redshift, since the SMBHs below $10^{10} M_{\odot}$ will have already decoupled from the seeding mechanism and have their mass growth dominated by baryonic accretion.

In Figure 4.8, we show the cosmic SMBH mass density as a function of redshift predicted by our seeding mechanism and compare it to the local SMBH mass

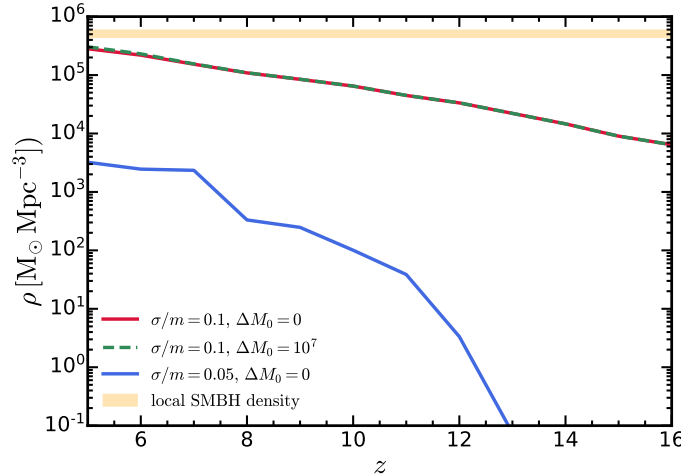


Figure 4.8: **The comoving SMBH mass density in the Universe versus redshift.** The cumulative mass density of SMBHs integrated over the mass function. The results with different model parameters are shown as labeled and compared to the local SMBH mass density, $4.4 - 5.9 \times 10^5 M_\odot \text{Mpc}^{-3}$ [21], as indicated by the horizontal line. The mass density from the model with $\sigma/m = 0.1 \text{ cm}^2 \text{ g}^{-1}$ approaches the local mass density already at $z \simeq 6$, which is potentially problematic since the integrated quasar luminosity density matches the local SMBH mass density [15] (at 0.5 dex level, assuming $\epsilon_r = 0.1$). Therefore, the mass density at high redshift needs to be significantly lower than the local value in order to be consistent with the observation of quasar luminosity functions, unless ϵ_r is larger (*i.e.* SMBHs are rapidly rotating).

density [21], which poses an upper limit. The mass density from the model with $\sigma/m = 0.1 \text{ cm}^2 \text{ g}^{-1}$ is close to the local value already at $z \simeq 6$. The mass density is quite sensitive to the self-interaction cross-section and the model with $\sigma/m = 0.05 \text{ cm}^2 \text{ g}^{-1}$ predicts about two orders of magnitude lower mass density at $z \simeq 6$. On the other hand, baryonic accretion has little impact on the SMBH mass density in our model. Quasar surveys indicate that the integrated quasar luminosity density matches the local SMBH mass density [15] (at 0.5 dex level, assuming $\epsilon_r = 0.1$). Therefore, the SMBH mass density at high redshift has to be significantly lower than the local value in order to be consistent with the observation of quasar luminosity functions, unless ϵ_r is larger (*i.e.* SMBHs are rapidly rotating). The model with $\sigma/m = 0.1 \text{ cm}^2 \text{ g}^{-1}$ is thus potentially in tension with the observations while the model with $\sigma/m = 0.05 \text{ cm}^2 \text{ g}^{-1}$ is still consistent with observations. Meanwhile, since the mass growth of the seeds is dominated by accretion of dissipative DM rather than baryonic matter, our model predicts that the integrated luminosity density of quasars (which reflects baryonic accretion) at high redshift will be significantly

smaller than the change in SMBH mass density at high redshift. Future surveys of high redshift quasars with the next-generation instruments, such as the Nancy Grace Roman Space Telescope, the Rubin Observatory Legacy Survey of Space and Time (LSST), and the James Webb Space Telescope (JWST), may be able to further test our seeding mechanism.

As mentioned above, the high redshift predictions and the comparisons with observations presented in this section are affected by many astrophysical uncertainties. These come from both modeling the seeding/growth of SMBHs and connecting them to the observed quasars. We have compared the predictions with the observationally inferred bolometric quasar luminosity functions at $z = 6$, where bolometric luminosities are affected by uncertainties in bolometric and extinction corrections (see discussions in [15]). Towards higher redshift, the measurements of quasar luminosity functions have been limited by the survey volume with respect to the vastly decreasing quasar number density (e.g. [15, 306, 365, 375, 376]). Meanwhile, in modeling the seeding, we have ignored the baryon content of early galaxies. If the baryons have a non-negligible contribution to the central gravitational potential, the collapse of halo into compact objects was shown to be accelerated [16]. However, the bursty star formation and feedback from the condensed baryon matter could compete with the dissipative collapse of DM (e.g. [56–58]). Moreover, in modeling SMBH growth, we have adopted scaling relations in connecting SMBH growth rates to host galaxy bulge properties and host halo properties, while these relations are largely based on low redshift observations. Finally, the largest uncertainty comes from the fuelling model to connect SMBHs to observed quasars, for which there is limited observational constraints even at moderate redshift. We essentially allow the ERDF and the quasar duty-cycle as free parameterized inputs. We expect that none of these uncertainties will likely overturn the general viability of the tdSIDM model, but improved constraints on the astrophysical inputs will certainly help pinpoint the working tdSIDM parameters more precisely. This will be explored in follow-up studies.

4.4 Consistency with low redshift SMBHs

There are two branches of halos that are most likely to host SMBH seeds, as illustrated in Fig. 4.2. The first branch consists of rare, massive halos at high redshift that can seed SMBHs shortly after they formed. These rare halos typically have low concentrations (usually below 4 as shown by most halo mass-concentration relations e.g. [337, 377]). However, the central DM density in these halos is still

very high since they form at unusually high redshift, as indicated by Eq. (4.14), leading to efficient SMBH formation. For this branch, according to Eq. (4.14), t_{col} depends on redshift as $\rho_{\text{crit}}^{-7/6}(z) \sim (1+z)^{-7/2}$, when M_{vir} and c_{vir} are fixed. At high redshift, when the dark energy is subdominant to matter, t_{h} depends on redshift as $(1+z)^{-3/2}$. Therefore, the ratio $t_{\text{diss}}/t_{\text{h}}$ of this branch has a simple redshift dependence as $(1+z)^{-2}$, indicating that the seeding is more likely to happen at earlier times assuming a fixed halo mass and concentration. The second branch consists of normal mass halos at low redshift with early assembly times, in which SMBH seeds do not form immediately but when they evolve to low redshift. These halos inherit high central DM densities at formation, which manifests as high halo concentrations after they accrete matter at late times. By first-order approximation, the central densities of such halos are roughly constant after the majority of their mass is assembled, and the redshift evolution of the ratio $t_{\text{diss}}/t_{\text{h}}$ is dominated by the evolution of the t_{h} term assuming a fixed halo mass, which approximately gives a redshift dependence $(1+z)^{3/2}$. This indicates that this branch of halos will more likely seed SMBHs at low redshift.

The model predicts the SMBH-to-halo mass ratio to be 3×10^{-3} at seeding, which is apparently much larger than that of local SMBHs in observations. Therefore, the second branch must be checked for the formation of overly massive SMBHs at low redshift. The distinct halos in the Local Universe (with halo masses as large as $10^{14-15} M_{\odot}$) with median concentration could evade the seeding criterion at low redshift and avoid hosting an overly massive SMBH. However, given the strong dependence of the collapse timescale on halo concentration, a highly concentrated progenitor (assembled early in cosmic time) could still seed an SMBH, which is later merged into the main progenitor. To investigate the SMBH seeds formed in this scenario and check the consistency of the model with local SMBHs, we generate a second set of merger trees, sampling 5 halos of mass $\sim 10^{12} M_{\odot}$ and 5 halos of mass $\sim 10^{14} M_{\odot}$ at $z = 0$, which correspond to the Milky Way mass and cluster mass galaxies in the Local Universe. The mass resolution and highest redshift they trace are the same as the first set. We explicitly track the mass growth history of all the progenitors in these trees to $z = 0$ and check if they are able to host SMBH seeds. We will show that the model with small cross-sections ($\sigma \lesssim 0.1 \text{ cm}^2 \text{ g}^{-1}$) can stay consistent with low redshift observations while explaining the massive high redshift SMBHs.

In the top row of Fig. 4.9, we show the mass growth history of the progenitors

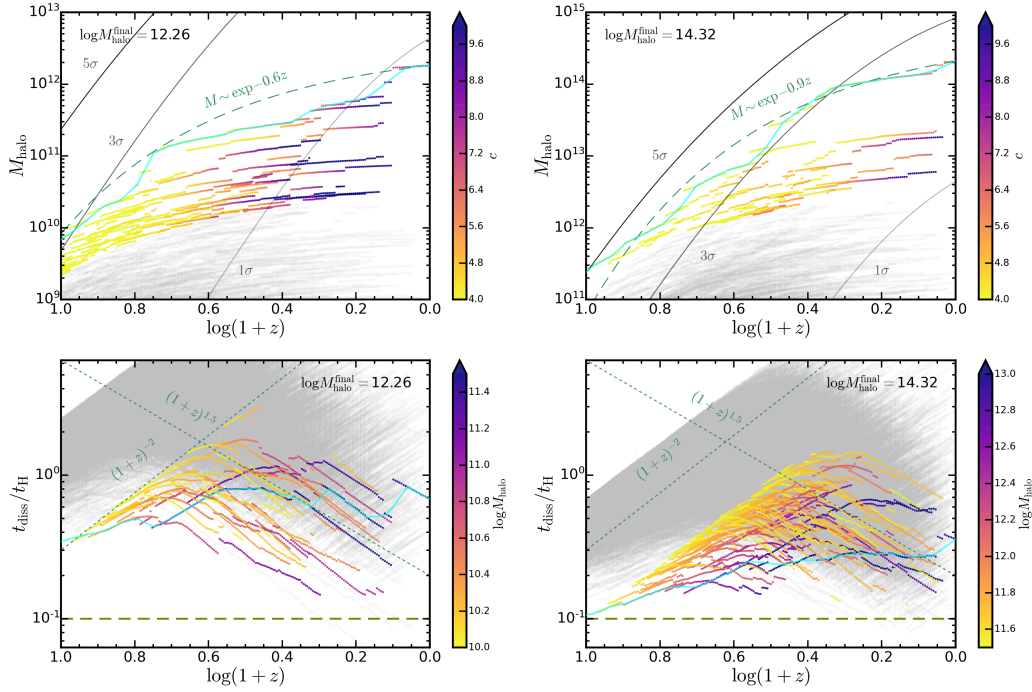


Figure 4.9: *Top: Mass growth history of halo progenitors.* The growth tracks of relatively massive progenitors are color-coded by their concentrations. Low-mass progenitors are shown by the gray cloud. The main progenitor is indicated by the cyan solid line. The green dashed line shows an analytic model for the main progenitor mass growth history [22]. The gray solid lines show the mass of the halo corresponding to a certain rareness of fluctuations. *Bottom: Ratio $t_{\text{diss}}/t_{\text{h}}$ of halo progenitors versus redshift.* The cross-section $(\sigma/m) = 0.05 \text{ cm}^2 \text{ g}^{-1}$ is assumed here. Progenitors that are more massive than $10^{10} M_{\odot}$ are color-coded by their halo masses. The labeling is the same as the top row. The green dashed lines show analytic expectations for the timescales of the low and high redshift branches (as discussed in the main text). The horizontal dashed line indicates the threshold where SMBH seeding will occur assuming $(\sigma/m) = 0.05 \text{ cm}^2 \text{ g}^{-1}$ and $\epsilon = 0.1$.

of a Milky Way mass halo (left) and a cluster mass halo (right). The evolution tracks of progenitors are color-coded by their halo concentration and end when the progenitors merge. The mass growth history of the main progenitor is well described by the analytical model $M \propto e^{-\alpha z}$ [22], with the α values consistent with the ones found therein for both halos. Apparently, for both halos, there exists a population of halos with early assembly times and with limited mass accretion at late times. These halos become much more concentrated than expected from a median mass-concentration relation. Such halos are more abundant in the Milky Way mass halo than in the cluster mass halo, due to the later assembly time of the cluster mass halo and its progenitor (i.e. larger α values). In the bottom row of

Fig. 4.9, we show the ratio $t_{\text{diss}}/t_{\text{h}}$ of halo progenitors as a function of redshift and compare it to the seeding threshold (assuming the fiducial choice of cross-section $\sigma/m = 0.05 \text{ cm}^2 \text{ g}^{-1}$) indicated by the dashed line. It is obvious that there are two branches of halos that are close to the seeding threshold, with the redshift dependence of the timescale as expected from the analytic estimations above. For a Milky Way mass halo, the low redshift branch is closer to the seeding threshold. These highly concentrated, massive progenitors have their central mass densities almost preserved towards low redshift before they merge into the main progenitor and the dissipation timescale is almost a constant in these halos. We note that in most of the Milky Way mass halo merger trees, under the choice of cross-section here, no progenitor can cross the seeding threshold. Occasionally, as indicated by the example in Fig. 4.9), a low-mass progenitor could cross the seeding threshold, but the mass of the SMBH seed formed and its statistics are still compatible with the observed local SMBHs. Such a low-mass seed (compared to the main progenitor) may take too long time to sink to the halo center under dynamical friction to cause any real issues (e.g. [378]). Whether this branch of SMBHs can fully explain the local SMBH populations requires more careful modeling of the late-time evolution of SMBHs and galaxies, which is beyond the scope of this chapter. For the cluster mass halo, the high redshift branch is closer to the seeding threshold. Although the entire population of progenitors is closer to the seeding threshold, the low redshift branch stays at roughly the same position as those in the Milky Way mass halo, primarily due to the late formation times and low halo concentrations. Again, the low redshift branch can hardly cross the seeding threshold. The high redshift branch in the cluster mass halo is at the edge of the seeding threshold such that seeding is most likely to happen in the main progenitor. It is expected that, for more massive halos, the seeding will continue favoring the high redshift branch and eventually SMBH seeds may form in the main progenitor at high redshift. This is exactly the SMBH population discussed in previous sections.

The discussion here demonstrates that there exists a parameter space of dissipative DM where the predictions are consistent with observations at both high and low redshift. The model with $\sigma/m = 0.05 \text{ cm}^2 \text{ g}^{-1}$ (or $\epsilon\sigma/m = 0.005 \text{ cm}^2 \text{ g}^{-1}$ if we make ϵ free) can give rise to the correct abundance of luminous quasars at high redshift while not producing overly massive SMBH in the low redshift Universe. Note again the seeding criterion depends on the product of σ/m and ϵ , so uncertainty in ϵ degenerates with uncertainty in σ/m . If a generic dSIDM model with a constant dissipation fraction f is considered, f is degenerate with the cross-section in the

seeding criterion and the relevant parameter is $f\epsilon\sigma/m$.

4.5 Observational constraints of tdSIDM

Most of the observational constraints for SIDM come from studies of the elastic case, with the stringent ones $(\sigma/m) \lesssim 0.3 - 1 \text{ cm}^2 \text{ g}^{-1}$ from merging galaxy clusters (e.g. [159–162]). The tdSIDM models with $(\sigma/m) \sim 0.05 - 0.1 \text{ cm}^2 \text{ g}^{-1}$ considered in this work are consistent with these constraints, although it is not clear whether dissipation will create any distinct signatures at the cluster scale compared to the elastic case.

Specifically, at the dwarf scale, dSIDM has been considered in some recent studies. For instance, dSIDM with a constant energy dissipation per collision, $E_{\text{loss}} \equiv m v_{\text{loss}}^2$, has been studied in [125] through semi-analytic modeling of dwarf galaxies. The central densities of dwarf galaxies were found to be significantly enhanced by dissipation–accelerated gravothermal collapse, which confronted with the observed local dwarfs led to constraints on dSIDM. The constraints they derived can be roughly translated to our model when the constant energy loss is comparable to the kinetic energy of DM particles. It is roughly equivalent to the $f \sim 0.5$ case, if $E_{\text{loss}} \sim E_{\text{k}}^{\text{rel}} \sim m \langle v_{\text{rel}}^2 \rangle / 4$, which is equivalent to $v_{\text{loss}} \sim 2/\sqrt{\pi} \sigma_v$ assuming the Maxwell-Boltzmann velocity distribution. Considering the typical one-dimensional velocity dispersion of the dwarfs they used, we get $f(\sigma/m) \lesssim 0.15 \text{ cm}^2 \text{ g}^{-1}$ approximately from their constraints. On the other hand, the dSIDM model with fractional energy dissipation, which is of the same family as the tdSIDM model, has been studied in [5] via hydrodynamical simulations of galaxies. Assuming a lower dissipation fraction of $f = 0.5$, they found that dSIDM with $(\sigma/m) \gtrsim 0.1 \text{ cm}^2 \text{ g}^{-1}$ could lead to cuspy and power-law-like central density profiles of dwarf galaxies at the sub-kpc scale. The cuspy profiles are potentially in tension with the kinematic and rotation curve measurements of Local dwarf galaxies (this aspect is expected to be analyzed in more detail in the follow-up work Shen *et al.* [in prep., 2021]). Further investigations are required to consolidate these constraints. Nevertheless, the favored tdSIDM models in this work are still consistent with these low-redshift studies.

In addition, dissipative DM has potential impacts on halo substructures and corresponding strong lensing signals, which remains an appealing aspect to explore. The condensation of dSIDM has implications in explaining the excess of small-scale gravitational lenses recently found in galaxy clusters [379] as well as the unexpected concentration of some substructures [380].

4.6 Summary of the chapter

In this chapter, we have studied a mechanism to seed high redshift SMBHs via the collapse of totally dissipative self-interacting DM (tdSIDM) halos, where the DM particle loses nearly all its kinetic energy during a single collision. The study is motivated by the existence of billion solar mass SMBHs observed in the early Universe ($z \gtrsim 6$), which are in tension with canonical seeding mechanisms. We develop an analytical model for the collapse criteria and timescale of tdSIDM halos, calibrated based on numerical N-body simulations of isolated halos, and then apply this model to Monte-Carlo halo merger trees to make predictions of SMBHs and observed quasars in the cosmological context. Our findings can be summarized as:

- We have performed N-body simulations of isolated, rare halos at high redshift initialized with the Navarro–Frenk–White (NFW) profile, with the inclusion of dissipative DM self-interactions. We find that a constant fraction, $f_{\text{col}} \simeq 3 \times 10^{-3}$, of the halo mass will eventually collapse to the scale below the spatial resolution of the simulations. Surprisingly, the collapsed fraction is insensitive to the mass, size, spin and redshift of the sampled halo. An analytic description of the collapse criteria and timescale is developed and calibrated based on these simulations. This analytic prescription can be applied to halos with various masses, concentrations, and formation redshifts as well as in different cosmological models.
- The unique feature of our seeding mechanism is the rapid formation of SMBHs seeds with an SMBH-to-halo mass ratio of $\sim 3 \times 10^{-3}$. The SMBHs directly seeded from the catastrophic collapse of tdSIDM halos are massive enough to explain the high mass end of SMBHs at $z \gtrsim 6$. The rapid formation of SMBHs in our model implies the existence of very young quasars at high redshift, which is consistent with recent studies that attempt to measure the lifetimes of quasars [202]. Such a young population of quasars is difficult to explain in standard scenarios where SMBHs have to live long enough to grow at some modest multiple of the Eddington limit from much smaller masses.
- We trace the seeding and growth of SMBHs via halo merger trees and derive predictions for the cosmological abundance of SMBHs. With little tuning of the fueling model of SMBHs (the ERDF and the quasar duty-cycle), our model with $\sigma/m = 0.05/0.1 \text{ cm}^2 \text{ g}^{-1}$ (or $\epsilon\sigma/m = 0.005/0.01 \text{ cm}^2 \text{ g}^{-1}$ if we make ϵ free) successfully reproduces the observed quasar luminosity functions at

high redshift, particularly at the bright end. The tuned ERDF and duty-cycle imply that a significant fraction of SMBHs seeded in this way must have low quasar activity, which will hopefully be tested by future quasar surveys.

- SMBHs seeded directly from tdSIDM halos exhibit much larger SMBH-to-halo mass ratios than local SMBHs and lie systematically above the local $M_{\text{BH}} - \sigma_v^*$ relation. This feature is in better agreement with [C II] gas velocity dispersion and host galaxy dynamical mass measured for high redshift massive quasars.
- We compare the cosmic SMBH mass density predicted in our model to the observed SMBH mass density in the Local Universe. We find that the model with $\sigma/m = 0.1 \text{ cm}^2 \text{ g}^{-1}$ (or $\epsilon\sigma/m = 0.01 \text{ cm}^2 \text{ g}^{-1}$) is potentially in tension with observations, since the mass density in this model approaches the local value already at $z \sim 6$, requiring large radiative efficiency to remain consistent with low redshift data. The model with $(\sigma/m) = 0.05 \text{ cm}^2 \text{ g}^{-1}$ (or $\epsilon\sigma/m = 0.005 \text{ cm}^2 \text{ g}^{-1}$) is still compatible with observations. In addition, we find that the growth of SMBHs at high redshift is dominated by dissipative DM rather than baryonic matter, predicting that the integrated luminosity density of quasars (which reflects baryonic accretion) will be significantly smaller than the change in SMBH mass density at high redshift, which is a testable feature of our seeding mechanism.
- While the large SMBH-to-halo mass ratio (3×10^{-3}) found in our N-body simulations can easily explain the most massive SMBHs at $z \gtrsim 6$, which are the most difficult to understand in the standard scenario, one must check with consistency at low redshift, particularly if halos with mass $M \gtrsim 10^{15} M_\odot$ also collapse to form overly massive SMBHs. We show this does not occur because the dissipation timescale sensitively depends on the halo central density, which is relatively low for those massive halos at $z \sim 0$. Therefore our seeding model based on dissipative self-interacting DM is capable of producing SMBHs that are challenging to explain in standard scenarios while remaining consistent with low redshift observations. Though this work focused on explaining the population of high redshift SMBHs, tdSIDM may also explain the origin of SMBHs in Milky Way mass halos. As shown in Fig. 4.2 and Fig. 4.9, Milky Way mass halos may contain progenitors that are formed from rare fluctuations at high redshift. Such rare progenitors have a large central density and are more likely to collapse compared to other progenitors.

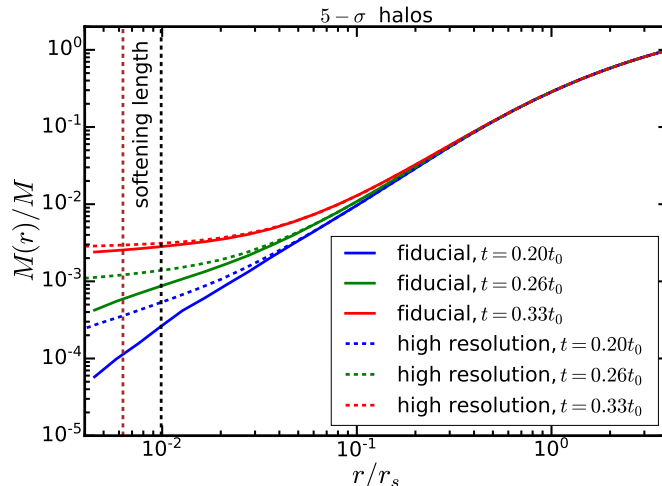


Figure 4.10: Enclosed mass profile of two $5 - \sigma$ halos at $z = 10$ with the same NFW parameters but different simulation parameters. Solid curves represent the mass profile at different times for the fiducial run, while the dashed curves are for a run with a factor of 4 improved resolution (improving both mass and force resolution accordingly). The vertical dashed lines indicate the gravitational force softening length for both the fiducial run and the high-resolution run.

Our model prefers a cross-section of $\sigma/m \sim 0.05 \text{ cm}^2 \text{ g}^{-1}$ (or $\epsilon\sigma/m \sim 0.005 \text{ cm}^2 \text{ g}^{-1}$) to explain the quasar luminosity function at high redshift while remaining consistent with low redshift observations. Such a model is testable in the future once the quasar luminosity function is measured at more redshifts. In the future, quasar surveys conducted with the Nancy Grace Roman Space Telescope, the Rubin Observatory Legacy Survey of Space and Time (LSST), and the James Webb Space Telescope (JWST) can further test our predictions of the quasar luminosity function and the density change of SMBHs at high redshift.

4.7 Convergence Testing

This appendix investigates whether our primary results for isolated NFW halos are sensitive to our choice of gravitational softening length. The worry is that the physics of SMBH formation is significantly different from structure formation, and simulations with different gravitational softening lengths may lead to very different results. We compare our fiducial run to a simulation with different particle numbers and gravitational softening lengths and show that the central regions of DM halos still collapse at the same timescale.

In a cosmological N-body simulation, the gravitational softening length is often taken to be the $d/30$, where d is the particle mean separation in the simulation box.

However, our simulations with isolated NFW halos are different from a cosmological simulation. Our focus in this work is the SMBH formation process at the halo center. Therefore, we are more interested in the particle separation length in the region where catastrophic collapse happens. We take our gravitational softening length to be $2d_0$ where d_0 is the particle mean separation within radius $0.07r_s$ at the beginning of the simulation.

In our fiducial run for various halo masses, the particle number is chosen to be 6×10^6 and the simulation box size is fixed to be 1000 pc. The fiducial run simulated the collapse of $5 - \sigma$ halos from $z = 4 - 10$. To test for convergence, we select a $5 - \sigma$ halo at $z = 10$ with NFW parameter $r_s = 3.3$ kpc and $\rho_0 = 0.316 M_\odot \text{pc}^{-3}$ with gravitational softening length 0.033 kpc. We then run another simulation with improved mass resolution and correspondingly improved force resolution. The particle number in the new run is taken to be 2.4×10^7 and the gravitational softening length is still $2d_0$, corresponding to 0.021 kpc.

As shown in Fig. 4.10, the enclosed mass profiles $M(r)/M$ converge very well when the time approaches the collapse time $0.35t_0$. Even though the simulation with an improved resolution has a larger $M(r)/M$ for small r before the catastrophic collapse, their final predictions for the collapse timescale and the SMBH-to-halo mass ratio do converge. Therefore, we conclude that our fiducial simulations reliably predict the collapse timescale to form an SMBH seed and the SMBH-to-halo mass ratio.

4.8 Considerations in Centrifugal Barrier and Fragmentation

The goal of this Appendix is to demonstrate that the halo angular momentum is not an important consideration for SMBH seeding with tdSIDM, justifying the neglect of angular momentum in the bulk of the analysis.

Centrifugal Barrier

The collapse of a realistic halo with non-zero spin may be halted by the centrifugal barrier [e.g., 381]. The scale of the centrifugal barrier ($\sim \lambda R_{\text{vir}}$) is much larger than the physical scale of SMBH seed formation.

Similar to the seeding mechanism in pristine gas disks [186, 194–199], we first note that the non-axial-symmetric structures originating from global gravitational instability transfer angular momentum outward and enable further collapse of the halo. As the halo center becomes denser, instability builds, triggering a further

collapse of the halo. Run-away collapse to compact objects is realized in this way, even when there is no microscopic physical mechanism to transfer angular momentum outward. Following [195–197], we consider the configuration of the system as a spherical isothermal DM halo of virial mass M_{vir} , with a constant circular velocity V_c and some of the DM condensed to a thick dark disk having mass $m_d M_{\text{vir}}$. The surface density of the dark disk is assumed to be

$$\Sigma(r) = \Sigma_0 e^{-r/R_d}, \quad (4.29)$$

where Σ_0 is the normalization of the surface density, R_d is the scale length of the disk. Note that the qualitative conclusion is not sensitive to the density profile assumed here. The instability of the dark disk is evaluated by the “Toomre Q ” parameter [382], defined as

$$Q = \frac{c_s \kappa}{\pi G \Sigma} = \sqrt{2} \frac{\sigma_v V_c}{\pi G \Sigma_0 R_d}, \quad (4.30)$$

where we have replaced the sound speed c_s with the one-dimensional velocity dispersion of DM in the dark disk σ_v , $\kappa = \sqrt{2} V_c / R_d$ is the epicyclic frequency and we use Σ_0 and R_d as a representative surface density and disk scale. The disk is considered unstable when Q drops below a critical value Q_c of order unity. Since the spherical halo plus dark disk we consider here is only a crude approximation of the dissipative DM configuration, the detailed value of Q_c is uncertain and is left as a free parameter.

If we assume that some mass, $m_a M$, is accreted at the center of the halo and the remaining mass in the disk is $(m_d - m_a)M$, Σ_0 and R_d are related with

$$(m_d - m_a)M = 2\pi \Sigma_0 R_d^2. \quad (4.31)$$

We assume that the dark disk has angular momentum $J_d = j_d J$, where J is the total angular momentum of the halo. J is related to the spin parameter λ of the halo [381]

$$J = \frac{\lambda G M^{5/2}}{|E|^{1/2}} = \sqrt{2} \frac{\lambda G M^2}{V_c}, \quad (4.32)$$

where E is the total energy of the halo, and we have assumed that the halo takes an isothermal distribution of matter (circular velocity is a constant). Taking the condensed dark disk to have the same circular velocity as the halo, we obtain

$$\begin{aligned} J_d &= \int V_c \Sigma_0 e^{-r/R_d} (2\pi r) r dr \\ &= 4\pi V_c \Sigma_0 R_d^3 \\ &= 2(m_d - m_a) M R_d V_c. \end{aligned} \quad (4.33)$$

Combining Eqs. (4.32) and (4.33), we obtain the disk scale length as

$$R_d = \frac{1}{\sqrt{2}} \lambda \left(\frac{j_d}{m_d} \right) \left(\frac{1}{1 - m_a/m_d} \right) \frac{GM}{V_c^2}. \quad (4.34)$$

Inserting this into Eq. (4.31), we obtain Σ_0 , and further substituting into Eq. (4.30) gives

$$Q = \frac{2\lambda}{m_d} \left(\frac{j_d}{m_d} \right) \frac{1}{(1 - m_a/m_d)^2} \frac{\sigma_v}{V_c}. \quad (4.35)$$

At the end of accretion and collapse, the configuration of the system is marginally stable, so that the accreted/collapsed mass m_a can be derived by replacing Q with Q_c

$$\frac{m_a}{m_d} = 1 - \sqrt{\frac{2\lambda}{m_d Q_c} \left(\frac{j_d}{m_d} \right) \left(\frac{\sigma_v}{V_c} \right)}. \quad (4.36)$$

If we neglect angular momentum transfer and the dark disk is formed adiabatically, j_d/m_d should be 1. In the absence of halo spin, the final SMBH seed mass is $m_d M$, so we replace m_d with the collapse fraction f_{col} of a zero-spin halo. Finally, since m_a/m_d cannot exceed unity, we obtain the instability criterion that collapse only occurs when

$$\lambda < \lambda_{\text{max}} = \frac{Q_c f_{\text{col}} V_c}{2 \sigma_v}. \quad (4.37)$$

The corresponding SMBH seed mass fraction is therefore

$$f = f_{\text{col}} \left(1 - \sqrt{\frac{2\lambda}{f_{\text{col}} Q_c} \left(\frac{\sigma_v}{V_c} \right)} \right). \quad (4.38)$$

If we approximate σ_v as $\sigma_v(0.07r_s)$ of an NFW halo given by Eq. (4.11), and calculate V_c with Eq. (4.24), the ratio V_c/σ_v will be a constant $\sqrt{f(2.15)/2.15/F(0.07)} \simeq 1.9$, and the angular momentum barrier for seed formation will thus be independent of halo mass. Under these assumptions, we obtain $\lambda_{\text{max}} \simeq 0.003$ when $Q_c = 1$. However, in simulations, we have found that halos with much larger spin parameters still collapse under dissipative DM self-interactions at a similar collapse timescale.

An alternative to the picture discussed above is angular momentum transfer through microscopic physical processes. In our case, the viscosity from DM self-interactions transports angular momentum through the dark disk. The viscosity of SIDM in the

long-mean-free-path regime ³ can be written as

$$\begin{aligned}\eta &= C\rho\frac{H^2}{t_{\text{r}}} \\ &\simeq \frac{\rho(\sigma/m)\sigma_{\text{v}}^3}{4\pi G},\end{aligned}\quad (4.39)$$

where C is a numerical constant of order unity, and $H = \sqrt{\sigma_{\text{v}}^2/4\pi G\rho}$ is the gravitational scale height. Similar to the theory of accretion disks, the typical timescale for angular momentum to be transported over a length scale L is

$$t_{\text{v}} = \frac{\rho L^2}{\eta} = \frac{4\pi G L^2}{(\sigma/m)\sigma_{\text{v}}^3},\quad (4.40)$$

where we have used Eq. (4.39) in the second line. If we assume that the typical length scale L for angular momentum transport is the collapse radius $\sim 0.07r_{\text{s}}$ found in our simulations, and approximate σ_{v} with $\sigma_{\text{v}}(0.07r_{\text{s}})$ of a NFW halo given by Eq. (4.11), we obtain

$$t_{\text{v}} = \frac{0.07^2}{(\sigma/m)F^{3/2}(0.07)} \frac{1}{\sqrt{4\pi G\rho_0^3 r_{\text{s}}^2}}.\quad (4.41)$$

The viscous timescale has exactly the same scaling behavior as the dissipation timescale in Eq. (4.12). The ratio between them can be estimated as

$$\begin{aligned}\frac{t_{\text{v}}}{t_{\text{diss}}} &\simeq \frac{t_{\text{v}}}{1/\rho(0.07r_{\text{s}})(\sigma/m)\sigma_{\text{v}}(0.07r_{\text{s}})} \\ &= \frac{0.07}{(1+0.07)F(0.07)} \sim O(1).\end{aligned}\quad (4.42)$$

This suggests that the viscous timescale is comparable to the dissipation timescale. In this case, angular momentum is transported efficiently, and the central collapse mimics the zero spin case. This is the reason why we do not observe the effect of the centrifugal barrier in the simulations.

Fragmentation limit

Another criterion is that the dissipation timescale remains larger than the dynamical timescale at the center of the halos, such that local fragmentation does not occur, preventing the formation of a single SMBH seed [383]. If fragmentation does occur, the concentration of the largest amount of mass in the center will be suppressed and

³The mean free path of DM particles is much longer than the gravitational scale height of the system. For the model studied in this chapter with $\sigma/m \lesssim 0.1 \text{ cm}^2 \text{ g}^{-1}$, the requirement is satisfied.

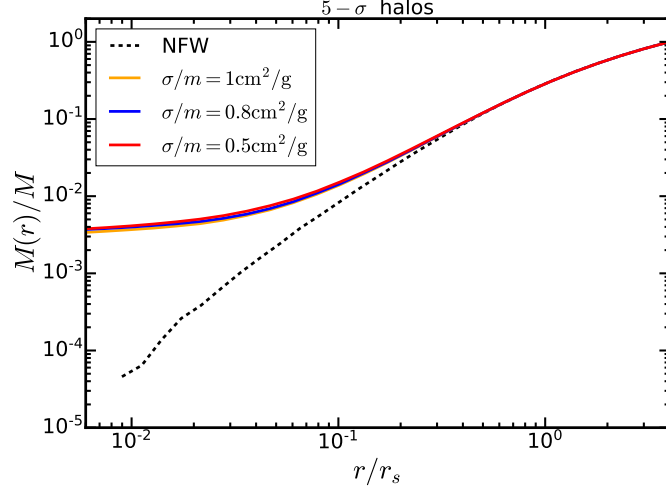


Figure 4.11: Enclosed mass profile of three collapsed $5 - \sigma$ halos at $z = 10$ with the same NFW profile parameters. The collapse of those halos is simulated with different cross-sections but the same mass and force resolution. The enclosed profiles are flat at small radii, suggesting the formation of SMBHs. Therefore, the universality of the collapse fraction is not violated by changing the cross-section of tdSIDM.

small clumps will form instead. The dynamical time within a collapse radius is defined as $t_{\text{dyn}} = 1/\sqrt{4\pi G \rho_{\text{col}}}$, where ρ_{col} is the average density of DM halo within collapse radius $0.07r_s$. We find the ratio of dissipation time to dynamical time is

$$\begin{aligned} \frac{t_{\text{diss}}}{t_{\text{dyn}}} &\approx 1.8 \left(\frac{4}{c}\right)^2 \left(\frac{10}{1+z}\right)^2 \left[\ln(1+c) - \frac{c}{1+c} \right] \\ &\times \left(\frac{1 \text{ cm}^2 \text{ g}^{-1}}{\sigma/m}\right) \left(\frac{10^{12} M_{\odot}}{M}\right)^{1/3}. \end{aligned} \quad (4.43)$$

For rare halos that can seed SMBHs, the dissipation timescale is always larger than the dynamical time when $\sigma/m \lesssim 1 \text{ cm}^2 \text{ g}^{-1}$. As we show in Sec. 4.3 and Sec. 4.4, the preferred cross-section for seeding SMBHs at high redshift, while maintaining consistency with low redshift observations, is $\sigma/m = 0.05 \text{ cm}^2 \text{ g}^{-1}$. In such cases, the dissipation time scale is always an order of magnitude larger than the dynamical timescale, preventing the fragmentation of the DM halo.

4.9 Consideration of the universal collapse fraction

In the paper, we find a universal collapse fraction, $f_{\text{col}} \approx 3 \times 10^{-3}$, of tdSIDM halos that is independent of halo mass, size, spin, and formation redshift. This universal collapse fraction corresponds to a collapse radius of $r_0 \approx 0.07r_s$. To further confirm the universality of the collapse fraction numerically, we run N-body simulations

with different DM self-interaction cross-sections for the same $5 - \sigma$ halo formed at $z = 10$. The enclosed profiles of the collapsed DM halos, as shown in Fig. 4.11, suggest that the collapse fraction is also universal for different cross-sections. The goal of the following is to explain the universal collapse fraction from the theoretical perspective.

The characteristic length scale of the gravitational collapse of gas clouds against thermal pressure support is the Jeans length

$$\lambda_j = c_s \sqrt{\frac{\pi}{G\rho}}, \quad (4.44)$$

where c_s is the sound speed and ρ is the mass density. Applying the concept to weakly collisional dSIDM fluid, we replace c_s with the one-dimensional velocity dispersion σ_v and calculate ρ as the averaged mass density within a radius r . Thus, we obtain

$$\frac{r}{\lambda_j(r)} \propto \sqrt{\frac{GM(r)/r^2}{\sigma_v^2(r)/r}}, \quad (4.45)$$

where $\sigma_v(r)$ is the velocity dispersion given by Eq. (4.11), $M(r)$ is the enclosed halo mass within radius r . When the ratio r/λ_j is at its maximum, it reaches the point with the maximum gravitational instability. If the enclosed halo mass is given by the NFW profile, one can obtain that r/λ_j reaches maximum at $r \simeq 0.06r_s$, which is close to the collapse radius $0.07r_s$ we found in our simulations. The surprising coincidence suggests that the size of the initially collapsed region is likely related to the gravitational instability.

Furthermore, after the mass within a radius r collapse to a point mass, the boundary of spherical accretion of the surrounding medium is given by the Bondi-Hoyle-Lyttleton (BHL) radius [384–387]

$$R_b(r) = \frac{2GM(r)}{c_s^2} = \frac{2GM(r)}{\sigma_v^2(r)}, \quad (4.46)$$

where the point mass has been assumed to be stationary with respect to the surrounding medium and we have substituted c_s with $\sigma_v(r)$ again. It is worth noting that the ratio of the BHL radius to r is proportional to $(r/\lambda_j)^2$. Therefore, the ratio R_b/r also reaches its maximum at $r \simeq 0.06r_s$ and the numeric value of the maximum is actually close to unity. This indicates that the accretion of surrounding DM is strongest at this universal radius and will be less effective when collapse extends to larger radii since $R_b(r)$ will quickly drop below r .

Although accretion will be prohibited when $R_b(r)$ drops below r , dissipative self-interactions can continually lower the kinetic energy of DM, decrease the velocity dispersion and enlarge the BHL radius, which will restore accretion again. But the accretion also relies on mechanisms to transfer angular momentum outward. As discussed in Section 4.8, in the system considered here, two important mechanisms would be torques of non-axial-symmetric structures originating from gravitational instability and viscous angular momentum transfer. As found earlier this section, the gravitational instability becomes weaker at larger radius beyond $r \simeq 0.06r_s$. For the viscosity, we can compute the ratio between t_v and t_{diss} as in Eq.(4.42)

$$\begin{aligned} t_v/t_{\text{diss}} &\simeq \frac{4\pi Gr^2}{(\sigma/m)\sigma_v^3(r)} \bigg/ \frac{1}{\bar{\rho}(r)(\sigma/m)\sigma_v(r)} \\ &= \frac{3GM(r)}{\sigma_v^2(r)r}, \end{aligned} \quad (4.47)$$

where we have used r as the characteristic length scale for angular momentum transfer and used the averaged mass density within radius r for the calculation of t_{diss} . It is surprising that the ratio t_v/t_{diss} is proportional to R_b/r as well as $(r/\lambda_j)^2$. The ratio also reaches its maximum at $r \simeq 0.06r_s$ and takes an order-unity value at its maximum. Beyond the radius $0.06r_s$, viscous angular momentum transfer will also quickly become ineffective. Therefore, the collapse of the central halo eventually stagnates at the universal radius $r \simeq 0.06r_s$. These arguments we discussed above should work for generic dissipative DM models. For instance, the fractional kinetic energy loss f does not change the form of the collapse timescale and the Jeans length. If the dissipation is velocity dependent, the arguments of the Jeans length and Bondi radius still applies. Therefore, even if the fractional kinetic energy loss f is significantly different from the current value or varies with velocities, one would still expect the collapse fraction to be universal. Baryonic physics can potentially affect the collapse fraction, which we leave for future work.

SIGNATURES OF ELASTIC SIDM IN CLUSTER MASS HALOS

Xuejian Shen, Thejs Brinckmann, David Rapetti, Mark Vogelsberger, Adam Mantz, Jesús Zavala, and Steven W. Allen. X-ray morphology of cluster-mass haloes in self-interacting dark matter. *MNRAS*, 516(1):1302–1319, October 2022. doi: 10.1093/mnras/stac2376.

5.1 Abstract of the chapter

We perform cosmological zoom-in simulations of 19 relaxed cluster-mass halos with the inclusion of adiabatic gas in the cold DM (CDM) and self-interacting DM (SIDM) models. These clusters are selected as dynamically relaxed clusters from a parent simulation with $M_{200} \simeq 1 - 3 \times 10^{15} M_{\odot}$. Both the DM and the intracluster gas distributions in SIDM appear more spherical than their CDM counterparts. Mock X-ray images are generated based on the simulations and are compared to the real X-ray images of 84 relaxed clusters selected from the *Chandra* and *ROSAT* archives. We perform ellipse fitting for the isophotes of mock and real X-ray images and obtain the ellipticities at cluster-centric radii of $r \simeq 0.1 - 0.2 R_{200}$. The X-ray isophotes in SIDM models with increasing cross-sections are rounder than their CDM counterparts, which manifests as a systematic shift in the distribution function of ellipticities. Unexpectedly, the X-ray morphology of the observed non-cool-core clusters agrees better with SIDM models with cross-section $(\sigma/m) = 0.5 - 1 \text{ cm}^2 \text{ g}^{-1}$ than CDM and SIDM with $(\sigma/m) = 0.1 \text{ cm}^2 \text{ g}^{-1}$. Our statistical analysis indicates that the latter two models are disfavored at the 68% confidence level (as conservative estimates). This conclusion is not altered by shifting the radial range of measurements or applying the temperature selection criterion. However, the primary uncertainty originates from the lack of baryonic physics in the adiabatic model, such as cooling, star formation, and feedback effects, which still have the potential to reconcile CDM simulations with observations.

The chapter is organized as follows: details of the simulations are introduced in Section 5.2, while the observational samples are introduced in Section 5.3. In Section 5.4, we discuss the modeling of the X-ray emission and the generation of mock images for the simulated clusters. Details of the morphological analysis of the mock and real X-ray images are also discussed in this section. The results

are presented in Section 5.5 and are discussed further in Section 5.6. Finally, we summarize and conclude in Section 5.7.

5.2 Simulations

The analysis in this chapter is based on a suite of cosmological zoom-in simulations of cluster-mass halos (with the DMO version presented in Brinckmann et al. 255, Sokolenko et al. 388). The simulations are performed using the moving-mesh code AREPO [389] with the inclusion of adiabatic gas. The code employs the tree-particle-mesh (Tree-PM) algorithm for gravity and a finite-volume/Godunov scheme for hydrodynamics on an unstructured, moving Voronoi mesh. The halos for zoom-in simulations were selected as dynamically relaxed systems from a large $1(\text{Gpc}/h)^3$ parent simulation with an effective resolution of 512^3 DM particles [see 255, for details on the relaxation criteria used]. The zoom-in simulations have an effective resolution of 4096^3 DM particles in the high resolution regions, which are surrounded by regions of intermediate resolution and finally low-resolution regions with an effective resolution of 256^3 particles. For the high-resolution region, the effective Plummer equivalent gravitational softening length of DM is $\epsilon = 5.4 \text{ kpc}/h$ and the DM particle mass resolution is $m_{\text{dm}} = 1.07 \times 10^9 M_{\odot}/h$.

DM self-interactions were simulated in a Monte Carlo fashion using the module developed in Vogelsberger et al. [87, 329], assuming isotropic and elastic scattering. In this work, we only study the case of a constant self-interaction cross-section, and in particular we perform simulations for three cases: $(\sigma/m) = 0.1 \text{ cm}^2 \text{ g}^{-1}$ (SIDM-c0.1), $(\sigma/m) = 0.5 \text{ cm}^2 \text{ g}^{-1}$ (SIDM-c0.5), $(\sigma/m) = 1 \text{ cm}^2 \text{ g}^{-1}$ (SIDM-c1), in addition to the CDM case for comparison. Our simulations use the cosmological parameters originally adopted in Brinckmann et al. [255]: $\Omega_{\text{m}} = 0.315$, $\Omega_{\Lambda} = 0.685$, $\Omega_{\text{b}} = 0.049$, $h = 0.673$, $\sigma_8 = 0.83$ and $n_{\text{s}} = 0.96$, which are consistent with Planck results [390].

Compared to the DMO version of the simulations in Brinckmann et al. [255], Sokolenko et al. [388], our simulations introduce adiabatic gas cells, which are generated in the initial conditions by splitting DM particles, with the mass ratio between gas and DM particles set initially by the universal baryon fraction. The gas cells (as Voronoi meshes) are regularized by their masses or face solid angles and are allowed to be split or merged. The baryonic mass resolution in the final halo is roughly the initial gas cell mass, $m_{\text{b}} \simeq m_{\text{dm}} \Omega_{\text{b}}/(\Omega_{\text{m}} - \Omega_{\text{b}}) \simeq 0.18 m_{\text{dm}} \simeq 2 \times 10^8 M_{\odot}/h$. The spatial resolution of hydrodynamics is roughly the cell equivalent

size (the radius of the sphere with the average volume of the cells) $h_b = 4.8 \text{ kpc}/h \times (\rho_b/10^5 \text{ M}_\odot/\text{kpc}^3)^{-1/3}$, where $10^5 \text{ M}_\odot/\text{kpc}^3$ is the typical gas density at cluster centers in our simulations. The gravitational softening length of adiabatic gas is chosen to be the same as that of DM, i.e., $\epsilon_{\text{gas}} = 5.4 \text{ kpc}/h$ and the adiabatic index of gas is chosen to be $5/3$.

The main target halos are identified in the zoom-in regions and the DM particles or gas cells are assigned to the main target halos using the Friends-of-Friends (FoF) algorithm. The virial mass and radius of each halo are defined based on the density criterion, 200 times the critical density at $z = 0$ ¹, and are therefore referred to as M_{200} and R_{200} , respectively. The virial temperature is defined as $T_{\text{vir}} = (\mu m_p/2k_b)GM_{200}/R_{200}$, where m_p is the proton mass, k_b is the Boltzmann constant and μ is the mean molecular weight that takes the value 0.59 (see also Equation 5.3).

The convergence radius of collisionless particles can be calculated using the Power et al. [26] criterion. Power et al. [26] argued that the artificial central “flattening” of DM profiles is driven by two-body relaxation, and that robust results should be obtained outside the radius where the relaxation time is comparable to the Hubble time. This is equivalent to the criterion

$$\frac{\sqrt{200}}{8} \frac{N(r)}{\ln(N(r))} \left(\frac{\bar{\rho}(r)}{\rho_{\text{crit}}} \right)^{-1/2} \geq 0.6, \quad (5.1)$$

where $N(r)$ is the number of particles within a radius r , ρ_{crit} is the critical density of the Universe at $z = 0$ and $\bar{\rho}(r)$ is the average density within r . We evaluate the convergence radius for each of our simulations based on this criterion and the obtained values are listed in Table 5.1. On the other hand, the convergence of the hydrodynamical properties of the gas is more complicated and depends on the numerical method employed. In Section 5.5, we will explicitly check how the hydrodynamical properties of the gas in our simulations are resolved and discuss the issue of convergence.

The typical virial mass of the simulated halos is $M_{200} \simeq (1 - 3) \times 10^{15} \text{ M}_\odot$ and the typical size is $R_{200} \simeq 2 - 3 \text{ Mpc}$. The detailed properties of all the simulated halos are listed in Table 5.1.

¹Some cluster studies adopt instead the redshift-dependent overdensity criterion from Bryan and Norman [249] which gives $\Delta_c(z = 0) \simeq 100$. This could lead to about 30% (10%) increase in the virial radius (mass).

Halo ^a name	M_{200}^{cdm} [$10^{15} M_{\odot}$]	R_{200}^{cdm} [Mpc]	$T_{\text{vir}}^{\text{cdm}}$ [10^7 K]	$R_{\text{conv}}^{\text{b}}$ [kpc]
halo11	2.91	3.03	14.7	35.9
halo39	1.47	2.41	9.29	33.7
halo43	1.54	2.45	9.61	35.0
halo55	1.38	2.36	8.94	35.0
halo83	1.52	2.43	9.50	35.8
halo84	1.66	2.51	10.1	34.7
halo92	1.32	2.33	8.68	34.3
halo102	1.39	2.37	8.98	33.8
halo128	1.40	2.37	9.00	35.6
halo136	1.10	2.18	7.65	33.0
halo144	1.50	2.42	9.43	34.1
halo159	1.25	2.28	8.35	35.5
halo162	1.34	2.34	8.75	34.8
halo165	1.26	2.28	8.38	36.1
halo171	1.30	2.31	8.59	34.8
halo194	1.54	2.45	9.61	35.3
halo210	1.15	2.22	7.88	36.1
halo215	1.24	2.27	8.30	36.0
halo217 ^c	1.29	2.57	7.68	38.9

Table 5.1: Simulated cluster-mass halos in the suite.

(a) Each halo is simulated in CDM, SIDM-c0.1, SIDM-c0.5, and SIDM-c1. The bulk properties of these halos are indistinguishable in different DM models, so we only list the properties in the CDM simulations here.

(b) The radius of convergence of DM properties (based on the Power et al. 26 criterion discussed in Section 5.2). We present the maximum convergence radius for simulations in all four DM models as a conservative estimate.

(c) Due to a technical issue, the simulation was stopped at $z \simeq 0.18$ instead of $z = 0$. We approximate the $z = 0$ results with this snapshot.

5.3 Observational samples

The observational samples we use consist of relaxed galaxy clusters as selected in Mantz et al. [23, 391] using three morphological indicators, symmetry, peakiness, and alignment of cluster X-ray images. Mantz et al. [23] developed a symmetry–peakiness–alignment (SPA) criterion for relaxation and applied this analysis to a large sample of galaxy clusters with archival *Chandra* and *ROSAT* observations, which resulted in 40 relaxed clusters at $z \lesssim 1$. Each of these clusters has the cleaned science image, the blank-sky event file, and an appropriate exposure map, along with the blank-sky normalization factor and its statistical error, which all serve as input to the morphological algorithm. Details of the sample selection, data reduction,

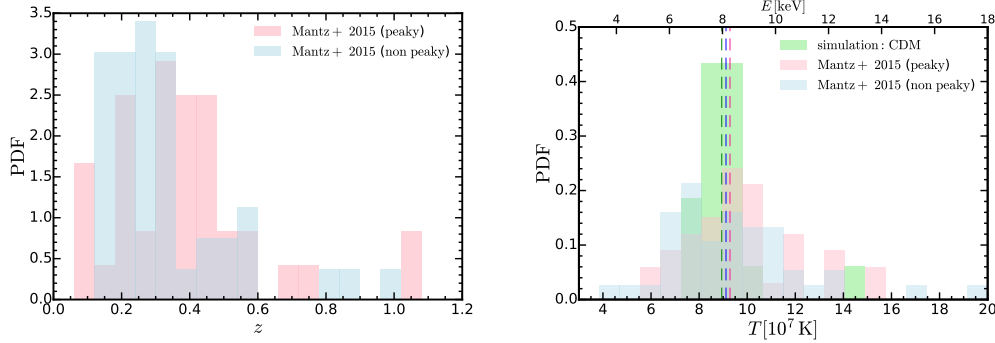


Figure 5.1: Redshift and temperature distributions of the observed clusters and temperature distribution for the simulated clusters. *Left:* Redshift distribution of the observed clusters. The distributions of the “peaky” and “non-peaky” samples are shown in red and blue. For both distributions, most of the clusters fall in the range $0.1 \lesssim z \lesssim 0.5$, with a few outliers out to $z \sim 1$. *Right:* Temperature distribution of the observed (red and blue) and the simulated clusters (green). The median temperature of each sample is shown by a corresponding vertical dashed line. On average, the temperatures of simulated clusters are fairly consistent with the observed samples, despite having a smaller dispersion in temperature.

and post-processing can be found in Mantz et al. [23, 391]. The typical ICM temperature of these clusters is 5 - 10 keV (about $5 - 10 \times 10^7$ K), which is in good agreement with the virial temperatures of the simulated clusters listed in Table 5.1. The original peakiness criterion, however, preferentially selects clusters with cool cores, which indicates strong radiative cooling processes at cluster centers. Cooling and the subsequent star formation as well as supernovae and active galactic nuclei (AGN) feedback could significantly impact the structure of the central halo. Since our simulations do not capture these processes, we specifically select another set of clusters that meet the symmetry–alignment criterion but not the peakiness criterion, referred to as the “non–peak” clusters, while the original set of SPA selected clusters is instead referred to as the “peaky” clusters. The new set of “non–peaky” clusters consists of 44 relaxed clusters. We will perform analyses on both sets of clusters to study the potential impact of cluster cool cores on X-ray morphology.

In Figure 5.1, we show the redshift (left panel) and temperature distributions (right panel) of the observed clusters and the temperature distribution for the simulated clusters (right panel). For simulations, the ICM gas temperature is approximated as the virial temperature T_{vir} , which is tested to be close to the X-ray surface-brightness weighted temperature of ICM gas. Most of the observed clusters, either the “peaky” or the “non-peaky” ones, fall in the redshift range $0.1 \lesssim z \lesssim 0.5$.

The median temperatures of the observational samples and the simulated clusters match reasonably well, but the observational samples show larger dispersion in temperature.

5.4 Methods

Brinckmann et al. [255] found that halo shapes are more sensitive to DM self-interactions at larger radii than spherically-averaged density profiles. Signatures of SIDM can be found in halo shapes out to the radii where density profiles already converge to the CDM prediction. The radial range of 10-20% R_{200} was found to be a suitable range where substantial differences between SIDM and CDM are observed in DMO simulations, and where it was speculated that the impact of complicated baryonic physics in the central galaxy would be limited. The primary goal of the present work is to have a more direct comparison of the halo morphology from simulations and observations, through more realistic modeling of the X-ray emission from simulated clusters and two-dimensional shape analysis of mock/real X-ray images in the radial range of interest.

Mock X-ray images

We begin by generating the X-ray spectrum for every gas cell in each of the halos based on a table of spectral templates. The templates are calculated using the Astrophysical Plasma Emission Code [APEC 392] model implemented in the `PyATOMDB` code, which utilized the atomic data from `AtomDB v3.0.9` [last described in 393]. The model gives the emission spectrum of collisional-ionized diffuse gas in equilibrium with a given temperature and metal abundance pattern. The temperature of a gas cell from the simulations is calculated as

$$T = \frac{(\gamma - 1)U\mu m_p}{k_b}, \quad (5.2)$$

where U is the internal energy of the gas cell, $\gamma = 5/3$ is the assumed adiabatic index and μ is the mean molecular weight, which can be calculated as

$$\mu = \frac{4}{1 + 3X_h + 4X_h x_e}, \quad (5.3)$$

where $X_h = 0.76$ is the hydrogen mass fraction in the Universe and $x_e (\equiv n_e/n_h)$ is the electron abundance, assumed to be 1.17 [394]. The abundance pattern is set to solar values following Anders and Grevesse [394], while the ICM metallicity is set to $0.25 Z_\odot$ [e.g., 395, 396]. We note that, for hot intracluster gas as considered here ($T \gtrsim 10^7$ K), the emission is dominated by thermal Bremsstrahlung and it

is insensitive to details of the abundance pattern. Then, we account for galactic absorption with the photoelectric absorption cross-section given by Morrison and McCammon [397], assuming a fixed galactic hydrogen column density of $N_h = 2 \times 10^{20} \text{ cm}^{-2}$. This effectively decreases the rest-frame soft X-ray luminosity by only $\sim 3\%$. The energy range and resolution of the spectra depend on the desired instrument. For example, an instrument similar to Chandra ACIS-I has an energy range of 0.5 - 10 keV with an energy resolution of 150 eV. For our templates, we adopt energy bins with high resolution 10 eV across 0.1 - 100 keV. These spectral templates describe the energy emitted per unit time in each energy bin, $f(E, T)$, normalized by the emission measure. Assuming the size of the cluster is much smaller than the cosmological distances involved, the observed X-ray flux (per unit energy per unit area and per unit time) can be calculated as

$$\begin{aligned} f^{\text{obs}}(E_{\text{obs}}) &= \frac{(1+z)}{4\pi D_L^2} \int_{\text{l.o.s.}} f^{\text{rst}}(E_{\text{rst}}, T) n_e n_h dV \\ &= \frac{(1+z)}{4\pi D_L^2} \int_{\text{l.o.s.}} f^{\text{rst}}((1+z)E_{\text{obs}}, T) n_e n_h dV, \end{aligned} \quad (5.4)$$

where D_L is the luminosity distance, n_h (n_e) is the hydrogen (electron) number density, “obs” and “rst” refer to the observer’s frame and the rest frame, respectively. The integration is performed along the line of sight. If we consider the integrated luminosity in an energy band in the observer’s frame, we obtain

$$\begin{aligned} F^{\text{obs}} &= \int_{E_{\text{min}}}^{E_{\text{max}}} f^{\text{obs}}(E_{\text{obs}}) dE_{\text{obs}} \\ &= \frac{1}{4\pi D_L^2} \int_{\text{l.o.s.}} n_e n_h dV \int_{(1+z)E_{\text{min}}}^{(1+z)E_{\text{max}}} f^{\text{rst}}(E_{\text{rst}}, T) dE_{\text{rst}}, \end{aligned} \quad (5.5)$$

where we choose $E_{\text{min}}, E_{\text{max}} = 0.6, 2 \text{ keV}$ for the soft X-ray band images, and for simulated halos (evolved to $z = 0$) we assume a small dummy “emission” redshift of 0.03, which does not have any real impact on the flux except for a constant normalization change. In practice, we choose to evaluate the integral over energy in Equation 5.5 first, solely based on the spectral templates. Then, we evaluate the line-of-sight integral based on the particle information obtained from simulations.

Finally, for each pixel with physical side length L_p , the surface brightness can be calculated as

$$S.B.(\text{pixel}) \simeq \frac{F^{\text{obs}}}{(L_p/D_a)^2}, \quad (5.6)$$

where D_a is the angular diameter distance. For an annulus with a surface area A and cluster-centric radius r , the surface brightness profile of a simulated cluster can

be calculated in a similar way

$$S.B.(r) \simeq \frac{F^{\text{obs}} D_a^2}{A(r)}. \quad (5.7)$$

For each simulated cluster, we pick 12 viewing angles that correspond to the 12 vertices of the $N = 1$ Healpix sphere [398] oriented in the simulation coordinates. Then, for each viewing angle, we generate an X-ray image of the cluster with a physical side length of $L = 0.6 R_{200}$ and $N_p = 1024$ pixels on each side, following the steps described above. Gas cells are binned in pixels and the X-ray surface brightness in the soft X-ray band (0.6 – 2 keV) is calculated for each pixel. We note that the equivalent size h_b of the gas cell could be larger than the physical size of the pixels. So the X-ray emitting gas cells should be considered as smoothed distributions of emitting material rather than discrete particles. As an approximate correction for this effect², the images are convolved with a Gaussian kernel with bandwidth h_b .

Shape analysis of X-ray isophotes

Based on the mock X-ray images created from the simulations, we use the ISOPHOTE package in the PHOTUTILS code to perform ellipse fitting of isophotes using the iterative algorithm introduced in Jedrzejewski [399]. Each isophote is fitted for a pre-defined semi-major axis length. The algorithm starts from a first guess of the elliptical isophote, defined by approximate values of center coordinates, ellipticity (e), and position angle (ϕ). The ellipticity is defined as

$$e = 1 - \frac{b}{a}, \quad (5.8)$$

where a and b are the semi-major and semi-minor axes of the ellipse, respectively. Then the fitting is done recursively to minimize the intensity variations of pixels along the elliptical path. For the first guess, we choose the semi-major axis to be 15% R_{200} (the median of the radial range of interest) and set the center of the ellipse as the cluster center. We then derive the first guess of the ellipticity and position angle by recursively doing isophote fitting at the semi-major axis of 15% R_{200} , until

²In principle, the gas cells should be smoothed before being binned in pixels and used in flux calculations. For our application, this is equivalent to smoothing after the images are generated. The argument is supported by the following estimations: The typical displacement of particle coordinates to the pixel center scales as $1/n^{1/2}$ [pixel], where n is the number of particles projected in a pixel $\sim (L/h_b)^3/N_p^2$. For reference, the smoothing kernel bandwidth is $N_p h_b/L$ [pixel]. The ratio of the two is a constant $\sim (h_b/L)^{1/2} \sim 0.07$, which corresponds to ~ 0.03 in the logarithm of the flux, and is therefore small enough to be neglected.

the ellipticity and position angle are converged ($\Delta e < 0.03$, $\Delta\phi < 0.03 \times 2\pi$). After fitting the ellipse that corresponds to a given value of the semi-major axis, the axis length is incremented (or decremented) following a pre-defined rule and the fitting procedure is repeated again at the new semi-major axis. The first guess for the ellipse parameters is taken from the previously fitted ellipse with the closest semi-major axis length to the current one. The fitting will be terminated when either the maximum acceptable relative error in the local radial intensity gradient is reached or a significant fraction of pixels on the ellipse lie outside the image. We define the effective radius of a fitted isophote as the geometric mean of the semi-major and semi-minor axes, $r_{\text{eff}} = \sqrt{(a^2 + b^2)/2}$, and the results can be translated into ellipticity values as a function of r_{eff} . To get a measure of the ellipticity in the radial range of interest, we compute the average ellipticity at 10 - 20% R_{200} .

For the X-ray images from observations, we use the SPA code developed in Mantz et al. [23, 391], which was used for the original sample selection and morphological analysis, to perform isophotes identification and ellipse fitting. Along with the cleaned science image, the algorithm takes the exposure map of observations, the sky background noise, the blank-sky normalization factor, and its statistical error as inputs. We refer readers to Mantz et al. [23] for a detailed description of the algorithm. To standardize the surface brightness of clusters, the code motivated a redshift- and temperature-dependent scaling of the surface brightness based on the self-similar model of Kaiser [400] [see also 170]. The surface brightness is normalized in units of

$$f_s = K(z, T, N_h) \frac{E(z)^3}{(1+z)^4} \left(\frac{k_b T}{\text{keV}} \right) \quad (5.9)$$

$$\text{photons Ms}^{-1} \text{ cm}^{-2} (0.984 \text{ arcsec})^{-2},$$

where $K(z, T, N_h)$ is the K-correction calculated with the APEC model as done in Section 5.4 and $E(z) \equiv H(z)/H_0$. The scaling reduces the redshift and halo mass dependence of the surface brightness in observational samples. Assuming the self-similarity of relaxed clusters, it becomes possible to approximately identify corresponding regions of clusters with different masses and redshifts, without explicitly assuming the angular diameter distance to each or a prescription for estimating some scale radius. The isophotes of the images will be determined based on flux levels (in unit of f_s) $S_j = N_j f_s$, where we set the number of isophotes to three so $j = 0, 1, 2, 3$. N_j will be uniformly spaced in the logarithm, and the minimum and maximum levels (N_0 and N_3) will be tuned such that the radii of the isophotes roughly match the

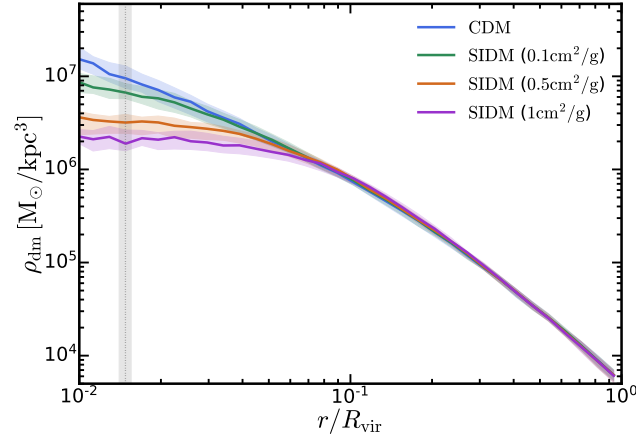


Figure 5.2: DM mass density profiles of the simulated clusters. For each DM model, we show the median and 1σ dispersion of the density profiles of the simulated clusters. The grey dotted line with a shaded region indicates the conservative estimation of the convergence radii of DM properties with its error. SIDM halos develop thermalized cores with flat central density profiles, in contrast to the cuspy central profile in CDM. The core size increases with greater self-interaction cross-sections. These differences exist outside the convergence radius, but eventually become negligible at the outskirts of the halos ($\gtrsim 5\%$ R_{200}).

radial range of interest (see Section 5.5 for the tuning), $10 - 20\%$ R_{200} . After an adaptive smoothing of the original flat-fielded image, the code identifies pixels in isophotes based on pre-defined surface brightness levels S_j . Then, an elliptical shape is fit to each of these isophotes, minimizing the sum of absolute distances from the ellipse to each pixel in the isophote along the line passing through the pixel and the ellipse center. The semi-major axis, center coordinates, position angle and ellipticity of each isophote are obtained. The uncertainties of the measured morphological parameters can be derived by performing the steps above on bootstrap realizations of each observation. Since the typical uncertainty in ellipticity is about two orders of magnitudes smaller than the halo-to-halo variation, in general, we ignore it in the following analysis.

5.5 Results

Density profile

In Figure 5.2, we show the DM mass density profiles of the simulated clusters. They are the average densities measured in uniformly spaced (in the logarithm) spherical shells. Both the median and 1σ dispersion of the density profiles are presented. The radius of convergence of DM properties is calculated using Equation 5.1 in

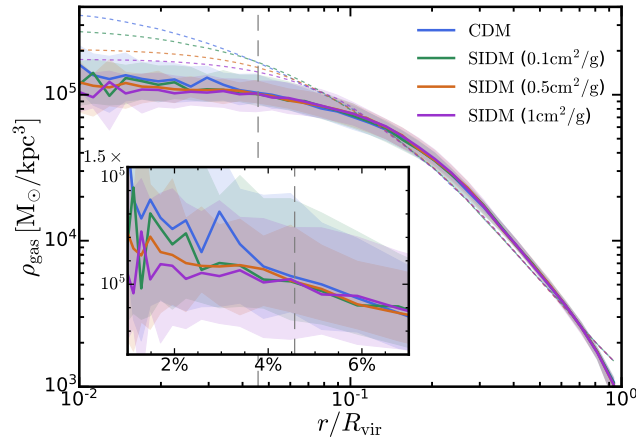


Figure 5.3: Gas mass density profiles of the simulated clusters. The labeling is the same as in Figure 5.2. The convergence radius for hydrodynamical properties of the gas is ambiguous, so we choose 16 times the hydro spatial resolution h_b as a reference, indicated with the grey dashed line (see Figure 5.4 and the discussion at the end of Section 5.5 for the convergence criterion). The colored short dashed lines show gas density profiles inferred from the gravitational potential of the gas, assuming that the intracluster gas is isothermal and in hydrostatic equilibrium. A zoom-in subplot is included to compare density profiles at the center. Unlike DM, the gas density profiles show little difference between DM models. The central densities are also lower than expected from the hydrostatic equilibrium predictions.

Section 5.2 and listed in Table 5.1. For each cluster, we choose the maximum convergence radius from all four DM models as a conservative estimate. The median and 1σ dispersion of the convergence radii of all simulated clusters are shown with the vertical dashed line and the shaded region. Unlike the cuspy central profile in CDM, SIDM halos develop flat and thermalized cores, with increasing core sizes with higher self-interaction cross-sections. Compared to the CDM case, the central DM density in the SIDM model with $(\sigma/m) = 1 \text{ cm}^2 \text{ g}^{-1}$ is about five times (circa 0.7 dex) lower at $r \sim 2\% R_{200}$. Even for the SIDM model with the lowest cross-section in the suite, $0.1 \text{ cm}^2 \text{ g}^{-1}$, the profile is distinguishable from the CDM case at the 2σ level outside the convergence radius. However, all the differences eventually diminish at the outskirts of the clusters, at larger than about $5\% R_{200}$. Although the discrepancy between SIDM and CDM predictions is significant at halo centers, contamination from gas cooling, star formation, and feedback effects in the central galaxies are expected to be important in those regions. These factors will be discussed in detail in Section 5.6.

We apply the same analysis to the intracluster gas in the simulations. In Figure 5.3,

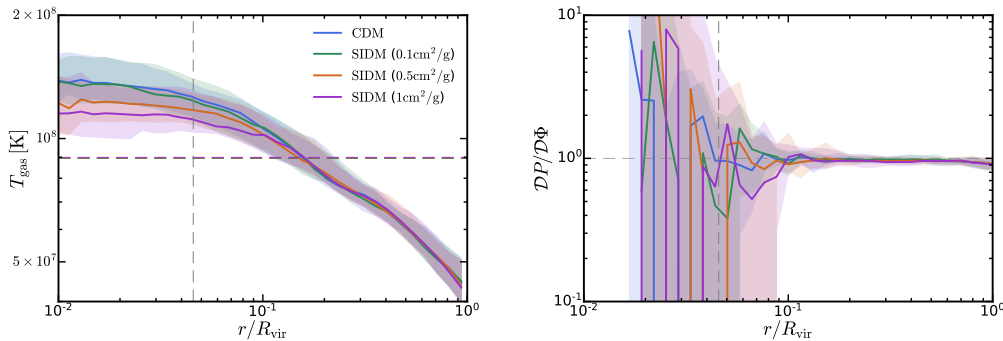


Figure 5.4: *Top*: Gas temperature profiles of the simulated clusters. The labeling is the same as in Figure 5.3. The vertical dashed line shows an estimate of the convergence radius for hydrodynamical properties. The horizontal dashed lines indicate the median virial temperatures of the halos in each DM model. Gas temperatures rise monotonically towards halo centers with the central temperature being slightly lower in SIDM models. *Bottom*: Thermal pressure gradient versus gravitational potential gradient as a function of radius. The thermal pressure support balances the gravitational attraction at $r \gtrsim 10\%$ R_{200} , indicating that the hydrostatic equilibrium is perfectly respected. At small radii, the dispersion in $\mathcal{D}P/\mathcal{D}\Phi$ gradually becomes larger. The convergence radius for hydrodynamical properties is estimated as 16 times the hydro spatial resolution h_b and is indicated with the grey vertical dashed line. Within the convergence radius, the median value of $\mathcal{D}P/\mathcal{D}\Phi$ shows order of magnitude fluctuations.

we show the gas mass density profiles of the simulated clusters. Assuming the intracluster gas is in hydrostatic equilibrium, the gas should distribute in a way that the thermal pressure balances the gravitational attraction (neglecting non-thermal pressure from, e.g., turbulent gas motions, which are subdominant in massive relaxed clusters, Lau et al. 401, Vazza et al. 402, Nelson et al. 403). If we further assume that the gas is isothermal, the gas density is simply related to the gravitational potential, Φ , as

$$\frac{\rho_{\text{gas}}(r)}{\rho_{\text{gas}}(0)} = \exp \left[-\frac{\mu m_p \Phi(0)}{k_b T} (\Phi(r)/\Phi(0) - 1) \right], \quad (5.10)$$

where the isothermal temperature T can be approximated as the virial temperature of the halo. In Figure 5.3, the profiles determined from the potential are shown in short dashed lines for reference. For both the gas mass density profile and the equilibrium-modeled gas density profile, the difference between different DM models is small, as opposed to the distinct signature of SIDM in the DM density profile. Part of the reason is that the gravitational potential is less sensitive to the DM density differences at small radii, thus the equilibrium-modeled gas density profiles are also less sensitive to SIDM physics. However, compared to the equilibrium-modeled

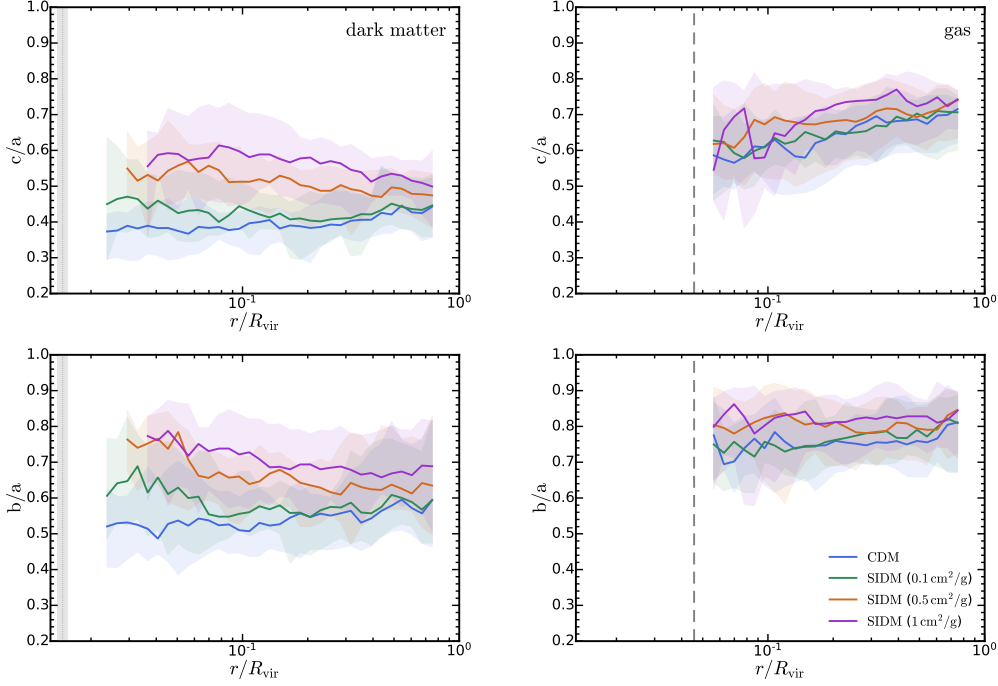


Figure 5.5: Three-dimensional axial ratios of the DM (gas) distribution of the simulated clusters. The left (right) column shows the axial ratios for DM (gas). The top row shows the minor-to-major axial ratio, c/a , and the bottom row shows the intermediate-to-major axial ratio, b/a . The shaded vertical regions on the left and dashed lines on the right indicate the convergence radii for DM and gas properties, respectively. Considerable differences between SIDM and CDM show up in the DM shape out to large radii, while the distinct signature of SIDM in the gas shape is much weaker. Meanwhile, the gas distribution is systematically rounder than the DM one, as a consequence of the X-ray emitting gas tracing more directly the isopotential surface of the matter distribution rather than the mass distribution.

ones, the gas mass density profiles are systematically lower at cluster centers and the SIDM-related differences are also smaller. This is likely related to a deviation from hydrostatic or thermal equilibrium, which we will investigate in the following.

Assuming spherical symmetry and neglecting non-thermal pressure support, the hydrostatic equilibrium implies

$$\begin{aligned} \frac{\partial \Phi(r)}{\partial r} &= -\frac{1}{\rho_{\text{gas}}(r)} \frac{\partial P(r)}{\partial r} \\ &= -\frac{k_{\text{b}} T(r)}{r \mu m_{\text{p}}} \left(\frac{\partial \ln \rho_{\text{gas}}(r)}{\partial \ln r} + \frac{\partial \ln T(r)}{\partial \ln r} \right), \end{aligned} \quad (5.11)$$

which simply represents that the gravitational attraction is balanced by the thermal pressure induced by either the density or temperature gradient. We denote the left-

hand side of the equation as “ $\mathcal{D}\Phi$ ” and the right-hand side as “ $\mathcal{D}P$ ”. In perfect hydrostatic equilibrium, we expect $\mathcal{D}P = \mathcal{D}\Phi$. In the top panel of Figure 5.4, we show the gas temperature profiles of the simulated clusters. With the absence of cooling processes, the gas temperature rises monotonically towards the cluster center, in line with the picture that the infalling gas is heated by strong accretion shocks. As described in Equation 5.11, the temperature gradient revealed here contributes to the thermal pressure support of gas and, as a result, the gas mass density profile rises slower than the isothermal profile towards the cluster center. Apart from this, SIDM models give slightly lower gas temperatures at $r \lesssim 0.1 R_{200}$ and the temperature gradients are also smaller, which makes the differences between gas density profiles in SIDM and CDM even smaller. In the bottom panel of Figure 5.4, we show $\mathcal{D}P/\mathcal{D}\Phi$ as a function of radius. To obtain $\mathcal{D}P$, the pressure and temperature gradients are evaluated between adjacent spherical shells. The hydrostatic equilibrium is perfectly respected at $r \gtrsim 10\% R_{200}$. The dispersion of $\mathcal{D}P/\mathcal{D}\Phi$ gradually becomes larger at smaller radii and SIDM models in general show greater dispersion. This dispersion is likely caused by the limited statistics of gas cells. For reference, the grey vertical dashed line indicates 16 times the hydro spatial resolution h_b (the equivalent size of gas cells), which roughly corresponds to 8 times the spatial spacing of gas cells. Within this reference radius, the median $\mathcal{D}P/\mathcal{D}\Phi$ in all DM models starts to deviate significantly from unity and exhibits order of magnitude oscillations. Therefore, we choose this radius as the convergence radius of the hydrodynamical properties of the gas. This radius is also plotted in Figure 5.3 and the top panel of Figure 5.4 as a reference for convergence.

Shapes of DM and gas distributions

Brinckmann et al. [255] found that the three-dimensional shape of DM halos is quite sensitive to SIDM physics. However, as demonstrated in the previous section, gas properties, in general, are much less sensitive to SIDM physics compared to DM. Therefore, it is important to check whether the shape changes in the DM distributions are reflected at the same level in the shape of the gas distribution.

To study the shapes of DM or gas distributions in simulated clusters, we adopt the code developed by Brinckmann et al. [255] based on the methodology in Zemp et al. [254]. The code determines the orientation and magnitude of the principal axes of a distribution of particles by computing the eigenvectors and eigenvalues of the shape

tensor, defined as

$$\mathbf{S} \equiv \frac{\int_V \rho \mathbf{r} \mathbf{r}^T dV}{\int_V \rho dV}, \quad (5.12)$$

where ρ is the density, \mathbf{r} is the position vector relative to the halo center and \mathbf{r}^T is the transpose of it. The discrete form of the shape tensor is defined as

$$S_{ij} \equiv \frac{\sum_k m_k r_k^i r_k^j}{\sum_k m_k}, \quad (5.13)$$

where m_k is the mass of the k th particle and r_k^i is the i th component of the position vector of the k th particle. In our analysis, we divide each halo into a number of ellipsoidal shells. The shells are initialized as spherical and are adaptively merged or split based on the particle number in each shell (adjacent shells with less than 2000 particles are merged and shells containing 50000 or more particles are split). The code computes the eigenvectors and eigenvalues of the shape tensor of the particles within each shell until convergence is achieved (when the axial ratios of both the minor and intermediate axes to the major axis deviate by less than one percent over the last ten iterations). For each iteration, the volume of the ellipsoidal shell will deform according to the axes determined in the previous loop, with particles being added or removed from the shell accordingly, while keeping the length of the major axis invariant. After convergence is reached, we document the minor-to-major axial ratio c/a and the intermediate-to-major axial ratio b/a for each shell and compute the effective radius of the shell as $r_{\text{eff}} = a\sqrt{[(c/a)^2 + (b/a)^2 + 1]}/3$, similarly to what we have done in the isophote analysis (see Section 5.4). We apply the method described above to both, the DM particles and gas cells in our simulated clusters.

In Figure 5.5, we show the three-dimensional axial ratios of the DM and gas distributions of the simulated clusters. For each model, we again present the median and 1σ dispersion of the axial ratios. Similar to what was found in Brinckmann et al. [255], we see that c/a for DM in the SIDM-c1 model can deviate from the CDM case at 2σ level out to about $0.2 R_{200}$. Note that at a similar radius the density profiles in SIDM and CDM are already indistinguishable, as shown in Figure 5.2. Even for the SIDM-c0.1 model, c/a for DM is distinguishable at about 1σ level out to $0.1 R_{200}$. These findings are consistent with other cosmological simulations of cluster-mass halos in SIDM [e.g., 164, 166]. On the contrary, gas shape differences between SIDM and CDM become much weaker and the shape profiles are systematically rounder than for DM. For example, at $r \sim 0.2 R_{200}$, we see that c/a in the SIDM-c1 model deviates from the CDM prediction at only about 1σ level. In hydrostatic equi-

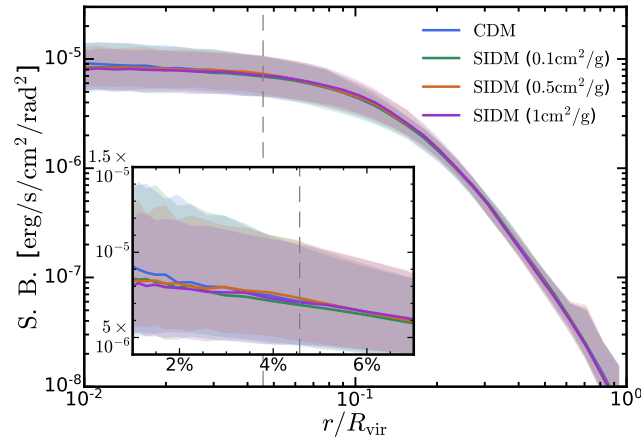


Figure 5.6: Soft X-ray surface brightness profiles of the simulated clusters in different DM models. For each model, we show the median and 1σ dispersion of the surface brightness profiles. A zoom-in subplot of the central surface brightness profiles is included. The hydro convergence radius is shown with the grey vertical dashed line. The surface brightness profile is basically insensitive to DM physics, due to a combination of projection effects and the weak response of the intracluster gas distribution to SIDM physics.

librium, the isodensity (and isotemperature) surface of the gas distribution should trace the isopotential surface of the matter distribution, also known as the *X-ray shape theorem* [404]; $\nabla \rho_{\text{gas}} \times \nabla \Phi = 0$. Since the isopotential surfaces are typically rounder than the source matter distribution [e.g., 264, 405, 406], the shape of the gas distribution is rounder than DM as a consequence. In Robertson et al. [164], it was found that the stellar and gas distributions in SIDM with $(\sigma/m) \lesssim 1 \text{ cm}^2 \text{ g}^{-1}$ and CDM show almost no difference in shape. However, in our results, we still find some residual differences between SIDM and CDM that could be tested statistically with large samples of simulated and observed galaxy clusters.

X-ray surface brightness profile

The next question to answer is how the differences in the three-dimensional shape of gas are reflected in the two-dimensional shape of X-ray isophotes. To answer this, we first create mock X-ray images for the simulated clusters following the procedure described in Section 5.4 and measure the surface brightness profile. For each DM model and each halo, 12 images are generated corresponding to 12 sampled viewing angles. In Figure 5.6, we show the median and 1σ dispersion of the soft X-ray surface brightness profiles from the simulated clusters. Similar to what has been found for the gas density profiles (see Fig. 5.3), SIDM and CDM predictions are

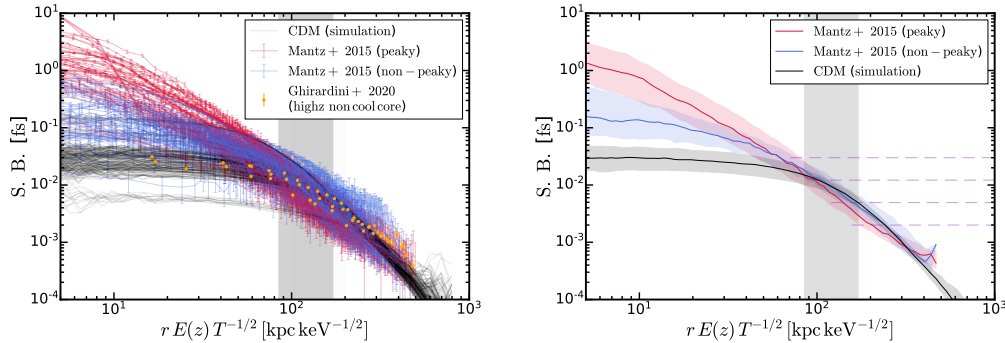


Figure 5.7: Comparisons of the soft X-ray surface brightness profiles of the simulated and observed clusters. *Top*: Surface brightness profiles (with observational error bars) of individual clusters. The observed clusters are grouped as the low-redshift “peaky” and “non-peaky” clusters [23], and the three SPT-selected clusters at $z \gtrsim 1.2$ [24] which do not exhibit cool-cores. The surface brightness profiles are normalized with the units defined in Equation 5.9. The shaded region indicates the radial range of interest, $0.1 - 0.2 R_{200}$. The cuspy central profiles of the low-redshift observed clusters, in particular the “peaky” sample, are not present in the simulated clusters with the absence of cooling processes. The high-redshift SPT-selected clusters appear to agree better with the simulations, due to the different thermodynamical properties compared to the low-redshift clusters. At large radii, including the radial range of interest for shape measurements, we find reasonable agreement in terms of normalization and slope between the simulated and observed profiles. *Bottom*: Median and 1σ dispersion of each group of surface brightness profiles. It is clear that the simulated clusters agree better with the “non-peaky” sample at the outskirts of the clusters. Based on the surface brightness in the radial range of interest ($0.1 - 0.2 R_{200}$, indicated with the shaded region), we pick the flux levels of the isophotes for morphology analysis. They are marked by the purple dashed lines.

nearly indistinguishable. For a given spherical annulus, the projection effects will mix the gas emission at small and large three-dimensional radii, which makes the surface brightness profiles more cored than the density profiles at $r \lesssim 0.1 R_{200}$ and further decreases the difference between SIDM and CDM.

The soft X-ray surface brightness profiles can be directly compared to observational results. For the observed clusters introduced in Section 5.3, the surface brightness profiles are measured using the SPA code introduced in Section 5.4. In the top panel of Figure 5.7, we compare the surface brightness profiles of the simulated clusters with the observed ones, the latter of which are grouped as the “peaky” (red) and “non-peaky” (blue) samples. For clarity, we only show the results of the CDM simulations, since we have shown above that the surface brightness profiles are insensitive to SIDM physics. We show explicitly the profile for each observed

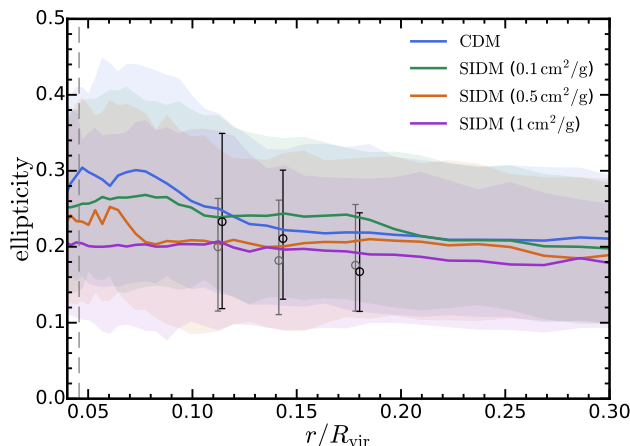


Figure 5.8: Ellipticity profiles of the simulated clusters compared to the observational results. We show the ellipticity of the isophotes as a function of the effective radius of the isophote. The median values and 1σ dispersions of the simulated samples are shown as solid lines and shaded regions. The results of the observed “non-peaky” (“peaky”) samples are shown by open black (grey) markers with error bars. The vertical dashed line on the left indicates the hydro convergence radius. The SIDM-c0.5 and SIDM-c1 models predict lower ellipticities and agree better with the observational results. However, the signal is smeared by large statistical uncertainties.

cluster, with the observational uncertainties as error bars, along with the profile for each image of the simulated clusters (recalling that we have multiple possible projection angles for each simulated cluster). The annuli radii and the surface brightness are normalized following the convention in Mantz et al. [23] to reduce potential redshift or temperature dependences. For reference, we show the profiles of three SPT-selected clusters at $z \gtrsim 1.2$ from Ghirardini et al. [24]³, which have distinct thermodynamical properties from the low-redshift clusters and do not exhibit cool cores. The clusters in the “peaky” observational sample have cuspy central profiles, in contrast with the cored profiles of our (adiabatic) simulated clusters. The “non-peaky” clusters are less cuspy, but the central surface brightness is still almost an order of magnitude higher than that of our simulated clusters. Since the simulations do not include gas cooling and physics of star formation and evolution, it is expected that the condensation of baryons at the center of clusters will be weaker for the simulated clusters compared to the observed ones. The shape of the surface brightness profile simply manifests the thermodynamical properties of the clusters.

³Modelled surface brightness profiles convolved with the PSF matrix and then fitted to the raw data, considering the exposed area and time for each annulus as well as the background.

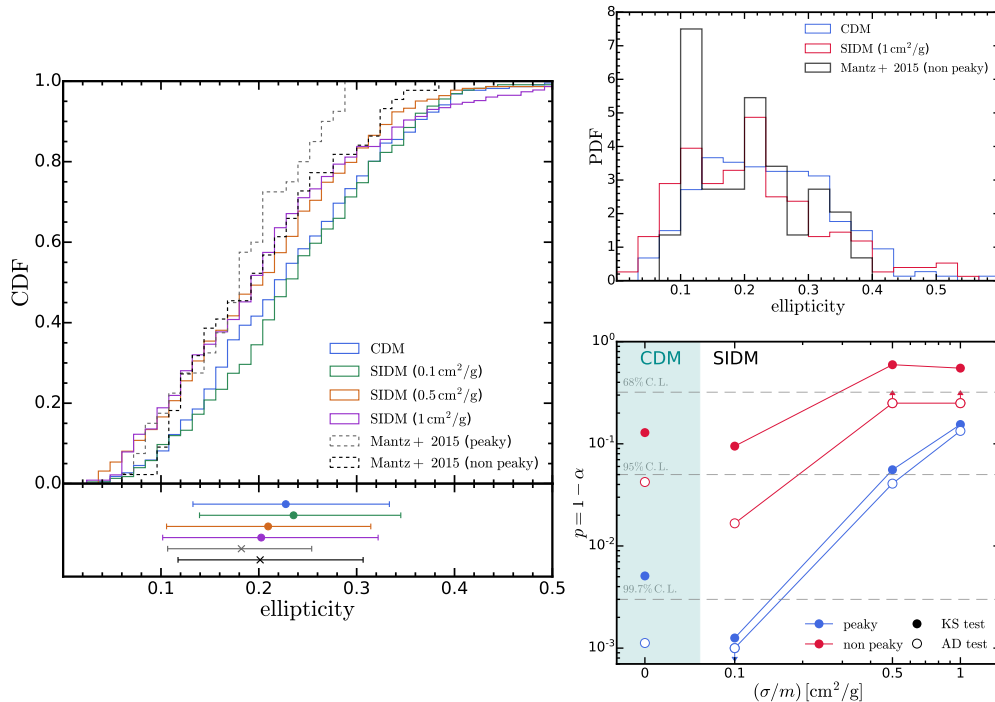


Figure 5.9: *Left*: Cumulative distribution function of the ellipticities of the X-ray isophotes. The fit to the isophotes is performed at $0.1 - 0.2 R_{200}$ for each viewing angle of each simulated halo. In the lower subpanel, we show the median ellipticities and 1σ dispersions for the different DM models and the observed cluster samples. *Top right*: Probability distribution function of the ellipticities. For simplicity, we only show PDFs of the CDM and SIDM-c1 models compared to observations. *Bottom right*: p value of the two-sample KS and AD tests. The tests are performed on the ellipticity distributions of observed and simulated clusters. The p value is the likelihood that the two samples are drawn from the same underlying continuous distribution function. Compared to the “non-peaky” sample, the KS and AD tests reject the CDM and SIDM-c0.1 models at about 90% confidence level.

This statement is supported by the agreement of the simulation results with the non-cool-core clusters selected at high redshift. Despite the dissimilarity at small radii, the surface brightness profiles of all samples agree well with each other at large radii, including the radial range of interest for this work ($0.1 - 0.2 R_{200}$). In the bottom panel of Figure 5.7, we condense the profiles shown on the upper panel to the median and 1σ dispersion of each sample. At $r \approx 0.1 - 0.2 R_{200}$, the simulation results are in better agreement with the “non-peaky” observed sample. The “peaky” clusters have slightly lower surface brightness at the radius of interest, but the differences are small (less than about 0.1 dex). Based on the surface brightness of simulated and observed clusters at $r \approx 0.1 - 0.2 R_{200}$, we choose the flux levels for isophotes

generation. Adopting the normalization convention in Section 5.4, N_0 and N_3 are determined as 2×10^{-3} and 3×10^{-2} , respectively. The flux levels bounding the three isophotes are marked as purple dashed lines in the figure.

Ellipticity of the isophotes

Given the flux levels determined above, we use the SPA code to select pixels for each isophote from the observed cluster images, and perform ellipse fitting to the isophotes as described in Section 5.4. For the images generated from the simulated clusters we also perform ellipse fitting, as described in Section 5.4. In Figure 5.8, we show the ellipticity of the isophotes as a function of the effective radius of the isophote (as defined in Section 5.4). For the simulation results, the median and 1σ dispersion are shown for each DM model. For the observational results, the measured ellipticity of each isophote is shown and the radius, r/R_{200} , is determined from the comparison of surface brightness profiles in Figure 5.7. Compared to the three-dimensional case, the two-dimensional shapes of the isophotes are much less sensitive to SIDM physics, primarily due to projection effects. First, a projected quantity (e.g. surface density, surface brightness) at a given projected radius r_{2d} gets contribution from all three-dimensional radii at $r_{3d} > r_{2d}$. This “mixing” of information at different radii could mitigate signal strength. In addition, observed in different lines-of-sight, the same three-dimensional mass/luminosity distribution can appear to have different projected shapes, which acts as an additional source of noise. As shown in Figure 5.8, the SIDM-c1 and SIDM-c0.5 models are still distinguishable from CDM and the SIDM-c0.1 model, but the difference is smeared by large halo-to-halo variations and thus has low statistical significance. The ellipticities of the observed “non-peaky” clusters show a somewhat stronger radial dependence than the simulated clusters and the observed “peaky” clusters, in addition to exhibiting slightly larger ellipticities at smaller radii. Nevertheless, the results for the “non-peaky” sample are still more consistent with large cross-section SIDM-c1 and SIDM-c0.5 models than with CDM or the SIDM-c0.1 model.

With the large sample size we have, higher order differences can be revealed from the distribution of the measured ellipticities. In the left panel of Figure 5.9, we show the cumulative distribution function (CDF) of the average ellipticities at $0.1 - 0.2 R_{200}$. In this domain, the two SIDM models with relatively high cross-sections (SIDM-c1 and SIDM-c0.5) give systematically lower ellipticities than CDM, while the SIDM-c0.1 model is indistinguishable from CDM. In some parts of the CDF, the SIDM-c0.1 model predicts even higher ellipticities than CDM, though we are unable

to tell if it is due to a physical effect or purely statistical noise. For the observed samples, the “non-peaky” case has a more extended high ellipticity tail than the “peaky” case and agrees better with the simulation results in general. Despite the even more extended high ellipticity tail, the SIDM-c1 and SIDM-c0.5 models agree best with the observed “non-peaky” sample, while CDM predicts systematically higher ellipticities by about 0.03 (manifested as the difference in the median values and a global shift in the CDF). However, the difference in the median ellipticity is significantly mitigated by the large sample variations. In the top right panel of Figure 5.9, we show the probability distribution function (PDF) of the ellipticities. The PDFs better reveal the features at the tails of the distributions. This comparison also demonstrates that the shift of the CDFs of SIDM-c1 and CDM are not caused by occasional peaks in the PDF driven by statistical noises, but by a real and systematic global shift in the PDF. Independent of the DM model employed, both the low ellipticity ($\lesssim 0.1$) and high ellipticity ($\gtrsim 0.4$) tails of the simulated clusters are missing in the observational samples. However, this could be related to the baryonic physics (e.g. radiative cooling, star formation, and stellar/AGN feedback) that are not included in the simulation. An evidence is that the “non-peaky” sample in observations (presumably less affected by cooling and star formation) shows much more high-ellipticity clusters than the “peaky” sample. The impact of baryonic physics and potential selection biases will be discussed in detail in Section 5.6.

Non-parametric statistical analysis

(1) *Kolmogorov-Smirnov statistic*: The two-sample Kolmogorov-Smirnov (KS) test is a nonparametric test that compares the (empirical) CDF of two datasets. It measures the likelihood that two univariate datasets are drawn from the same underlying parent probability distribution. Let x_1, x_2, \dots, x_m and y_1, y_2, \dots, y_n be samples of independent observations of populations with continuous distribution functions F and G , respectively. The empirical CDFs are F_m and G_n (i.e. the number of observations x_i 's which do not exceed u is $m F_m(u)$ and similarly for G). To test the null hypothesis $F = G$, the KS statistic is defined as

$$D_{m,n} \equiv \sqrt{\frac{m n}{m + n}} \sup_u |F_m(u) - G_n(u)|, \quad (5.14)$$

where \sup represents the supremum of the set of distances. The probability distribution $P_{\text{ks}}(t) \equiv \text{Pr}(D_{m,n} \leq t \mid F = G)$ is mathematically proven to be independent of the detailed form of F or G , if F and G are continuous. We use the `SCIPY` implementation of the two-sample KS test, which follows Hodges [407] treatment

of the probability function $P_{\text{ks}}(t)$. The null hypothesis is rejected at the significance level α if $D_{\text{m,n}} > K_\alpha$, where K_α is found from $\text{Pr}(D_{\text{m,n}} \leq K_\alpha | F = G) = \alpha$. In the following, the value $1 - \alpha$ will be referred to as the p value. The p value should be interpreted as *the probability of observing an equal or larger discrepancy in the empirical CDFs, F_{m} and G_{n} , than what was observed from the data in the hypothetical context where $F = G$, instead of the probability that the null hypothesis $F = G$ is true.*

For our purpose here, we perform KS tests between the samples of ellipticities measured from simulations and observations. The tests will be performed between simulations of each DM model and each observational group, respectively. The null hypothesis is that the simulation and observational samples are randomly drawn from the same underlying distribution of ellipticities. For each test, we obtain the statistical significance α at which this null hypothesis is rejected. In the bottom right panel of Figure 5.9, we show the value $p \equiv 1 - \alpha$ versus SIDM cross-section. For the “non-peaky” sample, the CDM model is rejected at about 90% confidence level, while the SIDM models with $(\sigma/m) \geq 0.5 \text{ cm}^2 \text{ g}^{-1}$ are only constrained at about 40% confidence level, and thus have greater chance of being consistent with the observational sample. On the other hand, for the “peaky” sample, even the SIDM-c1 model is rejected at about 90% confidence level. In terms of the KS statistics, CDM appears to be more consistent with the data than the SIDM-c0.1 model. This is due to the fact that the SIDM-c0.1 model predicts even higher ellipticities than CDM in some parts of the CDF, as shown in the left panel of Figure 5.9. However, we are unable to tell if this is due to a physical effect or purely statistical noise.

(II) *Anderson-Darling statistic*: The KS test is most sensitive when the empirical CDFs differ in a global fashion, but could be misleading if there are repeated crossings between the CDFs or the deviations take place at the tails of the distributions. Alternatively, the Anderson-Darling [AD, 408, 409] test was designed to overcome these problems and has been proven more sensitive than the KS test with extensive implications. The two-sample AD statistic is defined as [410–412]

$$A_{\text{m,n}}^2 = \frac{mn}{N} \int_{-\infty}^{\infty} \frac{[F_{\text{m}}(u) - G_{\text{n}}(u)]^2}{H_{\text{N}}(u) [1 - H_{\text{N}}(u)]} dH_{\text{N}}(u), \quad (5.15)$$

where $N = m + n$ and $H_{\text{N}}(u) = [mF_{\text{m}}(u) + nG_{\text{n}}(u)]/N$. The weighting term $1/H_{\text{N}}(u) [1 - H_{\text{N}}(u)]$ gives greater weight to displacements at the tails of the distribution. The probability distribution of the AD statistics has also proven to be independent of the detailed form of F and G . For numerical computation and as-

assessment of the statistical significance, we adopt the `SCIPY` implementation of the method following Scholz and Stephens [412]. Similar to the KS tests, we perform the AD tests between the simulated and the observed samples, and the results are illustrated in the bottom right panel of Figure 5.9. Since the table of AD statistics and significance levels in Scholz and Stephens [412] only covers p values from 0.1% to 25%, the p values we get from this test are capped accordingly, as marked by the arrows in the figure. The AD tests generally give lower p values than the KS tests, which suggests that the models are rejected at a higher confidence level.

5.6 Discussions

Statistical uncertainties

To measure the statistical uncertainties from the limited sample size and viewing angle choices, we generate 1000 bootstrapped realizations for each observational sample and for simulations in each DM model. The number is chosen to give a converged assessment of the KS or AD statistics. The bootstrapped realizations of the sample have the same sample size as the original one. In the top panel of Figure 5.10, we present the median CDFs and the 1σ dispersions from the bootstrapped samples of the simulated CDM and SIDM-c1 samples and the observed “non-peaky” sample. The displacement between CDM and the observed sample is robust against the statistical uncertainties measured here. The SIDM-c1 model and its bootstrapped realizations are in good agreement with the observed sample, particularly around the center of the distribution, though with more extended tails at both ends of the distribution. In the bottom panel of Figure 5.10, the median p values and 1σ dispersions of the KS and AD statistics are shown. The statistics have been computed for each pair of the bootstrapped realizations, leading to in total of one million measurements. For the KS test, the p values of the bootstrapped samples are systematically lower than that of the original sample, and in some cases, the original value even lies outside the 1σ scatter. This would be expected when the CDFs of the original sample differ in a global fashion⁴ ($|F - G|$ weakly depends on ellipticity). On the other hand, the median p value of the AD tests of bootstrapped samples agrees well with the original measurement. Neglecting the cap at $p = 0.1\%$ and $p = 25\%$, the bootstrapped results of the KS and AD tests agree remarkably

⁴A small displacement from this state in bootstrapping will more likely lead to a larger KS statistic $\sup_u |F - G|$ (thus lower p value) and a shift of the location where the maximum is reached.

Stated in another way, a lower p value (a higher KS statistic) corresponds to a larger number of realizations of bootstrapped samples (and thus a larger entropy). So this can be understood as the entropy gain when deviating from a (quasi-)equilibrium state.

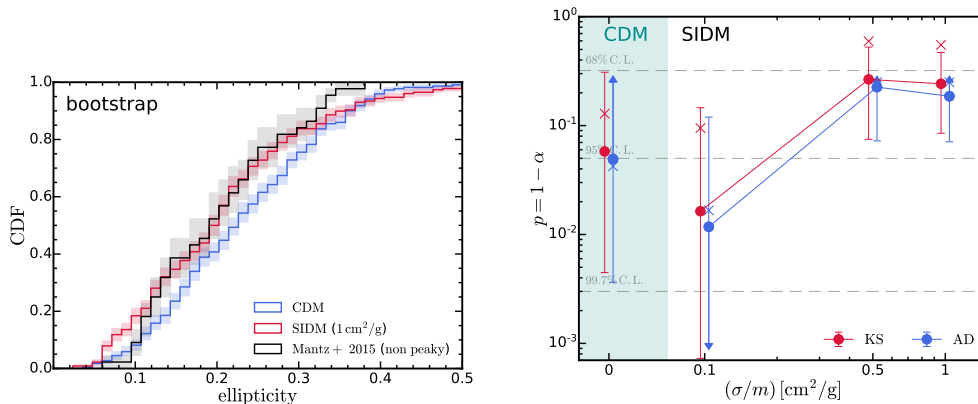


Figure 5.10: Ellipticity CDFs and statistics from the bootstrapped samples. *Top:* Ellipticity CDFs of the bootstrapped samples for the CDM and SIDM-c1 models and the “non-peaky” sample from observations. The 1σ dispersions of the CDFs are shown by the shaded regions. The discrepancy found between CDM and the observed sample is larger than the statistical uncertainties illustrated here. *Bottom:* The p values of KS and AD tests for the bootstrapped samples. The median p values and the 1σ scatters are shown by solid circles with error bars. The p values from the measurements of the original samples are shown by crosses. Since the numerical implementation of the AD test only covers the p values from 0.1% to 25%, the bootstrapped results are thus capped, as marked by the arrows in the figure. Even taking into account the scatter in p value, the CDM and SIDM-c0.1 models are rejected with a 68% confidence level.

well and both of them suggest that the CDM and SIDM-c0.1 models are rejected at 68% confidence level, as conservative estimates.

Selection bias and systematic uncertainties

Our analysis is potentially subject to selection biases in cluster redshift and temperature. In the top (bottom) panel of Figure 5.11, we show the ellipticity versus cluster redshift (temperature). The ICM temperatures of the simulated clusters are approximated as the virial temperature. Although no obvious redshift or temperature dependence is found for the measured ellipticity, the simulated clusters have a narrower temperature distribution. This is likely related to the selection criteria for these clusters from the parent large-box simulation. They are the most massive halos that are classified as dynamically relaxed and have not undergone recent mergers. Clusters of even higher masses are most likely perturbed by recent mergers.

As illustrated in Figure 5.8, the ellipticity of the isophotes of the simulated clusters exhibit a weak radial dependence, an effect that is more apparent at small radii and

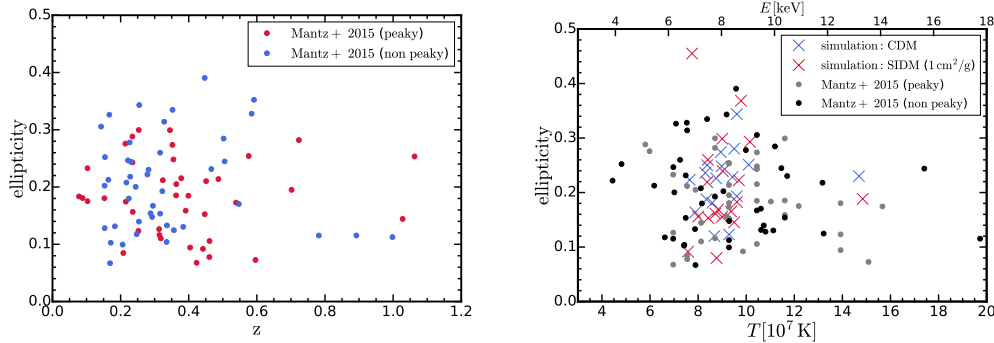


Figure 5.11: *Top*: Ellipticity versus redshift of the observed clusters. The ellipticity does not show any apparent dependence on redshift. Note that these clusters have been pre-selected as dynamically relaxed objects through the SPA criteria. *Bottom*: Ellipticity versus temperature. No apparent dependence on temperature is found either. However, the simulated clusters have a narrower distribution in temperature.

in CDM. The observed samples show a similar trend as well, albeit with the “non-peaky” clusters displaying a much stronger radial dependence. In the top panel of Figure 5.12, we show the CDF of ellipticities measured at slightly smaller/larger ($\pm 25\%$) radii as solid/dotted lines. The ellipticities measured at smaller radii are typically larger. As expected, the ellipticity CDF in CDM is more affected by the aperture than in the SIDM-c1 model, but their systematic difference is robust against the shift of the aperture. In the middle panel of Figure 5.10, we test the results against the scatter in cluster temperature (or equivalently cluster mass). As shown in the right panel of Figure 5.1, the observational samples have larger scatters in the temperature distribution than the simulated ones and a few hot cluster outliers. To test if these outliers would affect the ellipticity measurements, we limit the analysis to clusters with $7 \times 10^7 \leq T_{\text{vir}} \leq 11 \times 10^7$ K and show the results as dashed lines in the figure. The results are robust against these outliers. In the bottom panel of Figure 5.12, we show the KS and AD statistics after applying the aperture shift or the temperature cut. None of the conclusions we drew in the previous sections is affected by these variations.

Another potential bias originates from the different definitions (and selection criteria) for “relaxed” clusters in simulations and observations. The sample of relaxed halos for zoom-in simulations were selected based on the virial ratio, center offset and subhalo mass fraction [255], which are expected to inherit some intrinsic bias from the morphologically selected observed samples. In the future, constructing a volume-limit sample of massive halos from large-volume, hydrodynamical

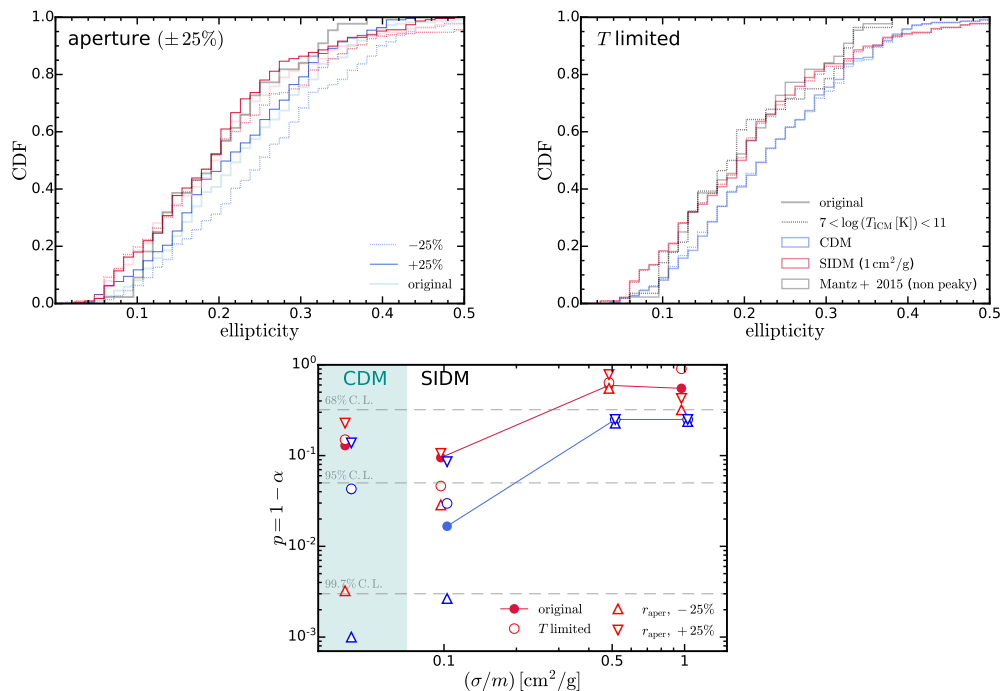


Figure 5.12: *Top*: Ellipticity CDFs when varying the radial aperture of the measurements. The CDF when increasing (decreasing) the radial aperture by 25% is shown as the solid (dotted) lines. The original CDMs are shown as transparent lines. The comparison demonstrates that the results are robust against aperture shifts. *Middle*: Ellipticity CDFs when excluding outliers in the ICM temperature distribution. The CDFs of the temperature-limited samples are presented in dashed lines while those of the original samples are shown in solid lines. The impact of the temperature outliers is small. *Bottom*: The p value of KS and AD tests when varying the radial aperture of the measurements or applying a temperature selection criterion. The conclusion that the CDM and dSIDM-c0.1 models are disfavored at 68% confidence level is not altered by either the aperture shift or the temperature selection criterion.

simulations would be an important future follow-up project. This would allow a morphology selection process based on mock X-ray images from simulated clusters, which is fully consistent with the observed sample. However, this certainly requires significantly higher computational cost and more development in the sub-grid models for cluster physics.

Impact of baryonic physics

The response of cluster morphology to baryonic physics is not yet fully understood. Radiative cooling of the intracluster plasma results in a condensed, rotating gas disk in the central part of the halo, fueling star formation and subsequent AGN activity in the Brightest Cluster Galaxy (BCG). The rotation support (and other

non-thermal processes in the intracluster plasma) breaks the hydrostatic equilibrium and the flattening of the three-dimensional gas distribution is reflected by the larger ellipticities of two-dimensional isophotes. Fang et al. [413] found that the ellipticities of X-ray isophotes are enhanced at small cluster-centric radii, $r \lesssim 0.4 R_{500} \sim 0.26 R_{200}$ ⁵, in simulations with radiative cooling and star formation (CSF) compared to adiabatic runs. The average ellipticity over sightlines reached 0.6 at $r \sim 0.1 R_{500}$ ($\sim 0.065 R_{200}$) as opposed to 0.3 in adiabatic runs. A similar phenomenon was found by Lau et al. [414] between non-radiative (NR, i.e. adiabatic) cooling runs and CSF runs. However, the flattening of the isophotes due to cooling was confined to smaller radii $r \lesssim 0.1 R_{500}$.

On the other hand, at the radii beyond the scale of the central gas disk, halos in CSF runs were more spherical than those in adiabatic models. For example, isophote ellipticities were lower at $r \gtrsim 0.1 - 0.2 R_{500}$ ($0.065 - 0.13 R_{200}$) in CSF simulations with respect to those in NR simulations by about 0.1 (see Lau et al. 414 and also Fang et al. 413, noting that the latter found a similar difference, but at larger radii). Similar effects were also found in Battaglia et al. [415] and Suto et al. [416] out to half of the virial radius with about 0.05 difference in two-dimensional axis-ratios. The azimuthal scatter of surface brightness was found to be substantially lower in cool-core clusters in observations and CSF simulations compared to adiabatic runs [417], suggesting rounder distributions of gas. The shapes of the gas (and DM) distributions are sensitive to the degree of the central concentration of the total mass. As intracluster gas cools and flows towards the halo center, the distribution becomes more spherical [e.g., 5, 416, 418–422]. In this study, the “peaky” clusters have lower isophote ellipticities than the “non-peaky” clusters, which is consistent with this picture. The fact that the “non-peaky” clusters in observations still have more concentrated surface brightness profiles than the simulated ones indicate some level of cooling even in the “non-peaky” sample that is not captured by the adiabatic simulations. This effect has the potential to make the CDM results presented in this chapter more consistent with observations.

Meanwhile, the cooling and condensation of gas can feed both star formation and accretion onto SMBHs harbored by the BCG. The resulting stellar/supernovae and AGN feedback can inject substantial amounts of energy into the ICM through radiation, kinetic outflows and power jets of relativistic particles. As important

⁵Assuming an NFW profile with concentration $c = 4$, a typical value for cluster-mass halos, $R_{500} \simeq 0.65 R_{200}$ and $R_{\text{vir}}(z = 0) \simeq R_{100} \simeq 1.35 R_{200}$, where the second argument assumes the redshift-dependence from Bryan and Norman [249] for $\Delta_c(z = 0) \simeq 100$.

heating mechanisms, they can compensate the energy loss due to radiative cooling and mitigate the sphericalizing effect of cooling. In addition, potential anisotropic feedback processes (e.g., bi-modal jets, bubbles, outflows from satellite galaxies) can disturb the ICM and create non-thermal pressure support for the intracluster gas in certain directions, further breaking the sphericity of the halo. In numerical simulations, Battaglia et al. [415] and Suto et al. [416] found that clusters are less spherical when AGN feedback is included relative to including only radiative cooling. As an enlightening attempt, Robertson et al. [423] performed a series of galaxy cluster simulations that includes baryonic physics and found diverse density profiles of cluster-mass halos, which can be understood in terms of their different final baryon distributions. This was followed by BAHAMAS–SIDM simulations [164], which is the first large-volume cosmological set of simulations including both SIDM and baryonic physics, including AGN feedback. Although considerable differences were found in the shape of DM distributions, the discrepancy is weakened by baryonic effects and were not reflected in the distribution of gas or stars within galaxy clusters. However, there is no consensus yet on the strength and underlying mechanism of AGN feedback as well as its numerical implementation. And the numerical challenge to resolve baryonic physics processes for the large simulation volumes required to sample massive clusters still exist. It is still hard to tell whether the baryonic physics that primarily influence the central part of the clusters, and which are not present in our simulations, can explain the discrepancy we report here between adiabatic CDM simulations and observations of clusters.

5.7 Summary of the chapter

In this chapter, we study the X-ray morphology of massive, dynamically relaxed clusters based on a suite of cosmological hydrodynamical zoom-in simulations of 19 halos with $M_{200} \simeq 1-2 \times 10^{15} M_{\odot}$, simulated in CDM and SIDM models with three different (constant) cross-sections per unit mass: $(\sigma/m) = 0.1, 0.5$ and $1.0 \text{ cm}^2 \text{ g}^{-1}$. The structural properties of both DM and intracluster gas in these clusters are studied quantitatively in detail. These simulations include adiabatic gas of which the X-ray emission is modeled to create mock soft X-ray images. We perform ellipse fitting on the isophotes at intermediate radii of the clusters and compare the ellipticities with those measured from real cluster X-ray images. Our findings can be summarized as follows.

- The intracluster gas in the adiabatic simulations is in almost perfect hydrostatic

equilibrium until reaching the hydro resolution limit. The gas temperature within $0.1 R_{200}$ is slightly lower in SIDM with increasing cross-sections. Although the central DM density profile in SIDM is distinct from that in CDM (when $(\sigma/m) \geq 0.1 \text{ cm}^2 \text{ g}^{-1}$ as tested by our simulation suite), the gas density profiles of the two cases are almost indistinguishable down to the resolution limit.

- Similar to what was found in Brinckmann et al. [255], the three-dimensional shapes of the DM distribution in CDM and SIDM-c1 exhibit at least 2σ level discrepancy out to large cluster-centric radii ($r \sim 0.2 R_{200}$). For all the models, the gas distributions are systematically more spherical than those of DM, as a consequence of gas in hydrostatic equilibrium tracing the isopotential surfaces, which are more spherical than the mass distribution. The variation in axial ratios decreases to about 1σ level at $r \sim 0.1 - 0.2 R_{200}$ between CDM and SIDM-c1.
- The surface brightness profiles in SIDM are remarkably similar to those produced in CDM. Both of them are in good agreement with observations at the outskirts of the clusters ($r \gtrsim 0.1 R_{200}$), while the observed clusters develop cuspy profiles at the center, especially for the selected cool-core (“peaky”) clusters.
- Two-dimensional shape analysis is performed on the real and mock X-ray images, of which the isophotes at the target radius ($r \gtrsim 0.1 - 0.2 R_{200}$) are fitted with ellipses. We find that the ellipticities of the observed “non-peaky” clusters are systematically lower than the CDM prediction, and interestingly in good agreement with the SIDM models with $(\sigma/m) \geq 0.5 \text{ cm}^2 \text{ g}^{-1}$. Based on statistical tests of the bootstrapped samples, we find that the CDM and SIDM-c0.1 models are conservatively disfavored at 68% confidence level. The result is robust against aperture choices and selection biases in cluster temperatures and redshifts.

In conclusion, we demonstrate that the X-ray morphology of massive, relaxed clusters is a promising channel to constrain DM self-interactions. Even though the DM model-dependent variations in shape is smaller in the gas distribution and weakened by projection effects, distinct signals can be identified with a large sample of observed and simulated clusters. Our analysis favors SIDM models with relatively high cross-sections. However, effects due to baryonic physics, including cooling,

star formation and feedback effects that are not captured by our adiabatic simulations is the primary source of uncertainty, and has the potential to reconcile simulations with observations within the CDM framework. Follow-up cluster simulations with full baryonic physics are required to confirm our findings.

Chapter 6

CONCLUSIONS

In this thesis, I discuss the motivations to study DM models with alternative behaviors to the classical collisionless CDM on astrophysical scales. The formation of cosmic structures and galaxies offers a powerful avenue to constrain the general properties of DM. Our primary focus is on DM with self-interactions, a dimension of DM properties that may be probed exclusively through cosmological observations. In the following, I will provide a comprehensive summary of the four research projects related to SIDM and the implications of these studies in elucidating various phenomena observed in the Universe.

6.1 DSIDM – simulations and observational signatures

In Chapter 2 and Chapter 3, we present the first suite of cosmological baryonic (hydrodynamical) zoom-in simulations of galaxies in dSIDM. We adopt a dSIDM model where a constant fraction of the kinetic energy is lost during DM self-interaction and sample models with different self-interaction cross-sections. The simulations utilize the FIRE-2 model for hydrodynamics and galaxy formation physics, which allows for realistic predictions of the structural and kinematic properties of galaxies. We primarily focus on the analysis of dwarf galaxies in dSIDM and explore galaxy/halo’s response to dissipative self-interactions of DM.

We find that energy dissipation due to DM self-interactions induces radial contraction of DM halo. This mechanism competes with baryonic feedback in shaping the central profiles of dwarf galaxies, which may give rise to the observed diversity of dwarf galaxy rotation curves. When the effective self-interaction cross-section is larger than $\sim 0.1 \text{ cm}^2 \text{ g}^{-1}$, the central density profiles of dwarf galaxies become cuspy and power-law-like. The slope of the profile can be well explained by the steady-state solution of a “dark cooling flow”. Through time scale analysis, we show that the dSIDM models with constant cross-sections will have a stronger impact in more massive galaxies while the velocity-dependent model has the opposite dependence.

The kinematic properties and the shape of the DM halo are changed in parallel to the contraction. As the self-interaction cross-section of dSIDM increases, the coherent

rotation becomes more prominent compared to random velocity dispersion. In the meantime, the velocity dispersions are more dominated by the tangential component than the radial component, reflected by the negative velocity anisotropies in dSIDM halos. The central parts of the galaxies are in transition from dispersion supported to rotation supported. In the dSIDM model with $(\sigma/m) = 1 \text{ cm}^2 \text{ g}^{-1}$, the halo becomes more spherical towards lower redshifts, contrary to the triaxial shape of CDM halos. The spherical “dark cooling flow” washes out the initial triaxiality of the halo and makes the halo compact and spherical in the end. However, in the dSIDM model with $(\sigma/m) = 10 \text{ cm}^2 \text{ g}^{-1}$, the halo shape shows a response to the more prominent coherent rotation of DM. Halos are initially on the track of becoming more spherical, but later turn oblate in shape due to the halt of spherical contraction and increased rotation support.

In Chapter 3, we attempt to compare these predictions to basic galaxy observables affected by the underlying structural changes of DM halos induced by dissipative interactions. The stellar morphology, the size-mass relation, and the circular velocity profiles of both field and satellite dwarf galaxies are studied.

We find that with moderate but not negligible interaction cross-sections ($(\sigma/m) \sim 1 \text{ cm}^2 \text{ g}^{-1}$), dSIDM makes the stellar content more concentrated and promotes the formation of thin stellar disks as well as neutral gas disks in massive bright dwarfs. The simulated galaxies in these models are still consistent with observations in the plane of the galaxy size-mass relation. However, perhaps surprisingly, when the cross-section becomes large enough ($\sigma/m \sim 10 \text{ cm}^2 \text{ g}^{-1}$), the stellar content of simulated dwarfs becomes fluffier even than the CDM case, owing to rotation and other emergent properties of the DM cusp.

In terms of the circular velocity profiles of simulated dwarfs, we separately consider the isolated classical and bright dwarfs in the suite as well as the satellites in the simulations of Milky Way-mass galaxies. The isolated classical dwarfs are compared to the field dwarf galaxies in the Local Group and we find all of the dSIDM models studied survive this comparison. The isolated bright dwarfs are compared to the LSBs with HI-based circular velocity measurements. We find that the dSIDM models with $(\sigma/m) \gtrsim 0.1 \text{ cm}^2 \text{ g}^{-1}$ are in tension with observations and the velocity-dependent model is favored. The constraints here should be treated with caution since we are limited by the number of simulated isolated halos at each representative mass scale.

The satellites in simulated Milky Way-mass galaxies are compared to the Local

Group satellites. Though we find little differences in the median and scatter of the circular velocity profiles between DM models, dSIDM models with $(\sigma/m) = 0.1 \text{ cm}^2 \text{ g}^{-1}$ produce outliers that agree better with the compact elliptical satellites in observations, whose analogs are missing in CDM.

6.2 SIDM in massive high-density systems

In Chapter 4, we have studied a mechanism to seed high redshift SMBHs via the collapse of tdSIDM halos, where the DM particle loses nearly all its kinetic energy during a single collision. The study is motivated by the existence of billion solar mass SMBHs observed in the early Universe ($z \gtrsim 6$), which are in tension with canonical seeding mechanisms. We develop an analytical model for the collapse criteria and timescale of tdSIDM halos, calibrated based on numerical N-body simulations of isolated halos, and then apply this model to Monte-Carlo halo merger trees to make predictions of SMBHs and observed quasars in the cosmological context.

We find that a constant fraction, $f_{\text{col}} \simeq 3 \times 10^{-3}$, of the halo mass will eventually collapse to the scale below the spatial resolution of the simulations. Surprisingly, the collapsed fraction is insensitive to the mass, size, spin, and redshift of the sampled halo. An analytic description of the collapse criteria and timescale is developed and calibrated based on these simulations. This analytic prescription can be applied to halos with various masses, concentrations, and formation redshifts as well as in different cosmological models.

The unique feature of our seeding mechanism is the rapid formation of SMBHs seeds with an SMBH-to-halo mass ratio of $\sim 3 \times 10^{-3}$. The SMBHs directly seeded from the catastrophic collapse of tdSIDM halos are massive enough to explain the high mass end of SMBHs at $z \gtrsim 6$. The rapid formation of SMBHs in our model implies the existence of very young quasars at high redshift. Such a young population of quasars is difficult to explain in standard scenarios where SMBHs have to live long enough to grow at some modest multiple of the Eddington limit from much smaller masses. SMBHs seeded directly from tdSIDM halos exhibit much larger SMBH-to-halo mass ratios than local SMBHs and lie systematically above the local $M_{\text{BH}} - \sigma_{\text{v}}^*$ relation. This feature is in better agreement with [C II] gas velocity dispersion and host galaxy dynamical mass measured for high redshift massive quasars.

We trace the seeding and growth of SMBHs via halo merger trees and derive predictions for the cosmological abundance of SMBHs. With little tuning of the fueling model of SMBHs (the ERDF and the quasar duty-cycle), our model with

$\sigma/m = 0.05/0.1 \text{ cm}^2 \text{ g}^{-1}$ (or $\epsilon\sigma/m = 0.005/0.01 \text{ cm}^2 \text{ g}^{-1}$ if we make ϵ free) successfully reproduces the observed quasar luminosity functions at high redshift, particularly at the bright end. The tuned ERDF and duty-cycle imply that a significant fraction of SMBHs seeded in this way must have low quasar activity, which will hopefully be tested by future quasar surveys.

Our model prefers a cross-section of $\sigma/m \sim 0.05 \text{ cm}^2 \text{ g}^{-1}$ (or $\epsilon\sigma/m \sim 0.005 \text{ cm}^2 \text{ g}^{-1}$) to explain the quasar luminosity function at high redshift while remaining consistent with low redshift observations. Such a model is testable in the future once the quasar luminosity function is measured at more redshifts. In the future, quasar surveys conducted with the Nancy Grace Roman Space Telescope, the Rubin Observatory Legacy Survey of Space and Time (LSST), and the James Webb Space Telescope (JWST) can further test our predictions of the quasar luminosity function and the density change of SMBHs at high redshift.

In Chapter 5, we study the X-ray morphology of massive, dynamically relaxed clusters based on a suite of cosmological hydrodynamical zoom-in simulations of 19 halos with $M_{200} \simeq 1 - 2 \times 10^{15} M_{\odot}$, simulated in CDM and SIDM models with three different (constant) cross-sections per unit mass: $(\sigma/m) = 0.1, 0.5$ and $1.0 \text{ cm}^2 \text{ g}^{-1}$. The structural properties of both DM and intracluster gas in these clusters are studied quantitatively in detail. These simulations include adiabatic gas of which the X-ray emission is modeled to create mock soft X-ray images. We perform ellipse fitting on the isophotes at the intermediate radii of the clusters and compare the ellipticities with those measured from real cluster X-ray images.

The three-dimensional shapes of the DM distribution in CDM and SIDM-c1 exhibit at least 2σ level discrepancy out to large cluster-centric radii ($r \sim 0.2 R_{200}$). For all the models, the gas distributions are systematically more spherical than those of DM, as a consequence of gas in hydrostatic equilibrium tracing the isopotential surfaces, which are more spherical than the mass distribution. The variation in axial ratios decreases to about 1σ level at $r \sim 0.1 - 0.2 R_{200}$ between CDM and SIDM-c1.

In two-dimensional shape analysis, we find that the ellipticities of the observed “non-peaky” clusters are systematically lower than the CDM prediction, and interestingly in good agreement with the SIDM models with $(\sigma/m) \geq 0.5 \text{ cm}^2 \text{ g}^{-1}$. Based on statistical tests of the bootstrapped samples, we find that the CDM and SIDM-c0.1 models are conservatively disfavored at a 68% confidence level. The result is robust against aperture choices and selection biases in cluster temperatures and redshifts.

We demonstrate that the X-ray morphology of massive, relaxed clusters is a promising channel to constrain DM self-interactions. Even though the DM model-dependent variations in shape are smaller in the gas distribution and weakened by projection effects, distinct signals can be identified with a large sample of observed and simulated clusters. Our analysis favors SIDM models with relatively high cross-sections. However, effects due to baryonic physics, including cooling, star formation, and feedback effects that are not captured by our adiabatic simulations is the primary source of uncertainty, and has the potential to reconcile simulations with observations within the CDM framework. Follow-up cluster simulations with full baryonic physics are required to confirm our findings.

6.3 Future works

There are three primary directions for my future research in constraining the nature of DM in structure formation. The first is to delve deeper into SIDM studies. With a few exceptions, the research on SIDM so far mainly involves empirical parameterizations with effective parameters. This strategy has the advantage of efficiently constraining the properties of a broad class of DM candidates but neglects the potential rich phenomenology in the dark sector. One ongoing effort of us is to simulate a more realistic dissipative DM model, such as DM with atomic structures, cooling, and star formation physics. We have developed the code to simulate fluid-like atomic DM alongside the standard model gas.

Another direction is to explore a broader range of DM candidates. This includes classical CDM candidates, such as the QCD axions, of which the parameter space has not been extensively searched in direct detections. The QCD axions in the post-inflationary scenario may lead to (sub-)Earth mass structures detectable through lensing and pulsar-timing observations. We have developed a semi-analytical model to study the cosmic evolution of these mini structures and their survival probability in the Milky Way environment. Other alternative DM types or properties, such as low-mass WDM candidates with large free streaming lengths or ultralight particles with quantum mechanical effects, can impact structure formation at small scales. Integrating these alternatives into existing simulation codes can help study cosmological structure formation in different scenarios.

The last direction is to investigate signatures in various astrophysical systems. The high redshift early Universe is a relatively unexplored territory that may be sensitive to various DM physics, such as effects in small-scale primordial fluctuations and

DM-baryon couplings. The next-generation observations will provide abundant new data for structure formation in this era. This includes the abundance of faint galaxies quantified by the UV luminosity function measured by JWST, rare massive halos searched by quasar surveys as well as the Lyman-alpha forest tomography and the 21 cm line intensity mapping that map the small-scale neutral gas structure at different epochs. The global 21 cm signal of the first stars is sensitive to cooling from DM-baryon coupling. Some recently develop numeric techniques will be useful to study alternative DM in these observations.

Bibliography

- [1] Benjamin P. Moster, Andrea V. Macciò, and Rachel S. Somerville. Numerical hydrodynamic simulations based on semi-analytic galaxy merger trees: method and Milky Way-like galaxies. *MNRAS*, 437(2):1027–1044, January 2014. doi: 10.1093/mnras/stt1702.
- [2] C. B. Brook, A. Di Cintio, A. Knebe, S. Gottlöber, Y. Hoffman, G. Yepes, and S. Garrison-Kimmel. The Stellar-to-halo Mass Relation for Local Group Galaxies. *ApJ*, 784(1):L14, March 2014. doi: 10.1088/2041-8205/784/1/L14.
- [3] Shea Garrison-Kimmel, James S. Bullock, Michael Boylan-Kolchin, and Emma Bardwell. Organized chaos: scatter in the relation between stellar mass and halo mass in small galaxies. *MNRAS*, 464(3):3108–3120, January 2017. doi: 10.1093/mnras/stw2564.
- [4] Philip F. Hopkins, Lars Hernquist, Paul Martini, Thomas J. Cox, Brant Robertson, Tiziana Di Matteo, and Volker Springel. A Physical Model for the Origin of Quasar Lifetimes. *ApJ*, 625(2):L71–L74, June 2005. doi: 10.1086/431146.
- [5] Xuejian Shen, Philip F. Hopkins, Lina Necib, Fangzhou Jiang, Michael Boylan-Kolchin, and Andrew Wetzel. Dissipative Dark Matter on FIRE: I. Structural and kinematic properties of dwarf galaxies. *arXiv e-prints*, art. arXiv:2102.09580, February 2021.
- [6] Alan W. McConnachie. The Observed Properties of Dwarf Galaxies in and around the Local Group. *AJ*, 144(1):4, July 2012. doi: 10.1088/0004-6256/144/1/4.
- [7] Paul Eigenthaler, Thomas H. Puzia, Matthew A. Taylor, Yasna Ordenes-Briceño, Roberto P. Muñoz, Karen X. Ribbeck, Karla A. Alamo-Martínez, Hongxin Zhang, Simón Ángel, Massimo Capaccioli, Patrick Côté, Laura Ferrarese, Gaspar Galaz, Eva K. Grebel, Maren Hempel, Michael Hilker, Ariane Lançon, Steffen Mieske, Bryan Miller, Maurizio Paolillo, Mathieu

- Powalka, Tom Richtler, Joel Roediger, Yu Rong, Ruben Sánchez-Janssen, and Chelsea Spengler. The Next Generation Fornax Survey (NGFS). II. The Central Dwarf Galaxy Population. *ApJ*, 855(2):142, March 2018. doi: 10.3847/1538-4357/aaab60.
- [8] Federico Lelli, Stacy S. McGaugh, and James M. Schombert. SPARC: Mass Models for 175 Disk Galaxies with Spitzer Photometry and Accurate Rotation Curves. *AJ*, 152(6):157, Dec 2016. doi: 10.3847/0004-6256/152/6/157.
- [9] Federico Lelli, Stacy S. McGaugh, James M. Schombert, and Marcel S. Pawlowski. The Relation between Stellar and Dynamical Surface Densities in the Central Regions of Disk Galaxies. *ApJ*, 827(1):L19, August 2016. doi: 10.3847/2041-8205/827/1/L19.
- [10] Pieter G. van Dokkum, Roberto Abraham, Allison Merritt, Jielai Zhang, Marla Geha, and Charlie Conroy. Forty-seven Milky Way-sized, Extremely Diffuse Galaxies in the Coma Cluster. *ApJ*, 798(2):L45, January 2015. doi: 10.1088/2041-8205/798/2/L45.
- [11] J. Christopher Mihos, Patrick R. Durrell, Laura Ferrarese, John J. Feldmeier, Patrick Côté, Eric W. Peng, Paul Harding, Chengze Liu, Stephen Gwyn, and Jean-Charles Cuillandre. Galaxies at the Extremes: Ultra-diffuse Galaxies in the Virgo Cluster. *ApJ*, 809(2):L21, August 2015. doi: 10.1088/2041-8205/809/2/L21.
- [12] Rebecca Lange, Simon P. Driver, Aaron S. G. Robotham, Lee S. Kelvin, Alister W. Graham, Mehmet Alpaslan, Stephen K. Andrews, Ivan K. Baldry, Steven Bamford, Joss Bland-Hawthorn, Sarah Brough, Michelle E. Cluver, Christopher J. Conselice, Luke J. M. Davies, Boris Haeussler, Iraklis S. Konstantopoulos, Jon Loveday, Amanda J. Moffett, Peder Norberg, Steven Phillipps, Edward N. Taylor, Ángel R. López-Sánchez, and Stephen M. Wilkins. Galaxy And Mass Assembly (GAMA): mass-size relations of $z < 0.1$ galaxies subdivided by Sérsic index, colour and morphology. *MNRAS*, 447(3):2603–2630, March 2015. doi: 10.1093/mnras/stu2467.
- [13] A. van der Wel, M. Franx, P. G. van Dokkum, R. E. Skelton, I. G. Momcheva, K. E. Whitaker, G. B. Brammer, E. F. Bell, H. W. Rix, S. Wuyts, H. C. Ferguson, B. P. Holden, G. Barro, A. M. Koekemoer, Yu-Yen Chang, E. J. McGrath, B. Häussler, A. Dekel, P. Behroozi, M. Fumagalli, J. Leja, B. F. Lundgren, M. V. Maseda, E. J. Nelson, D. A. Wake, S. G. Patel, I. Labbé, S. M. Faber, N. A. Grogin, and D. D. Kocevski. 3D-HST+CANDELS: The Evolution of the Galaxy Size-Mass Distribution since $z = 3$. *ApJ*, 788(1):28, June 2014. doi: 10.1088/0004-637X/788/1/28.
- [14] Jeremy Tinker, Andrey V. Kravtsov, Anatoly Klypin, Kevork Abazajian, Michael Warren, Gustavo Yepes, Stefan Gottlöber, and Daniel E. Holz. Toward a Halo Mass Function for Precision Cosmology: The Limits of Universality. *ApJ*, 688(2):709–728, December 2008. doi: 10.1086/591439.

- [15] Xuejian Shen, Philip F. Hopkins, Claude-André Faucher-Giguère, D.M. Alexander, Gordon T. Richards, Nicholas P. Ross, and R.C. Hickox. The bolometric quasar luminosity function at $z = 0-7$. *Mon. Not. Roy. Astron. Soc.*, 495(3):3252–3275, 2020. doi: 10.1093/mnras/staa1381.
- [16] Wei-Xiang Feng, Hai-Bo Yu, and Yi-Ming Zhong. Seeding supermassive black holes with self-interacting dark matter, 2020.
- [17] Feige Wang, Ran Wang, Xiaohui Fan, Xue-Bing Wu, Jinyi Yang, Roberto Neri, and Minghao Yue. Spatially Resolved Interstellar Medium and Highly Excited Dense Molecular Gas in the Most Luminous Quasar at $z = 6.327$. *ApJ*, 880(1):2, July 2019. doi: 10.3847/1538-4357/ab2717.
- [18] Kohei Inayoshi, Eli Visbal, and Zoltán Haiman. The assembly of the first massive black holes. *Annual Review of Astronomy and Astrophysics*, 58(1): 27–97, Aug 2020. ISSN 1545-4282. doi: 10.1146/annurev-astro-120419-014455. URL <http://dx.doi.org/10.1146/annurev-astro-120419-014455>.
- [19] John Kormendy and Luis C. Ho. Coevolution (Or Not) of Supermassive Black Holes and Host Galaxies. *ARA&A*, 51(1):511–653, August 2013. doi: 10.1146/annurev-astro-082708-101811.
- [20] Roberto Decarli, Fabian Walter, Bram P. Venemans, Eduardo Bañados, Frank Bertoldi, Chris Carilli, Xiaohui Fan, Emanuele Paolo Farina, Chiara Mazzucchelli, Dominik Riechers, Hans-Walter Rix, Michael A. Strauss, Ran Wang, and Yujin Yang. An ALMA [C II] Survey of 27 Quasars at $z > 5.94$. *ApJ*, 854(2):97, February 2018. doi: 10.3847/1538-4357/aaa5aa.
- [21] Alister W. Graham and Simon P. Driver. The local supermassive black hole mass density: corrections for dependencies on the Hubble constant. *MNRAS*, 380(1):L15–L19, September 2007. doi: 10.1111/j.1745-3933.2007.00340.x.
- [22] Risa H. Wechsler, James S. Bullock, Joel R. Primack, Andrey V. Kravtsov, and Avishai Dekel. Concentrations of dark halos from their assembly histories. *The Astrophysical Journal*, 568(1):52–70, Mar 2002. ISSN 1538-4357. doi: 10.1086/338765. URL <http://dx.doi.org/10.1086/338765>.
- [23] Adam B. Mantz, Steven W. Allen, R. Glenn Morris, Robert W. Schmidt, Anja von der Linden, and Ondrej Urban. Cosmology and astrophysics from relaxed galaxy clusters - I. Sample selection. *MNRAS*, 449(1):199–219, May 2015. doi: 10.1093/mnras/stv219.
- [24] Vittorio Ghirardini, Esra Bulbul, Ralph Kraft, Matt Bayliss, Bradford Benson, Lindsey Bleem, Sebastian Bocquet, Micheal Calzadilla, Dominique Eckert, William Forman, Juan David Remolina Da González, Gourav Khullar, Guillaume Mahler, and Michael McDonald. Evolution of the Thermodynamic Properties of Clusters of Galaxies out to Redshift of 1.8. *ApJ*, 910(1):14, March 2021. doi: 10.3847/1538-4357/abc68d.

- [25] Philip F. Hopkins, Andrew Wetzel, Dušan Kereš, Claude-André Faucher-Giguère, Eliot Quataert, Michael Boylan-Kolchin, Norman Murray, Christopher C. Hayward, Shea Garrison-Kimmel, Cameron Hummels, Robert Feldmann, Paul Torrey, Xiangcheng Ma, Daniel Anglés-Alcázar, Kung-Yi Su, Matthew Orr, Denise Schmitz, Ivanna Escala, Robyn Sanderson, Michael Y. Grudić, Zachary Hafen, Ji-Hoon Kim, Alex Fitts, James S. Bullock, Coral Wheeler, T. K. Chan, Oliver D. Elbert, and Desika Narayanan. FIRE-2 simulations: physics versus numerics in galaxy formation. *MNRAS*, 480(1): 800–863, Oct 2018. doi: 10.1093/mnras/sty1690.
- [26] C. Power, J. F. Navarro, A. Jenkins, C. S. Frenk, S. D. M. White, V. Springel, J. Stadel, and T. Quinn. The inner structure of Λ CDM haloes - I. A numerical convergence study. *MNRAS*, 338(1):14–34, January 2003. doi: 10.1046/j.1365-8711.2003.05925.x.
- [27] G. R. Blumenthal, S. M. Faber, J. R. Primack, and M. J. Rees. Formation of galaxies and large-scale structure with cold dark matter. *Nature*, 311: 517–525, Oct 1984. doi: 10.1038/311517a0.
- [28] M. Davis, G. Efstathiou, C. S. Frenk, and S. D. M. White. The evolution of large-scale structure in a universe dominated by cold dark matter. *ApJ*, 292: 371–394, May 1985. doi: 10.1086/163168.
- [29] James S. Bullock and Michael Boylan-Kolchin. Small-Scale Challenges to the Λ CDM Paradigm. *ARA&A*, 55(1):343–387, August 2017. doi: 10.1146/annurev-astro-091916-055313.
- [30] Ricardo A. Flores and Joel R. Primack. Observational and Theoretical Constraints on Singular Dark Matter Halos. *ApJ*, 427:L1, May 1994. doi: 10.1086/187350.
- [31] Ben Moore. Evidence against dissipation-less dark matter from observations of galaxy haloes. *Nature*, 370(6491):629–631, Aug 1994. doi: 10.1038/370629a0.
- [32] W. J. G. de Blok, Stacy S. McGaugh, and Vera C. Rubin. High-Resolution Rotation Curves of Low Surface Brightness Galaxies. II. Mass Models. *AJ*, 122(5):2396–2427, Nov 2001. doi: 10.1086/323450.
- [33] Rachel Kuzio de Naray, Stacy S. McGaugh, W. J. G. de Blok, and A. Bosma. High-Resolution Optical Velocity Fields of 11 Low Surface Brightness Galaxies. *ApJS*, 165(2):461–479, Aug 2006. doi: 10.1086/505345.
- [34] G. Gentile, P. Salucci, U. Klein, D. Vergani, and P. Kalberla. The cored distribution of dark matter in spiral galaxies. *MNRAS*, 351(3):903–922, Jul 2004. doi: 10.1111/j.1365-2966.2004.07836.x.

- [35] Joshua D. Simon, Alberto D. Bolatto, Adam Leroy, Leo Blitz, and Elinor L. Gates. High-Resolution Measurements of the Halos of Four Dark Matter-Dominated Galaxies: Deviations from a Universal Density Profile. *ApJ*, 621(2):757–776, Mar 2005. doi: 10.1086/427684.
- [36] M. Spano, M. Marcelin, P. Amram, C. Carignan, B. Epinat, and O. Hernandez. GHASP: an $H\alpha$ kinematic survey of spiral and irregular galaxies - V. Dark matter distribution in 36 nearby spiral galaxies. *MNRAS*, 383(1):297–316, Jan 2008. doi: 10.1111/j.1365-2966.2007.12545.x.
- [37] Rachel Kuzio de Naray and Tobias Kaufmann. Recovering cores and cusps in dark matter haloes using mock velocity field observations. *MNRAS*, 414(4):3617–3626, Jul 2011. doi: 10.1111/j.1365-2966.2011.18656.x.
- [38] Rachel Kuzio de Naray and Kristine Spekkens. Do Baryons Alter the Halos of Low Surface Brightness Galaxies? *ApJ*, 741(2):L29, Nov 2011. doi: 10.1088/2041-8205/741/2/L29.
- [39] Se-Heon Oh, Chris Brook, Fabio Governato, Elias Brinks, Lucio Mayer, W. J. G. de Blok, Alyson Brooks, and Fabian Walter. The Central Slope of Dark Matter Cores in Dwarf Galaxies: Simulations versus THINGS. *AJ*, 142(1):24, Jul 2011. doi: 10.1088/0004-6256/142/1/24.
- [40] Matthew G. Walker and Jorge Peñarrubia. A Method for Measuring (Slopes of) the Mass Profiles of Dwarf Spheroidal Galaxies. *ApJ*, 742(1):20, Nov 2011. doi: 10.1088/0004-637X/742/1/20.
- [41] Se-Heon Oh, Deidre A. Hunter, Elias Brinks, Bruce G. Elmegreen, Andreas Schruba, Fabian Walter, Michael P. Rupen, Lisa M. Young, Caroline E. Simpson, Megan C. Johnson, Kimberly A. Herrmann, Dana Ficut-Vicas, Phil Cigan, Volker Heesen, Trisha Ashley, and Hong-Xin Zhang. High-resolution Mass Models of Dwarf Galaxies from LITTLE THINGS. *AJ*, 149(6):180, Jun 2015. doi: 10.1088/0004-6256/149/6/180.
- [42] T. K. Chan, D. Kereš, J. Oñorbe, P. F. Hopkins, A. L. Muratov, C. A. Faucher-Giguère, and E. Quataert. The impact of baryonic physics on the structure of dark matter haloes: the view from the FIRE cosmological simulations. *MNRAS*, 454(3):2981–3001, Dec 2015. doi: 10.1093/mnras/stv2165.
- [43] Qirong Zhu, Federico Marinacci, Moupiya Maji, Yuexing Li, Volker Springel, and Lars Hernquist. Baryonic impact on the dark matter distribution in Milky Way-sized galaxies and their satellites. *MNRAS*, 458(2):1559–1580, May 2016. doi: 10.1093/mnras/stw374.
- [44] Julio F. Navarro, Carlos S. Frenk, and Simon D. M. White. The Structure of Cold Dark Matter Halos. *ApJ*, 462:563, May 1996. doi: 10.1086/177173.

- [45] Julio F. Navarro, Carlos S. Frenk, and Simon D. M. White. A Universal Density Profile from Hierarchical Clustering. *ApJ*, 490(2):493–508, Dec 1997. doi: 10.1086/304888.
- [46] Ben Moore, Sebastiano Ghigna, Fabio Governato, George Lake, Thomas Quinn, Joachim Stadel, and Paolo Tozzi. Dark Matter Substructure within Galactic Halos. *ApJ*, 524(1):L19–L22, Oct 1999. doi: 10.1086/312287.
- [47] Anatoly Klypin, Andrey V. Kravtsov, James S. Bullock, and Joel R. Primack. Resolving the Structure of Cold Dark Matter Halos. *ApJ*, 554(2):903–915, Jun 2001. doi: 10.1086/321400.
- [48] J. F. Navarro, E. Hayashi, C. Power, A. R. Jenkins, C. S. Frenk, S. D. M. White, V. Springel, J. Stadel, and T. R. Quinn. The inner structure of Λ CDM haloes - III. Universality and asymptotic slopes. *MNRAS*, 349(3):1039–1051, Apr 2004. doi: 10.1111/j.1365-2966.2004.07586.x.
- [49] Jürg Diemand, Marcel Zemp, Ben Moore, Joachim Stadel, and C. Marcella Carollo. Cusps in cold dark matter haloes. *MNRAS*, 364(2):665–673, Dec 2005. doi: 10.1111/j.1365-2966.2005.09601.x.
- [50] M. Boylan-Kolchin, James S. Bullock, and Manoj Kaplinghat. Too big to fail? The puzzling darkness of massive Milky Way subhaloes. *MNRAS*, 415(1):L40–L44, Jul 2011. doi: 10.1111/j.1745-3933.2011.01074.x.
- [51] Michael Boylan-Kolchin, James S. Bullock, and Manoj Kaplinghat. The Milky Way’s bright satellites as an apparent failure of Λ CDM. *MNRAS*, 422(2):1203–1218, May 2012. doi: 10.1111/j.1365-2966.2012.20695.x.
- [52] Erik J. Tollerud, Michael Boylan-Kolchin, and James S. Bullock. M31 satellite masses compared to Λ CDM subhaloes. *MNRAS*, 440(4):3511–3519, Jun 2014. doi: 10.1093/mnras/stu474.
- [53] Shea Garrison-Kimmel, Michael Boylan-Kolchin, James S. Bullock, and Evan N. Kirby. Too big to fail in the Local Group. *MNRAS*, 444(1):222–236, Oct 2014. doi: 10.1093/mnras/stu1477.
- [54] Evan N. Kirby, James S. Bullock, Michael Boylan-Kolchin, Manoj Kaplinghat, and Judith G. Cohen. The dynamics of isolated Local Group galaxies. *MNRAS*, 439(1):1015–1027, Mar 2014. doi: 10.1093/mnras/stu025.
- [55] E. Papastergis, R. Giovanelli, M. P. Haynes, and F. Shankar. Is there a “too big to fail” problem in the field? *A&A*, 574:A113, Feb 2015. doi: 10.1051/0004-6361/201424909.
- [56] F. Governato, C. Brook, L. Mayer, A. Brooks, G. Rhee, J. Wadsley, P. Jonsson, B. Willman, G. Stinson, T. Quinn, and P. Madau. Bulgeless dwarf galaxies and dark matter cores from supernova-driven outflows. *Nature*, 463(7278):203–206, January 2010. doi: 10.1038/nature08640.

- [57] Andrew Pontzen and Fabio Governato. How supernova feedback turns dark matter cusps into cores. *MNRAS*, 421(4):3464–3471, Apr 2012. doi: 10.1111/j.1365-2966.2012.20571.x.
- [58] Piero Madau, Sijing Shen, and Fabio Governato. Dark Matter Heating and Early Core Formation in Dwarf Galaxies. *ApJ*, 789(1):L17, Jul 2014. doi: 10.1088/2041-8205/789/1/L17.
- [59] Alyson M. Brooks and Adi Zolotov. Why Baryons Matter: The Kinematics of Dwarf Spheroidal Satellites. *ApJ*, 786(2):87, May 2014. doi: 10.1088/0004-637X/786/2/87.
- [60] Andrew R. Wetzel, Philip F. Hopkins, Ji-hoon Kim, Claude-André Faucher-Giguère, Dušan Kereš, and Eliot Quataert. Reconciling Dwarf Galaxies with Λ CDM Cosmology: Simulating a Realistic Population of Satellites around a Milky Way-mass Galaxy. *ApJ*, 827(2):L23, Aug 2016. doi: 10.3847/2041-8205/827/2/L23.
- [61] Till Sawala, Carlos S. Frenk, Azadeh Fattahi, Julio F. Navarro, Richard G. Bower, Robert A. Crain, Claudio Dalla Vecchia, Michelle Furlong, John. C. Helly, Adrian Jenkins, Kyle A. Oman, Matthieu Schaller, Joop Schaye, Tom Theuns, James Trayford, and Simon D. M. White. The APOSTLE simulations: solutions to the Local Group’s cosmic puzzles. *MNRAS*, 457(2): 1931–1943, Apr 2016. doi: 10.1093/mnras/stw145.
- [62] Shea Garrison-Kimmel, Philip F. Hopkins, Andrew Wetzel, James S. Bullock, Michael Boylan-Kolchin, Dušan Kereš, Claude-André Faucher-Giguère, Kareem El-Badry, Astrid Lamberts, Eliot Quataert, and Robyn Sanderson. The Local Group on FIRE: dwarf galaxy populations across a suite of hydrodynamic simulations. *MNRAS*, 487(1):1380–1399, Jul 2019. doi: 10.1093/mnras/stz1317.
- [63] Isabel M. Santos-Santos, Arianna Di Cintio, Chris B. Brook, Andrea Macciò, Aaron Dutton, and Rosa Domínguez-Tenreiro. NIHAO - XIV. Reproducing the observed diversity of dwarf galaxy rotation curve shapes in Λ CDM. *MNRAS*, 473(4):4392–4403, February 2018. doi: 10.1093/mnras/stx2660.
- [64] Fangzhou Jiang, Avishai Dekel, Jonathan Freundlich, Aaron J. Romanowsky, Aaron A. Dutton, Andrea V. Macciò, and Arianna Di Cintio. Formation of ultra-diffuse galaxies in the field and in galaxy groups. *MNRAS*, 487(4): 5272–5290, August 2019. doi: 10.1093/mnras/stz1499.
- [65] Kyle A. Oman, Julio F. Navarro, Azadeh Fattahi, Carlos S. Frenk, Till Sawala, Simon D. M. White, Richard Bower, Robert A. Crain, Michelle Furlong, Matthieu Schaller, Joop Schaye, and Tom Theuns. The unexpected diversity of dwarf galaxy rotation curves. *MNRAS*, 452(4):3650–3665, October 2015. doi: 10.1093/mnras/stv1504.

- [66] Manoj Kaplinghat, Mauro Valli, and Hai-Bo Yu. Too big to fail in light of Gaia. *MNRAS*, 490(1):231–242, November 2019. doi: 10.1093/mnras/stz2511.
- [67] Gianfranco Bertone, Dan Hooper, and Joseph Silk. Particle dark matter: evidence, candidates and constraints. *Phys. Rep.*, 405(5-6):279–390, Jan 2005. doi: 10.1016/j.physrep.2004.08.031.
- [68] Gianfranco Bertone. The moment of truth for WIMP dark matter. *Nature*, 468(7322):389–393, Nov 2010. doi: 10.1038/nature09509.
- [69] E. Aprile, J. Aalbers, F. Agostini, M. Alfonsi, L. Althueser, F. D. Amaro, M. Anthony, F. Arneodo, L. Baudis, B. Bauermeister, M. L. Benabderrahmane, T. Berger, P. A. Breur, A. Brown, A. Brown, E. Brown, S. Bruenner, G. Bruno, R. Budnik, C. Capelli, J. M. R. Cardoso, D. Cichon, D. Coderre, A. P. Colijn, J. Conrad, J. P. Cussonneau, M. P. Decowski, P. de Perio, P. di Gangi, A. di Giovanni, S. Diglio, A. Elykov, G. Eurin, J. Fei, A. D. Ferella, A. Fieguth, W. Fulgione, A. Gallo Rosso, M. Galloway, F. Gao, M. Garbini, C. Geis, L. Grandi, Z. Greene, H. Qiu, C. Hasterok, E. Hogenbirk, J. Howlett, R. Itay, F. Joerg, B. Kaminsky, S. Kazama, A. Kish, G. Koltman, H. Landsman, R. F. Lang, L. Levinson, Q. Lin, S. Lindemann, M. Lindner, F. Lombardi, J. A. M. Lopes, J. Mahlstedt, A. Manfredini, T. Marrodán Undagoitia, J. Masbou, D. Masson, M. Messina, K. Micheneau, K. Miller, A. Molinario, K. Morâ, M. Murra, J. Naganoma, K. Ni, U. Oberlack, B. Pelsers, F. Piastra, J. Pienaar, V. Pizzella, G. Plante, R. Podviiianiuk, N. Priel, D. Ramírez García, L. Rauch, S. Reichard, C. Reuter, B. Riedel, A. Rizzo, A. Rocchetti, N. Rupp, J. M. F. Dos Santos, G. Sartorelli, M. Scheibelhut, S. Schindler, J. Schreiner, D. Schulte, M. Schumann, L. Scotto Lavina, M. Selvi, P. Shagin, E. Shockley, M. Silva, H. Simgen, D. Thers, F. Toschi, G. Trincherro, C. Tunnell, N. Upole, M. Vargas, O. Wack, H. Wang, Z. Wang, Y. Wei, C. Weinheimer, C. Wittweg, J. Wulf, J. Ye, Y. Zhang, T. Zhu, and Xenon Collaboration. Dark Matter Search Results from a One Ton-Year Exposure of XENON1T. *Phys. Rev. Lett.*, 121(11):111302, Sep 2018. doi: 10.1103/PhysRevLett.121.111302.
- [70] Craig J. Hogan and Julianne J. Dalcanton. New dark matter physics: Clues from halo structure. *Phys. Rev. D*, 62(6):063511, September 2000. doi: 10.1103/PhysRevD.62.063511.
- [71] David N. Spergel and Paul J. Steinhardt. Observational Evidence for Self-Interacting Cold Dark Matter. *Phys. Rev. Lett.*, 84(17):3760–3763, Apr 2000. doi: 10.1103/PhysRevLett.84.3760.
- [72] Julianne J. Dalcanton and Craig J. Hogan. Halo Cores and Phase-Space Densities: Observational Constraints on Dark Matter Physics and Structure Formation. *ApJ*, 561(1):35–45, November 2001. doi: 10.1086/323207.

- [73] Matthew R. Buckley and Annika H. G. Peter. Gravitational probes of dark matter physics. *Phys. Rep.*, 761:1–60, Oct 2018. doi: 10.1016/j.physrep.2018.07.003.
- [74] Eric D. Carlson, Marie E. Machacek, and Lawrence J. Hall. Self-interacting Dark Matter. *ApJ*, 398:43, Oct 1992. doi: 10.1086/171833.
- [75] Andrew A. de Laix, Robert J. Scherrer, and Robert K. Schaefer. Constraints on Self-interacting Dark Matter. *ApJ*, 452:495, Oct 1995. doi: 10.1086/176322.
- [76] C. Firmani, E. D’Onghia, V. Avila-Reese, G. Chincarini, and X. Hernández. Evidence of self-interacting cold dark matter from galactic to galaxy cluster scales. *MNRAS*, 315(3):L29–L32, Jul 2000. doi: 10.1046/j.1365-8711.2000.03555.x.
- [77] Lotty Ackerman, Matthew R. Buckley, Sean M. Carroll, and Marc Kamionkowski. Dark matter and dark radiation. *Phys. Rev. D*, 79(2):023519, Jan 2009. doi: 10.1103/PhysRevD.79.023519.
- [78] Nima Arkani-Hamed, Douglas P. Finkbeiner, Tracy R. Slatyer, and Neal Weiner. A theory of dark matter. *Phys. Rev. D*, 79(1):015014, Jan 2009. doi: 10.1103/PhysRevD.79.015014.
- [79] Jonathan L. Feng, Manoj Kaplinghat, Huitzu Tu, and Hai-Bo Yu. Hidden charged dark matter. *J. Cosmol. Astropart. Phys.*, 2009(7):004, Jul 2009. doi: 10.1088/1475-7516/2009/07/004.
- [80] Jonathan L. Feng, Manoj Kaplinghat, and Hai-Bo Yu. Halo-Shape and Relic-Density Exclusions of Sommerfeld-Enhanced Dark Matter Explanations of Cosmic Ray Excesses. *Phys. Rev. Lett.*, 104(15):151301, Apr 2010. doi: 10.1103/PhysRevLett.104.151301.
- [81] Abraham Loeb and Neal Weiner. Cores in Dwarf Galaxies from Dark Matter with a Yukawa Potential. *Phys. Rev. Lett.*, 106(17):171302, Apr 2011. doi: 10.1103/PhysRevLett.106.171302.
- [82] Laura G. van den Aarssen, Torsten Bringmann, and Christoph Pfrommer. Is Dark Matter with Long-Range Interactions a Solution to All Small-Scale Problems of Λ Cold Dark Matter Cosmology? *Phys. Rev. Lett.*, 109(23):231301, Dec 2012. doi: 10.1103/PhysRevLett.109.231301.
- [83] Francis-Yan Cyr-Racine and Kris Sigurdson. Cosmology of atomic dark matter. *Phys. Rev. D*, 87(10):103515, May 2013. doi: 10.1103/PhysRevD.87.103515.
- [84] Sean Tulin, Hai-Bo Yu, and Kathryn M. Zurek. Beyond collisionless dark matter: Particle physics dynamics for dark matter halo structure. *Phys. Rev. D*, 87(11):115007, Jun 2013. doi: 10.1103/PhysRevD.87.115007.

- [85] James M. Cline, Zuowei Liu, Guy D. Moore, and Wei Xue. Composite strongly interacting dark matter. *Phys. Rev. D*, 90(1):015023, Jul 2014. doi: 10.1103/PhysRevD.90.015023.
- [86] Sean Tulin and Hai-Bo Yu. Dark matter self-interactions and small scale structure. *Phys. Rep.*, 730:1–57, Feb 2018. doi: 10.1016/j.physrep.2017.11.004.
- [87] Mark Vogelsberger, Jesus Zavala, and Abraham Loeb. Subhaloes in self-interacting galactic dark matter haloes. *MNRAS*, 423(4):3740–3752, Jul 2012. doi: 10.1111/j.1365-2966.2012.21182.x.
- [88] Miguel Rocha, Annika H. G. Peter, James S. Bullock, Manoj Kaplinghat, Shea Garrison-Kimmel, Jose Oñorbe, and Leonidas A. Moustakas. Cosmological simulations with self-interacting dark matter - I. Constant-density cores and substructure. *MNRAS*, 430(1):81–104, Mar 2013. doi: 10.1093/mnras/sts514.
- [89] J. Zavala, M. Vogelsberger, and M. G. Walker. Constraining self-interacting dark matter with the Milky way’s dwarf spheroidals. *MNRAS*, 431:L20–L24, Apr 2013. doi: 10.1093/mnrasl/sls053.
- [90] Oliver D. Elbert, James S. Bullock, Shea Garrison-Kimmel, Miguel Rocha, Jose Oñorbe, and Annika H. G. Peter. Core formation in dwarf haloes with self-interacting dark matter: no fine-tuning necessary. *MNRAS*, 453(1):29–37, Oct 2015. doi: 10.1093/mnras/stv1470.
- [91] Ayuki Kamada, Manoj Kaplinghat, Andrew B. Pace, and Hai-Bo Yu. Self-Interacting Dark Matter Can Explain Diverse Galactic Rotation Curves. *Phys. Rev. Lett.*, 119(11):111102, September 2017. doi: 10.1103/PhysRevLett.119.111102.
- [92] Peter Creasey, Omid Sameie, Laura V. Sales, Hai-Bo Yu, Mark Vogelsberger, and Jesús Zavala. Spreading out and staying sharp - creating diverse rotation curves via baryonic and self-interaction effects. *MNRAS*, 468(2):2283–2295, June 2017. doi: 10.1093/mnras/stx522.
- [93] Omid Sameie, Hai-Bo Yu, Laura V. Sales, Mark Vogelsberger, and Jesús Zavala. Self-Interacting Dark Matter Subhalos in the Milky Way’s Tides. *Phys. Rev. Lett.*, 124(14):141102, April 2020. doi: 10.1103/PhysRevLett.124.141102.
- [94] Manoj Kaplinghat, Sean Tulin, and Hai-Bo Yu. Dark Matter Halos as Particle Colliders: Unified Solution to Small-Scale Structure Puzzles from Dwarfs to Clusters. *Phys. Rev. Lett.*, 116(4):041302, January 2016. doi: 10.1103/PhysRevLett.116.041302.

- [95] Oliver D. Elbert, James S. Bullock, Manoj Kaplinghat, Shea Garrison-Kimmel, Andrew S. Graus, and Miguel Rocha. A Testable Conspiracy: Simulating Baryonic Effects on Self-interacting Dark Matter Halos. *ApJ*, 853(2):109, February 2018. doi: 10.3847/1538-4357/aa9710.
- [96] Daniele S. M. Alves, Siavosh R. Behbahani, Philip Schuster, and Jay G. Wacker. Composite inelastic dark matter. *Physics Letters B*, 692(5):323–326, September 2010. doi: 10.1016/j.physletb.2010.08.006.
- [97] David E. Kaplan, Gordan Z. Krnjaic, Keith R. Rehermann, and Christopher M. Wells. Atomic dark matter. *J. Cosmol. Astropart. Phys.*, 2010(5):021, May 2010. doi: 10.1088/1475-7516/2010/05/021.
- [98] Kimberly K. Boddy, Jonathan L. Feng, Manoj Kaplinghat, and Tim M. P. Tait. Self-interacting dark matter from a non-Abelian hidden sector. *Phys. Rev. D*, 89(11):115017, Jun 2014. doi: 10.1103/PhysRevD.89.115017.
- [99] Mark B. Wise and Yue Zhang. Stable bound states of asymmetric dark matter. *Phys. Rev. D*, 90(5):055030, September 2014. doi: 10.1103/PhysRevD.90.055030.
- [100] R. Foot and S. Vagnozzi. Dissipative hidden sector dark matter. *Phys. Rev. D*, 91(2):023512, Jan 2015. doi: 10.1103/PhysRevD.91.023512.
- [101] Katelin Schutz and Tracy R. Slatyer. Self-scattering for Dark Matter with an excited state. *J. Cosmol. Astropart. Phys.*, 2015(1):021, Jan 2015. doi: 10.1088/1475-7516/2015/01/021.
- [102] Kimberly K. Boddy, Manoj Kaplinghat, Anna Kwa, and Annika H. G. Peter. Hidden sector hydrogen as dark matter: Small-scale structure formation predictions and the importance of hyperfine interactions. *Phys. Rev. D*, 94(12):123017, Dec 2016. doi: 10.1103/PhysRevD.94.123017.
- [103] Douglas P. Finkbeiner and Neal Weiner. X-ray line from exciting dark matter. *Phys. Rev. D*, 94(8):083002, Oct 2016. doi: 10.1103/PhysRevD.94.083002.
- [104] Yue Zhang. Self-interacting dark matter without direct detection constraints. *Physics of the Dark Universe*, 15:82–89, Mar 2017. doi: 10.1016/j.dark.2016.12.003.
- [105] Mattias Blennow, Stefan Clementz, and Juan Herrero-Garcia. Self-interacting inelastic dark matter: a viable solution to the small scale structure problems. *J. Cosmol. Astropart. Phys.*, 2017(3):048, Mar 2017. doi: 10.1088/1475-7516/2017/03/048.
- [106] Moira I. Gresham, Hou Keong Lou, and Kathryn M. Zurek. Astrophysical signatures of asymmetric dark matter bound states. *Phys. Rev. D*, 98(9):096001, November 2018. doi: 10.1103/PhysRevD.98.096001.

- [107] F. Governato, A. Zolotov, A. Pontzen, C. Christensen, S. H. Oh, A. M. Brooks, T. Quinn, S. Shen, and J. Wadsley. Cuspy no more: how outflows affect the central dark matter and baryon distribution in Λ cold dark matter galaxies. *MNRAS*, 422(2):1231–1240, May 2012. doi: 10.1111/j.1365-2966.2012.20696.x.
- [108] Aaron A. Dutton, Andrea V. Macciò, Jonas Frings, Liang Wang, Gregory S. Stinson, Camilla Penzo, and Xi Kang. NIHAO V: too big does not fail - reconciling the conflict between Λ CDM predictions and the circular velocities of nearby field galaxies. *MNRAS*, 457(1):L74–L78, Mar 2016. doi: 10.1093/mnras/slv193.
- [109] Azadeh Fattahi, Julio F. Navarro, Till Sawala, Carlos S. Frenk, Kyle A. Oman, Robert A. Crain, Michelle Furlong, Matthieu Schaller, Joop Schaye, Tom Theuns, and Adrian Jenkins. The APOSTLE project: Local Group kinematic mass constraints and simulation candidate selection. *MNRAS*, 457(1):844–856, Mar 2016. doi: 10.1093/mnras/stv2970.
- [110] Tobias Buck, Andrea V. Macciò, Aaron A. Dutton, Aura Obreja, and Jonas Frings. NIHAO XV: the environmental impact of the host galaxy on galactic satellite and field dwarf galaxies. *MNRAS*, 483(1):1314–1341, Feb 2019. doi: 10.1093/mnras/sty2913.
- [111] Mark Vogelsberger, Jesus Zavala, Christine Simpson, and Adrian Jenkins. Dwarf galaxies in CDM and SIDM with baryons: observational probes of the nature of dark matter. *MNRAS*, 444(4):3684–3698, Nov 2014. doi: 10.1093/mnras/stu1713.
- [112] A. Bastidas Fry, F. Governato, A. Pontzen, T. Quinn, M. Tremmel, L. Anderson, H. Menon, A. M. Brooks, and J. Wadsley. All about baryons: revisiting SIDM predictions at small halo masses. *MNRAS*, 452(2):1468–1479, September 2015. doi: 10.1093/mnras/stv1330.
- [113] Victor H. Robles, James S. Bullock, Oliver D. Elbert, Alex Fitts, Alejandro González-Samaniego, Michael Boylan-Kolchin, Philip F. Hopkins, Claude-André Faucher-Giguère, Dušan Kereš, and Christopher C. Hayward. SIDM on FIRE: hydrodynamical self-interacting dark matter simulations of low-mass dwarf galaxies. *MNRAS*, 472(3):2945–2954, Dec 2017. doi: 10.1093/mnras/stx2253.
- [114] Giulia Despali, Martin Sparre, Simona Vegetti, Mark Vogelsberger, Jesús Zavala, and Federico Marinacci. The interplay of self-interacting dark matter and baryons in shaping the halo evolution. *MNRAS*, 484(4):4563–4573, April 2019. doi: 10.1093/mnras/stz273.
- [115] Alex Fitts, Michael Boylan-Kolchin, Brandon Bozek, James S. Bullock, Andrew Graus, Victor Robles, Philip F. Hopkins, Kareem El-Badry, Shea Garrison-Kimmel, Claude-André Faucher-Giguère, Andrew Wetzel, and

- Dušan Kereš. Dwarf galaxies in CDM, WDM, and SIDM: disentangling baryons and dark matter physics. *MNRAS*, 490(1):962–977, Nov 2019. doi: 10.1093/mnras/stz2613.
- [116] Victor H. Robles, James S. Bullock, and Michael Boylan-Kolchin. Scalar field dark matter: helping or hurting small-scale problems in cosmology? *MNRAS*, 483(1):289–298, Feb 2019. doi: 10.1093/mnras/sty3190.
- [117] D. Lynden-Bell and Roger Wood. The gravo-thermal catastrophe in isothermal spheres and the onset of red-giant structure for stellar systems. *MNRAS*, 138:495, Jan 1968. doi: 10.1093/mnras/138.4.495.
- [118] D. Lynden-Bell and P. P. Eggleton. On the consequences of the gravothermal catastrophe. *MNRAS*, 191:483–498, May 1980. doi: 10.1093/mnras/191.3.483.
- [119] Andreas Burkert. The Structure and Evolution of Weakly Self-interacting Cold Dark Matter Halos. *ApJ*, 534(2):L143–L146, May 2000. doi: 10.1086/312674.
- [120] C. S. Kochanek and Martin White. A Quantitative Study of Interacting Dark Matter in Halos. *ApJ*, 543(2):514–520, November 2000. doi: 10.1086/317149.
- [121] Shmuel Balberg, Stuart L. Shapiro, and Shogo Inagaki. Self-Interacting Dark Matter Halos and the Gravothermal Catastrophe. *ApJ*, 568(2):475–487, Apr 2002. doi: 10.1086/339038.
- [122] Pedro Colín, Vladimir Avila-Reese, Octavio Valenzuela, and Claudio Firmani. Structure and Subhalo Population of Halos in a Self-interacting Dark Matter Cosmology. *ApJ*, 581(2):777–793, December 2002. doi: 10.1086/344259.
- [123] Jun Koda and Paul R. Shapiro. Gravothermal collapse of isolated self-interacting dark matter haloes: N-body simulation versus the fluid model. *MNRAS*, 415(2):1125–1137, August 2011. doi: 10.1111/j.1365-2966.2011.18684.x.
- [124] Camila A. Correa. Constraining velocity-dependent self-interacting dark matter with the Milky Way’s dwarf spheroidal galaxies. *MNRAS*, 503(1):920–937, May 2021. doi: 10.1093/mnras/stab506.
- [125] Rouven Essig, Samuel D. McDermott, Hai-Bo Yu, and Yi-Ming Zhong. Constraining Dissipative Dark Matter Self-Interactions. *Phys. Rev. Lett.*, 123(12):121102, Sep 2019. doi: 10.1103/PhysRevLett.123.121102.
- [126] Ran Huo, Hai-Bo Yu, and Yi-Ming Zhong. The Structure of Dissipative Dark Matter Halos. *arXiv e-prints*, art. arXiv:1912.06757, December 2019.

- [127] Julio F. Navarro, Carlos S. Frenk, and Simon D. M. White. The Structure of Cold Dark Matter Halos. *ApJ*, 462:563, May 1996. doi: 10.1086/177173.
- [128] JiJi Fan, Andrey Katz, Lisa Randall, and Matthew Reece. Double-Disk Dark Matter. *Physics of the Dark Universe*, 2(3):139–156, Sep 2013. doi: 10.1016/j.dark.2013.07.001.
- [129] JiJi Fan, Andrey Katz, Lisa Randall, and Matthew Reece. Dark-Disk Universe. *Phys. Rev. Lett.*, 110(21):211302, May 2013. doi: 10.1103/PhysRevLett.110.211302.
- [130] JiJi Fan, Andrey Katz, and Jessie Shelton. Direct and indirect detection of dissipative dark matter. *J. Cosmol. Astropart. Phys.*, 2014(6):059, Jun 2014. doi: 10.1088/1475-7516/2014/06/059.
- [131] Lisa Randall and Jakub Scholtz. Dissipative dark matter and the Andromeda plane of satellites. *J. Cosmol. Astropart. Phys.*, 2015(9):057, Sep 2015. doi: 10.1088/1475-7516/2015/09/057.
- [132] R. Foot. Galactic structure explained with dissipative mirror dark matter. *Phys. Rev. D*, 88(2):023520, Jul 2013. doi: 10.1103/PhysRevD.88.023520.
- [133] Robert Foot and Sunny Vagnozzi. Solving the small-scale structure puzzles with dissipative dark matter. *J. Cosmol. Astropart. Phys.*, 2016(7):013, Jul 2016. doi: 10.1088/1475-7516/2016/07/013.
- [134] Jae Hyeok Chang, Daniel Egana-Ugrinovic, Rouven Essig, and Chris Kouvaris. Structure formation and exotic compact objects in a dissipative dark sector. *J. Cosmol. Astropart. Phys.*, 2019(3):036, March 2019. doi: 10.1088/1475-7516/2019/03/036.
- [135] Keita Todoroki and Mikhail V. Medvedev. Dark matter haloes in the multicomponent model - I. Substructure. *MNRAS*, 483(3):3983–4003, March 2019. doi: 10.1093/mnras/sty3401.
- [136] Mark Vogelsberger, Jesús Zavala, Katelin Schutz, and Tracy R. Slatyer. Evaporating the Milky Way halo and its satellites with inelastic self-interacting dark matter. *MNRAS*, 484(4):5437–5452, April 2019. doi: 10.1093/mnras/stz340.
- [137] Dark Energy Survey Collaboration, T. Abbott, F. B. Abdalla, J. Aleksić, S. Allam, A. Amara, D. Bacon, E. Balbinot, M. Banerji, K. Bechtol, A. Benoit-Lévy, G. M. Bernstein, E. Bertin, J. Blazek, C. Bonnett, S. Bridle, D. Brooks, R. J. Brunner, E. Buckley-Geer, D. L. Burke, G. B. Caminha, D. Capozzi, J. Carlsen, A. Carnero-Rosell, M. Carollo, M. Carrasco-Kind, J. Carretero, F. J. Castander, L. Clerkin, T. Collett, C. Conselice, M. Crocce, C. E. Cunha, C. B. D’Andrea, L. N. da Costa, T. M. Davis, S. Desai, H. T. Diehl, J. P. Dietrich, S. Dodelson, P. Doel, A. Drlica-Wagner, J. Estrada, J. Etherington, A. E.

- Evrard, J. Fabbri, D. A. Finley, B. Flaugher, R. J. Foley, P. Fosalba, J. Frieman, J. García-Bellido, E. Gaztanaga, D. W. Gerdes, T. Giannantonio, D. A. Goldstein, D. Gruen, R. A. Gruendl, P. Guarnieri, G. Gutierrez, W. Hartley, K. Honscheid, B. Jain, D. J. James, T. Jeltema, S. Jouvel, R. Kessler, A. King, D. Kirk, R. Kron, K. Kuehn, N. Kuropatkin, O. Lahav, T. S. Li, M. Lima, H. Lin, M. A. G. Maia, M. Makler, M. Manera, C. Maraston, J. L. Marshall, P. Martini, R. G. McMahon, P. Melchior, A. Merson, C. J. Miller, R. Miquel, J. J. Mohr, X. Morice-Atkinson, K. Naidoo, E. Neilsen, R. C. Nichol, B. Nord, R. Ogando, F. Ostrovski, A. Palmese, A. Papadopoulos, H. V. Peiris, J. Peoples, W. J. Percival, A. A. Plazas, S. L. Reed, A. Refregier, A. K. Romer, A. Roodman, A. Ross, E. Roza, E. S. Rykoff, I. Sadeh, M. Sako, C. Sánchez, E. Sanchez, B. Santiago, V. Scarpine, M. Schubnell, I. Sevilla-Noarbe, E. Sheldon, M. Smith, R. C. Smith, M. Soares-Santos, F. Sobreira, M. Soumagnac, E. Suchyta, M. Sullivan, M. Swanson, G. Tarle, J. Thaler, D. Thomas, R. C. Thomas, D. Tucker, J. D. Vieira, V. Vikram, A. R. Walker, R. H. Wechsler, J. Weller, W. Wester, L. Whiteway, H. Wilcox, B. Yanny, Y. Zhang, and J. Zuntz. The Dark Energy Survey: more than dark energy - an overview. *MNRAS*, 460(2):1270–1299, August 2016. doi: 10.1093/mnras/stw641.
- [138] A. Drlica-Wagner, K. Bechtol, E. S. Rykoff, E. Luque, A. Queiroz, Y. Y. Mao, R. H. Wechsler, J. D. Simon, B. Santiago, B. Yanny, E. Balbinot, S. Dodelson, A. Fausti Neto, D. J. James, T. S. Li, M. A. G. Maia, J. L. Marshall, A. Pieres, K. Stringer, A. R. Walker, T. M. C. Abbott, F. B. Abdalla, S. Allam, A. Benoit-Lévy, G. M. Bernstein, E. Bertin, D. Brooks, E. Buckley-Geer, D. L. Burke, A. Carnero Rosell, M. Carrasco Kind, J. Carretero, M. Crocce, L. N. da Costa, S. Desai, H. T. Diehl, J. P. Dietrich, P. Doel, T. F. Eifler, A. E. Evrard, D. A. Finley, B. Flaugher, P. Fosalba, J. Frieman, E. Gaztanaga, D. W. Gerdes, D. Gruen, R. A. Gruendl, G. Gutierrez, K. Honscheid, K. Kuehn, N. Kuropatkin, O. Lahav, P. Martini, R. Miquel, B. Nord, R. Ogando, A. A. Plazas, K. Reil, A. Roodman, M. Sako, E. Sanchez, V. Scarpine, M. Schubnell, I. Sevilla-Noarbe, R. C. Smith, M. Soares-Santos, F. Sobreira, E. Suchyta, M. E. C. Swanson, G. Tarle, D. Tucker, V. Vikram, W. Wester, Y. Zhang, J. Zuntz, and DES Collaboration. Eight Ultra-faint Galaxy Candidates Discovered in Year Two of the Dark Energy Survey. *ApJ*, 813(2):109, November 2015. doi: 10.1088/0004-637X/813/2/109.
- [139] K. Bechtol, A. Drlica-Wagner, E. Balbinot, A. Pieres, J. D. Simon, B. Yanny, B. Santiago, R. H. Wechsler, J. Frieman, A. R. Walker, P. Williams, E. Roza, E. S. Rykoff, A. Queiroz, E. Luque, A. Benoit-Lévy, D. Tucker, I. Sevilla, R. A. Gruendl, L. N. da Costa, A. Fausti Neto, M. A. G. Maia, T. Abbott, S. Allam, R. Armstrong, A. H. Bauer, G. M. Bernstein, R. A. Bernstein, E. Bertin, D. Brooks, E. Buckley-Geer, D. L. Burke, A. Carnero Rosell, F. J. Castander, R. Covarrubias, C. B. D’Andrea, D. L. DePoy, S. Desai, H. T. Diehl, T. F. Eifler, J. Estrada, A. E. Evrard, E. Fernandez, D. A. Finley, B. Flaugher,

- E. Gaztanaga, D. Gerdes, L. Girardi, M. Gladders, D. Gruen, G. Gutierrez, J. Hao, K. Honscheid, B. Jain, D. James, S. Kent, R. Kron, K. Kuehn, N. Kuropatkin, O. Lahav, T. S. Li, H. Lin, M. Makler, M. March, J. Marshall, P. Martini, K. W. Merritt, C. Miller, R. Miquel, J. Mohr, E. Neilsen, R. Nichol, B. Nord, R. Ogando, J. Peoples, D. Petravick, A. A. Plazas, A. K. Romer, A. Roodman, M. Sako, E. Sanchez, V. Scarpine, M. Schubnell, R. C. Smith, M. Soares-Santos, F. Sobreira, E. Suchyta, M. E. C. Swanson, G. Tarle, J. Thaler, D. Thomas, W. Wester, J. Zuntz, and DES Collaboration. Eight New Milky Way Companions Discovered in First-year Dark Energy Survey Data. *ApJ*, 807(1):50, July 2015. doi: 10.1088/0004-637X/807/1/50.
- [140] A. Drlica-Wagner, K. Bechtol, S. Mau, M. McNanna, E. O. Nadler, A. B. Pace, T. S. Li, A. Pieres, E. Rozo, J. D. Simon, A. R. Walker, R. H. Wechsler, T. M. C. Abbott, S. Allam, J. Annis, E. Bertin, D. Brooks, D. L. Burke, A. Carnero Rosell, M. Carrasco Kind, J. Carretero, M. Costanzi, L. N. da Costa, J. De Vicente, S. Desai, H. T. Diehl, P. Doel, T. F. Eifler, S. Everett, B. Flaugher, J. Frieman, J. García-Bellido, E. Gaztanaga, D. Gruen, R. A. Gruendl, J. Gschwend, G. Gutierrez, K. Honscheid, D. J. James, E. Krause, K. Kuehn, N. Kuropatkin, O. Lahav, M. A. G. Maia, J. L. Marshall, P. Melchior, F. Menanteau, R. Miquel, A. Palmese, A. A. Plazas, E. Sanchez, V. Scarpine, M. Schubnell, S. Serrano, I. Sevilla-Noarbe, M. Smith, E. Suchyta, G. Tarle, and DES Collaboration. Milky Way Satellite Census. I. The Observational Selection Function for Milky Way Satellites in DES Y3 and Pan-STARRS DR1. *ApJ*, 893(1):47, April 2020. doi: 10.3847/1538-4357/ab7eb9.
- [141] Benjamin P. M. Laevens, Nicolas F. Martin, Rodrigo A. Ibata, Hans-Walter Rix, Edouard J. Bernard, Eric F. Bell, Branimir Sesar, Annette M. N. Ferguson, Edward F. Schlafly, Colin T. Slater, William S. Burgett, Kenneth C. Chambers, Heather Flewelling, Klaus A. Hodapp, Nicholas Kaiser, Rolf-Peter Kudritzki, Robert H. Lupton, Eugene A. Magnier, Nigel Metcalfe, Jeffrey S. Morgan, Paul A. Price, John L. Tonry, Richard J. Wainscoat, and Christopher Waters. A New Faint Milky Way Satellite Discovered in the Pan-STARRS1 3π Survey. *ApJ*, 802(2):L18, April 2015. doi: 10.1088/2041-8205/802/2/L18.
- [142] Benjamin P. M. Laevens, Nicolas F. Martin, Edouard J. Bernard, Edward F. Schlafly, Branimir Sesar, Hans-Walter Rix, Eric F. Bell, Annette M. N. Ferguson, Colin T. Slater, William E. Sweeney, Rosemary F. G. Wyse, Avon P. Huxor, William S. Burgett, Kenneth C. Chambers, Peter W. Draper, Klaus A. Hodapp, Nicholas Kaiser, Eugene A. Magnier, Nigel Metcalfe, John L. Tonry, Richard J. Wainscoat, and Christopher Waters. Sagittarius II, Draco II and Laevens 3: Three New Milky Way Satellites Discovered in the Pan-STARRS 1 3π Survey. *ApJ*, 813(1):44, November 2015. doi: 10.1088/0004-637X/813/1/44.

- [143] G. Torrealba, S. E. Koposov, V. Belokurov, and M. Irwin. The feeble giant. Discovery of a large and diffuse Milky Way dwarf galaxy in the constellation of Crater. *MNRAS*, 459(3):2370–2378, July 2016. doi: 10.1093/mnras/stw733.
- [144] G. Torrealba, V. Belokurov, S. E. Koposov, T. S. Li, M. G. Walker, J. L. Sanders, A. Geringer-Sameth, D. B. Zucker, K. Kuehn, N. W. Evans, and W. Dehnen. The hidden giant: discovery of an enormous Galactic dwarf satellite in Gaia DR2. *MNRAS*, 488(2):2743–2766, September 2019. doi: 10.1093/mnras/stz1624.
- [145] Sergey E. Koposov, Vasily Belokurov, Gabriel Torrealba, and N. Wyn Evans. Beasts of the Southern Wild: Discovery of Nine Ultra Faint Satellites in the Vicinity of the Magellanic Clouds. *ApJ*, 805(2):130, June 2015. doi: 10.1088/0004-637X/805/2/130.
- [146] Coral Wheeler, Jose Oñorbe, James S. Bullock, Michael Boylan-Kolchin, Oliver D. Elbert, Shea Garrison-Kimmel, Philip F. Hopkins, and Dušan Kereš. Sweating the small stuff: simulating dwarf galaxies, ultra-faint dwarf galaxies, and their own tiny satellites. *MNRAS*, 453(2):1305–1316, October 2015. doi: 10.1093/mnras/stv1691.
- [147] LSST Science Collaboration, Paul A. Abell, Julius Allison, Scott F. Anderson, John R. Andrew, J. Roger P. Angel, Lee Armus, David Arnett, S. J. Asztalos, Tim S. Axelrod, Stephen Bailey, D. R. Ballantyne, Justin R. Bankert, Wayne A. Barkhouse, Jeffrey D. Barr, L. Felipe Barrientos, Aaron J. Barth, James G. Bartlett, Andrew C. Becker, Jacek Becla, Timothy C. Beers, Joseph P. Bernstein, Rahul Biswas, Michael R. Blanton, Joshua S. Bloom, John J. Bochanski, Pat Boeshaar, Kirk D. Borne, Marusa Bradac, W. N. Brandt, Carrie R. Bridge, Michael E. Brown, Robert J. Brunner, James S. Bullock, Adam J. Burgasser, James H. Burge, David L. Burke, Phillip A. Cargile, Srinivasan Chandrasekharan, George Chartas, Steven R. Chesley, You-Hua Chu, David Cinabro, Mark W. Claire, Charles F. Claver, Douglas Clowe, A. J. Connolly, Kem H. Cook, Jeff Cooke, Asantha Cooray, Kevin R. Covey, Christopher S. Culliton, Roelof de Jong, Willem H. de Vries, Victor P. Debattista, Francisco Delgado, Ian P. Dell’Antonio, Saurav Dhital, Rosanne Di Stefano, Mark Dickinson, Benjamin Dilday, S. G. Djorgovski, Gregory Dobler, Ciro Donalek, Gregory Dubois-Felsmann, Josef Durech, Ardis Eliasdottir, Michael Eracleous, Laurent Eyler, Emilio E. Falco, Xiaohui Fan, Christopher D. Fassnacht, Harry C. Ferguson, Yanga R. Fernandez, Brian D. Fields, Douglas Finkbeiner, Eduardo E. Figuera, Derek B. Fox, Harold Francke, James S. Frank, Josh Frieman, Sebastien Fromenteau, Muhammad Furqan, Gaspar Galaz, A. Gal-Yam, Peter Garnavich, Eric Gawiser, John Geary, Perry Gee, Robert R. Gibson, Kirk Gilmore, Emily A. Grace, Richard F. Green, William J. Gressler, Carl J. Grillmair, Salman Habib, J. S. Haggerty, Mario Hamuy, Alan W. Harris, Suzanne L. Hawley,

Alan F. Heavens, Leslie Hebb, Todd J. Henry, Edward Hileman, Eric J. Hilton, Keri Hoadley, J. B. Holberg, Matt J. Holman, Steve B. Howell, Leopoldo Infante, Zeljko Ivezic, Suzanne H. Jacoby, Bhuvnesh Jain, R. Jedicke, M. James Jee, J. Garrett Jernigan, Saurabh W. Jha, Kathryn V. Johnston, R. Lynne Jones, Mario Juric, Mikko Kaasalainen, Styliani, Kafka, Steven M. Kahn, Nathan A. Kaib, Jason Kalirai, Jeff Kantor, Mansi M. Kasliwal, Charles R. Keeton, Richard Kessler, Zoran Knezevic, Adam Kowalski, Victor L. Krabbendam, K. Simon Krughoff, Shrinivas Kulkarni, Stephen Kuhlman, Mark Lacy, Sebastien Lepine, Ming Liang, Amy Lien, Paulina Lira, Knox S. Long, Suzanne Lorenz, Jennifer M. Lotz, R. H. Lupton, Julie Lutz, Lucas M. Macri, Ashish A. Mahabal, Rachel Mandelbaum, Phil Marshall, Morgan May, Peregrine M. McGehee, Brian T. Meadows, Alan Meert, Andrea Milani, Christopher J. Miller, Michelle Miller, David Mills, Dante Minniti, David Monet, Anjum S. Mukadam, Ehud Nakar, Douglas R. Neill, Jeffrey A. Newman, Sergei Nikolaev, Martin Nordby, Paul O'Connor, Masamune Oguri, John Oliver, Scot S. Olivier, Julia K. Olsen, Knut Olsen, Edward W. Olszewski, Hakeem Oluseyi, Nelson D. Padilla, Alex Parker, Joshua Pepper, John R. Peterson, Catherine Petry, Philip A. Pinto, James L. Pizagno, Bogdan Popescu, Andrej Prsa, Veljko Radcka, M. Jordan Raddick, Andrew Rasmussen, Arne Rau, Jeonghee Rho, James E. Rhoads, Gordon T. Richards, Stephen T. Ridgway, Brant E. Robertson, Rok Roskar, Abhijit Saha, Ata Sarajedini, Evan Scannapieco, Terry Schalk, Rafe Schindler, Samuel Schmidt, Sarah Schmidt, Donald P. Schneider, German Schumacher, Ryan Scranton, Jacques Sebag, Lynn G. Seppala, Ohad Shemmer, Joshua D. Simon, M. Sivertz, Howard A. Smith, J. Allyn Smith, Nathan Smith, Anna H. Spitz, Adam Stanford, Keivan G. Stassun, Jay Strader, Michael A. Strauss, Christopher W. Stubbs, Donald W. Sweeney, Alex Szalay, Paula Szkody, Masahiro Takada, Paul Thorman, David E. Trilling, Virginia Trimble, Anthony Tyson, Richard Van Berg, Daniel Vanden Berk, Jake VanderPlas, Licia Verde, Bojan Vrsnak, Lucianne M. Walkowicz, Benjamin D. Wandelt, Sheng Wang, Yun Wang, Michael Warner, Risa H. Wechsler, Andrew A. West, Oliver Wiecha, Benjamin F. Williams, Beth Willman, David Wittman, Sidney C. Wolff, W. Michael Wood-Vasey, Przemek Wozniak, Patrick Young, Andrew Zentner, and Hu Zhan. LSST Science Book, Version 2.0. *arXiv e-prints*, art. arXiv:0912.0201, December 2009.

- [148] Donald G. York, J. Adelman, Jr. Anderson, John E., Scott F. Anderson, James Annis, Neta A. Bahcall, J. A. Bakken, Robert Barkhouser, Steven Bastian, Eileen Berman, William N. Boroski, Steve Bracker, Charlie Briegel, John W. Briggs, J. Brinkmann, Robert Brunner, Scott Burles, Larry Carey, Michael A. Carr, Francisco J. Castander, Bing Chen, Patrick L. Colestock, A. J. Connolly, J. H. Crocker, István Csabai, Paul C. Czarapata, John Eric Davis, Mamoru Doi, Tom Dombeck, Daniel Eisenstein, Nancy Ellman, Brian R. Elms, Michael L. Evans, Xiaohui Fan, Glenn R. Federwitz, Larry Fiscelli, Scott Friedman, Joshua A. Frieman, Masataka Fukugita, Bruce Gillespie,

James E. Gunn, Vijay K. Gurbani, Ernst de Haas, Merle Haldeman, Frederick H. Harris, J. Hayes, Timothy M. Heckman, G. S. Hennessy, Robert B. Hindsley, Scott Holm, Donald J. Holmgren, Chi-hao Huang, Charles Hull, Don Husby, Shin-Ichi Ichikawa, Takashi Ichikawa, Željko Ivezić, Stephen Kent, Rita S. J. Kim, E. Kinney, Mark Klaene, A. N. Kleinman, S. Kleinman, G. R. Knapp, John Korienek, Richard G. Kron, Peter Z. Kunszt, D. Q. Lamb, B. Lee, R. French Leger, Siriluk Limmongkol, Carl Lindenmeyer, Daniel C. Long, Craig Loomis, Jon Loveday, Rich Lucinio, Robert H. Lupton, Bryan MacKinnon, Edward J. Mannery, P. M. Mantsch, Bruce Margon, Peregrine McGehee, Timothy A. McKay, Avery Meiksin, Aronne Merelli, David G. Monet, Jeffrey A. Munn, Vijay K. Narayanan, Thomas Nash, Eric Neilsen, Rich Neswold, Heidi Jo Newberg, R. C. Nichol, Tom Nicinski, Mario Nonino, Norio Okada, Sadanori Okamura, Jeremiah P. Ostriker, Russell Owen, A. George Pauls, John Peoples, R. L. Peterson, Donald Petravick, Jeffrey R. Pier, Adrian Pope, Ruth Pordes, Angela Prosapio, Ron Rechenmacher, Thomas R. Quinn, Gordon T. Richards, Michael W. Richmond, Claudio H. Rivetta, Constance M. Rockosi, Kurt Ruthmansdorfer, Dale Sandford, David J. Schlegel, Donald P. Schneider, Maki Sekiguchi, Gary Sergey, Kazuhiro Shimasaku, Walter A. Siegmund, Stephen Smee, J. Allyn Smith, S. Snedden, R. Stone, Chris Stoughton, Michael A. Strauss, Christopher Stubbs, Mark SubbaRao, Alexander S. Szalay, Istvan Szapudi, Gyula P. Szokoly, Anirudda R. Thakar, Christy Tremonti, Douglas L. Tucker, Alan Uomoto, Dan Vanden Berk, Michael S. Vogeley, Patrick Waddell, Shu-i. Wang, Masaru Watanabe, David H. Weinberg, Brian Yanny, Naoki Yasuda, and SDSS Collaboration. *The Sloan Digital Sky Survey: Technical Summary*. *AJ*, 120(3):1579–1587, September 2000. doi: 10.1086/301513.

- [149] B. Flaugher, H. T. Diehl, K. Honscheid, T. M. C. Abbott, O. Alvarez, R. Angstadt, J. T. Annis, M. Antonik, O. Ballester, L. Beaufore, G. M. Bernstein, R. A. Bernstein, B. Bigelow, M. Bonati, D. Boprie, D. Brooks, E. J. Buckley-Geer, J. Campa, L. Cardiel-Sas, F. J. Castander, J. Castilla, H. Cease, J. M. Cela-Ruiz, S. Chappa, E. Chi, C. Cooper, L. N. da Costa, E. Dede, G. Derylo, D. L. DePoy, J. de Vicente, P. Doel, A. Drlica-Wagner, J. Eiting, A. E. Elliott, J. Emes, J. Estrada, A. Fausti Neto, D. A. Finley, R. Flores, J. Frieman, D. Gerdes, M. D. Gladders, B. Gregory, G. R. Gutierrez, J. Hao, S. E. Holland, S. Holm, D. Huffman, C. Jackson, D. J. James, M. Jonas, A. Karcher, I. Karliner, S. Kent, R. Kessler, M. Kozlovsky, R. G. Kron, D. Kubik, K. Kuehn, S. Kuhlmann, K. Kuk, O. Lahav, A. Lathrop, J. Lee, M. E. Levi, P. Lewis, T. S. Li, I. Mandrichenko, J. L. Marshall, G. Martinez, K. W. Merritt, R. Miquel, F. Muñoz, E. H. Neilsen, R. C. Nichol, B. Nord, R. Ogando, J. Olsen, N. Palaio, K. Patton, J. Peoples, A. A. Plazas, J. Rauch, K. Reil, J. P. Rheault, N. A. Roe, H. Rogers, A. Roodman, E. Sanchez, V. Scarpine, R. H. Schindler, R. Schmidt, R. Schmitt, M. Schubnell, K. Schultz, P. Schurter, L. Scott, S. Serrano, T. M. Shaw, R. C. Smith, M. Soares-Santos, A. Stefanik, W. Stuermer, E. Suchyta, A. Sypniewski,

- G. Tarle, J. Thaler, R. Tighe, C. Tran, D. Tucker, A. R. Walker, G. Wang, M. Watson, C. Weaverdyck, W. Wester, R. Woods, B. Yanny, and DES Collaboration. The Dark Energy Camera. *AJ*, 150(5):150, November 2015. doi: 10.1088/0004-6256/150/5/150.
- [150] Satoshi Miyazaki, Yutaka Komiyama, Maki Sekiguchi, Sadanori Okamura, Mamoru Doi, Hisanori Furusawa, Masaru Hamabe, Katsumi Imi, Masahiko Kimura, Fumiaki Nakata, Norio Okada, Masami Ouchi, Kazuhiro Shimasaku, Masafumi Yagi, and Naoki Yasuda. Subaru Prime Focus Camera – Suprime-Cam. *Publications of the Astronomical Society of Japan*, 54:833–853, December 2002. doi: 10.1093/pasj/54.6.833.
- [151] Satoshi Miyazaki, Yutaka Komiyama, Satoshi Kawanomoto, Yoshiyuki Doi, Hisanori Furusawa, Takashi Hamana, Yusuke Hayashi, Hiroyuki Ikeda, Yukiko Kamata, Hiroshi Karoji, Michitaro Koike, Tomio Kurakami, Shoken Miyama, Tomoki Morokuma, Fumiaki Nakata, Kazuhito Namikawa, Hidehiko Nakaya, Kyoji Nariai, Yoshiyuki Obuchi, Yukie Oishi, Norio Okada, Yuki Okura, Philip Tait, Tadafumi Takata, Yoko Tanaka, Masayuki Tanaka, Tsuyoshi Terai, Daigo Tomono, Fumihiro Uruguchi, Tomonori Usuda, Yousuke Utsumi, Yoshihiko Yamada, Hitomi Yamanoi, Hiroaki Aihara, Hiroki Fujimori, Sogo Mineo, Hironao Miyatake, Masamune Oguri, Tomohisa Uchida, Manobu M. Tanaka, Naoki Yasuda, Masahiro Takada, Hitoshi Murayama, Atsushi J. Nishizawa, Naoshi Sugiyama, Masashi Chiba, Toshifumi Futamase, Shiang-Yu Wang, Hsin-Yo Chen, Paul T. P. Ho, Eric J. Y. Liaw, Chi-Fang Chiu, Cheng-Lin Ho, Tsang-Chih Lai, Yao-Cheng Lee, Dun-Zen Jeng, Satoru Iwamura, Robert Armstrong, Steve Bickerton, James Bosch, James E. Gunn, Robert H. Lupton, Craig Loomis, Paul Price, Steward Smith, Michael A. Strauss, Edwin L. Turner, Hisanori Suzuki, Yasuhito Miyazaki, Masaharu Muramatsu, Koei Yamamoto, Makoto Endo, Yutaka Ezaki, Noboru Ito, Noboru Kawaguchi, Satoshi Sofuku, Tomoaki Taniike, Kotaro Akutsu, Naoto Dojo, Kazuyuki Kasumi, Toru Matsuda, Kohei Imoto, Yoshinori Miwa, Masayuki Suzuki, Kunio Takeshi, and Hideo Yokota. Hyper Suprime-Cam: System design and verification of image quality. *Publications of the Astronomical Society of Japan*, 70:S1, January 2018. doi: 10.1093/pasj/psx063.
- [152] D. J. Sand, K. Spekkens, D. Crnojević, J. R. Hargis, B. Willman, J. Strader, and C. J. Grillmair. Antlia B: A Faint Dwarf Galaxy Member of the NGC 3109 Association. *ApJ*, 812(1):L13, October 2015. doi: 10.1088/2041-8205/812/1/L13.
- [153] D. Crnojević, D. J. Sand, K. Spekkens, N. Caldwell, P. Guhathakurta, B. McLeod, A. Seth, J. D. Simon, J. Strader, and E. Toloba. The Extended Halo of Centaurus A: Uncovering Satellites, Streams, and Substructures. *ApJ*, 823(1):19, May 2016. doi: 10.3847/0004-637X/823/1/19.
- [154] Jeffrey L. Carlin, David J. Sand, Paul Price, Beth Willman, Ananthan Karunakaran, Kristine Spekkens, Eric F. Bell, Jean P. Brodie, Denija Crnoje-

- vić, Duncan A. Forbes, Jonathan Hargis, Evan Kirby, Robert Lupton, Annika H. G. Peter, Aaron J. Romanowsky, and Jay Strader. First Results from the MADCASH Survey: A Faint Dwarf Galaxy Companion to the Low-mass Spiral Galaxy NGC 2403 at 3.2 Mpc. *ApJ*, 828(1):L5, September 2016. doi: 10.3847/2041-8205/828/1/L5.
- [155] Jin Koda, Masafumi Yagi, Hitomi Yamanoi, and Yutaka Komiyama. Approximately a Thousand Ultra-diffuse Galaxies in the Coma Cluster. *ApJ*, 807(1):L2, July 2015. doi: 10.1088/2041-8205/807/1/L2.
- [156] Roberto P. Muñoz, Paul Eigenthaler, Thomas H. Puzia, Matthew A. Taylor, Yasna Ordenes-Briceño, Karla Alamo-Martínez, Karen X. Ribbeck, Simón Ángel, Massimo Capaccioli, Patrick Côté, Laura Ferrarese, Gaspar Galaz, Maren Hempel, Michael Hilker, Andrés Jordán, Ariane Lançon, Steffen Mieske, Maurizio Paolillo, Tom Richtler, Ruben Sánchez-Janssen, and Hongxin Zhang. Unveiling a Rich System of Faint Dwarf Galaxies in the Next Generation Fornax Survey. *ApJ*, 813(1):L15, November 2015. doi: 10.1088/2041-8205/813/1/L15.
- [157] Jürgen Ott, Adrienne M. Stilp, Steven R. Warren, Evan D. Skillman, Julianne J. Dalcanton, Fabian Walter, W. J. G. de Blok, Bärbel Koribalski, and Andrew A. West. VLA-ANGST: A High-resolution H I Survey of Nearby Dwarf Galaxies. *AJ*, 144(4):123, October 2012. doi: 10.1088/0004-6256/144/4/123.
- [158] Douglas Clowe, Maruša Bradač, Anthony H. Gonzalez, Maxim Markevitch, Scott W. Randall, Christine Jones, and Dennis Zaritsky. A Direct Empirical Proof of the Existence of Dark Matter. *ApJ*, 648(2):L109–L113, September 2006. doi: 10.1086/508162.
- [159] Scott W. Randall, Maxim Markevitch, Douglas Clowe, Anthony H. Gonzalez, and Marusa Bradac. Constraints on the Self-Interaction Cross Section of Dark Matter from Numerical Simulations of the Merging Galaxy Cluster. *ApJ*, 679(2):1173–1180, June 2008. doi: 10.1086/587859.
- [160] Felix Kahlhoefer, Kai Schmidt-Hoberg, Janis Kummer, and Subir Sarkar. On the interpretation of dark matter self-interactions in Abell 3827. *MNRAS*, 452(1):L54–L58, September 2015. doi: 10.1093/mnras/slv088.
- [161] David Harvey, Richard Massey, Thomas Kitching, Andy Taylor, and Eric Tittley. The nongravitational interactions of dark matter in colliding galaxy clusters. *Science*, 347(6229):1462–1465, March 2015. doi: 10.1126/science.1261381.
- [162] David Wittman, Nathan Golovich, and William A. Dawson. The Mismeasure of Mergers: Revised Limits on Self-interacting Dark Matter in Merging Galaxy Clusters. *ApJ*, 869(2):104, December 2018. doi: 10.3847/1538-4357/aace77.

- [163] David Harvey, Andrew Robertson, Richard Massey, and Ian G. McCarthy. Observable tests of self-interacting dark matter in galaxy clusters: BCG wobbles in a constant density core. *MNRAS*, 488(2):1572–1579, September 2019. doi: 10.1093/mnras/stz1816.
- [164] Andrew Robertson, David Harvey, Richard Massey, Vincent Eke, Ian G. McCarthy, Mathilde Jauzac, Baojiu Li, and Joop Schaye. Observable tests of self-interacting dark matter in galaxy clusters: cosmological simulations with SIDM and baryons. *MNRAS*, 488(3):3646–3662, September 2019. doi: 10.1093/mnras/stz1815.
- [165] Jordi Miralda-Escudé. A Test of the Collisional Dark Matter Hypothesis from Cluster Lensing. *ApJ*, 564(1):60–64, January 2002. doi: 10.1086/324138.
- [166] Annika H. G. Peter, Miguel Rocha, James S. Bullock, and Manoj Kaplinghat. Cosmological simulations with self-interacting dark matter - II. Halo shapes versus observations. *MNRAS*, 430(1):105–120, March 2013. doi: 10.1093/mnras/sts535.
- [167] Yasuhiro Hashimoto, H. Böhringer, J. P. Henry, G. Hasinger, and G. Szokoly. Robust quantitative measures of cluster X-ray morphology, and comparisons between cluster characteristics. *A&A*, 467(2):485–499, May 2007. doi: 10.1051/0004-6361:20065125.
- [168] Hajime Kawahara. The Axis Ratio Distribution of X-ray Clusters Observed by XMM-Newton. *ApJ*, 719(2):1926–1931, August 2010. doi: 10.1088/0004-637X/719/2/1926.
- [169] Tesla E. Jeltema, Claude R. Canizares, Mark W. Bautz, and David A. Buote. The Evolution of Structure in X-Ray Clusters of Galaxies. *ApJ*, 624(2): 606–629, May 2005. doi: 10.1086/428940.
- [170] J. S. Santos, P. Rosati, P. Tozzi, H. Böhringer, S. Ettori, and A. Bignamini. Searching for cool core clusters at high redshift. *A&A*, 483(1):35–47, May 2008. doi: 10.1051/0004-6361:20078815.
- [171] H. Böhringer, G. W. Pratt, M. Arnaud, S. Borgani, J. H. Croston, T. J. Ponman, S. Ameglio, R. F. Temple, and K. Dolag. Substructure of the galaxy clusters in the REXCESS sample: observed statistics and comparison to numerical simulations. *A&A*, 514:A32, May 2010. doi: 10.1051/0004-6361/200913911.
- [172] D. Nurgaliev, M. McDonald, B. A. Benson, E. D. Miller, C. W. Stubbs, and A. Vikhlinin. A Robust Quantification of Galaxy Cluster Morphology Using Asymmetry and Central Concentration. *ApJ*, 779(2):112, December 2013. doi: 10.1088/0004-637X/779/2/112.

- [173] Elena Rasia, Massimo Meneghetti, and Stefano Ettori. X-ray Morphological Estimators for Galaxy Clusters. *The Astronomical Review*, 8:40–70, January 2013. doi: 10.1080/21672857.2013.11519713.
- [174] Yoshiki Matsuoka, Masafusa Onoue, Nobunari Kashikawa, Kazushi Iwasawa, Michael A. Strauss, Tohru Nagao, Masatoshi Imanishi, Mana Niida, Yoshiki Toba, Masayuki Akiyama, and et al. Subaru high-z exploration of low-luminosity quasars (shellqs). i. discovery of 15 quasars and bright galaxies at $5.7 < z < 6.9$. *The Astrophysical Journal*, 828(1):26, Aug 2016. ISSN 1538-4357. doi: 10.3847/0004-637x/828/1/26. URL <http://dx.doi.org/10.3847/0004-637x/828/1/26>.
- [175] Eduardo Bañados, Bram P. Venemans, Chiara Mazzucchelli, Emanuele P. Farina, Fabian Walter, Feige Wang, Roberto Decarli, Daniel Stern, Xiaohui Fan, Frederick B. Davies, and et al. An 800-million-solar-mass black hole in a significantly neutral universe at a redshift of 7.5. *Nature*, 553(7689): 473–476, Dec 2017. ISSN 1476-4687. doi: 10.1038/nature25180. URL <http://dx.doi.org/10.1038/nature25180>.
- [176] Feige Wang, Jinyi Yang, Xiaohui Fan, Minghao Yue, Xue-Bing Wu, Jan-Torge Schindler, Fuyan Bian, Jiang-Tao Li, Emanuele P. Farina, Eduardo Bañados, and et al. The discovery of a luminous broad absorption line quasar at a redshift of 7.02. *The Astrophysical Journal*, 869(1):L9, Dec 2018. ISSN 2041-8213. doi: 10.3847/2041-8213/aaf1d2. URL <http://dx.doi.org/10.3847/2041-8213/aaf1d2>.
- [177] Yoshiki Matsuoka, Masafusa Onoue, Nobunari Kashikawa, Michael A Strauss, Kazushi Iwasawa, Chien-Hsiu Lee, Masatoshi Imanishi, Tohru Nagao, Masayuki Akiyama, Naoko Asami, James Bosch, Hisanori Furusawa, Tomotsugu Goto, James E Gunn, Yuichi Harikane, Hiroyuki Ikeda, Takuma Izumi, Toshihiro Kawaguchi, Nanako Kato, Satoshi Kikuta, Kotaro Kohno, Yutaka Komiyama, Shuhei Koyama, Robert H Lupton, Takeo Minezaki, Satoshi Miyazaki, Hitoshi Murayama, Mana Niida, Atsushi J Nishizawa, Akatoki Noboriguchi, Masamune Oguri, Yoshiaki Ono, Masami Ouchi, Paul A Price, Hiroaki Sameshima, Andreas Schulze, Hikari Shirakata, John D Silverman, Naoshi Sugiyama, Philip J Tait, Masahiro Takada, Tadafumi Takata, Masayuki Tanaka, Ji-Jia Tang, Yoshiki Toba, Yousuke Utsumi, Shiang-Yu Wang, and Takuji Yamashita. Discovery of the first low-luminosity quasar at $z > 7$. *The Astrophysical Journal*, 872(1):L2, feb 2019. doi: 10.3847/2041-8213/ab0216. URL <https://doi.org/10.3847/2041-8213/ab0216>.
- [178] Jinyi Yang, Feige Wang, Xiaohui Fan, Joseph F. Hennawi, Frederick B. Davies, Minghao Yue, Eduardo Banados, Xue-Bing Wu, Bram Venemans, Aaron J. Barth, Fuyan Bian, Konstantina Boutsia, Roberto Decarli, Emanuele Paolo Farina, Richard Green, Linhua Jiang, Jiang-Tao Li, Chiara Mazzucchelli, and Fabian Walter. Pōniuā‘ena: A luminous $z =$

7.5 quasar hosting a 1.5 billion solar mass black hole. *The Astrophysical Journal*, 897(1):L14, jul 2020. doi: 10.3847/2041-8213/ab9c26. URL <https://doi.org/10.3847/2041-8213/ab9c26>.

- [179] Piero Madau and Martin J. Rees. Massive Black Holes as Population III Remnants. *ApJ*, 551(1):L27–L30, April 2001. doi: 10.1086/319848.
- [180] Tom Abel, Greg L. Bryan, and Michael L. Norman. The Formation of the First Star in the Universe. *Science*, 295(5552):93–98, January 2002. doi: 10.1126/science.295.5552.93.
- [181] Volker Bromm, Paolo S. Coppi, and Richard B. Larson. The Formation of the First Stars. I. The Primordial Star-forming Cloud. *ApJ*, 564(1):23–51, January 2002. doi: 10.1086/323947.
- [182] Brian W. O’Shea and Michael L. Norman. Population III Star Formation in a Λ CDM Universe. I. The Effect of Formation Redshift and Environment on Protostellar Accretion Rate. *ApJ*, 654(1):66–92, January 2007. doi: 10.1086/509250.
- [183] Matthew J. Turk, Tom Abel, and Brian O’Shea. The Formation of Population III Binaries from Cosmological Initial Conditions. *Science*, 325(5940):601, July 2009. doi: 10.1126/science.1173540.
- [184] Takamitsu Tanaka and Zoltán Haiman. The Assembly of Supermassive Black Holes at High Redshifts. *ApJ*, 696(2):1798–1822, May 2009. doi: 10.1088/0004-637X/696/2/1798.
- [185] Thomas H. Greif, Volker Bromm, Paul C. Clark, Simon C. O. Glover, Rowan J. Smith, Ralf S. Klessen, Naoki Yoshida, and Volker Springel. Formation and evolution of primordial protostellar systems. *MNRAS*, 424(1):399–415, July 2012. doi: 10.1111/j.1365-2966.2012.21212.x.
- [186] Rosa Valiante, Raffaella Schneider, Marta Volonteri, and Kazuyuki Omukai. From the first stars to the first black holes. *MNRAS*, 457(3):3356–3371, April 2016. doi: 10.1093/mnras/stw225.
- [187] Shingo Hirano, Takashi Hosokawa, Naoki Yoshida, Hideyuki Umeda, Kazuyuki Omukai, Gen Chiaki, and Harold W. Yorke. ONE HUNDRED FIRST STARS: PROTOSTELLAR EVOLUTION AND THE FINAL MASSES. *The Astrophysical Journal*, 781(2):60, jan 2014. doi: 10.1088/0004-637x/781/2/60. URL <https://doi.org/10.1088%2F0004-637x%2F781%2F2%2F60>.
- [188] Jarrett L. Johnson and Volker Bromm. The aftermath of the first stars: massive black holes. *Monthly Notices of the Royal Astronomical Society*, 374(4):1557–1568, 01 2007. ISSN 0035-8711. doi: 10.1111/j.1365-2966.2006.11275.x. URL <https://doi.org/10.1111/j.1365-2966.2006.11275.x>.

- [189] Daniel Whalen, Bob van Veelen, Brian W. O’Shea, and Michael L. Norman. The destruction of cosmological minihalos by primordial supernovae. *The Astrophysical Journal*, 682(1):49–67, jul 2008. doi: 10.1086/589643. URL <https://doi.org/10.1086/589643>.
- [190] Miloš Milosavljević, Sean M. Couch, and Volker Bromm. ACCRETION ONTO INTERMEDIATE-MASS BLACK HOLES IN DENSE PROTO-GALACTIC CLOUDS. *The Astrophysical Journal*, 696(2):L146–L149, apr 2009. doi: 10.1088/0004-637x/696/2/1146. URL <https://doi.org/10.1088/0004-637x/696/2/1146>.
- [191] Marcelo A. Alvarez, John H. Wise, and Tom Abel. ACCRETION ONTO THE FIRST STELLAR-MASS BLACK HOLES. *The Astrophysical Journal*, 701(2):L133–L137, aug 2009. doi: 10.1088/0004-637x/701/2/1133. URL <https://doi.org/10.1088/0004-637x/701/2/1133>.
- [192] M. Brightman, M. Bachetti, H. P. Earnshaw, F. Fürst, J. García, B. Grefenstette, M. Heida, E. Kara, K. K. Madsen, M. J. Middleton, D. Stern, F. Tombesi, and D. J. Walton. Breaking the limit: Super-eddington accretion onto black holes and neutron stars, 2019.
- [193] Piero Madau, Francesco Haardt, and Massimo Dotti. SUPER-CRITICAL GROWTH OF MASSIVE BLACK HOLES FROM STELLAR-MASS SEEDS. *The Astrophysical Journal*, 784(2):L38, mar 2014. doi: 10.1088/2041-8205/784/2/138. URL <https://doi.org/10.1088/2041-8205/784/2/138>.
- [194] Volker Bromm and Abraham Loeb. Formation of the First Supermassive Black Holes. *ApJ*, 596(1):34–46, October 2003. doi: 10.1086/377529.
- [195] Savvas M. Koushiappas, James S. Bullock, and Avishai Dekel. Massive black hole seeds from low angular momentum material. *MNRAS*, 354(1):292–304, October 2004. doi: 10.1111/j.1365-2966.2004.08190.x.
- [196] Mitchell C. Begelman, Marta Volonteri, and Martin J. Rees. Formation of supermassive black holes by direct collapse in pre-galactic haloes. *MNRAS*, 370(1):289–298, July 2006. doi: 10.1111/j.1365-2966.2006.10467.x.
- [197] Giuseppe Lodato and Priyamvada Natarajan. Supermassive black hole formation during the assembly of pre-galactic discs. *MNRAS*, 371(4):1813–1823, October 2006. doi: 10.1111/j.1365-2966.2006.10801.x.
- [198] A. Ferrara, S. Salvadori, B. Yue, and D. Schleicher. Initial mass function of intermediate-mass black hole seeds. *MNRAS*, 443(3):2410–2425, September 2014. doi: 10.1093/mnras/stu1280.
- [199] Fabio Pacucci, Marta Volonteri, and Andrea Ferrara. The growth efficiency of high-redshift black holes. *MNRAS*, 452(2):1922–1933, September 2015. doi: 10.1093/mnras/stv1465.

- [200] Yoshiki Matsuoka, Masafusa Onoue, Nobunari Kashikawa, Michael A. Strauss, Kazushi Iwasawa, Chien-Hsiu Lee, Masatoshi Imanishi, Tohru Nagao, Masayuki Akiyama, Naoko Asami, James Bosch, Hisanori Furusawa, Tomotsugu Goto, James E. Gunn, Yuichi Harikane, Hiroyuki Ikeda, Takuma Izumi, Toshihiro Kawaguchi, Nanako Kato, Satoshi Kikuta, Kotaro Kohno, Yutaka Komiyama, Shuhei Koyama, Robert H. Lupton, Takeo Minezaki, Satoshi Miyazaki, Hitoshi Murayama, Mana Niida, Atsushi J. Nishizawa, Akatoki Noboriguchi, Masamune Oguri, Yoshiaki Ono, Masami Ouchi, Paul A. Price, Hiroaki Sameshima, Andreas Schulze, Hikari Shirakata, John D. Silverman, Naoshi Sugiyama, Philip J. Tait, Masahiro Takada, Tadafumi Takata, Masayuki Tanaka, Ji-Jia Tang, Yoshiki Toba, Yousuke Utsumi, Shiang-Yu Wang, and Takuji Yamashita. Discovery of the First Low-luminosity Quasar at $z > 7$. *ApJ*, 872(1):L2, February 2019. doi: 10.3847/2041-8213/ab0216.
- [201] Masafusa Onoue, Nobunari Kashikawa, Yoshiki Matsuoka, Nanako Kato, Takuma Izumi, Tohru Nagao, Michael A. Strauss, Yuichi Harikane, Masatoshi Imanishi, Kei Ito, Kazushi Iwasawa, Toshihiro Kawaguchi, Chien-Hsiu Lee, Akatoki Noboriguchi, Hyewon Suh, Masayuki Tanaka, and Yoshiki Toba. Subaru High- z Exploration of Low-luminosity Quasars (SHELLQs). VI. Black Hole Mass Measurements of Six Quasars at $6.1 \leq z \leq 6.7$. *ApJ*, 880(2):77, August 2019. doi: 10.3847/1538-4357/ab29e9.
- [202] Anna-Christina Eilers et al. Detecting and Characterizing Young Quasars. I. Systemic Redshifts and Proximity Zone Measurements. *Astrophys. J.*, 900(1):37, 2020. doi: 10.3847/1538-4357/aba52e.
- [203] Anna-Christina Eilers, Frederick B. Davies, Joseph F. Hennawi, J. Xavier Prochaska, Zarija Lukić, and Chiara Mazzucchelli. Implications of $z \sim 6$ Quasar Proximity Zones for the Epoch of Reionization and Quasar Lifetimes. *ApJ*, 840(1):24, May 2017. doi: 10.3847/1538-4357/aa6c60.
- [204] Anna-Christina Eilers, Joseph F. Hennawi, and Frederick B. Davies. First spectroscopic study of a young quasar. *The Astrophysical Journal*, 867(1):30, Oct 2018. ISSN 1538-4357. doi: 10.3847/1538-4357/aae081. URL <http://dx.doi.org/10.3847/1538-4357/aae081>.
- [205] Frederick B. Davies, Joseph F. Hennawi, and Anna-Christina Eilers. Time-dependent behaviour of quasar proximity zones at $z \sim 6$. *MNRAS*, 493(1):1330–1343, March 2020. doi: 10.1093/mnras/stz3303.
- [206] Irham Taufik Andika, Knud Jahnke, Masafusa Onoue, Eduardo Bañados, Chiara Mazzucchelli, Mladen Novak, Anna-Christina Eilers, Bram P. Venemans, Jan-Torge Schindler, Fabian Walter, and et al. Probing the nature of high-redshift weak emission line quasars: A young quasar with a starburst

- host galaxy. *The Astrophysical Journal*, 903(1):34, Oct 2020. ISSN 1538-4357. doi: 10.3847/1538-4357/abb9a6. URL <http://dx.doi.org/10.3847/1538-4357/abb9a6>.
- [207] Shmuel Balberg, Stuart L. Shapiro, and Shogo Inagaki. Selfinteracting dark matter halos and the gravothermal catastrophe. *Astrophys. J.*, 568:475–487, 2002. doi: 10.1086/339038.
- [208] Jason Pollack, David N. Spergel, and Paul J. Steinhardt. Supermassive Black Holes from Ultra-Strongly Self-Interacting Dark Matter. *Astrophys. J.*, 804(2):131, 2015. doi: 10.1088/0004-637X/804/2/131.
- [209] Jian Hu, Yue Shen, Yu-Qing Lou, and Shuangnan Zhang. Forming supermassive black holes by accreting dark and baryon matter. *Monthly Notices of the Royal Astronomical Society*, 365(1):345–351, Jan 2006. ISSN 1365-2966. doi: 10.1111/j.1365-2966.2005.09712.x. URL <http://dx.doi.org/10.1111/j.1365-2966.2005.09712.x>.
- [210] Luis E. Padilla, Tanja Rindler-Daller, Paul R. Shapiro, Tonatiuh Matos, and J. Alberto Vázquez. On the core-halo mass relation in scalar field dark matter models and its consequences for the formation of supermassive black holes, 2020.
- [211] Jeremie Choquette, James M. Cline, and Jonathan M. Cornell. Early formation of supermassive black holes via dark matter self-interactions. *JCAP*, 07:036, 2019. doi: 10.1088/1475-7516/2019/07/036.
- [212] Ran Huo, Hai-Bo Yu, and Yi-Ming Zhong. The Structure of Dissipative Dark Matter Halos. *JCAP*, 06:051, 2020. doi: 10.1088/1475-7516/2020/06/051.
- [213] Moira I. Gresham, Hou Keong Lou, and Kathryn M. Zurek. Astrophysical Signatures of Asymmetric Dark Matter Bound States. *Phys. Rev. D*, 98(9):096001, 2018. doi: 10.1103/PhysRevD.98.096001.
- [214] Moira I. Gresham, Hou Keong Lou, and Kathryn M. Zurek. Early Universe synthesis of asymmetric dark matter nuggets. *Phys. Rev. D*, 97(3):036003, 2018. doi: 10.1103/PhysRevD.97.036003.
- [215] Moira I. Gresham, Hou Keong Lou, and Kathryn M. Zurek. Nuclear Structure of Bound States of Asymmetric Dark Matter. *Phys. Rev. D*, 96(9):096012, 2017. doi: 10.1103/PhysRevD.96.096012.
- [216] Mark B. Wise and Yue Zhang. Stable Bound States of Asymmetric Dark Matter. *Phys. Rev. D*, 90(5):055030, 2014. doi: 10.1103/PhysRevD.90.055030. [Erratum: *Phys.Rev.D* 91, 039907 (2015)].
- [217] Mark B. Wise and Yue Zhang. Yukawa Bound States of a Large Number of Fermions. *JHEP*, 02:023, 2015. doi: 10.1007/JHEP02(2015)023. [Erratum: *JHEP* 10, 165 (2015)].

- [218] JiJi Fan, Andrey Katz, Lisa Randall, and Matthew Reece. Dark-Disk Universe. *Phys. Rev. Lett.*, 110(21):211302, 2013. doi: 10.1103/PhysRevLett.110.211302.
- [219] JiJi Fan, Andrey Katz, Lisa Randall, and Matthew Reece. Double-Disk Dark Matter. *Phys. Dark Univ.*, 2:139–156, 2013. doi: 10.1016/j.dark.2013.07.001.
- [220] R. Foot and S. Vagnozzi. Dissipative hidden sector dark matter. *Physical Review D*, 91(2), Jan 2015. ISSN 1550-2368. doi: 10.1103/physrevd.91.023512. URL <http://dx.doi.org/10.1103/PhysRevD.91.023512>.
- [221] David E Kaplan, Gordan Z Krnjaic, Keith R Rehermann, and Christopher M Wells. Atomic dark matter. *Journal of Cosmology and Astroparticle Physics*, 2010(05):021–021, May 2010. ISSN 1475-7516. doi: 10.1088/1475-7516/2010/05/021. URL <http://dx.doi.org/10.1088/1475-7516/2010/05/021>.
- [222] Francis-Yan Cyr-Racine and Kris Sigurdson. Cosmology of atomic dark matter. *Phys. Rev. D*, 87(10):103515, 2013. doi: 10.1103/PhysRevD.87.103515.
- [223] James M. Cline, Zuowei Liu, Guy Moore, and Wei Xue. Scattering properties of dark atoms and molecules. *Phys. Rev. D*, 89(4):043514, 2014. doi: 10.1103/PhysRevD.89.043514.
- [224] Douglas P. Finkbeiner and Neal Weiner. X-ray line from exciting dark matter. *Phys. Rev. D*, 94(8):083002, 2016. doi: 10.1103/PhysRevD.94.083002.
- [225] Kimberly K. Boddy, Manoj Kaplinghat, Anna Kwa, and Annika H. G. Peter. Hidden Sector Hydrogen as Dark Matter: Small-scale Structure Formation Predictions and the Importance of Hyperfine Interactions. *Phys. Rev. D*, 94(12):123017, 2016. doi: 10.1103/PhysRevD.94.123017.
- [226] Katelin Schutz and Tracy R. Slatyer. Self-Scattering for Dark Matter with an Excited State. *JCAP*, 01:021, 2015. doi: 10.1088/1475-7516/2015/01/021.
- [227] Anirban Das and Basudeb Dasgupta. New dissipation mechanisms from multilevel dark matter scattering. *Phys. Rev. D*, 97(2):023002, 2018. doi: 10.1103/PhysRevD.97.023002.
- [228] Bugeon Jo, Hyeontae Kim, Hyung Do Kim, and Chang Sub Shin. Exploring the universe with dark light scalars, 2020.
- [229] Philip F. Hopkins, Dušan Kereš, José Oñorbe, Claude-André Faucher-Giguère, Eliot Quataert, Norman Murray, and James S. Bullock. Galaxies on FIRE (Feedback In Realistic Environments): stellar feedback explains cosmologically inefficient star formation. *MNRAS*, 445(1):581–603, Nov 2014. doi: 10.1093/mnras/stu1738.

- [230] Philip F. Hopkins. A new class of accurate, mesh-free hydrodynamic simulation methods. *MNRAS*, 450(1):53–110, Jun 2015. doi: 10.1093/mnras/stv195.
- [231] Shea Garrison-Kimmel, Andrew Wetzel, Philip F. Hopkins, Robyn Sanderson, Kareem El-Badry, Andrew Graus, T. K. Chan, Robert Feldmann, Michael Boylan-Kolchin, Christopher C. Hayward, James S. Bullock, Alex Fitts, Jenna Samuel, Coral Wheeler, Dušan Kereš, and Claude-André Faucher-Giguère. Star formation histories of dwarf galaxies in the FIRE simulations: dependence on mass and Local Group environment. *MNRAS*, 489(4):4574–4588, November 2019. doi: 10.1093/mnras/stz2507.
- [232] D. J. Price and J. J. Monaghan. An energy-conserving formalism for adaptive gravitational force softening in smoothed particle hydrodynamics and N-body codes. *MNRAS*, 374(4):1347–1358, Feb 2007. doi: 10.1111/j.1365-2966.2006.11241.x.
- [233] Peter S. Behroozi, Risa H. Wechsler, and Hao-Yi Wu. The ROCKSTAR Phase-space Temporal Halo Finder and the Velocity Offsets of Cluster Cores. *ApJ*, 762(2):109, Jan 2013. doi: 10.1088/0004-637X/762/2/109.
- [234] Peter S. Behroozi, Risa H. Wechsler, Hao-Yi Wu, Michael T. Busha, Anatoly A. Klypin, and Joel R. Primack. Consistent Trees: Gravitationally Consistent Halo Catalogs and Merger Trees for Precision Cosmology, Oct 2012.
- [235] Peter S. Behroozi, Risa H. Wechsler, Hao-Yi Wu, Michael T. Busha, Anatoly A. Klypin, and Joel R. Primack. Gravitationally Consistent Halo Catalogs and Merger Trees for Precision Cosmology. *ApJ*, 763(1):18, Jan 2013. doi: 10.1088/0004-637X/763/1/18.
- [236] Mark B. Wise and Yue Zhang. Yukawa bound states of a large number of fermions. *Journal of High Energy Physics*, 2015:23, February 2015. doi: 10.1007/JHEP02(2015)023.
- [237] William Detmold, Matthew McCullough, and Andrew Pochinsky. Dark nuclei. I. Cosmology and indirect detection. *Phys. Rev. D*, 90(11):115013, December 2014. doi: 10.1103/PhysRevD.90.115013.
- [238] Gordan Krnjaic and Kris Sigurdson. Big bang darkleosynthesis. *Physics Letters B*, 751:464–468, December 2015. doi: 10.1016/j.physletb.2015.11.001.
- [239] Kathryn M. Zurek. Asymmetric Dark Matter: Theories, signatures, and constraints. *Phys. Rep.*, 537(3):91–121, April 2014. doi: 10.1016/j.physrep.2013.12.001.

- [240] Daniele S. M. Alves, Siavosh R. Behbahani, Philip Schuster, and Jay G. Wacker. The cosmology of composite inelastic dark matter. *Journal of High Energy Physics*, 2010:113, June 2010. doi: 10.1007/JHEP06(2010)113.
- [241] Fang Chen, James M. Cline, and Andrew R. Frey. Non-Abelian dark matter: Models and constraints. *Phys. Rev. D*, 80(8):083516, October 2009. doi: 10.1103/PhysRevD.80.083516.
- [242] Marco Cirelli and James M. Cline. Can multistate dark matter annihilation explain the high-energy cosmic ray lepton anomalies? *Phys. Rev. D*, 82(2):023503, July 2010. doi: 10.1103/PhysRevD.82.023503.
- [243] R. Foot and S. Vagnozzi. Diurnal modulation signal from dissipative hidden sector dark matter. *Physics Letters B*, 748:61–66, Sep 2015. doi: 10.1016/j.physletb.2015.06.063.
- [244] M. Markevitch, A. H. Gonzalez, D. Clowe, A. Vikhlinin, W. Forman, C. Jones, S. Murray, and W. Tucker. Direct Constraints on the Dark Matter Self-Interaction Cross Section from the Merging Galaxy Cluster 1E 0657-56. *ApJ*, 606(2):819–824, May 2004. doi: 10.1086/383178.
- [245] Arianna Di Cintio, Chris B. Brook, Andrea V. Macciò, Greg S. Stinson, Alexander Knebe, Aaron A. Dutton, and James Wadsley. The dependence of dark matter profiles on the stellar-to-halo mass ratio: a prediction for cusps versus cores. *MNRAS*, 437(1):415–423, January 2014. doi: 10.1093/mnras/stt1891.
- [246] Jose Oñorbe, Michael Boylan-Kolchin, James S. Bullock, Philip F. Hopkins, Dušan Kereš, Claude-André Faucher-Giguère, Eliot Quataert, and Norman Murray. Forged in FIRE: cusps, cores and baryons in low-mass dwarf galaxies. *MNRAS*, 454(2):2092–2106, December 2015. doi: 10.1093/mnras/stv2072.
- [247] Edouard Tolley, Andrea V. Macciò, Aaron A. Dutton, Greg S. Stinson, Liang Wang, Camilla Penzo, Thales A. Gutcke, Tobias Buck, Xi Kang, Chris Brook, Arianna Di Cintio, Ben W. Keller, and James Wadsley. NIHAO - IV: core creation and destruction in dark matter density profiles across cosmic time. *MNRAS*, 456(4):3542–3552, March 2016. doi: 10.1093/mnras/stv2856.
- [248] Alexandres Lazar, James S. Bullock, Michael Boylan-Kolchin, T. K. Chan, Philip F. Hopkins, Andrew S. Graus, Andrew Wetzel, Kareem El-Badry, Coral Wheeler, Maria C. Straight, Dušan Kereš, Claude-André Faucher-Giguère, Alex Fitts, and Shea Garrison-Kimmel. A dark matter profile to model diverse feedback-induced core sizes of Λ CDM haloes. *MNRAS*, 497(2):2393–2417, September 2020. doi: 10.1093/mnras/staa2101.
- [249] Greg L. Bryan and Michael L. Norman. Statistical Properties of X-Ray Clusters: Analytic and Numerical Comparisons. *ApJ*, 495(1):80–99, March 1998. doi: 10.1086/305262.

- [250] H. J. Mo, Shude Mao, and Simon D. M. White. The formation of galactic discs. *MNRAS*, 295(2):319–336, April 1998. doi: 10.1046/j.1365-8711.1998.01227.x.
- [251] Doron Lemze, Rick Wagner, Yoel Rephaeli, Sharon Sadeh, Michael L. Norman, Rennan Barkana, Tom Broadhurst, Holland Ford, and Marc Postman. Profiles of Dark Matter Velocity Anisotropy in Simulated Clusters. *ApJ*, 752(2):141, June 2012. doi: 10.1088/0004-637X/752/2/141.
- [252] Martin Sparre and Steen H. Hansen. The behaviour of shape and velocity anisotropy in dark matter haloes. *J. Cosmol. Astropart. Phys.*, 2012(10):049, October 2012. doi: 10.1088/1475-7516/2012/10/049.
- [253] Radosław Wojtak, Stefan Gottlöber, and Anatoly Klypin. Orbital anisotropy in cosmological haloes revisited. *MNRAS*, 434(2):1576–1585, September 2013. doi: 10.1093/mnras/stt1113.
- [254] Marcel Zemp, Oleg Y. Gnedin, Nickolay Y. Gnedin, and Andrey V. Kravtsov. On Determining the Shape of Matter Distributions. *ApJS*, 197(2):30, December 2011. doi: 10.1088/0067-0049/197/2/30.
- [255] Thejs Brinckmann, Jesús Zavala, David Rapetti, Steen H. Hansen, and Mark Vogelsberger. The structure and assembly history of cluster-sized haloes in self-interacting dark matter. *MNRAS*, 474(1):746–759, February 2018. doi: 10.1093/mnras/stx2782.
- [256] Omid Sameie, Peter Creasey, Hai-Bo Yu, Laura V. Sales, Mark Vogelsberger, and Jesús Zavala. The impact of baryonic discs on the shapes and profiles of self-interacting dark matter haloes. *MNRAS*, 479(1):359–367, September 2018. doi: 10.1093/mnras/sty1516.
- [257] Michael S. Warren, Peter J. Quinn, John K. Salmon, and Wojciech H. Zurek. Dark Halos Formed via Dissipationless Collapse. I. Shapes and Alignment of Angular Momentum. *ApJ*, 399:405, November 1992. doi: 10.1086/171937.
- [258] Philip Bett, Vincent Eke, Carlos S. Frenk, Adrian Jenkins, John Helly, and Julio Navarro. The spin and shape of dark matter haloes in the Millennium simulation of a Λ cold dark matter universe. *MNRAS*, 376(1):215–232, March 2007. doi: 10.1111/j.1365-2966.2007.11432.x.
- [259] Eric Hayashi, Julio F. Navarro, and Volker Springel. The shape of the gravitational potential in cold dark matter haloes. *MNRAS*, 377(1):50–62, May 2007. doi: 10.1111/j.1365-2966.2007.11599.x.
- [260] R. L. Davies, G. Efsthathiou, S. M. Fall, G. Illingworth, and P. L. Schechter. The kinematic properties of faint elliptical galaxies. *ApJ*, 266:41–57, March 1983. doi: 10.1086/160757.

- [261] Michele Cappellari, Eric Emsellem, R. Bacon, M. Bureau, Roger L. Davies, P. T. de Zeeuw, Jesús Falcón-Barroso, Davor Krajinović, Harald Kuntschner, Richard M. McDermid, Reynier F. Peletier, Marc Sarzi, Remco C. E. van den Bosch, and Glenn van de Ven. The SAURON project - X. The orbital anisotropy of elliptical and lenticular galaxies: revisiting the $(V/\sigma, \epsilon)$ diagram with integral-field stellar kinematics. *MNRAS*, 379(2):418–444, August 2007. doi: 10.1111/j.1365-2966.2007.11963.x.
- [262] J. Binney. On the rotation of elliptical galaxies. *MNRAS*, 183:501–514, May 1978. doi: 10.1093/mnras/183.3.501.
- [263] James Binney and Scott Tremaine. *Galactic dynamics*. 1987.
- [264] James Binney and Scott Tremaine. *Galactic Dynamics: Second Edition*. 2008.
- [265] F. Hoyle. On the Fragmentation of Gas Clouds Into Galaxies and Stars. *ApJ*, 118:513, November 1953. doi: 10.1086/145780.
- [266] M. J. Rees. Opacity-limited hierarchical fragmentation and the masses of protostars. *MNRAS*, 176:483–486, September 1976. doi: 10.1093/mnras/176.3.483.
- [267] Charles F. Gammie. Nonlinear Outcome of Gravitational Instability in Cooling, Gaseous Disks. *ApJ*, 553(1):174–183, May 2001. doi: 10.1086/320631.
- [268] J. P. Ostriker and P. J. E. Peebles. A Numerical Study of the Stability of Flattened Galaxies: or, can Cold Galaxies Survive? *ApJ*, 186:467–480, December 1973. doi: 10.1086/152513.
- [269] Dimitris M. Christodoulou, Isaac Shlosman, and Joel E. Tohline. A New Criterion for Bar-forming Instability in Rapidly Rotating Gaseous and Stellar Systems. I. Axisymmetric Form. *ApJ*, 443:551, April 1995. doi: 10.1086/175547.
- [270] John E. Gaustad. The Opacity of Diffuse Cosmic Matter and the Early Stages of Star Formation. *ApJ*, 138:1050, November 1963. doi: 10.1086/147705.
- [271] F. H. Shu. Self-similar collapse of isothermal spheres and star formation. *ApJ*, 214:488–497, June 1977. doi: 10.1086/155274.
- [272] Peter Bodenheimer and Allen Sweigart. Dynamic Collapse of the Isothermal Sphere. *ApJ*, 152:515, May 1968. doi: 10.1086/149568.
- [273] M. V. Penston. Dynamics of self-gravitating gaseous spheres-III. Analytical results in the free-fall of isothermal cases. *MNRAS*, 144:425, January 1969. doi: 10.1093/mnras/144.4.425.

- [274] M. V. Penston. Dynamics of self-gravitating gaseous spheres-II. Collapses of gas spheres with cooling and the behaviour of polytropic gas spheres. *MNRAS*, 145:457, January 1969. doi: 10.1093/mnras/145.4.457.
- [275] Richard B. Larson. Numerical calculations of the dynamics of collapsing proto-star. *MNRAS*, 145:271, January 1969. doi: 10.1093/mnras/145.3.271.
- [276] C. Hunter. The collapse of unstable isothermal spheres. *ApJ*, 218:834–845, December 1977. doi: 10.1086/155739.
- [277] Prudence N. Foster and Roger A. Chevalier. Gravitational Collapse of an Isothermal Sphere. *ApJ*, 416:303, October 1993. doi: 10.1086/173236.
- [278] Jonathan Stern, Drummond Fielding, Claude-André Faucher-Giguère, and Eliot Quataert. Cooling flow solutions for the circumgalactic medium. *MNRAS*, 488(2):2549–2572, September 2019. doi: 10.1093/mnras/stz1859.
- [279] Yasushi Suto and Joseph Silk. Self-similar Dynamics of Polytropic Gaseous Spheres. *ApJ*, 326:527, March 1988. doi: 10.1086/166114.
- [280] Sydeny Chapman and T. G. Cowling. *The mathematical theory of non-uniform gases. an account of the kinetic theory of viscosity, thermal conduction and diffusion in gases.* 1970.
- [281] E. M. Lifshitz and L. P. Pitaevskii. *Physical kinetics.* 1981.
- [282] G. R. Blumenthal, S. M. Faber, R. Flores, and J. R. Primack. Contraction of Dark Matter Galactic Halos Due to Baryonic Infall. *ApJ*, 301:27, February 1986. doi: 10.1086/163867.
- [283] Oleg Y. Gnedin, Andrey V. Kravtsov, Anatoly A. Klypin, and Daisuke Nagai. Response of Dark Matter Halos to Condensation of Baryons: Cosmological Simulations and Improved Adiabatic Contraction Model. *ApJ*, 616(1):16–26, November 2004. doi: 10.1086/424914.
- [284] Volker Springel. The cosmological simulation code GADGET-2. *MNRAS*, 364(4):1105–1134, December 2005. doi: 10.1111/j.1365-2966.2005.09655.x.
- [285] Andrew Robertson, Richard Massey, and Vincent Eke. Cosmic particle colliders: simulations of self-interacting dark matter with anisotropic scattering. *MNRAS*, 467(4):4719–4730, June 2017. doi: 10.1093/mnras/stx463.
- [286] Lina Necib, Mariangela Lisanti, Shea Garrison-Kimmel, Andrew Wetzel, Robyn Sanderson, Philip F. Hopkins, Claude-André Faucher-Giguère, and Dušan Kereš. Under the FIRElight: Stellar Tracers of the Local Dark Matter Velocity Distribution in the Milky Way. *ApJ*, 883(1):27, September 2019. doi: 10.3847/1538-4357/ab3afc.

- [287] Jenna Samuel, Andrew Wetzel, Erik Tollerud, Shea Garrison-Kimmel, Sarah Loebman, Kareem El-Badry, Philip F. Hopkins, Michael Boylan-Kolchin, Claude-André Faucher-Giguère, James S. Bullock, Samantha Benincasa, and Jeremy Bailin. A profile in FIRE: resolving the radial distributions of satellite galaxies in the Local Group with simulations. *MNRAS*, 491(1):1471–1490, January 2020. doi: 10.1093/mnras/stz3054.
- [288] Andrew Wetzel and Shea Garrison-Kimmel. HaloAnalysis: Read and analyze halo catalogs and merger trees. Astrophysics Source Code Library, record ascl:2002.014, February 2020.
- [289] Claus Leitherer, Daniel Schaerer, Jeffrey D. Goldader, Rosa M. González Delgado, Carmelle Robert, Denis Foo Kune, Duília F. de Mello, Daniel Devost, and Timothy M. Heckman. Starburst99: Synthesis Models for Galaxies with Active Star Formation. *ApJS*, 123(1):3–40, July 1999. doi: 10.1086/313233.
- [290] Aura Obreja, Gregory S. Stinson, Aaron A. Dutton, Andrea V. Macciò, Liang Wang, and Xi Kang. NIHAO VI. The hidden discs of simulated galaxies. *MNRAS*, 459(1):467–486, June 2016. doi: 10.1093/mnras/stw690.
- [291] Kareem El-Badry, Eliot Quataert, Andrew Wetzel, Philip F. Hopkins, Daniel R. Weisz, T. K. Chan, Alex Fitts, Michael Boylan-Kolchin, Dušan Kereš, Claude-André Faucher-Giguère, and Shea Garrison-Kimmel. Gas kinematics, morphology and angular momentum in the FIRE simulations. *MNRAS*, 473(2):1930–1955, January 2018. doi: 10.1093/mnras/stx2482.
- [292] Michael Y. Grudić, Michael Boylan-Kolchin, Claude-André Faucher-Giguère, and Philip F. Hopkins. The universal acceleration scale from stellar feedback. *MNRAS*, 496(1):L127–L132, July 2020. doi: 10.1093/mnras/slaa103.
- [293] Joe Wolf, Gregory D. Martinez, James S. Bullock, Manoj Kaplinghat, Marla Geha, Ricardo R. Muñoz, Joshua D. Simon, and Frank F. Avedo. Accurate masses for dispersion-supported galaxies. *MNRAS*, 406(2):1220–1237, August 2010. doi: 10.1111/j.1365-2966.2010.16753.x.
- [294] Coral Wheeler, Philip F. Hopkins, Andrew B. Pace, Shea Garrison-Kimmel, Michael Boylan-Kolchin, Andrew Wetzel, James S. Bullock, Dušan Kereš, Claude-André Faucher-Giguère, and Eliot Quataert. Be it therefore resolved: cosmological simulations of dwarf galaxies with 30 solar mass resolution. *MNRAS*, 490(3):4447–4463, December 2019. doi: 10.1093/mnras/stz2887.
- [295] S. Stanimirović, L. Staveley-Smith, and P. A. Jones. A New Look at the Kinematics of Neutral Hydrogen in the Small Magellanic Cloud. *ApJ*, 604(1):176–186, March 2004. doi: 10.1086/381869.
- [296] Roeland P. van der Marel and Nitya Kallivayalil. Third-epoch Magellanic Cloud Proper Motions. II. The Large Magellanic Cloud Rotation Field in

- Three Dimensions. *ApJ*, 781(2):121, February 2014. doi: 10.1088/0004-637X/781/2/121.
- [297] S. Taibi, G. Battaglia, M. Rejkuba, R. Leaman, N. Kacharov, G. Iorio, P. Jablonka, and M. Zoccali. The Tucana dwarf spheroidal galaxy: not such a massive failure after all. *arXiv e-prints*, art. arXiv:2001.11410, Jan 2020.
- [298] F. Fraternali, E. Tolstoy, M. J. Irwin, and A. A. Cole. Life at the periphery of the Local Group: the kinematics of the Tucana dwarf galaxy. *A&A*, 499(1): 121–128, May 2009. doi: 10.1051/0004-6361/200810830.
- [299] Alexandra L. Gregory, Michelle L. M. Collins, Justin I. Read, Michael J. Irwin, Rodrigo A. Ibata, Nicolas F. Martin, Alan W. McConnachie, and Daniel R. Weisz. Kinematics of the Tucana Dwarf Galaxy: an unusually dense dwarf in the Local Group. *MNRAS*, 485(2):2010–2025, May 2019. doi: 10.1093/mnras/stz518.
- [300] Zhichao Carton Zeng, Annika H. G. Peter, Xiaolong Du, Andrew Benson, Stacy Kim, Fangzhou Jiang, Francis-Yan Cyr-Racine, and Mark Vogelsberger. Core-collapse, evaporation, and tidal effects: the life story of a self-interacting dark matter subhalo. *MNRAS*, 513(4):4845–4868, July 2022. doi: 10.1093/mnras/stac1094.
- [301] P. J. Quinn and Jeremy Goodman. Sinking Satellites of Spiral Systems. *ApJ*, 309:472, October 1986. doi: 10.1086/164619.
- [302] Monica Colpi, Lucio Mayer, and Fabio Governato. Dynamical Friction and the Evolution of Satellites in Virialized Halos: The Theory of Linear Response. *ApJ*, 525(2):720–733, November 1999. doi: 10.1086/307952.
- [303] James E. Taylor and Arif Babul. The Dynamics of Sinking Satellites around Disk Galaxies: A Poor Man’s Alternative to High-Resolution Numerical Simulations. *ApJ*, 559(2):716–735, October 2001. doi: 10.1086/322276.
- [304] Andrew R. Zentner and James S. Bullock. Halo Substructure and the Power Spectrum. *ApJ*, 598(1):49–72, November 2003. doi: 10.1086/378797.
- [305] Jianling Gan, Xi Kang, Frank C. van den Bosch, and Jinliang Hou. An improved model for the dynamical evolution of dark matter subhaloes. *MNRAS*, 408(4):2201–2212, November 2010. doi: 10.1111/j.1365-2966.2010.17266.x.
- [306] Fangzhou Jiang and Frank C. van den Bosch. Statistics of dark matter substructure - I. Model and universal fitting functions. *MNRAS*, 458(3):2848–2869, May 2016. doi: 10.1093/mnras/stw439.

- [307] X. Ma, P. F. Hopkins, M. Boylan-Kolchin, C.-A. Faucher-Giguère, E. Quataert, R. Feldmann, S. Garrison-Kimmel, C. C. Hayward, D. Kereš, and A. Wetzel. Simulating galaxies in the reionization era with FIRE-2: morphologies and sizes. *MNRAS*, 477:219–229, June 2018. doi: 10.1093/mnras/sty684.
- [308] Anatoly Klypin, Andrey V. Kravtsov, Octavio Valenzuela, and Francisco Prada. Where Are the Missing Galactic Satellites? *ApJ*, 522(1):82–92, September 1999. doi: 10.1086/307643.
- [309] E. O. Nadler, A. Drlica-Wagner, K. Bechtol, S. Mau, R. H. Wechsler, V. Gluscevic, K. Boddy, A. B. Pace, T. S. Li, M. McNanna, A. H. Riley, J. García-Bellido, Y. Y. Mao, G. Green, D. L. Burke, A. Peter, B. Jain, T. M. C. Abbott, M. Aguena, S. Allam, J. Annis, S. Avila, D. Brooks, M. Carrasco Kind, J. Carretero, M. Costanzi, L. N. da Costa, J. De Vicente, S. Desai, H. T. Diehl, P. Doel, S. Everett, A. E. Evrard, B. Flaugher, J. Frieman, D. W. Gerdes, D. Gruen, R. A. Gruendl, J. Gschwend, G. Gutierrez, S. R. Hinton, K. Honscheid, D. Huterer, D. J. James, E. Krause, K. Kuehn, N. Kuropatkin, O. Lahav, M. A. G. Maia, J. L. Marshall, F. Menanteau, R. Miquel, A. Palmese, F. Paz-Chinchón, A. A. Plazas, A. K. Romer, E. Sanchez, V. Scarpine, S. Serrano, I. Sevilla-Noarbe, M. Smith, M. Soares-Santos, E. Suchyta, M. E. C. Swanson, G. Tarle, D. L. Tucker, A. R. Walker, W. Wester, and DES Collaboration. Constraints on Dark Matter Properties from Observations of Milky Way Satellite Galaxies. *Phys. Rev. Lett.*, 126(9):091101, March 2021. doi: 10.1103/PhysRevLett.126.091101.
- [310] Arka Banerjee, Susmita Adhikari, Neal Dalal, Surhud More, and Andrey Kravtsov. Signatures of self-interacting dark matter on cluster density profile and subhalo distributions. *J. Cosmol. Astropart. Phys.*, 2020(2):024, February 2020. doi: 10.1088/1475-7516/2020/02/024.
- [311] Ethan O. Nadler, Arka Banerjee, Susmita Adhikari, Yao-Yuan Mao, and Risa H. Wechsler. Signatures of Velocity-dependent Dark Matter Self-interactions in Milky Way-mass Halos. *ApJ*, 896(2):112, June 2020. doi: 10.3847/1538-4357/ab94b0.
- [312] Moritz S. Fischer, Marcus Brüggen, Kai Schmidt-Hoberg, Klaus Dolag, Felix Kahlhoefer, Antonio Ragagnin, and Andrew Robertson. Cosmological simulations with rare and frequent dark matter self-interactions. *MNRAS*, 516(2):1923–1940, October 2022. doi: 10.1093/mnras/stac2207.
- [313] Marla Geha, Risa H. Wechsler, Yao-Yuan Mao, Erik J. Tollerud, Benjamin Weiner, Rebecca Bernstein, Ben Hoyle, Sebastian Marchi, Phil J. Marshall, Ricardo Muñoz, and Yu Lu. The SAGA Survey. I. Satellite Galaxy Populations around Eight Milky Way Analogs. *ApJ*, 847(1):4, September 2017. doi: 10.3847/1538-4357/aa8626.

- [314] Yao-Yuan Mao, Marla Geha, Risa H. Wechsler, Benjamin Weiner, Erik J. Tollerud, Ethan O. Nadler, and Nitya Kallivayalil. The SAGA Survey. II. Building a Statistical Sample of Satellite Systems around Milky Way-like Galaxies. *ApJ*, 907(2):85, February 2021. doi: 10.3847/1538-4357/abce58.
- [315] Eric F. Bell, Daniel H. McIntosh, Neal Katz, and Martin D. Weinberg. The Optical and Near-Infrared Properties of Galaxies. I. Luminosity and Stellar Mass Functions. *ApJS*, 149(2):289–312, December 2003. doi: 10.1086/378847.
- [316] Matthew G. Walker, Mario Mateo, Edward W. Olszewski, Jorge Peñarrubia, N. Wyn Evans, and Gerard Gilmore. A Universal Mass Profile for Dwarf Spheroidal Galaxies? *ApJ*, 704(2):1274–1287, October 2009. doi: 10.1088/0004-637X/704/2/1274.
- [317] D. Lynden-Bell. Dwarf galaxies and globular clusters in high velocity hydrogen streams. *MNRAS*, 174:695–710, March 1976. doi: 10.1093/mnras/174.3.695.
- [318] P. Kroupa, C. Theis, and C. M. Boily. The great disk of Milky-Way satellites and cosmological sub-structures. *A&A*, 431:517–521, February 2005. doi: 10.1051/0004-6361:20041122.
- [319] M. S. Pawlowski, J. Pflamm-Altenburg, and P. Kroupa. The VPOS: a vast polar structure of satellite galaxies, globular clusters and streams around the Milky Way. *MNRAS*, 423(2):1109–1126, June 2012. doi: 10.1111/j.1365-2966.2012.20937.x.
- [320] T. K. Fritz, G. Battaglia, M. S. Pawlowski, N. Kallivayalil, R. van der Marel, S. T. Sohn, C. Brook, and G. Besla. Gaia DR2 proper motions of dwarf galaxies within 420 kpc. Orbits, Milky Way mass, tidal influences, planar alignments, and group infall. *A&A*, 619:A103, November 2018. doi: 10.1051/0004-6361/201833343.
- [321] Marcel S. Pawlowski and Pavel Kroupa. The Milky Way’s disc of classical satellite galaxies in light of Gaia DR2. *MNRAS*, 491(2):3042–3059, January 2020. doi: 10.1093/mnras/stz3163.
- [322] Jenna Samuel, Andrew Wetzel, Sierra Chapman, Erik Tollerud, Philip F. Hopkins, Michael Boylan-Kolchin, Jeremy Bailin, and Claude-André Faucher-Giguère. Planes of satellites around Milky Way/M31-mass galaxies in the FIRE simulations and comparisons with the Local Group. *MNRAS*, 504(1):1379–1397, June 2021. doi: 10.1093/mnras/stab955.
- [323] Eleanor R. Downing and Kyle A. Oman. The many reasons that the rotation curves of low-mass galaxies can fail as tracers of their matter distributions. *arXiv e-prints*, art. arXiv:2301.05242, January 2023.

- [324] Philip F. Hopkins. A new class of accurate, mesh-free hydrodynamic simulation methods. *Monthly Notices of the Royal Astronomical Society*, 450(1):53–110, Apr 2015. ISSN 1365-2966. doi: 10.1093/mnras/stv195. URL <http://dx.doi.org/10.1093/mnras/stv195>.
- [325] J. Herpich, G. S. Stinson, H. W. Rix, M. Martig, and A. A. Dutton. How to bend galaxy disc profiles - II. Stars surfing the bar in Type-III discs. *MNRAS*, 470(4):4941–4955, October 2017. doi: 10.1093/mnras/stx1511.
- [326] Michael Boylan-Kolchin, Volker Springel, Simon D. M. White, Adrian Jenkins, and Gerard Lemson. Resolving cosmic structure formation with the Millennium-II Simulation. *MNRAS*, 398(3):1150–1164, September 2009. doi: 10.1111/j.1365-2966.2009.15191.x.
- [327] Anatoly A. Klypin, Sebastian Trujillo-Gomez, and Joel Primack. Dark Matter Halos in the Standard Cosmological Model: Results from the Bolshoi Simulation. *ApJ*, 740(2):102, October 2011. doi: 10.1088/0004-637X/740/2/102.
- [328] Annalisa Pillepich, Volker Springel, Dylan Nelson, Shy Genel, Jill Naiman, Rüdiger Pakmor, Lars Hernquist, Paul Torrey, Mark Vogelsberger, Rainer Weinberger, and Federico Marinacci. Simulating galaxy formation with the IllustrisTNG model. *MNRAS*, 473(3):4077–4106, January 2018. doi: 10.1093/mnras/stx2656.
- [329] Mark Vogelsberger, Jesús Zavala, Francis-Yan Cyr-Racine, Christoph Pfrommer, Torsten Bringmann, and Kris Sigurdson. ETHOS - an effective theory of structure formation: dark matter physics as a possible explanation of the small-scale CDM problems. *MNRAS*, 460(2):1399–1416, August 2016. doi: 10.1093/mnras/stw1076.
- [330] Mark R. Lovell, Jesús Zavala, Mark Vogelsberger, Xuejian Shen, Francis-Yan Cyr-Racine, Christoph Pfrommer, Kris Sigurdson, Michael Boylan-Kolchin, and Annalisa Pillepich. ETHOS - an effective theory of structure formation: predictions for the high-redshift Universe - abundance of galaxies and reionization. *MNRAS*, 477(3):2886–2899, July 2018. doi: 10.1093/mnras/sty818.
- [331] Andrea V. Macciò, Aaron A. Dutton, and Frank C. van den Bosch. Concentration, spin and shape of dark matter haloes as a function of the cosmological model: WMAP1, WMAP3 and WMAP5 results. *MNRAS*, 391(4):1940–1954, December 2008. doi: 10.1111/j.1365-2966.2008.14029.x.
- [332] J. S. Bullock, T. S. Kolatt, Y. Sigad, R. S. Somerville, A. V. Kravtsov, A. A. Klypin, J. R. Primack, and A. Dekel. Profiles of dark haloes: evolution, scatter and environment. *Monthly Notices of the Royal Astronomical Society*, 321(3):559–575, Mar 2001. ISSN 1365-2966. doi: 10.1046/j.1365-8711.2001.04068.x. URL <http://dx.doi.org/10.1046/j.1365-8711.2001.04068.x>.

- [333] Julio F. Navarro, Carlos S. Frenk, and Simon D. M. White. The structure of cold dark matter halos. *The Astrophysical Journal*, 462:563, May 1996. ISSN 1538-4357. doi: 10.1086/177173. URL <http://dx.doi.org/10.1086/177173>.
- [334] D. H. Zhao, Y. P. Jing, H. J. Mo, and G. Brner. Mass and redshift dependence of dark halo structure. *The Astrophysical Journal*, 597(1):L9–L12, oct 2003. doi: 10.1086/379734. URL <https://doi.org/10.1086/379734>.
- [335] Benedikt Diemer, Surhud More, and Andrey V. Kravtsov. The pseudo-evolution of halo mass. *The Astrophysical Journal*, 766(1):25, Mar 2013. ISSN 1538-4357. doi: 10.1088/0004-637x/766/1/25. URL <http://dx.doi.org/10.1088/0004-637X/766/1/25>.
- [336] Ewa L. Łokas and Gary A. Mamon. Properties of spherical galaxies and clusters with an NFW density profile. *MNRAS*, 321(1):155–166, February 2001. doi: 10.1046/j.1365-8711.2001.04007.x.
- [337] Benedikt Diemer and Michael Joyce. An accurate physical model for halo concentrations. *The Astrophysical Journal*, 871(2):168, Jan 2019. ISSN 1538-4357. doi: 10.3847/1538-4357/aafad6. URL <http://dx.doi.org/10.3847/1538-4357/aafad6>.
- [338] Benedikt Diemer and Andrey V. Kravtsov. A universal model for halo concentrations. *The Astrophysical Journal*, 799(1):108, Jan 2015. ISSN 1538-4357. doi: 10.1088/0004-637x/799/1/108. URL <http://dx.doi.org/10.1088/0004-637X/799/1/108>.
- [339] Tomoaki Ishiyama, Francisco Prada, Anatoly A. Klypin, Manodeep Sinha, R. Benton Metcalf, Eric Jullo, Bruno Altieri, Sofía A. Cora, Darren Croton, Sylvain de la Torre, David E. Millán-Calero, Taira Oogi, José Ruedas, and Cristian A. Vega-Martínez. The uchuu simulations: Data release 1 and dark matter halo concentrations, 2020.
- [340] J. S. Bullock, T. S. Kolatt, Y. Sigad, R. S. Somerville, A. V. Kravtsov, A. A. Klypin, J. R. Primack, and A. Dekel. Profiles of dark haloes: evolution, scatter and environment. *MNRAS*, 321(3):559–575, March 2001. doi: 10.1046/j.1365-8711.2001.04068.x.
- [341] Daniel J. Mortlock, Stephen J. Warren, Bram P. Venemans, Mitesh Patel, Paul C. Hewett, Richard G. McMahon, Chris Simpson, Tom Theuns, Eduardo A. González-Solares, Andy Adamson, Simon Dye, Nigel C. Hambly, Paul Hirst, Mike J. Irwin, Ernst Kuiper, Andy Lawrence, and Huub J. A. Röttgering. A luminous quasar at a redshift of $z = 7.085$. *Nature*, 474(7353): 616–619, June 2011. doi: 10.1038/nature10159.
- [342] B. P. Venemans, J. R. Findlay, W. J. Sutherland, G. De Rosa, R. G. McMahon, R. Simcoe, E. A. González-Solares, K. Kuijken, and J. R. Lewis. Discovery of

Three $z > 6.5$ Quasars in the VISTA Kilo-Degree Infrared Galaxy (VIKING) Survey. *ApJ*, 779(1):24, December 2013. doi: 10.1088/0004-637X/779/1/24.

- [343] Xue-Bing Wu, Feige Wang, Xiaohui Fan, Weimin Yi, Wenwen Zuo, Fuyan Bian, Linhua Jiang, Ian D. McGreer, Ran Wang, Jinyi Yang, Qian Yang, David Thompson, and Yuri Beletsky. An ultraluminous quasar with a twelve-billion-solar-mass black hole at redshift 6.30. *Nature*, 518(7540):512–515, February 2015. doi: 10.1038/nature14241.
- [344] C. Mazzucchelli, E. Bañados, B. P. Venemans, R. Decarli, E. P. Farina, F. Walter, A. C. Eilers, H. W. Rix, R. Simcoe, D. Stern, X. Fan, E. Schlafly, G. De Rosa, J. Hennawi, K. C. Chambers, J. Greiner, W. Burgett, P. W. Draper, N. Kaiser, R. P. Kudritzki, E. Magnier, N. Metcalfe, C. Waters, and R. J. Wainscoat. Physical Properties of 15 Quasars at $z \gtrsim 6.5$. *ApJ*, 849(2): 91, November 2017. doi: 10.3847/1538-4357/aa9185.
- [345] Eduardo Bañados, Bram P. Venemans, Chiara Mazzucchelli, Emanuele P. Farina, Fabian Walter, Feige Wang, Roberto Decarli, Daniel Stern, Xiaohui Fan, Frederick B. Davies, Joseph F. Hennawi, Robert A. Simcoe, Monica L. Turner, Hans-Walter Rix, Jinyi Yang, Daniel D. Kelson, Gwen C. Rudie, and Jan Martin Winters. An 800-million-solar-mass black hole in a significantly neutral Universe at a redshift of 7.5. *Nature*, 553(7689):473–476, January 2018. doi: 10.1038/nature25180.
- [346] Feige Wang, Jinyi Yang, Xiaohui Fan, Minghao Yue, Xue-Bing Wu, Jan-Torge Schindler, Fuyan Bian, Jiang-Tao Li, Emanuele P. Farina, Eduardo Bañados, Frederick B. Davies, Roberto Decarli, Richard Green, Linhua Jiang, Joseph F. Hennawi, Yun-Hsin Huang, Chiara Mazzucchelli, Ian D. McGreer, Bram Venemans, Fabian Walter, and Yuri Beletsky. The Discovery of a Luminous Broad Absorption Line Quasar at a Redshift of 7.02. *ApJ*, 869(1): L9, December 2018. doi: 10.3847/2041-8213/aaf1d2.
- [347] Jinyi Yang, Feige Wang, Xiaohui Fan, Joseph F. Hennawi, Frederick B. Davies, Minghao Yue, Eduardo Banados, Xue-Bing Wu, Bram Venemans, Aaron J. Barth, Fuyan Bian, Konstantina Boutsia, Roberto Decarli, Emanuele Paolo Farina, Richard Green, Linhua Jiang, Jiang-Tao Li, Chiara Mazzucchelli, and Fabian Walter. Pōniuā'ena: A Luminous $z = 7.5$ Quasar Hosting a 1.5 Billion Solar Mass Black Hole. *ApJ*, 897(1):L14, July 2020. doi: 10.3847/2041-8213/ab9c26.
- [348] D. H. Zhao, Y. P. Jing, H. J. Mo, and G. Börner. ACCURATE UNIVERSAL MODELS FOR THE MASS ACCRETION HISTORIES AND CONCENTRATIONS OF DARK MATTER HALOS. *The Astrophysical Journal*, 707(1):354–369, nov 2009. doi: 10.1088/0004-637x/707/1/354. URL <https://doi.org/10.1088%2F0004-637x%2F707%2F1%2F354>.

- [349] Fangzhou Jiang, Avishai Dekel, Jonathan Freundlich, Frank C. van den Bosch, Sheridan B. Green, Philip F. Hopkins, Andrew Benson, and Xiaolong Du. SatGen: a semi-analytical satellite galaxy generator – I. The model and its application to Local-Group satellite statistics. *arXiv e-prints*, art. arXiv:2005.05974, May 2020.
- [350] Cedric Lacey and Shaun Cole. Merger rates in hierarchical models of galaxy formation. *MNRAS*, 262(3):627–649, June 1993. doi: 10.1093/mnras/262.3.627.
- [351] Hannah Parkinson, Shaun Cole, and John Helly. Generating dark matter halo merger trees. *MNRAS*, 383(2):557–564, January 2008. doi: 10.1111/j.1365-2966.2007.12517.x.
- [352] Andrew J. Benson. The mass function of unprocessed dark matter haloes and merger tree branching rates. *MNRAS*, 467(3):3454–3466, May 2017. doi: 10.1093/mnras/stx343.
- [353] Barbara S. Ryden and James E. Gunn. Galaxy Formation by Gravitational Collapse. *ApJ*, 318:15, July 1987. doi: 10.1086/165349.
- [354] S. G. Murray, C. Power, and A. S. G. Robotham. HMFcalc: An online tool for calculating dark matter halo mass functions. *Astronomy and Computing*, 3:23–34, November 2013. doi: 10.1016/j.ascom.2013.11.001.
- [355] Marta Volonteri, Francesco Haardt, and Piero Madau. The Assembly and merging history of supermassive black holes in hierarchical models of galaxy formation. *Astrophys. J.*, 582:559–573, 2003. doi: 10.1086/344675.
- [356] Masaki Iwasawa, Yoko Funato, and Junichiro Makino. Evolution of Massive Black Hole Triples. I. Equal-Mass Binary-Single Systems. *ApJ*, 651(2):1059–1067, November 2006. doi: 10.1086/507473.
- [357] Loren Hoffman and Abraham Loeb. Dynamics of triple black hole systems in hierarchically merging massive galaxies. *MNRAS*, 377(3):957–976, May 2007. doi: 10.1111/j.1365-2966.2007.11694.x.
- [358] M. J. Fitchett. The influence of gravitational wave momentum losses on the centre of mass motion of a Newtonian binary system. *MNRAS*, 203:1049–1062, June 1983. doi: 10.1093/mnras/203.4.1049.
- [359] Marta Volonteri, Ruben Salvaterra, and Francesco Haardt. Constraints on the accretion history of massive black holes from faint X-ray counts. *MNRAS*, 373(1):121–127, November 2006. doi: 10.1111/j.1365-2966.2006.10976.x.
- [360] Marta Volonteri, Giuseppe Lodato, and Priyamvada Natarajan. The evolution of massive black hole seeds. *MNRAS*, 383(3):1079–1088, January 2008. doi: 10.1111/j.1365-2966.2007.12589.x.

- [361] Priyamvada Natarajan. Seeds to monsters: tracing the growth of black holes in the universe. *General Relativity and Gravitation*, 46:1702, May 2014. doi: 10.1007/s10714-014-1702-6.
- [362] Laura Ferrarese. Beyond the bulge: a fundamental relation between supermassive black holes and dark matter halos. *Astrophys. J.*, 578:90–97, 2002. doi: 10.1086/342308.
- [363] Benny Trakhtenbrot. What do observations tell us about the highest-redshift supermassive black holes? *arXiv e-prints*, art. arXiv:2002.00972, February 2020.
- [364] Girish Kulkarni, Gábor Worseck, and Joseph F. Hennawi. Evolution of the AGN UV luminosity function from redshift 7.5. *MNRAS*, 488(1):1035–1065, September 2019. doi: 10.1093/mnras/stz1493.
- [365] Feige Wang, Jinyi Yang, Xiaohui Fan, Xue-Bing Wu, Minghao Yue, Jiang-Tao Li, Fuyan Bian, Linhua Jiang, Eduardo Bañados, Jan-Torge Schindler, Joseph R. Findlay, Frederick B. Davies, Roberto Decarli, Emanuele P. Farina, Richard Green, Joseph F. Hennawi, Yun-Hsin Huang, Chiara Mazzuccheli, Ian D. McGreer, Bram Venemans, Fabian Walter, Simon Dye, Brad W. Lyke, Adam D. Myers, and Evan Haze Nunez. Exploring Reionization-era Quasars. III. Discovery of 16 Quasars at $6.4 \lesssim z \lesssim 6.9$ with DESI Legacy Imaging Surveys and the UKIRT Hemisphere Survey and Quasar Luminosity Function at $z \sim 6.7$. *ApJ*, 884(1):30, October 2019. doi: 10.3847/1538-4357/ab2be5.
- [366] Chris J. Willott, Loic Albert, Doris Arzoumanian, Jacqueline Bergeron, David Crampton, Philippe Delorme, John B. Hutchings, Alain Omont, Céline Reylé, and David Schade. Eddington-limited Accretion and the Black Hole Mass Function at Redshift 6. *AJ*, 140(2):546–560, August 2010. doi: 10.1088/0004-6256/140/2/546.
- [367] Brandon C. Kelly and Yue Shen. The Demographics of Broad-line Quasars in the Mass-Luminosity Plane. II. Black Hole Mass and Eddington Ratio Functions. *ApJ*, 764(1):45, February 2013. doi: 10.1088/0004-637X/764/1/45.
- [368] Marco Tucci and Marta Volonteri. Constraining supermassive black hole evolution through the continuity equation. *Astron. Astrophys.*, 600:A64, 2017. doi: 10.1051/0004-6361/201628419.
- [369] Yue Shen, Michael A. Strauss, Masamune Oguri, Joseph F. Hennawi, Xiaohui Fan, Gordon T. Richards, Patrick B. Hall, James E. Gunn, Donald P. Schneider, Alexander S. Szalay, Anirudda R. Thakar, Daniel E. Vanden Berk, Scott F. Anderson, Neta A. Bahcall, Andrew J. Connolly, and Gillian R. Knapp. Clustering of High-Redshift ($z \geq 2.9$) Quasars from the Sloan Digital Sky Survey. *AJ*, 133(5):2222–2241, May 2007. doi: 10.1086/513517.

- [370] Martin White, Paul Martini, and J. D. Cohn. Constraints on the correlation between QSO luminosity and host halo mass from high-redshift quasar clustering. *MNRAS*, 390(3):1179–1184, November 2008. doi: 10.1111/j.1365-2966.2008.13817.x.
- [371] Francesco Shankar, Martin Crocce, Jordi Miralda-Escudé, Pablo Fosalba, and David H. Weinberg. On the Radiative Efficiencies, Eddington Ratios, and Duty Cycles of Luminous High-redshift Quasars. *ApJ*, 718(1):231–250, July 2010. doi: 10.1088/0004-637X/718/1/231.
- [372] Huanqing Chen and Nickolay Y. Gnedin. Constraints on the Duty Cycles of Quasars at $z \sim 6$. *ApJ*, 868(2):126, December 2018. doi: 10.3847/1538-4357/aae8e8.
- [373] Feige Wang, Frederick B. Davies, Jinyi Yang, Joseph F. Hennawi, Xiaohui Fan, Aaron J. Barth, Linhua Jiang, Xue-Bing Wu, Dale M. Mudd, Eduardo Bañados, Fuyan Bian, Roberto Decarli, Anna-Christina Eilers, Emanuele Paolo Farina, Bram Venemans, Fabian Walter, and Minghao Yue. A Significantly Neutral Intergalactic Medium Around the Luminous $z = 7$ Quasar J0252-0503. *ApJ*, 896(1):23, June 2020. doi: 10.3847/1538-4357/ab8c45.
- [374] Marcel Neeleman, Mladen Novak, Bram P. Venemans, Fabian Walter, Roberto Decarli, Melanie Kaasinen, Jan-Torge Schindler, Eduardo Bana-dos, Chris L. Carilli, Alyssa B. Drake, Xiaohui Fan, and Hans-Walter Rix. The Kinematics of $z \sim 6$ Quasar Host Galaxies. *arXiv e-prints*, art. arXiv:2102.05679, February 2021.
- [375] F. Fiore, S. Puccetti, A. Grazian, N. Menci, F. Shankar, P. Santini, E. Picon-celli, A. M. Koekemoer, A. Fontana, K. Boutsia, M. Castellano, A. Lamastra, C. Malacaria, C. Feruglio, S. Mathur, N. Miller, and M. Pannella. Faint high-redshift AGN in the Chandra deep field south: the evolution of the AGN luminosity function and black hole demography. *A&A*, 537:A16, January 2012. doi: 10.1051/0004-6361/201117581.
- [376] Yoshiki Matsuoka, Michael A. Strauss, Nobunari Kashikawa, Masafusa Onoue, Kazushi Iwasawa, Ji-Jia Tang, Chien-Hsiu Lee, Masatoshi Imanishi, Tohru Nagao, Masayuki Akiyama, Naoko Asami, James Bosch, Hisanori Furusawa, Tomotsugu Goto, James E. Gunn, Yuichi Harikane, Hiroyuki Ikeda, Takuma Izumi, Toshihiro Kawaguchi, Nanako Kato, Satoshi Kikuta, Kotaro Kohno, Yutaka Komiyama, Robert H. Lupton, Takeo Minezaki, Satoshi Miyazaki, Hitoshi Murayama, Mana Niida, Atsushi J. Nishizawa, Akatoki Noboriguchi, Masamune Oguri, Yoshiaki Ono, Masami Ouchi, Paul A. Price, Hiroaki Sameshima, Andreas Schulze, Hikari Shirakata, John D. Silverman, Naoshi Sugiyama, Philip J. Tait, Masahiro Takada, Tada-fumi Takata, Masayuki Tanaka, Yoshiki Toba, Yousuke Utsumi, Shiang-Yu Wang, and Takuji Yamashita. Subaru High- z Exploration of Low-luminosity

- Quasars (SHELLQs). V. Quasar Luminosity Function and Contribution to Cosmic Reionization at $z = 6$. *ApJ*, 869(2):150, December 2018. doi: 10.3847/1538-4357/aace7a.
- [377] Aaron A. Dutton and Andrea V. Macciò. Cold dark matter haloes in the Planck era: evolution of structural parameters for Einasto and NFW profiles. *MNRAS*, 441(4):3359–3374, July 2014. doi: 10.1093/mnras/stu742.
- [378] Linhao Ma, Philip F. Hopkins, Xiangcheng Ma, Daniel Anglés-Alcázar, Claude-André Faucher-Giguère, and Luke Zoltan Kelley. Seeds Don’t Sink: Even Massive Black Hole “Seeds” Cannot Migrate to Galaxy Centers Efficiently. *arXiv e-prints*, art. arXiv:2101.02727, January 2021.
- [379] Massimo Meneghetti, Guido Davoli, Pietro Bergamini, Piero Rosati, Priyamvada Natarajan, Carlo Giocoli, Gabriel B. Caminha, R. Benton Metcalf, Elena Rasia, Stefano Borgani, Francesco Calura, Claudio Grillo, Amata Mercurio, and Eros Vanzella. An excess of small-scale gravitational lenses observed in galaxy clusters. *Science*, 369(6509):1347–1351, September 2020. doi: 10.1126/science.aax5164.
- [380] Quinn E. Minor, Sophia Gad-Nasr, Manoj Kaplinghat, and Simona Vegetti. An unexpected high concentration for the dark substructure in the gravitational lens SDSSJ0946+1006. *arXiv e-prints*, art. arXiv:2011.10627, November 2020.
- [381] H. J. Mo, Shude Mao, and Simon D. M. White. The formation of galactic discs. *MNRAS*, 295(2):319–336, April 1998. doi: 10.1046/j.1365-8711.1998.01227.x.
- [382] A. Toomre. On the gravitational stability of a disk of stars. *ApJ*, 139:1217–1238, May 1964. doi: 10.1086/147861.
- [383] Giuseppe Lodato and Priyamvada Natarajan. Supermassive black hole formation during the assembly of pre-galactic discs. *MNRAS*, 371(4):1813–1823, October 2006. doi: 10.1111/j.1365-2966.2006.10801.x.
- [384] F. Hoyle and R. A. Lyttleton. The effect of interstellar matter on climatic variation. *Proceedings of the Cambridge Philosophical Society*, 35(3):405, January 1939. doi: 10.1017/S0305004100021150.
- [385] H. Bondi and F. Hoyle. On the mechanism of accretion by stars. *MNRAS*, 104:273, January 1944. doi: 10.1093/mnras/104.5.273.
- [386] H. Bondi. On spherically symmetrical accretion. *MNRAS*, 112:195, January 1952. doi: 10.1093/mnras/112.2.195.
- [387] E. Shima, T. Matsuda, H. Takeda, and K. Sawada. Hydrodynamic calculations of axisymmetric accretion flow. *MNRAS*, 217:367–386, November 1985. doi: 10.1093/mnras/217.2.367.

- [388] Anastasia Sokolenko, Kyrylo Bondarenko, Thejs Brinckmann, Jesús Zavala, Mark Vogelsberger, Torsten Bringmann, and Alexey Boyarsky. Towards an improved model of self-interacting dark matter haloes. *J. Cosmol. Astropart. Phys.*, 2018(12):038, December 2018. doi: 10.1088/1475-7516/2018/12/038.
- [389] Volker Springel. E pur si muove: Galilean-invariant cosmological hydrodynamical simulations on a moving mesh. *MNRAS*, 401(2):791–851, January 2010. doi: 10.1111/j.1365-2966.2009.15715.x.
- [390] Planck Collaboration, P. A. R. Ade, N. Aghanim, M. Arnaud, M. Ashdown, J. Aumont, C. Baccigalupi, A. J. Banday, R. B. Barreiro, J. G. Bartlett, N. Bartolo, E. Battaner, R. Battye, K. Benabed, A. Benoît, A. Benoit-Lévy, J. P. Bernard, M. Bersanelli, P. Bielewicz, J. J. Bock, A. Bonaldi, L. Bonavera, J. R. Bond, J. Borrill, F. R. Bouchet, F. Boulanger, M. Bucher, C. Burigana, R. C. Butler, E. Calabrese, J. F. Cardoso, A. Catalano, A. Challinor, A. Chamballu, R. R. Chary, H. C. Chiang, J. Chluba, P. R. Christensen, S. Church, D. L. Clements, S. Colombi, L. P. L. Colombo, C. Combet, A. Coulais, B. P. Crill, A. Curto, F. Cuttaia, L. Danese, R. D. Davies, R. J. Davis, P. de Bernardis, A. de Rosa, G. de Zotti, J. Delabrouille, F. X. Désert, E. Di Valentino, C. Dickinson, J. M. Diego, K. Dolag, H. Dole, S. Donzelli, O. Doré, M. Douspis, A. Ducout, J. Dunkley, X. Dupac, G. Efstathiou, F. Elsner, T. A. Enßlin, H. K. Eriksen, M. Farhang, J. Fergusson, F. Finelli, O. Forni, M. Frailis, A. A. Fraisse, E. Franceschi, A. Frejsel, S. Galeotta, S. Galli, K. Ganga, C. Gauthier, M. Gerbino, T. Ghosh, M. Giard, Y. Giraud-Héraud, E. Giusarma, E. Gjerløw, J. González-Nuevo, K. M. Górski, S. Gratton, A. Gregorio, A. Gruppuso, J. E. Gudmundsson, J. Hamann, F. K. Hansen, D. Hanson, D. L. Harrison, G. Helou, S. Henrot-Versillé, C. Hernández-Monteagudo, D. Herranz, S. R. Hildebrandt, E. Hivon, M. Hobson, W. A. Holmes, A. Hornstrup, W. Hovest, Z. Huang, K. M. Huffenberger, G. Hurier, A. H. Jaffe, T. R. Jaffe, W. C. Jones, M. Juvela, E. Keihänen, R. Keskitalo, T. S. Kisner, R. Kneissl, J. Knoche, L. Knox, M. Kunz, H. Kurki-Suonio, G. Lagache, A. Lähteenmäki, J. M. Lamarre, A. Lasenby, M. Lattanzi, C. R. Lawrence, J. P. Leahy, R. Leonardi, J. Lesgourgues, F. Levrier, A. Lewis, M. Liguori, P. B. Lilje, M. Linden-Vørnle, M. López-Cañiego, P. M. Lubin, J. F. Macías-Pérez, G. Maggio, D. Maino, N. Mandolesi, A. Mangilli, A. Marchini, M. Maris, P. G. Martin, M. Martinelli, E. Martínez-González, S. Masi, S. Matarrese, P. McGee, P. R. Meinhold, A. Melchiorri, J. B. Melin, L. Mendes, A. Mennella, M. Migliaccio, M. Millea, S. Mitra, M. A. Miville-Deschênes, A. Moneti, L. Montier, G. Morgante, D. Mortlock, A. Moss, D. Munshi, J. A. Murphy, P. Naselsky, F. Nati, P. Natoli, C. B. Netterfield, H. U. Nørgaard-Nielsen, F. Noviello, D. Novikov, I. Novikov, C. A. Oxborrow, F. Paci, L. Pagano, F. Pajot, R. Paladini, D. Paoletti, B. Partridge, F. Pasian, G. Patanchon, T. J. Pearson, O. Perdereau, L. Perotto, F. Perrotta, V. Pettorino, F. Piacentini, M. Piat, E. Pierpaoli, D. Pietrobon, S. Plaszczynski, E. Pointecouteau, G. Polenta,

- L. Popa, G. W. Pratt, G. Prézeau, S. Prunet, J. L. Puget, J. P. Rachen, W. T. Reach, R. Rebolo, M. Reinecke, M. Remazeilles, C. Renault, A. Renzi, I. Ristortocelli, G. Rocha, C. Rosset, M. Rossetti, G. Roudier, B. Rouillé d'Orfeuille, M. Rowan-Robinson, J. A. Rubiño-Martín, B. Rusholme, N. Said, V. Salvatelli, L. Salvati, M. Sandri, D. Santos, M. Savelainen, G. Savini, D. Scott, M. D. Seiffert, P. Serra, E. P. S. Shellard, L. D. Spencer, M. Spinelli, V. Stolyarov, R. Stompor, R. Sudiwala, R. Sunyaev, D. Sutton, A. S. Suur-Uski, J. F. Sygnet, J. A. Tauber, L. Terenzi, L. Toffolatti, M. Tomasi, M. Tristram, T. Trombetti, M. Tucci, J. Tuovinen, M. Türler, G. Umana, L. Valenziano, J. Valiviita, F. Van Tent, P. Vielva, F. Villa, L. A. Wade, B. D. Wandelt, I. K. Wehus, M. White, S. D. M. White, A. Wilkinson, D. Yvon, A. Zacchei, and A. Zonca. Planck 2015 results. XIII. Cosmological parameters. *A&A*, 594: A13, September 2016. doi: 10.1051/0004-6361/201525830.
- [391] A. B. Mantz, S. W. Allen, R. G. Morris, D. A. Rapetti, D. E. Applegate, P. L. Kelly, A. von der Linden, and R. W. Schmidt. Cosmology and astrophysics from relaxed galaxy clusters - II. Cosmological constraints. *MNRAS*, 440(3): 2077–2098, May 2014. doi: 10.1093/mnras/stu368.
- [392] Randall K. Smith, Nancy S. Brickhouse, Duane A. Liedahl, and John C. Raymond. Collisional Plasma Models with APEC/APED: Emission-Line Diagnostics of Hydrogen-like and Helium-like Ions. *ApJ*, 556(2):L91–L95, August 2001. doi: 10.1086/322992.
- [393] A. R. Foster, L. Ji, R. K. Smith, and N. S. Brickhouse. Updated Atomic Data and Calculations for X-Ray Spectroscopy. *ApJ*, 756(2):128, September 2012. doi: 10.1088/0004-637X/756/2/128.
- [394] E. Anders and N. Grevesse. Abundances of the elements: Meteoritic and solar. *Geochimica et Cosmochimica Acta*, 53(1):197–214, January 1989. doi: 10.1016/0016-7037(89)90286-X.
- [395] M. McDonald, E. Bulbul, T. de Haan, E. D. Miller, B. A. Benson, L. E. Bleem, M. Brodwin, J. E. Carlstrom, I. Chiu, W. R. Forman, J. Hlavacek-Larrondo, G. P. Garmire, N. Gupta, J. J. Mohr, C. L. Reichardt, A. Saro, B. Stalder, A. A. Stark, and J. D. Vieira. The Evolution of the Intracluster Medium Metallicity in Sunyaev Zel'dovich-selected Galaxy Clusters at $0 < z < 1.5$. *ApJ*, 826(2):124, August 2016. doi: 10.3847/0004-637X/826/2/124.
- [396] Adam B. Mantz, Steven W. Allen, R. Glenn Morris, Aurora Simionescu, Ondrej Urban, Norbert Werner, and Irina Zhuravleva. The metallicity of the intracluster medium over cosmic time: further evidence for early enrichment. *MNRAS*, 472(3):2877–2888, December 2017. doi: 10.1093/mnras/stx2200.
- [397] R. Morrison and D. McCammon. Interstellar photoelectric absorption cross sections, 0.03-10 keV. *ApJ*, 270:119–122, July 1983. doi: 10.1086/161102.

- [398] K. M. Górski, E. Hivon, A. J. Banday, B. D. Wandelt, F. K. Hansen, M. Reinecke, and M. Bartelmann. HEALPix: A Framework for High-Resolution Discretization and Fast Analysis of Data Distributed on the Sphere. *ApJ*, 622(2):759–771, April 2005. doi: 10.1086/427976.
- [399] Robert I. Jedrzejewski. CCD surface photometry of elliptical galaxies - I. Observations, reduction and results. *MNRAS*, 226:747–768, June 1987. doi: 10.1093/mnras/226.4.747.
- [400] N. Kaiser. Evolution and clustering of rich clusters. *MNRAS*, 222:323–345, September 1986. doi: 10.1093/mnras/222.2.323.
- [401] Erwin T. Lau, Andrey V. Kravtsov, and Daisuke Nagai. Residual Gas Motions in the Intracluster Medium and Bias in Hydrostatic Measurements of Mass Profiles of Clusters. *ApJ*, 705(2):1129–1138, November 2009. doi: 10.1088/0004-637X/705/2/1129.
- [402] F. Vazza, G. Brunetti, C. Gheller, R. Brunino, and M. Brüggen. Massive and refined. II. The statistical properties of turbulent motions in massive galaxy clusters with high spatial resolution. *A&A*, 529:A17, May 2011. doi: 10.1051/0004-6361/201016015.
- [403] Kaylea Nelson, Erwin T. Lau, and Daisuke Nagai. Hydrodynamic Simulation of Non-thermal Pressure Profiles of Galaxy Clusters. *ApJ*, 792(1):25, September 2014. doi: 10.1088/0004-637X/792/1/25.
- [404] David A. Buote and Claude R. Canizares. Geometrical Evidence for Dark Matter: X-Ray Constraints on the Mass of the Elliptical Galaxy NGC 720. *ApJ*, 427:86, May 1994. doi: 10.1086/174123.
- [405] Andrea Morandi, Kristian Pedersen, and Marceau Limousin. Unveiling the Three-dimensional Structure of Galaxy Clusters: Resolving the Discrepancy Between X-ray and Lensing Masses. *ApJ*, 713(1):491–502, April 2010. doi: 10.1088/0004-637X/713/1/491.
- [406] Marceau Limousin, Andrea Morandi, Mauro Sereno, Massimo Meneghetti, Stefano Ettori, Matthias Bartelmann, and Tomas Verdugo. The Three-Dimensional Shapes of Galaxy Clusters. *Space Science Reviews*, 177(1-4): 155–194, August 2013. doi: 10.1007/s11214-013-9980-y.
- [407] John L Hodges. The significance probability of the smirnov two-sample test. *Arkiv för Matematik*, 3(5):469–486, 1958.
- [408] Theodore W Anderson and Donald A Darling. Asymptotic theory of certain "goodness of fit" criteria based on stochastic processes. *The annals of mathematical statistics*, pages 193–212, 1952.
- [409] Theodore W Anderson and Donald A Darling. A test of goodness of fit. *Journal of the American statistical association*, 49(268):765–769, 1954.

- [410] Donald A Darling. The kolmogorov-smirnov, cramer-von mises tests. *The Annals of Mathematical Statistics*, 28(4):823–838, 1957.
- [411] Ao No Pettitt. A two-sample anderson-darling rank statistic. *Biometrika*, 63(1):161–168, 1976.
- [412] Fritz W Scholz and Michael A Stephens. K-sample anderson–darling tests. *Journal of the American Statistical Association*, 82(399):918–924, 1987.
- [413] Taotao Fang, Philip Humphrey, and David Buote. Rotation and Turbulence of the Hot Intracluster Medium in Galaxy Clusters. *ApJ*, 691(2):1648–1659, February 2009. doi: 10.1088/0004-637X/691/2/1648.
- [414] Erwin T. Lau, Daisuke Nagai, Andrey V. Kravtsov, and Andrew R. Zentner. Shapes of Gas, Gravitational Potential, and Dark Matter in Λ CDM Clusters. *ApJ*, 734(2):93, June 2011. doi: 10.1088/0004-637X/734/2/93.
- [415] N. Battaglia, J. R. Bond, C. Pfrommer, and J. L. Sievers. On the Cluster Physics of Sunyaev-Zel’dovich and X-Ray Surveys. I. The Influence of Feedback, Non-thermal Pressure, and Cluster Shapes on Y-M Scaling Relations. *ApJ*, 758(2):74, October 2012. doi: 10.1088/0004-637X/758/2/74.
- [416] Daichi Suto, Sébastien Peirani, Yohan Dubois, Tetsu Kitayama, Takahiro Nishimichi, Shin Sasaki, and Yasushi Suto. Projected axis ratios of galaxy clusters in the Horizon-AGN simulation: Impact of baryon physics and comparison with observations. *Publications of the Astronomical Society of Japan*, 69(1):14, February 2017. doi: 10.1093/pasj/psw118.
- [417] D. Eckert, F. Vazza, S. Ettori, S. Molendi, D. Nagai, E. T. Lau, M. Roncarelli, M. Rossetti, S. L. Snowden, and F. Gastaldello. The gas distribution in the outer regions of galaxy clusters. *A&A*, 541:A57, May 2012. doi: 10.1051/0004-6361/201118281.
- [418] John Dubinski. The Effect of Dissipation on the Shapes of Dark Halos. *ApJ*, 431:617, August 1994. doi: 10.1086/174512.
- [419] August E. Evrard, F. J. Summers, and Marc Davis. Two-Fluid Simulations of Galaxy Formation. *ApJ*, 422:11, February 1994. doi: 10.1086/173700.
- [420] P. B. Tissera and R. Dominguez-Tenreiro. Dark matter halo structure in CDM hydrodynamical simulations. *MNRAS*, 297(1):177–194, June 1998. doi: 10.1046/j.1365-8711.1998.01440.x.
- [421] Stelios Kazantzidis, Andrey V. Kravtsov, Andrew R. Zentner, Brandon Allgood, Daisuke Nagai, and Ben Moore. The Effect of Gas Cooling on the Shapes of Dark Matter Halos. *ApJ*, 611(2):L73–L76, August 2004. doi: 10.1086/423992.

- [422] Victor P. Debattista, Ben Moore, Thomas Quinn, Stelios Kazantzidis, Ryan Maas, Lucio Mayer, Justin Read, and Joachim Stadel. The Causes of Halo Shape Changes Induced by Cooling Baryons: Disks versus Substructures. *ApJ*, 681(2):1076–1088, July 2008. doi: 10.1086/587977.
- [423] Andrew Robertson, Richard Massey, Vincent Eke, Sean Tulin, Hai-Bo Yu, Yannick Bahé, David J. Barnes, Richard G. Bower, Robert A. Crain, Claudio Dalla Vecchia, Scott T. Kay, Matthieu Schaller, and Joop Schaye. The diverse density profiles of galaxy clusters with self-interacting dark matter plus baryons. *MNRAS*, 476(1):L20–L24, May 2018. doi: 10.1093/mnras/sly024.